Technical Physics, Vol. 48, No. 3, 2003, pp. 275–283. Translated from Zhurnal Tekhnicheskoĭ Fiziki, Vol. 73, No. 3, 2003, pp. 1–9.

THEORETICAL AND MATHEMATICAL PHYSICS

Nonlinear Dynamics of the Interface between Continuous Media with Different Densities

N. B. Volkov, A. E. Maĭer, and A. P. Yalovets

Institute of Electrophysics, Ural Division, Russian Academy of Sciences, ul. Amundsena 106, Yekaterinburg, 620016 Russia

e-mail: nbv@ami.uran.ru, nbv@iep.uran.ru

Received April 27, 2002; in final form, September 16, 2002

Abstract—By reducing the hydrodynamic flow in the volume occupied by one or two fluids with different densities to the dynamics of the free surface or interface, equations describing their evolution are derived. These equations make it possible to study the essentially nonlinear stages of instability of free surfaces or interfaces in simple mathematical terms. It is shown that a perturbation of the free surface, however small, causes the formation and separation of a drop for a finite time. Accordingly, a perturbation, however small, of the interface between media with different densities results in the formation and subsequent separation of a large-scale vortex of the heavier fluid. Theoretical results agree qualitatively and quantitatively with experiments performed in [1, 2]. © *2003 MAIK "Nauka/Interperiodica".*

INTRODUCTION

Theoretical investigation into the stability of the free surface or interface between two continuous media (fluids) with different densities in the gravitational field (Rayleigh–Taylor gravitational instability) or in a magnetic field (Rayleigh–Taylor magnetohydrodynamic instability) [3], as well as instabilities caused by a shock-wave- or pressure-pulse-induced acceleration (Richtmyer–Meshkov instabilities [4, 5]), are of great scientific and applied interest [6, 7]. Examples of their application are the generation of pulsed powerful X-ray radiation from a plasma [8] and solid surface modification by the action of intense beams of charged particles [9–11]. The essentially nonlinear stages, including the vortex stage, are usually studied numerically. As a rule, an initial distribution of point vortices (the vortex method [12]) or a distribution of small finite-size vortices (the vortex drop method [13]) is specified at the interface. These methods, while providing fairly reasonable results, suffer from the considerable disadvantage that the vortex distributions over the interface and sizes are uncertain. The purpose of this work is to elaborate a method for studying the interface dynamics such that the distribution of point or finite-size vortices is unneeded. Our study is based on the method [14], with which we analyzed the vortex-free stage of nonlinear interface dynamics. Also, we rely on the fact that the interface dynamics can be adequately studied on the assumption that the fluids are incompressible [4, 14–16].

DYNAMIC EQUATIONS FOR FREE SURFACE AND INTERFACE

We will deal with an ideal incompressible fluid occupying a volume bounded above by the surface $F(X, Z, t) = 0$ (hereafter, X and Z are the coordinates of boundary points). Our first goal is to reduce the hydrodynamic volume flow of the fluid to the dynamics of its boundary. The equations of motion of an ideal incompressible fluid have the form [17]

$$(\nabla \cdot \mathbf{v}) = 0; \tag{1}$$

$$\frac{\partial \mathbf{v}}{\partial t} + [\Omega \times \mathbf{v}] = -\nabla\left(\frac{P}{\rho} + \frac{v^2}{2} + G\right), \tag{2}$$

where $\mathbf{v} = \{v_x(x, z, t), 0, v_z(x, z, t)\}$ is the hydrodynamic velocity, $\Omega = [\nabla \times \mathbf{v}] = \{0, \Omega(x, z, t), 0\}$ is the vorticity, $P(x, z, t)$ is pressure, and $G(x, z, t)$ is the external field potential. The vectors in the parentheses and brackets mean the scalar and vector products, respectively.

According to the well-known Helmholtz theorem, one can put $\mathbf{v} = \nabla\varphi + [\nabla \times \mathbf{A}]$. Here, $\varphi(x, z, t)$ is the scalar velocity potential and $\mathbf{A} = \{0, -\psi(x, z, t), 0\}$ is the vector velocity potential satisfying Coulomb gauge $(\nabla \cdot \mathbf{A}) = 0$. Then, it follows from (1) that the scalar potential satisfies the Laplace equation

$$\Delta\varphi(x, z, t) = 0, \tag{3}$$

where Δ is Laplacian.

Applying the operator $[\nabla \times \mathbf{v}]$ to Eq. (2), we will obtain for the vorticity $\Omega = \Delta\psi$

$$\frac{\partial \Delta\psi}{\partial t} + (\mathbf{v} \cdot \nabla)\Delta\psi = 0. \tag{4}$$

1063-7842/03/4803-0275$24.00 © 2003 MAIK "Nauka/Interperiodica"

From Eq. (4), it follows that if the vorticity $\Omega(x, z, 0) = \Delta\psi(x, z, 0) = 0$ at the initial time instant, it also equals zero at any other time instant:

$$\Omega(x, z, t) = \Delta\psi(x, z, t) = 0. \quad (5)$$

In an ideal incompressible fluid, vorticity may appear only when its free surface (or interface) becomes unstable [18] and is introduced into a forbidden area by convection. It is the latter prerequisite that prompted the authors of [12, 13] to specify the initial distribution of point [12] or finite-size [13] vortices at the interface when they analyzed the vortex stage of Richtmyer–Meshkov instability. We will show below that there is no need to do this.

From Eq. (2) in view of (5), we arrive at the Bernoulli equation [17]

$$\left.\frac{\partial\varphi}{\partial t}\right|_{(X, Z)} = -\frac{v^2(X, Z, t)}{2} - G(X, Z, t) = 0, \quad (6)$$

which also applies to the free boundary $P(X, Z, t) = 0$ [17, 19].

Bernoulli equation (6) and the so-called kinematic condition $D(X, Z, t) - (\mathbf{v}(X, Z, t) \cdot \mathbf{n}(X, Z, t)) = 0$ (D is the phase velocity of the boundary and $\mathbf{n}$ is the normal to the boundary), according to which boundary points are "frozen" in the fluid, constitute boundary conditions on the free surface for the Laplace equation. At the lower boundary $z = -\infty$, the range of solutions for the velocity and the potentials vanish. At the left and right boundaries, the periodic conditions are specified: the equality of the velocities and potentials at the points $x = 0$ and λ.

At the essentially nonlinear stages of boundary instability, there may appear a situation where the boundary dynamics cannot be uniquely described by a function of one variable X. In the case of a large-scale disturbance ("large scale" is limited below by the condition of existence of tangent, $\boldsymbol{\tau}(X, Z, t)$, and normal, $\mathbf{n}(X, Z, t)$, vectors at an arbitrary point and also by the condition of applicability of the hydrodynamic approximation), the boundary should be described parametrically using two functions: $x = X(l, t)$ and $z = Z(l, t)$ (where l is the contour length along the boundary starting from some separated point). The remaining parameters of the fluid that are specified at the boundary are also functions of l and t. According to the kinematic condition, boundary points are frozen in the fluid and move with a velocity $\mathbf{v}(X, Z, t)$. Consequently, the value of the parameter l for a fixed boundary point also varies with time: $l = l(l_0, t)$, where l_0 is some Lagrangean coordinate of the fixed boundary point, for example, the value of l at the initial time instant. In this case,

$$\frac{dX(l, t)}{dt} = v_x(l, t), \quad (7)$$

$$\frac{dZ(l, t)}{dt} = v_z(l, t). \quad (8)$$

The vectors $\boldsymbol{\tau}(l, t)$ and $\mathbf{n}(l, t)$ are given by

$$\tau_x(l, t) = n_z(l, t) = \frac{\partial X}{\partial l}\left(\left(\frac{\partial X}{\partial l}\right)^2 + \left(\frac{\partial Z}{\partial l}\right)^2\right)^{-1/2}, \quad (9)$$

$$\tau_z(l, t) = -n_x(l, t) = \frac{\partial Z}{\partial l}\left(\left(\frac{\partial X}{\partial l}\right)^2 + \left(\frac{\partial Z}{\partial l}\right)^2\right)^{-1/2}. \quad (10)$$

Taking into account that $(\mathbf{v} \cdot \boldsymbol{\tau}) = \partial\varphi(l, t)/\partial l$ and $(\mathbf{v} \cdot \mathbf{n}) = -\partial\psi(l, t)/\partial l$ and also (9) and (10), we can now relate the velocities to the derivatives of the potential φ and stream function ψ along the boundary:

$$v_x(l, t) = \frac{\partial\varphi(l, t)}{\partial l}\tau_x(l, t) + \frac{\partial\psi(l, t)}{\partial l}\tau_z(l, t)$$
$$= \left(\frac{\partial\varphi(l, t)}{\partial l}\frac{\partial X}{\partial l} + \frac{\partial\psi(l, t)}{\partial l}\frac{\partial Z}{\partial l}\right)\left(\left(\frac{\partial X}{\partial l}\right)^2 + \left(\frac{\partial Z}{\partial l}\right)^2\right)^{-1/2}, \quad (11)$$

$$v_z(l, t) = \frac{\partial\varphi(l, t)}{\partial l}\tau_z(l, t) - \frac{\partial\psi(l, t)}{\partial l}\tau_x(l, t)$$
$$= \left(\frac{\partial\varphi(l, t)}{\partial l}\frac{\partial Z}{\partial l} - \frac{\partial\psi(l, t)}{\partial l}\frac{\partial X}{\partial l}\right)\left(\left(\frac{\partial X}{\partial l}\right)^2 + \left(\frac{\partial Z}{\partial l}\right)^2\right)^{-1/2}. \quad (12)$$

The total derivative of the potential at a fixed point of the moving boundary and the partial derivative of the potential are related as

$$\frac{d\varphi(l, t)}{dt} = \frac{\partial\varphi(l, t)}{\partial t} + v_x(l, t)\frac{dX}{dt} + v_z(l, t)\frac{dZ}{dt}$$
$$= \frac{\partial\varphi(l, t)}{\partial t} + v^2(l, t), \quad (13)$$

where the second term describes the variation of the potential as the point of observation moves.

Relationships (11)–(13) allow one to rewrite Bernoulli equation (6) in the form

$$\frac{d\varphi(l, t)}{dt} = \frac{1}{2}\left(\left(\frac{\partial\varphi(l, t)}{\partial l}\right)^2 + \left(\frac{\partial\psi(l, t)}{\partial l}\right)^2\right) - G(l, t). \quad (14)$$

Following our work [14], we will describe the evolution of the free surface without calculating the volume flow. Such an approach is basically validated by the fact that the velocity potential φ and the stream function ψ are harmonic functions and, hence, are completely defined by the boundary conditions. In this case, it is necessary to find the normal derivative of the potential from its boundary value or, which is the same, to establish a relationship between $\psi(l, t)$ and $\varphi(l, t)$.

In [20], the Laplace equation for an area with an irregular boundary was solved with conformal transformations. Let us perform coordinate transformation

$(x, z) \longrightarrow (\xi, \eta)$. In terms of the new variables, Eq. (3) takes the form

$$\frac{\partial^2\varphi}{\partial\xi^2}|\nabla_{(x,z)}\xi|^2 + \frac{\partial^2\varphi}{\partial\eta^2}|\nabla_{(x,z)}\eta|^2 + 2\frac{\partial^2\varphi}{\partial\xi\partial\eta}(\nabla_{(x,z)}\xi\cdot\nabla_{(x,z)}\eta) + \frac{\partial\varphi}{\partial\xi}\Delta_{(x,z)}\xi + \frac{\partial\varphi}{\partial\eta}\Delta_{(x,z)}\eta = 0. \quad (15)$$

In order for Eq. (15) in the variables (ξ, η) to be the Laplace equation in the form $\Delta_{(\xi,\eta)}\varphi(\xi, \eta) = 0$, it is necessary that the following conditions be fulfilled:

$$|\nabla_{(x,z)}\xi|^2 = |\nabla_{(x,z)}\eta|^2, \quad (16)$$

$$(\nabla_{(x,z)}\xi\cdot\nabla_{(x,z)}\eta) = 0, \quad (17)$$

$$\Delta_{(x,z)}\xi = 0, \quad \Delta_{(x,z)}\eta = 0. \quad (18)$$

Since the new coordinate system is arbitrary, we put

$$\nabla_{(x,z)}\eta = [\nabla_{(x,z)}\xi\times\mathbf{e}_y]. \quad (19)$$

Now conditions (16) and (17), as well as the second equation of (18), are fulfilled automatically.

The coordinate transformation performed above must not only retain the form of the Laplace equation but also convert the fluid-filled space to a half-plane, e.g., $\eta \le 0$. Let us define the unit vector $\boldsymbol{\tau}$ tangent to the boundary as

$$\boldsymbol{\tau} = \nabla_{(x,z)}\xi|_{(X(l),\,Z(l))}. \quad (20)$$

Then, from (19), $\nabla_{(x,z)}\eta|_{(X(l),\,Z(l))} = \mathbf{n}$, where $\mathbf{n}$ is the outer normal to the boundary. Hence, $\partial\eta/\partial l = (\nabla_{(x,z)}\eta\cdot\boldsymbol{\tau}) = 0$ along the boundary and the coordinate η at the boundary has some constant value, which can be set equal to zero. Such a coordinate transformation does convert the fluid-filled space to the half-plane $\eta \le 0$. The variable ξ at the boundary can be found from the relationship $\partial\xi/\partial l = (\nabla_{(x,z)}\xi\cdot\boldsymbol{\tau}) = 1$ for its derivative along the boundary. Integrating this relationship along the contour yields

$$\xi(X(l), Z(l)) = l \quad (21)$$

up to a constant.

Another boundary condition can be specified, e.g., by putting

$$\xi(x, z) \longrightarrow x \quad \text{for} \quad x \longrightarrow -\infty. \quad (22)$$

The first of Eqs. (18) in combination with boundary conditions (21) and (22) represent the first boundary-value problem for the Laplace equation for the function $\xi(x, z)$ and, consequently, has a unique solution. Thus, it is possible to find coordinates (ξ, η) such that they meet conditions (19) and (20) and do not change the form of the Laplace equation. The transformation defined by conditions (19) and (20) converts the fluid-filled space to a half-plane. It should be noted that finding a specific transformation of this type is a problem no less complicated than the initial problem, since it also requires the Laplace equation to be solved in a complex-geometry area. Fortunately, to establish a relation between the value of a harmonic function at the boundary and its normal derivative does not require finding $\xi(x, z)$ and $\eta(x, z)$ in explicit form. With this aim in view, we note that this transformation has the important properties that $\eta = 0$ and $(\mathbf{n}\cdot\nabla) = \partial/\partial\eta$ along the contour $\xi = l$. The latter equality follows from the fact that by definition $\nabla_{(x,z)}\xi$ and $\nabla_{(x,z)}\eta$ are the vectors of the reciprocal basis [21]. Since this set of vectors is orthonormalized along the boundary, the local basis coincides with the reciprocal basis at boundary points; that is, $\mathbf{e}_\xi|_{(X(l),\,Z(l))} = \nabla_{(x,z)}\xi|_{(X(l),\,Z(l))} = \boldsymbol{\tau}$ and $\mathbf{e}_\eta|_{(X(l),\,Z(l))} = \nabla_{(x,z)}\eta|_{(X(l),\,Z(l))} = \mathbf{n}$. Then, the derivative $\partial/\partial\eta = (\mathbf{e}_\eta\cdot\nabla) = (\mathbf{n}\cdot\nabla)$ at boundary points.

The decaying (at $\eta \longrightarrow -\infty$) solution to the Laplace equation for the function $\varphi(\xi, \eta)$ in the domain $\eta \le 0$ can be written through $\varphi(\xi, 0, t)$ as

$$\varphi(\xi, \eta, t) = \frac{1}{2\pi}\int_{-\infty}^{+\infty}dk\int_{-\infty}^{+\infty}\varphi(\xi', 0, t)e^{|k|\eta}\cos(k(\xi-\xi'))d\xi'.$$

Differentiating this expression with respect to η yields (in view of (19)–(21)) an expression for the derivative of φ normal to the boundary:

$$(\mathbf{n}\cdot\nabla\varphi) = \left.\frac{\partial\varphi}{\partial\eta}\right|_{\eta=0} = \hat{k}\varphi|_{\eta=0}. \quad (23)$$

Here, $\hat{k}$ is the integral operator [22]:

$$\hat{k}f(l) = \frac{1}{2\pi}\int_{-\infty}^{+\infty}|k|dk\int_{-\infty}^{+\infty}f(l')\cos(k(l-l'))dl'. \quad (24)$$

The important properties of the operator k and reciprocal operator $\hat{k}^{-1}$ are the following:

$$\hat{k}e^{ikl} = |k|e^{ikl}, \quad \hat{k}^{-1}e^{ikl} = \frac{1}{|k|}e^{ikl}.$$

The stream function ψ also meets Laplace equation (5). Taking into account that $(\mathbf{v}\cdot\boldsymbol{\tau}) = (\mathbf{n}\cdot\nabla\psi)$, we can write

$$(\mathbf{v}\cdot\boldsymbol{\tau}) = \left.\frac{\partial\psi}{\partial\eta}\right|_{\eta=0} = \hat{k}\psi|_{\eta=0}.$$

On the other hand, the tangential velocity component is $(\mathbf{v}\cdot\boldsymbol{\tau}) = \partial\varphi(l, \eta = 0)/\partial l$. Hence, we can relate the stream function and the derivative of the potential (hereafter, we consider only values at the boundary and omit the argument $\eta = 0$):

$$\psi(l, t) = \hat{k}^{-1}\frac{\partial\varphi(l, t)}{\partial l}. \quad (25)$$

Relationship (25) is valid for a smooth contour where the normal and tangent vectors are defined at each point.

Expanding the potential at the boundary into the Fourier series in l yields for Eq. (25)

$$\psi(l,t) = \frac{2}{L(t)}\sum_{n=1}^{\infty}\int_{0}^{L(t)}\varphi(l',t)\sin(nK(t)(l'-l))dl', \quad (26)$$

where $L(t)$ is the current total length of the contour and $K(t) = 2\pi/L(t)$ is its associated wavenumber.

Equations (7), (8), and (14) combined with relationships (11), (12), and (25) (or (26)) make up a closed set that describes the evolution of the free surface of the fluid.

Consider now a system of two perfect incompressible fluids with different densities. Let the upper fluid have a density ρ^- and the lower, a density ρ^+ ($\rho^- < \rho^+$). All quantities that refer to the heavier and lighter fluids will have the associated superscript (+ and –, respectively). Then, Eqs. (6), (11), (12), and (25) are recast as follows:

$$\frac{\partial\varphi^{\pm}(l,t)}{\partial t} = -\frac{1}{2}\left(\left(\frac{\partial\varphi^{\pm}}{\partial l}\right)^2+\left(\frac{\partial\psi^{\pm}}{\partial l}\right)^2\right)-\frac{P^{\pm}}{\rho^{\pm}}-G(l,t), \quad (27)$$

$$\begin{aligned} v_x^{\pm}(l,t) &= \frac{\partial\varphi^{\pm}(l,t)}{\partial l}\tau_x(l,t)+\frac{\partial\psi^{\pm}(l,t)}{\partial l}\tau_z(l,t)\\ &= \left(\frac{\partial\varphi^{\pm}(l,t)}{\partial l}\frac{\partial X}{\partial l}+\frac{\partial\psi^{\pm}(l,t)}{\partial l}\frac{\partial Z}{\partial l}\right)\\ &\quad\times\left(\left(\frac{\partial X}{\partial l}\right)^2+\left(\frac{\partial Z}{\partial l}\right)^2\right)^{-1/2}, \end{aligned} \quad (28)$$

$$\begin{aligned} v_z^{\pm}(l,t) &= \frac{\partial\varphi^{\pm}(l,t)}{\partial l}\tau_z(l,t)-\frac{\partial\psi^{\pm}(l,t)}{\partial l}\tau_x(l,t)\\ &= \left(\frac{\partial\varphi^{\pm}(l,t)}{\partial l}\frac{\partial Z}{\partial l}-\frac{\partial\psi^{\pm}(l,t)}{\partial l}\frac{\partial X}{\partial l}\right)\\ &\quad\times\left(\left(\frac{\partial X}{\partial l}\right)^2+\left(\frac{\partial Z}{\partial l}\right)^2\right)^{-1/2}, \end{aligned} \quad (29)$$

$$\psi^{\pm}(l,t) = \pm\hat{k}^{-1}\frac{\partial\varphi^{\pm}(l,t)}{\partial l}. \quad (30)$$

Let points at the interface be frozen in the heavier fluid. We then have

$$\frac{dX(l,t)}{dt} = v_x^+(l,t), \quad (31)$$

$$\frac{dZ(l,t)}{dt} = v_z^+(l,t). \quad (32)$$

In this case, the kinematic condition has the form [17, 19] $D - (\mathbf{v}^+\cdot\mathbf{n}) = D - (\mathbf{v}^-\cdot\mathbf{n}) = 0$; hence, we have continuity of the normal velocities of the fluids at the interface: $(\mathbf{v}^+\cdot\mathbf{n}) = (\mathbf{v}^-\cdot\mathbf{n}) = 0$ or $\partial\psi^+/\partial l = \partial\psi^-/\partial l$. Integrating the latter equality yields

$$\psi^+(l,t) = \psi^-(l,t). \quad (33)$$

From (30) in view of (33), it follows that $\partial\varphi^+/\partial l = -\partial\varphi^-/\partial l$. Integrating, we find that

$$\varphi^+(l,t) = -\varphi^-(l,t) \quad (34)$$

at the interface.

The equality of the normal velocities leads to the equality of the pressures at the interface [17, 19]: $P^+(l,t) = P^-(l,t) = P(l,t)$.

The total time derivative of the potential $\varphi^+(l,t)$ and its partial derivative are related as

$$\frac{d\varphi^+}{dt} = \frac{\partial\varphi^+}{\partial t}+(v^+)^2 = \frac{\partial\varphi^+}{\partial t}+\left(\frac{\partial\varphi^+}{\partial l}\right)^2+\left(\frac{\partial\psi^+}{\partial l}\right)^2. \quad (35)$$

Accordingly, the total time derivative of the potential $\varphi^-(l,t)$ is

$$\begin{aligned} \frac{d\varphi^-}{dt} &= \frac{d\varphi^-}{\partial t}+v_x^-\frac{dX}{dt}+v_z^-\frac{dZ}{dt} = \frac{\partial\varphi^-}{\partial t}+v_x^-v_x^++v_z^-v_z^+\\ &= \frac{\partial\varphi^-}{\partial t}+\frac{\partial\varphi^-}{\partial l}\frac{\partial\varphi^+}{\partial l}+\frac{\partial\psi^-}{\partial l}\frac{\partial\psi^+}{\partial l}. \end{aligned} \quad (36)$$

With (35) and (36), Bernoulli equation (27) takes the form

$$\frac{d\varphi^+(l,t)}{\partial t} = \frac{1}{2}\left(\left(\frac{\partial\varphi^+}{\partial x}\right)^2+\left(\frac{\partial\psi^+}{\partial x}\right)^2\right)-\frac{P}{\rho^+}-G(l,t), \quad (37)$$

$$\begin{aligned} \frac{d\varphi^-(l,t)}{dt} &= \frac{\partial\varphi^-}{\partial l}\frac{\partial\varphi^+}{\partial l}+\frac{\partial\psi^-}{\partial l}\frac{\partial\psi^+}{\partial l}\\ &\quad-\frac{1}{2}\left(\left(\frac{\partial\varphi^-}{\partial x}\right)^2+\left(\frac{\partial\psi^-}{\partial x}\right)^2\right)-\frac{P}{\rho^-}-G(l,t). \end{aligned} \quad (38)$$

Eliminating the pressure from (37) and (38) and taking into account equalities (33) and (34), we arrive at an equation for the velocity potential of the heavier fluid at the interface:

$$\frac{d\varphi^+(l,t)}{\partial t} = \frac{A}{2}\left(\frac{\partial\psi^+}{\partial l}\right)^2+\left(1-\frac{A}{2}\right)\left(\frac{\partial\varphi^+}{\partial l}\right)^2-AG(l,t), \quad (39)$$

where $A = (\rho^+ - \rho^-)/(\rho^+ + \rho^-)$ is the Atwood number.

Consequently, the action of the lighter fluid on the dynamics of the heavier one modifies the Bernoulli equation for the free surface (cf. (39) and (14)). Equations (31), (32), and (39) supplemented by equalities (28)–(30) for the heavier fluid make up a closed set. Below, we will omit the superscript "+" and always consider the system of two fluids. Then, in the set of equations describing the dynamics of the free surface, $A = 1$.

Thus, we derived the closed set of dynamic equations for the interface between two ideal incompressible fluids with different densities:

$$\frac{d\varphi(l,t)}{dt} = \frac{A}{2}\left(\frac{\partial\psi}{\partial l}\right)^2 + \left(1-\frac{A}{2}\right)\left(\frac{\partial\varphi}{\partial l}\right)^2 - AG(l,t), \quad (40)$$

$$\frac{dX(l,t)}{dt} = v_x(l,t) = \left(\frac{\partial\varphi(l,t)}{\partial l}\frac{\partial X}{\partial l} + \frac{\partial\psi(l,t)}{\partial l}\frac{\partial Z}{\partial l}\right) \times\left(\left(\frac{\partial X}{\partial l}\right)^2 + \left(\frac{\partial Z}{\partial l}\right)^2\right)^{-1/2}, \quad (41)$$

$$\frac{dZ(l,t)}{dt} = v_z(l,t) = \left(\frac{\partial\varphi(l,t)}{\partial l}\frac{\partial Z}{\partial l} - \frac{\partial\psi(l,t)}{\partial l}\frac{\partial X}{\partial l}\right) \times\left(\left(\frac{\partial X}{\partial l}\right)^2 + \left(\frac{\partial Z}{\partial l}\right)^2\right)^{-1/2}, \quad (42)$$

$$\psi(l,t) = \frac{2}{L(t)}\sum_{n=1}^{\infty}\int_0^{L(t)}\varphi(l',t)\sin(nK(t)(l'-l))dl'. \quad (43)$$

SOLUTION METHOD AND NUMERICAL EXPERIMENT

The seemingly simple set (40)–(43) turns out to be difficult to solve analytically. Therefore, it was solved numerically. The contour of the boundary was specified by a set of points $X_i(t)$ and $Z_i(t)$ ($i \in [0, I_0]$) so that the spacing between adjacent points was the same: $l_{i+1}(t) - l_i(t) = h(t) = L(t)/(I_0 - 1)$. The time dependence was also discrete: $l_i^{(m)} = l_i(t^m)$, $\varphi_i^{(m)} = \varphi(l_i^{(m)}, t^m)$, $\psi_i^{(m)} = \psi(l_i^{(m)}, t^m)$, etc.

Taking the integral in (43) with the finite-difference grid yields

$$\psi_j(t) = \sum_{i=1}^{I_0-1}\varphi_i(t) \times\left\{\Lambda\left(\frac{l_j(t) - l_{i+\frac{1}{2}}(t)}{L(t)}\right) - \Lambda\left(\frac{l_j(t) - l_{i-\frac{1}{2}}(t)}{L(t)}\right)\right\}, \quad (44)$$

where

$$\Lambda(y) = -\frac{1}{\pi}\sum_{n=1}^{\infty}\frac{1}{n}\cos(2\pi ny). \quad (45)$$

This functions is periodic, $\Lambda(y+1) = \Lambda(y)$, and even, $\Lambda(y) = \Lambda(-y)$. In calculations, summation in (45) is up to some number N. The uniformity of the computational grid in l makes it possible to calculate the function $\Lambda_{i+\frac{1}{2}} = \Lambda\left(\left(i+\frac{1}{2}\right)/(I_0-1)\right)$ ($i = 0, 1, \ldots, (I_0-1)$) once and use it subsequently (with regard for the parity and symmetry properties) to transform the velocity potential into stream function (44). Such an approach can take into account any number of harmonics in the transformation.

The transition between time layers proceeds in two stages. First, boundary points are shifted and a new value of the potential is determined. Then, the computational grid is regularized. Thus, at the first stage, we integrate Eqs. (40)–(42) over time:

$$\tilde{X}_i^{(m+1)} = X_i^{(m)} + \Delta t(v_x)_i^{(m+1)}, \quad (46)$$

$$\tilde{Z}_i^{(m+1)} = Z_i^m + \Delta t(v_z)_i^{(m+1)}, \quad (47)$$

$$\tilde{\varphi}_i^{(m+1)} = \varphi_i^{(m)} + \Delta t\left\{\frac{A}{2}\left(\frac{\partial\psi}{\partial l}\right)^2 + \left(1-\frac{A}{2}\right)\left(\frac{\partial\varphi}{\partial l}\right)^2 - AG\right\}_i^{(m+1)}, \quad (48)$$

where Δt is the time step.

To improve the stability of the solution, the integration was performed in implicit form and Eqs. (46)–(48) were solved by the method of successive iterations. The time step was constant and much smaller than the characteristic time of boundary evolution. The validation of the time step was the convergence of a solution to Eqs. (46)–(48) within a reasonable (say, no more than ten) number of iterations. Once new positions of boundary points have been found, a new value of the parameter $\tilde{l}_i^{(m+1)}$, which is the distance from the initial point ($\tilde{X}_0^{(m+1)}$, $\tilde{Z}_0^{(m+1)}$) to the moving point ($\tilde{X}_i^{(m+1)}$, $\tilde{Z}_i^{(m+1)}$), and a new total length $\Lambda^{(m+1)}$ of the contour are determined.

At the second stage, the grid was reconfigured so as to restore the uniform distribution of Lagrangean points in terms of l. To this end, a new computational grid $l_i^{(m+1)} = \Lambda^{(m+1)}(i-1)/(I_0-1)$ was applied. All quantities ($X_i^{(l+1)}$, $Z_i^{(l+1)}$, $\varphi_i^{(l+1)}$, etc.) at points of the new grid were calculated through the quantities ($\tilde{X}_i^{(l+1)}$, $\tilde{Z}_i^{(l+1)}$, $\tilde{\varphi}_i^{(l+1)}$, etc.) specified on the previous grid $\tilde{l}_i^{(m+1)}$ by linear interpolation in l. The regularization of the grid at either stage allowed us to avoid the excessive thickening or rarefaction of calculation points.

The method described above was used to calculate the interface evolution under Richtmyer–Meshkov instability. This type of instability arises when a shock wave passes through the interface between fluids of different density. In our statement for an incompressible fluid, a shock wave is replaced by the field of inertial forces $G(X, Z, t) = -g(t)Z$, where $g(t) = U\delta(t)$ is the

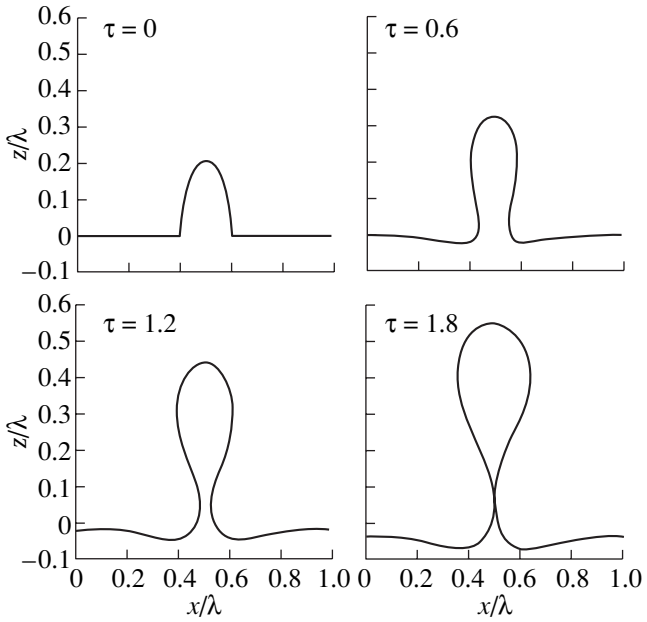

Fig. 1. Initial perturbation and its evolution due to Richtmyer–Meshkov instability on the free surface (A = 1, U = 1).

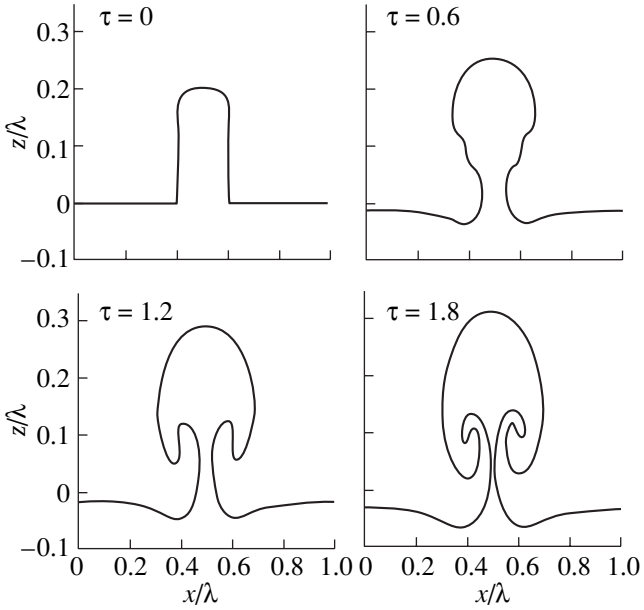

Fig. 2. The same at the interface between two fluids (A = 0.1, U = 1).

accelerating momentum and U is the velocity imparted to the medium by a shock wave. Integrating Bernoulli equation (40) over time from $t = -0$ to $t = +0$ yields the initial condition for the velocity potential:

$$\varphi(l, t = +0) = \mathrm{A}UZ(l, 0). \qquad (49)$$

The linear theory [4] of Richtmyer–Meshkov instability predicts a constant growth rate of the perturbation amplitude: $\dot{Z}_{RM} = \mathrm{A}Uka_0$. The interface evolution is conveniently described by the dimensionless time $\tau = (k^2\mathrm{A}Ua_0)t$, where a_0 is either the initial harmonic perturbation amplitude, $Z(l, 0) = a_0\cos(kX(l, 0))$, or the initial perturbation height relative to the OX axis (if the perturbation is of a complex shape).

Figures 1 and 2 show the initial perturbations and their evolution with time for the free surface (A = 1) and interface between fluids of various density (A = 0.1). It is seen that even the free surface ceases to be a unique function of x as time passes, as distinct from results obtained in [12]. Instead, the elongated fluid stream turns to a drop and at $\tau \approx 1.8$ separates from the fluid. Note that drops on the free surface form at any amplitude of the initial perturbation. With A = 0.1, a stream of the heavier fluid penetrates into the lighter one and forms a mushroomlike vortex, rather than a drop. However, at $\tau \approx 2$, the mushroom's stipe also has a waist.

Figure 3 demonstrates the growth rates of the stream, Γ_s, and bubble, Γ_b, for the free surface (A = 1) that are normalized to the linear rate vs. dimensional time for initial harmonic perturbation amplitudes a_0k = 0.005 and 0.5. For comparison, analytical results [16] corresponding to an infinitesimal initial perturbation and results of calculation by the vortex method [12] are also shown. As follows from our calculations, for a small initial perturbation (a_0k = 0.005), the growth rate of the stream becomes constant with time: $\Gamma_s \approx 3.5$. That of the bubble varies in a complicated manner: it first decreases, then (at $\tau = 0.6$) starts increasing, and at $\tau > 1.9$ slowly decreases again. In [12], the growth rate of the stream for a small perturbation was also found to be constant but at a level of ≈2.2 and the growth rate of a bubble tends to zero monotonically. At a_0k = 0.5, both our results and the results of [12] give a steady-state value of the stream growth rate at a level $\Gamma_s \approx 2.4$, which is much lower than for the small initial perturbation. As for the bubble growth rate at a_0k = 0.5, it monotonically declines, according to our calculations. Generally, our calculations give higher growth rates than in [12, 16].

As the initial perturbation amplitude grows (Fig. 4), both the initial values and variation of the rates change. The bubble growth rate tends to zero, and the shapes of the curves for a_0k = 1–4 are roughly the same. For a_0k = 1 and 2, the stream growth rate first rises and then starts decreasing (at $\tau > 2$ and $\tau > 1$, respectively). For a_0k = 3 and 4, the stream growth rate first increases and then exhibits a plateau.

Figure 5 compares our results with those obtained by the vortex method [12] for a system of two fluids with the Atwood number A = 0.33. The run of the curves is in accordance with [12]. However, as for A = 1, our rates exceed those obtained by the vortex method.

The growth rates of the stream and bubble for a system of two fluids with various Atwood numbers (small perturbation) are shown in Fig. 6. The growth rate of

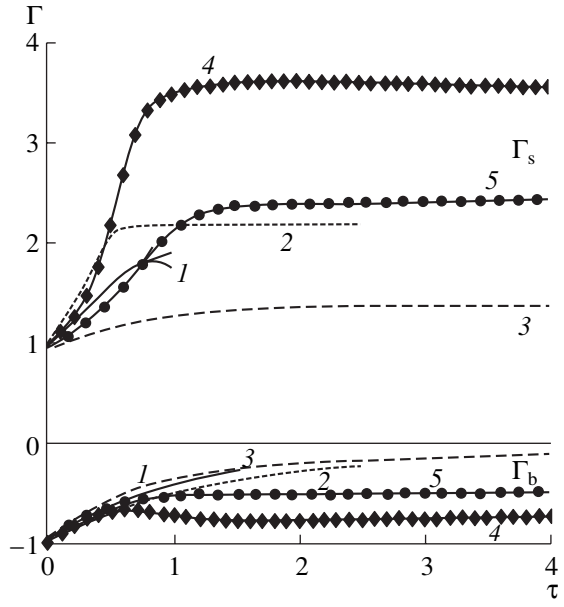

Fig. 3. Growth rates of the stream, Γ_s, and bubble, Γ_b, normalized to the linear rate vs. dimensional time for the free surface: (*1*) [16]; (*2*, *3*) vortex method [12] for $a_0k = 0.005$ and 0.5, respectively; and (*4*, *5*) our calculation for the same initial perturbations.

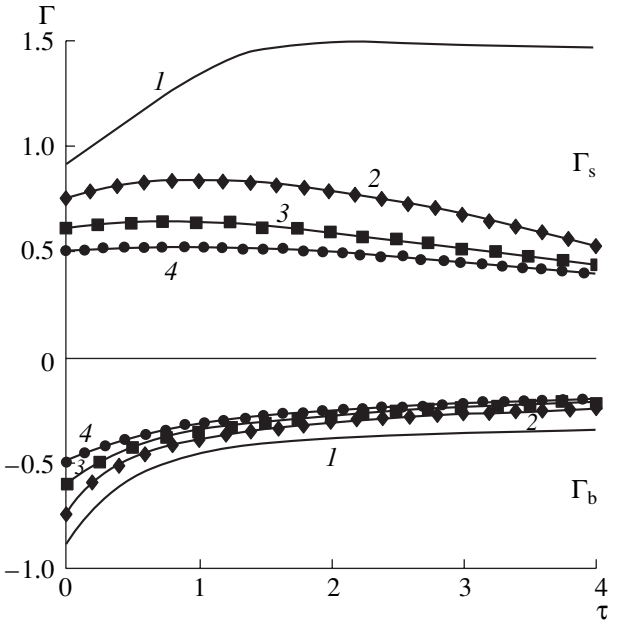

Fig. 4. Dynamics of the free surface (A = 1) for different initial perturbation amplitudes. The nonlinearity coefficients for the initial perturbation are (*1*) 1, (*2*) 2, (*3*) 3, and (*4*) 4.

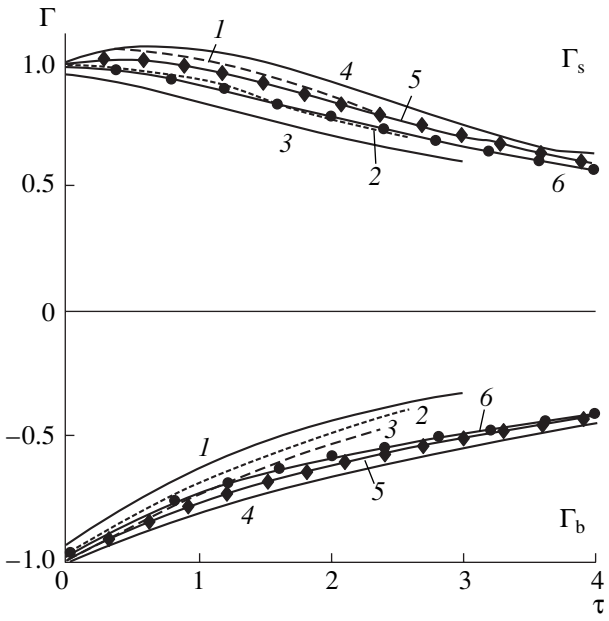

Fig. 5. Dynamics of the interface for A = 0.33. (*1–3*) Vortex method [12] with $a_0k = 0.1$, 0.3, and 0.5, respectively; (*4–6*) our calculations for the same a_0k.

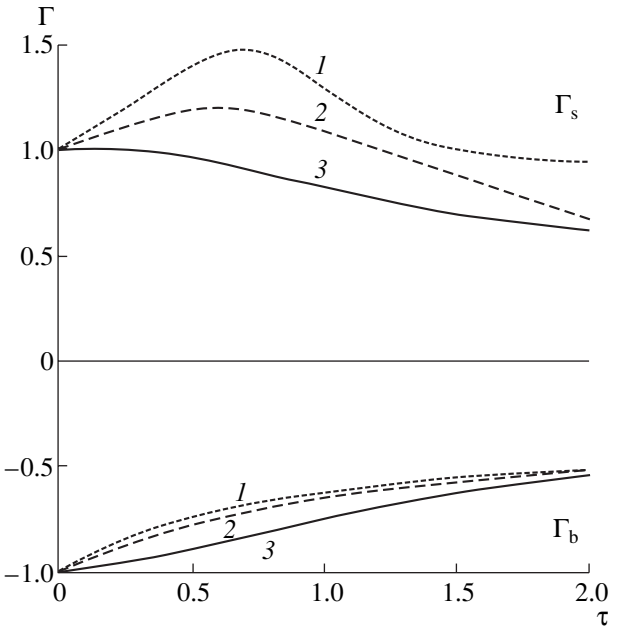

Fig. 6. Dynamics of the interface for A = 0.7 (*1*), 0.5 (*2*), and 0.1 (*3*). The initial amplitude $a_0k = 0.005$.

the bubble decreases monotonically with time. That of the stream first increases, peaks, and then decreases monotonically. As the Atwood number decreases, so does the maximal value of Γ_s. With A = 0.1, the region of initial rise almost degenerates into a plateau.

We compared our calculations with the experiments of Zaĭtsev [1] (Fig. 7) and Vasilenko [2, 13] (Fig. 8), as well as with results of processing these experiments by other authors [13, 23]. As follows from Figs. 7 and 8, our analytical curves fit the experimental data qualita-

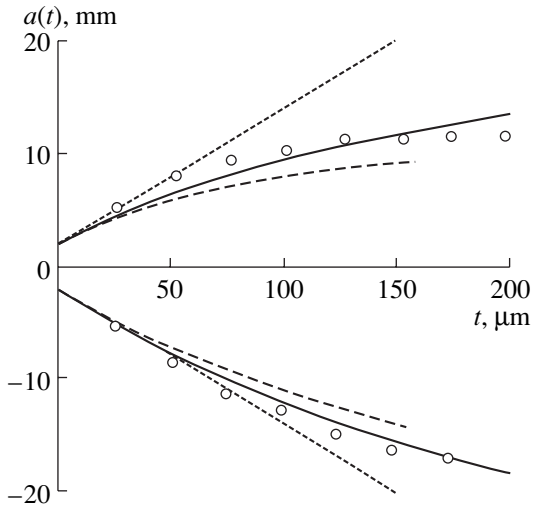

Fig. 7. Coordinates of the stream tip (lower quadrant) and bubble (upper quadrant) vs. time in the experiments of Zaĭtsev [1]. A shock wave passes from argon to xenon. The shock wave velocity D = 1273 m/s, fluid velocity increment U = 764 m/s, and A = 0.45 [13]. The initial perturbation: a_0 = 5 mm and λ = 36 mm. Circles, Zaĭtsev experimental data [1]; dotted lines, linear theory [4]; solid lines, our calculations; and dashed lines, vortex drop method [13].

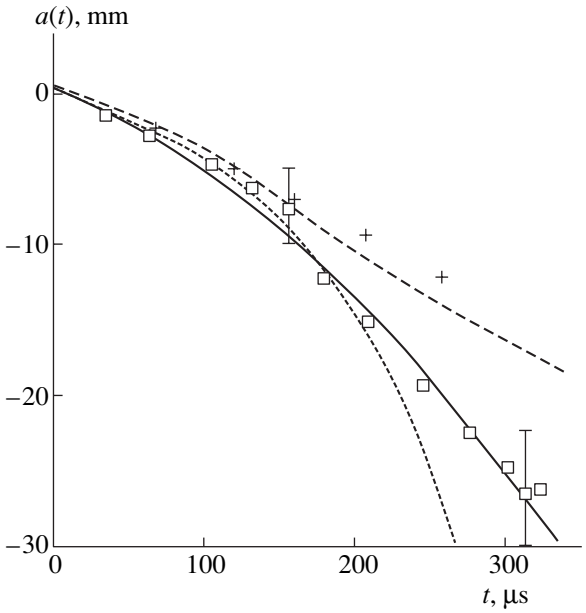

Fig. 8. Time dependence of the mean height (amplitude) of the interface, $a(t) = 0.5(|Z_s(t)| + |Z_b(t)|)$, for the experiments of Vasilenko [2, 13]. A slowing-down shock wave propagates from krypton to helium. The combined action of the pulsed and constant accelerations is noteworthy. The shock wave velocity D = –811.4 m/s, fluid velocity increment U = –940 m/s, constant acceleration $g = 10^6$ m/s^2, and A = 0.8644 [13]. The initial perturbation: a_0 = 1 mm and λ = 50 mm. Squares, Vasilenko experimental data [2, 13]; dotted line, linear theory [2]; solid line, our calculation; crosses, calculation with the TIGR gasdynamic method [24]; and dashed line, vortex drop method [13].

tively and quantitatively. Note that the vortex method [12] and the vortex drop method [13] give perturbation growth rates that are somewhat lower than those found experimentally, unlike our theory.

CONCLUSION

Thus, by reducing the hydrodynamic flow in a volume occupied by perfect incompressible fluids with different densities to the interface evolution, we obtained a closed set of Eqs. (40)–(43). For the 2D flow geometry, exact relationship (25), which relates the stream function and the velocity potential derivative at the interface, was derived. Its applicability is limited by the condition of existence of vectors tangent and normal to the interface and also by the validity of the hydrodynamic approximation. Our numerical experiment showed that actually there is no need to specify the initial distribution of point or finite-size vortices at the interface. A perturbation, however small, of the free surface or interface causes the formation and separation, respectively, of a drop or large-scale vortex of the heavier fluid for a finite time. Our results agree with experimental data [1, 2] both qualitatively and quantitatively.

Note in conclusion that our approach is certainly inapplicable to studying the stage of turbulent mixing of light and heavy fluids, when many vortices of different sizes appear and their interaction must be taken into account.

ACKNOWLEDGMENTS

The authors thank N.M. Zubarev for support and valuable discussions.

REFERENCES

1. A. N. Aleshin, E. V. Lazareva, S. G. Zaĭtsev, *et al.*, Dokl. Akad. Nauk SSSR **310**, 1105 (1990) [Sov. Phys. Dokl. **35**, 159 (1990)].
2. V. B. Rozanov, I. G. Lebo, S. G. Zaĭtsev, *et al.*, Preprint No. 56, FIAN (Lebedev Physical Institute, Academy of Sciences of USSR, Moscow, 1990).
3. S. Chandrasekhar, *Hydrodynamic and Hydromagnetic Stability* (Clarendon, Oxford, 1961).
4. R. D. Richtmyer, Commun. Pure Appl. Math. **12**, 297 (1960).
5. E. E. Meshkov, Izv. Akad. Nauk SSSR, Mekh. Zhidk. Gaza **5**, 151 (1969).
6. D. H. Sharp, Physica D **12**, 3 (1984).
7. N. A. Inogamov, A. Yu. Dem'yanov, and E. E. Son, *Hydrodynamics of Mixing, Periodic Structures, Amplification of Subharmonics, and Inversion Cascade* (Moscow Institute of Physics and Technology, Moscow, 1999).
8. D. D. Ryutov, M. S. Derzon, and M. K. Matzen, Rev. Mod. Phys. **72**, 167 (2000).

9. A. D. Korotaev, S. V. Ovchinnikov, Yu. I. Pochivalov, *et al.*, Surf. Coat. Technol. **105**, 84 (1998).
10. A. D. Korotaev, A. N. Tyumentsev, M. V. Tretjak, *et al.*, Structure, Phase Transformations and Diffusion **89**, 54 (2000).
11. N. B. Volkov, A. E. Maĭer, and A. P. Yalovets, Zh. Tekh. Fiz. **72**, 34 (2002) [Tech. Phys. **47**, 968 (2002)].
12. V. E. Neuvazhayev and I. E. Parshukov, *Mathematical Modelling and Applied Mathematics*, Ed. by A. A. Samarsky and M. P. Sapagovas (North-Holland: Elsevier Science Publishers B.V., IMACS, 1992), p. 323.
13. V. E. Neuvazhaev and I. É. Parshukov, Math. Model. **5** (2), 16 (1993).
14. N. B. Volkov, A. E. Maĭer, and A. P. Yalovets, Pis'ma Zh. Tekh. Fiz. **27** (1), 47 (2001) [Tech. Phys. Lett. **27**, 20 (2001)].
15. E. Fermi, *Scientific Works* (Nauka, Moscow, 1972), Vol. 2, p. 493; É. Fermi and J. von Neumann, *Scientific Works* (Nauka, Moscow, 1972), Vol. 2, p. 498.
16. A. L. Velikovich and G. Dimonte, Phys. Rev. Lett. **76**, 3112 (1996).
17. L. D. Landau and E. M. Lifshitz, *Course of Theoretical Physics*, Vol. 6: *Fluid Mechanics* (Nauka, Moscow, 1986; Pergamon, New York, 1987).
18. P. G. Saffman, *Vortex Dynamics* (University Press, Cambridge, 1992).
19. L. I. Sedov, *A Course in Continuum Mechanics* (Wolters-Noordhoff, Groningen, 1971; Nauka, Moscow, 1976), 3rd ed., Vol. 1.
20. A. I. Dyachenko, A. E. Kuznetsov, M. D. Spector, *et al.*, Phys. Lett. A **221**, 73 (1996).
21. E. Madelung, *Die Mathematischen Hilfsmittel des Physikers* (Springer, Berlin, 1957; Nauka, Moscow, 1968).
22. N. M. Zubarev and O. V. Zubareva, Zh. Tekh. Fiz. **71**, 21 (2001) [Tech. Phys. **46**, 806 (2001)].
23. K. A. Meyer and P. J. Blewett, Phys. Fluids **15**, 753 (1972).
24. F. Yu. Bisyarin, V. M. Gribov, A. D. Zubov, *et al.*, Vopr. At. Nauki Tekh., Ser. Chisl. Met. Mat. Fiz. **3** (17), 34 (1984).

Translated by V. Isaakyan

Technical Physics, Vol. 48, No. 3, 2003, pp. 284–289. Translated from Zhurnal Tekhnicheskoĭ Fiziki, Vol. 73, No. 3, 2003, pp. 10–15.

THEORETICAL AND MATHEMATICAL PHYSICS

Shielding of Low-Frequency Electric Fields by a Set of Shields Consisting of a Thin Unclosed Spherical Sheath and Thin-Walled Pervious Spherical Shell

V. T. Erofeenko* and G. Ch. Shushkevich**

** Belorussian State University, Leningradskaya ul. 14, Minsk, 220050 Belarus*

*** Kupala State University, Grodno, 230023 Belarus*

e-mail: sys@mail.grsu.grodno.by

Received February 22, 2002; in final form, August 29, 2002

Abstract—The penetration of low-frequency electric fields through a thin-walled spherical conducting shell in the presence of a thin unclosed spherical perfectly conducting sheath is considered. The problem is solved by the method of pair summational equations with averaged boundary conditions. The effect of the central angle of the unclosed spherical sheath and field source position on the field attenuation inside the closed thin-walled shell is studied numerically for different shell thicknesses and materials. © *2003 MAIK "Nauka/Interperiodica".*

INTRODUCTION

Among the problems of electrodynamics, the problem of electromagnetic field (EMF) shielding is of special importance from both the practical and theoretical standpoints. In the case of thin-walled shields, electromagnetic processes in the shield itself are not considered. Instead, the EMFs on both sides of the conducting shield are related by the equivalent boundary conditions defined on its median surface. Such an approach is strictly justified if the shield thickness does not exceed the EMF penetration depth. To consider single thin-walled shields, approximate averaged boundary conditions of the second kind are used [1–3]. In this paper, we study the penetration of the low-frequency electric dipole field through a thin-walled spherical conducting shell in the presence of a thin unclosed spherical perfectly conducting sheath using approximate averaged boundary conditions of the third kind.

STATEMENT OF SHIELDING PROBLEM

Let us consider a uniform isotropic space R^3 of permittivity ε_0 where a thin unclosed spherical sheath Γ with a central angle θ_0 covering a sphere Γ_1 of radius a_1 and a thin-walled spherical shell S of thickness Δ are placed (see figure). The thickness of the spherical sheath Γ is assumed to be small in comparison with other geometrical sizes. The medium filling the shell S is described by permitivity ε, permeability μ, and conductivity γ.

Let a low-frequency electric dipole oscillating by the law $e^{-i\omega t}$ and having the moment directed along the axis Oz_3 ($\theta_3 = 0$) be located at the point O_3.

To solve the problem, we relate spherical coordinates $\{r_j, \theta_j, \varphi\}$ to the point O_j ($j = 1, 2, 3$):

$$x_j = r_j\cos\varphi\sin\theta_j,\ y_j = r_j\sin\varphi\sin\theta_j,\ z_j = r_j\cos\theta_j$$
$$(0 \le r_j < \infty,\ 0 \le \theta_j \le \pi,\ 0 \le \varphi \le 2\pi).$$

Now we assume by convention that the sphere Γ_1 and the median surface S of the thin-walled shield S divide the space R^3 into three domains: D_1 (inside the

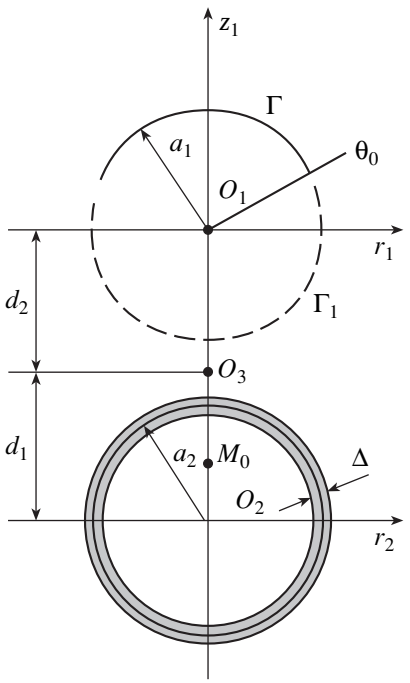

Figure.

1063-7842/03/4803-0284$24.00 © 2003 MAIK "Nauka/Interperiodica"

sphere Γ_1), D_2 (inside the sphere $\tilde{S}$), and $D_3 = R^3/(D_1 \cup D_2)$. Let the distance between the points O_1 and O_3 be d_2 and the distance between the points O_2 and O_3, d_1; $d = d_1 + d_2$.

The problem to be studied is the scattering of the electric dipole field by the system of the shields Γ and S with allowance for field penetration through the spherical layer S. Here, the unclosed spherical sheath Γ is assumed to be impenetrable to the field.

Let U_d be the potential of the electric dipole placed at the point O_3 and U_j be the potential of the field in the domain D_j (j = 1, 2, 3).

In the quasi-stationary approximation, the solution of the problem is reduced to determining the electrical potentials U_j in the domains D_j (j = 1, 2, 3). These potentials must satisfy the Laplace equation $\Delta U_j = 0$ and the boundary conditions on the sphere $\tilde{S}$ [4, p. 86], which describe the field penetration through the thin spherical layer S:

$$\frac{\partial}{\partial r_2}(U_3 + U_\mathrm{d} - U_2)\bigg|_{\tilde{S}} = -pF(U_3 + U_\mathrm{d} + U_2)|_{\tilde{S}}, \quad (1)$$

$$\frac{\partial}{\partial r_2}(U_3 + U_\mathrm{d} + U_2)\bigg|_{\tilde{S}} = qF\left(U_3 + U_\mathrm{d} - U_2 - \frac{\delta\varepsilon_0}{2\varepsilon'}\left(\frac{\partial(U_3 + U_\mathrm{d} + U_2)}{\partial r_2}\right)\right)\bigg|_{\tilde{S}}, \quad (2)$$

where

$$p = \frac{\varepsilon'\delta}{2\varepsilon_0}, \quad q = \frac{2}{\omega^2\delta\mu\varepsilon_0}, \quad \delta = \frac{2}{\kappa}\tan\left(\frac{\kappa\Delta}{2}\right),$$

$$\kappa = \omega\sqrt{\mu\varepsilon'}, \quad 0 \le \arg\kappa < \pi,$$

$\varepsilon' = \varepsilon + i(\gamma/\omega)$ is the complex permittivity, and $\omega = 2\pi f$ is the angular frequency of the field. The potentials must also meet the boundary condition on the surface of the thin unclosed spherical perfectly conducting sheath Γ

$$(U_3 + U_\mathrm{d})|_\Gamma = V - \mathrm{const} \quad \text{at} \quad r_1 = a_1, \ 0 \le \theta_1 < \theta_0 \quad (3)$$

and the condition at infinity

$$U_3(M) + U_\mathrm{d}(M) \longrightarrow 0 \quad \text{at} \quad M \longrightarrow \infty, \quad (4)$$

where M is an arbitrary point in the space.

Finally, we require that the continuity conditions for the potential on the sphere Γ_1 and for the field on the nonconducting part of the sphere Γ_1 be satisfied:

$$U_1 = U_3 + U_D \quad \text{at} \quad r_1 = a_1, \ 0 \le \theta_1 \le \pi, \quad (5)$$

$$\frac{\partial U_1}{\partial r_1} = \frac{\partial(U_3 + U_\mathrm{d})}{\partial r_1} \quad \text{at} \quad r_1 = a_1, \ 0 \le \theta_1 \le \pi. \quad (6)$$

The operator $F(U_j)$ entering into boundary conditions (1) and (2) can be represented as [4, p. 86]

$$F(U_j) = (\mathbf{n} \cdot \mathrm{curl}[\mathbf{n} \times \mathrm{grad}\, U_j]),$$

where $\mathbf{n}$ is the unit normal to the median surface $\tilde{S}$ that is directed inward to the domain D_3.

In the spherical coordinates, this operator is transformed into the form [3]

$$F(U_j) = \frac{1}{r^2\sin\theta}\left[\frac{\partial}{\partial\theta}\left(\sin\theta\frac{\partial}{\partial\theta}U_j\right) + \frac{1}{\sin\theta}\frac{\partial^2}{\partial\varphi^2}U_j\right]. \quad (7)$$

SOLUTION TO THE PROBLEM

The potential of an electric dipole in spherical coordinates can be represented as [4–6]

$$U_\mathrm{d}(r_3, \theta_3) = M_z\left(\frac{a_2}{r_3}\right)^2 P_1(\cos\theta_3), \quad (8)$$

where M_z is the dipole moment.

The potentials U_j can be expressed as the superposition of spherical functions such that condition at infinity (4) is satisfied:

$$U_1(r_1, \theta_1) = M_Z\sum_{n=0}^{\infty} x_n^{(1)}\left(\frac{r_1}{a_1}\right)^n P_n(\cos\theta_1), \quad (9)$$

$$U_2(r_2, \theta_2) = M_z\sum_{n=0}^{\infty} x_n^{(2)}\left(\frac{r_2}{a_2}\right)^n P_n(\cos\theta_2),$$

$$U_3 = U_3^{(1)}(r_1, \theta_1) + U_3^{(2)}(r_2, \theta_2), \quad (10)$$

where,

$$U_3^{(1)}(r_1, \theta_1) = M_z\sum_{n=0}^{\infty} y_n^{(1)}\left(\frac{a_1}{r_1}\right)^{n+1} P_n(\cos\theta_1), \quad (11)$$

$$U_3^{(2)}(r_2, \theta_2) = M_z\sum_{n=0}^{\infty} y_n^{(2)}\left(\frac{a_2}{r_2}\right)^{n+1} P_n(\cos\theta_2). \quad (12)$$

Here, $P_n(\cos\theta)$ are the Legendre polynomials [5–8]. The unknown coefficients $x_n^{(j)}$ and $y_n^{(j)}$ (j = 1, 2) are determined from the boundary conditions.

FULFILLMENT OF BOUNDARY CONDITIONS

To satisfy boundary conditions (3), (5), and (6), let us express the potentials $U_3^{(2)}(r_2, \theta_2)$ and $U_\mathrm{d}(r_3, \theta_3)$ through spherical harmonic functions related to the coordinate system with the origin at the point O_1. Using

the formula [3, 9]

$$\frac{1}{r_2^{n+1}}P_n(\cos\theta_2) = \sum_{k=0}^{\infty}(-1)^k\frac{(n+k)!}{n!k!} \times\frac{1}{d^{n+k+1}}r_1^kP_k(\cos\theta_1), \quad r_2<d,$$

we arrive at

$$U_3^{(2)}(r_1,\theta_1) = M_z\sum_{n=0}^{\infty}f_n^{(1)}r_1^nP_n(\cos\theta_1), \tag{13}$$

$$U_{\mathrm{d}}(r_1,\theta_1) = M_z\sum_{n=0}^{\infty}L_{n1}(a_2,d_2)r_1^nP_n(\cos\theta_1), \tag{14}$$

where

$$f_n^{(1)} = \sum_{k=0}^{\infty}L_{nk}(a_2,d)y_k^{(2)}, \tag{15}$$

$$L_{nk}(a_2,d) = \frac{(-1)^n(n+k)!}{n!k!d^n}\left(\frac{a_2}{d}\right)^{k+1}. \tag{16}$$

Taking into account Eqs. (9), (11), (13), and (14) and satisfying boundary conditions (3), (5), and (6), we obtain the pair summational equations in Legendre polynomials

$$\sum_{n=0}^{\infty}y_n^{(1)}P_n(\cos\theta_1) = \sum_{n=0}^{\infty}(V\delta_{0n}-f_n^{(1)}-L_{n1}(a_2,d_2)) \times a_1^nP_n(\cos\theta_1), \quad 0\le\theta_1<\theta_0,$$

$$\sum_{n=0}^{\infty}(2n+1)y_n^{(1)}P_n(\cos\theta_1) = 0, \quad \theta_0<\theta_1\le\pi,$$

where δ_{0n} is the Kronecker delta.

These pair summational equations can be transformed into an infinite set of linear algebraic equations of second kind for the coefficients $y_n^{(1)} \in l_2$ [8, 9]:

$$y_s^{(1)} = \sum_{n=0}^{\infty}(V\delta_{0n}-f_n^{(1)}-L_{n1}(a_2,d_2))a_1^nQ_{ns}(\theta_0); \quad s = 0, 1, 2, \ldots, \tag{17}$$

where

$$Q_{ns}(\theta_0) = \frac{2}{\pi}\int_0^{\theta_0}\cos\left(n+\frac{1}{2}\right)x\cos\left(s+\frac{1}{2}\right)xdx$$

or

$$Q_{ns}(\theta_0) = \frac{1}{\pi}\left[\frac{\sin(n-s)\theta_0}{(n-s)}-\frac{\sin(n+s+1)\theta_0}{(n+s+1)}\right],$$

$$\left.\frac{\sin(n-s)\theta_0}{(n-s)}\right|_{n=s} = \theta_0.$$

Taking into account (15), from Eq. (17) we obtain the relation between the coefficients $y_s^{(1)}$ and $y_n^{(2)}$

$$y_s^{(1)} = -\sum_{k=0}^{\infty}I_{ks}y_k^{(2)}+\sum_{n=0}^{\infty}(V\delta_{0n}-L_{n1}(a_2,d_2))a_1^nQ_{ns}(\theta_0); \quad s = 0, 1, 2, \ldots,$$

where

$$I_{ks} = \sum_{n=0}^{\infty}\frac{(-1)^n(n+k)!}{n!k!}\mu_1^n\mu_2^{k+1}Q_{ns}(\theta_0),$$

$$\mu_j = \frac{a_j}{d}; \quad j = 1, 2.$$

To satisfy boundary conditions (1) and (2), we express the potentials $U_3^{(1)}(r_1, \theta_1)$ and $U_{\mathrm{d}}(r_3, \theta_3)$ through spherical harmonic functions that are related to the coordinate system with the origin at the point O_2. Using the formula [3, 9]

$$\frac{1}{r_1^{n+1}}P_n(\cos\theta_1) = \sum_{k=0}^{\infty}(-1)^n\frac{(n+k)!}{n!k!} \times\frac{1}{d^{n+k+1}}r_2^kP_k(\cos\theta_2), \quad r_2<d,$$

we have

$$U_3^{(1)}(r_2,\theta_2) = M_z\sum_{n=0}^{\infty}f_n^{(2)}r_2^nP_n(\cos\theta_2), \tag{18}$$

$$U_{\mathrm{d}}(r_2,\theta_2) = M_z\sum_{n=0}^{\infty}p_nr_2^nP_n(\cos\theta_2), \tag{19}$$

where

$$f_n^{(2)} = \sum_{k=0}^{\infty}(-1)^{n+k}L_{nk}(a_1,d)y_k^{(1)}, \qquad p_n = (-1)^{n+1}L_{n1}(a_2,d_1). \tag{20}$$

Taking into account (10), (12), (18), (19), and representation (7) of the operator $F(U_j)$ in the spherical coordinates and also satisfying boundary conditions (1) and (2), we obtain the system

$$(pG_n+n+1)y_n^{(2)}+(n+pG_n)x_n^{(2)} = (n-pG_n)a_2^n(f_n^{(2)}+p_n),$$

$$(n+1-qG_n-(n+1)\alpha G_n)y_n^{(2)} \tag{21}$$

$$+ (qG_n + n\alpha G_n - n)x_n^{(2)}$$
$$= (n + qG_n - n\alpha G_n)a_2^n(f_n^{(2)} + p_n),$$

where

$$G_n = \frac{n(n+1)}{a_2}, \quad \alpha = \frac{\varepsilon_0\delta}{2\varepsilon'}\frac{q}{a_2}.$$

Solving system (21), we find that

$$y_n^{(2)} = -T_n a_2^n(f_n^{(2)} + p_n); \quad n = 0, 1, 2, \ldots, \qquad (22)$$

$$x_n^{(2)} = N_n a_2^n(f_n^{(2)} + p_n); \quad n = 0, 1, 2, \ldots, \qquad (23)$$

where

$$T_n = \frac{2n}{n+1}\frac{1 + (n+1)^2\frac{pq}{a_2^2} - n(n+1)\frac{\alpha}{a_2}}{\Delta},$$

$$N_n = \frac{(2n+1)\frac{p+q}{a_2} - n(n+1)(2n+1)\frac{p}{a_2}\frac{\alpha}{a_2}}{\Delta},$$

$$\Delta = (2n+1)\frac{q-p}{a_2} + \frac{2n(n+1)pq}{a_2^2}$$
$$- 2 + 2n(n+1)\frac{\alpha}{a_2} + n(n+1)(2n+1)\frac{p}{a_2}\frac{\alpha}{a_2}.$$

Substituting the representation of $f_n^{(2)}$ from Eq. (20) into Eq. (22) yields the relation between the coefficients $y_n^{(2)}$ and $y_k^{(1)}$:

$$y_n^{(2)} = -T_n a_2^n p_n - T_n a_2^n \sum_{k=0}^{\infty}(-1)^{n+k}L_{nk}(a_1, d)y_k^{(1)}.$$

Thus, the solution of the problem is reduced to the solution of coupled equations

$$y_s^{(1)} = -\sum_{k=0}^{\infty} I_{ks}y_k^{(2)} + \sum_{n=0}^{\infty}(V\delta_{0n} - L_{n1}(a_2, d_2))a_1^n Q_{ns}(\theta_0); \quad s = 0, 1, 2, \ldots, \qquad (24)$$

$$y_n^{(2)} = -T_n a_2^n p_n - T_n a_2^n \sum_{k=0}^{\infty}(-1)^{n+k}L_{nk}(a_1, d)y_k^{(1)}; \quad n = 0, 1, 2, \ldots \qquad (25)$$

or to the solution of an infinite system of linear algebraic equations (SLAE) of second kind for $y_s^{(1)} \in l_2$ if $y_k^{(2)}$ in Eq. (24) is replaced by representation (25):

$$y_s^{(1)} - \sum_{p=0}^{\infty} M_{ps}y_p^{(1)} = F_s; \quad s = 0, 1, 2, \ldots, \qquad (26)$$

where

$$M_{ps} = \sum_{k=0}^{\infty}(-1)^p I_{ks}T_k F(k, p, a_2, a_1, d), \qquad (27)$$

$$I_{ks} = \sum_{n=0}^{\infty}(-1)^n F(n, k, a_1, a_2, d)Q_{ns}(\theta_0), \qquad (28)$$

$$F(p, k, a_1, a_2, d) = \frac{(p+k)!}{p!k!}\left(\frac{a_1}{d}\right)^P\left(\frac{a_2}{d}\right)^{k+1}, \qquad (29)$$

$$F_s = -\frac{a_2}{a_1}\sum_{k=0}^{\infty} I_{ks}T_k F(1, k, a_1, a_2, d_1) + \sum_{n=0}^{\infty}(V\delta_{0n} - (-1)^n F(n, 1, a_1, a_2, d_2))Q_{ns}(\theta_0). \qquad (30)$$

If the dipole is placed at the point O_1, the right of system (26) is calculated by the formula

$$F_s = VQ_{0s}(\theta_0) + \left(\frac{a_2}{a_1}\right)^2(\delta_{1s} - Q_{1s}(\theta_0)).$$

CALCULATION OF THE FIELD SHIELDING (ATTENUATION) CONSTANTS

In the absence of the shields, the electric field intensity of the dipole at an arbitrary point $M_0(r_2, \theta_2)$ of the space is given by

$$\mathbf{E}_\mathrm{d}(M_0) = -\mathrm{grad}U_\mathrm{d}(M_0) = -\left(\frac{\partial U_\mathrm{d}}{\partial r_2}\mathbf{e}_{r_2} + \frac{1}{r_2}\frac{\partial U_\mathrm{d}}{\partial\theta_2}\mathbf{e}_{\theta_2}\right)$$

or, in view of representation (19),

$$\mathbf{E}_\mathrm{d}(M_0) = -M_z\sum_{n=0}^{\infty} np_n r_2^{n-1}P_n(\cos\theta_2)\mathbf{e}_{r_2}$$
$$+ M_z\frac{1}{r_2}\sum_{n=0}^{\infty} p_n r_2^n\frac{d}{dx}P_n(x)|_{x=\cos\theta_2}\sin\theta_2\mathbf{e}_{\theta_2}.$$

If the point M_0 is at the axis Oz_2, $\theta_2 = 0$ or π and $\sin\theta_2 = 0$; then, according to Eqs. (20) and (16),

$$\mathbf{E}_\mathrm{d}^+ = \mathbf{E}_\mathrm{d}(r_2, 0) = M_z\frac{1}{r_2}\left(\frac{a_2}{d_1}\right)^2\sum_{n=1}^{\infty} n(n+1)\left(\frac{r_2}{d_1}\right)^n\mathbf{e}_{z_2},$$

$$\mathbf{E}_\mathrm{d}^- = \mathbf{E}_\mathrm{d}(r_2, \pi)$$
$$= M_z\frac{1}{r_2}\left(\frac{a_2}{d_1}\right)^2\sum_{n=1}^{\infty}(-1)^n n(n+1)\left(\frac{r_2}{d_1}\right)^n\mathbf{e}_{z_2}.$$

The intensity of the secondary electric field at an

Table 1

d_1/a_2	r_2/a_2				
	0	0.2	0.4	0.6	0.8
1.1	0.975	0.962	0.943	0.911	0.844
	0.0000042	0.0000032	0.0000023	0.000016	0.0000008
2.0	0.986	0.978	0.968	0.956	0.941
	0.0000043	0.0000037	0.0000032	0.0000026	0.0000022
2.5	1.008	0.999	0.989	0.978	0.965
	0.0000043	0.0000039	0.0000034	0.0000031	0.0000026
4	1.521	1.479	1.438	1.397	1.356
	0.0000065	0.0000059	0.0000055	0.0000051	0.000046

arbitrary point $M_0(r_2, \theta_2)$ in the domain D_2 is given by

$$\mathbf{E}_2(M_0) = -\left(\frac{\partial U_2}{\partial r_2}\mathbf{e}_{r_2} + \frac{1}{r_2}\frac{\partial U_2}{\partial \theta_2}\mathbf{e}_{\theta_2}\right)$$

$$= -M_z\sum_{n=1}^{\infty} n x_n^{(2)}\frac{r_2^{n-1}}{a_2^n}P_n(\cos\theta_2)\mathbf{e}_{r_2}$$

$$+ M_z\frac{1}{r_2}\sum_{n=0}^{\infty} x_n^{(2)}\left(\frac{r_2}{a_2}\right)^n\frac{d}{dx}P_n(x)|_{x=\cos\theta_2}\sin\theta_2\mathbf{e}_{\theta_2}.$$

If the point M_0 is on the axis Oz_2, $\theta_2 = 0$ or π and

$$\mathbf{E}_2^+ = \mathbf{E}_2(r_2, 0) = -M_z\sum_{n=1}^{\infty} n x_n^{(2)}\frac{r_2^{n-1}}{a_2^n}\mathbf{e}_{z_2},$$

$$\mathbf{E}_2^- = \mathbf{E}_2(r_2, \pi) = -M_z\sum_{n=1}^{\infty} (-1)^n n x_n^{(2)}\frac{r_2^{n-1}}{a_2^n}\mathbf{e}_{z_2}.$$

Using Eqs. (23), (20), and (16), we find that the coefficients $x_n^{(2)}$ are expressed through the solutions to the infinite system of linear algebraic equations (26) as

$$x_n^{(2)} = N_n\left[-\frac{a_2}{a_1}F(1, n, a_1, a_2, d_1)\right.$$

$$\left. + \sum_{k=0}^{\infty}(-1)^k F(n, k, a_2, a_1, d)y_k^{(1)}\right].$$

If the dipole is at the point O_1, the coefficients $x_n^{(2)}$ are calculated by the formula

$$x_n^{(2)} = N_n\sum_{k=0}^{\infty}(-1)^k F(n, k, a_2, a_1, d)y_k^{(1)}.$$

The shielding (attenuation) constant at the point $M_0(r_2, \theta_2)$ in the domain D_2 can be calculated by the formula

$$K^{(\pm)}(r_2) = \frac{|\mathbf{E}_2^{(\pm)}|}{|\mathbf{E}_d^{(\pm)}|}.$$

In the absence of the unclosed spherical sheath Γ, the shielding constant $K^{(\pm)}(r_2)$ at the point $M_0(0, 0)$ is equal to

$$K^{(\pm)}(0) = |N_1|.$$

COMPUTING EXPERIMENT

Using the MathCAD 2000 software package [10], we calculated the shielding constant $K^{(\pm)}(r_2)$ for different geometrical parameters of the shields and for different materials of the thin-walled shell. The coefficients given by (27), (28), and (30), which are convergent series, were calculated with an accuracy of 10^{-6}. Infinite system (26) was solved by the truncation method [11]. The order of truncation was taken to be equal to 40, which provided the solution of system (26) with an accuracy of 10^{-6} for all the parameters of the problem that were considered. The calculations were performed for thin-walled shells S made of organic glass ($\varepsilon_r = 3.7$, $\gamma = 10^{-12}\frac{1}{\Omega m}$) [12] and *PPV* material[1] ($\varepsilon_r = 5$, $\gamma = 0.1\frac{1}{\Omega m}$). Here, $\varepsilon = \varepsilon_r\varepsilon_0$, $\varepsilon_0 = \frac{1}{36\pi}10^{-9}\frac{F}{m}$, and $\mu = \mu_0 = 4\pi\times 10^{-7}\frac{H}{m}$.

The shielding constant $K^{(+)}(r_2)$ as a function of the dipole position is given in Table 1: $d_1/a_2 = 1.1$ (first row), $d_1/a_2 = 2.0$ (second row), and $d_1/a_2 = 2.5$ (third row). The fourth row refers to the case when the dipole is at the point O_1 ($d_1 = d$, $d_1/a_2 = 4$). The other parameters were $\theta_0 = \pi/3$, $a_1/a_2 = 1$, $d/a_2 = 4$, $\Delta = 0.01a_2$, $V = 0$, and $f = 50$ Hz. In each of the rows, the upper values cor-

[1] http://infomag.apc.relarn.ru/texts/b007r/1995_V002_%23013_notes.txt

Table 2

d_1/a_2	Δ/a_2			
	0.01	0.005	0.002	0.001
1.1	0.931	0.964	0.986	0.994
	0.000039	0.000078	0.000194	0.000388
1.5	0.955	0.982	0.984	0.999
	0.000051	0.00011	0.000252	0.000503
1.9	0.988	1.012	1.026	1.030
	0.000059	0.000118	0.000295	0.000589
3	1.121	1.141	1.154	1.158
	0.000078	0.000156	0.000389	0.000778

Table 3

d_1/a_2	τ_0, deg				
	30	60	90	120	150
1.1	0.987	0.988	0.989	0.991	1.005
	0.0000083	0.0000084	0.0000084	0.0000084	0.0000087
1.5	0.988	0.991	0.993	0.994	1.038
	0.0000083	0.0000084	0.0000084	0.0000085	0.0000089
1.8	0.991	0.995	1.001	0.981	1.067
	0.0000083	0.0000084	0.0000085	0.0000083	0.0000092
4	1.122	1.182	1.096	0.789	0.258
	0.0000095	0.0000098	0.0000093	0.0000067	0.0000022

respond to organic glass and the lower ones, to *PPV* material.

The shielding constant $K^{(+)}(a_2/2)$ as a function of the dipole position and thickness Δ of the spherical shell S is listed in Table 2 for a central angle $\theta_0 = \pi/2$, $a_1/a_2 = 1$, $d/a_2 = 3$, $V = 0$, and $f = 1000$ Hz.

The shielding constant $K^{(+)}(0)$ as a function of the dipole position and the central angle θ_0 of the unclosed spherical sheath S is listed in Table 3 for $a_1/a_2 = 2$, $d/a_2 = 4$, $\Delta = 0.005a_2$, $V = 0$, and $f = 50$ Hz.

Based on the computing experiment, we may conclude the following.

(1) If a thin-walled shell is made of *PPV* material, the shielding constant is virtually zero; i.e., the field does not penetrate through the shell.

(2) As the distance between the field source and the thin-walled shell S in the domain D_3 ($d_2 > a_1$) increases, the shielding constant increases irrespective of the angle θ_0 of the spherical sheath Γ; i.e., a grounded perfectly conducting unclosed sheath acts as a reflector and raises the field inside the domain D_2. If the field source is in the domain D_1 ($0 \le d_2 < a_1$), the shielding constant increases if $\theta_0 < 90°$ and decreases if $\theta_0 \ge 90°$.

(3) The last term on the right of boundary condition (2), being a third-order differential expression, influences the value of the shielding constant if the field source is at a distance $d_1 \le 1.25a_2$.

REFERENCES

1. S. V. Zhukov, Izv. Akad. Nauk SSSR, Energ. Transp., No. 5, 54 (1983).
2. V. E. Shpitsberg, Izv. Akad. Nauk SSSR, Energ. Transp., No. 1, 110 (1989).
3. S. M. Apollonskiĭ and V. T. Erofeenko, *Electromagnetic Fields in Shielding Shells* (Minsk. Gos. Univ., Minsk, 1988).
4. S. M. Apollonskiĭ and V. T. Erofeenko, *Equivalent Boundary Conditions in Electrodynamics* (Bezopasnost', St. Petersburg, 1999).
5. N. N. Lebedev, *Special Functions and Their Applications* (GITTL, Moscow, 1953).
6. V. Ya. Arsenin, *Methods of Mathematical Physics and Special Functions* (Nauka, Moscow, 1984).
7. *Handbook of Mathematical Functions*, Ed. by M. Abramowitz and I. A. Steagun (National Bureau of Standards, Washington, 1964; Nauka, Moscow, 1979).
8. Ya. S. Uflyand, *Method of Pair Equations in Mathematical Physics* (Nauka, Leningrad, 1977).
9. G. Ch. Shushkevich, *Analysis of Electrostatic Fields by the Method of Pair and Triple Equations Using Summation Theorems* (Grodn. Gos. Univ., Grodno, 1999).
10. G. Ch. Shushkevich and S. V. Shushkevich, *Introduction to the MathCAD* (Grodn. Gos. Univ., Grodno, 2001).
11. L. V. Kantorovich and V. I. Krylov, *Approximate Methods of Higher Analysis* (Fizmatgiz, Moscow, 1962).
12. A. S. Enokhovich, *A Handbook of Physics* (Prosveshchenie, Moscow, 1990).

Translated by M. Astrov

Technical Physics, Vol. 48, No. 3, 2003, pp. 290–297. Translated from Zhurnal Tekhnicheskoĭ Fiziki, Vol. 73, No. 3, 2003, pp. 16–22.

THEORETICAL AND MATHEMATICAL PHYSICS

Effect of Electron Reflection from the Surface on the Electromagnetic Properties of Cylindrical Particles

É. V. Zavitaev, A. A. Yushkanov, and Yu. I. Yalamov

Moscow Pedagogical Institute, ul. Radio 10a, Moscow, 107005 Russia

Received April 29, 2002

Abstract—The cross section of the absorption of a magnetic field by a cylindrical metal particle is calculated. The general case when the ratio of the electron mean free path to the particle transverse size may take arbitrary values is considered. The boundary conditions imply the mixed mirror–diffuse reflection of electrons from the inner surface of the particle. The limiting cases are considered and results obtained are discussed. © *2003 MAIK "Nauka/Interperiodica".*

INTRODUCTION

The electromagnetic properties of small metal particles exhibit a number of special features [1, 2]. These features stem from the fact that the electron mean free path in such particles is comparable to their linear size. In this case, nonlocal effects come to play an essential role and the classical theory of interaction of electromagnetic radiation with metal particles (the Mie theory) [3], which is based on local equations of macroscopic electrodynamics, turns out to be inapplicable.

The problem of the magnetic dipole absorption of infrared radiation by spherical particles was considered in [4, 5], where the conventional kinetic theory of the degenerate Fermi gas of conduction electrons in metals was used for the description of the particle's electromagnetic response [6]. Consideration was restricted to the purely diffuse scattering of conduction electrons from the inner surface of the particle.

Later [7–9], the influence of the mirror reflection of electrons on the electromagnetic properties of fine metal particles was touched upon. The absorption of the magnetic dipole radiation by a spherical particle was considered in detail in [10], where the electron reflection from the particle surface was assumed to be of a mixed mirror–diffuse character [6].

In this paper, which is a generalization of [11], we construct a theory of interaction between electromagnetic radiation and a cylindrical particle with allowance for the mixed (mirror–diffuse) character of electron reflection.

STATEMENT OF THE PROBLEM

Consider an infinite metal cylinder with a radius R and length L ($L \gg R$) in the field of a plane electromagnetic wave. We assume that the magnetic field of the wave is aligned with the cylinder axis. In this system, the absorption of electromagnetic radiation is due to the occurrence of eddy currents. In the dipole approximation and with the neglect of the skin effect (it is assumed that $R < \delta$, where δ is the skin depth), an eddy electric field inducing these currents has the form

$$\mathbf{E} = \frac{1}{2c}\left[\mathbf{r} \times \frac{\partial \mathbf{H}}{\partial t}\right] = \frac{\omega}{2ic}[\mathbf{r} \times \mathbf{H}_0]\exp(-i\omega t), \quad (1)$$

where $\mathbf{H} = \mathbf{H}_0\exp(-i\omega t)$ is the magnetic field, $\mathbf{r}$ is the radius vector (the origin of the coordinates is placed on the axis of the particle), $\mathbf{H}_0$ is the amplitude of the magnetic field of the wave, ω is the circular frequency, and c is the speed of light.

The average dissipated power $\bar{Q}$ per particle is found from the formula [12]

$$\bar{Q} = \int \overline{(\mathrm{Re}\mathbf{E}) \cdot (\mathrm{Re}\,\mathbf{j})} d^3r = \frac{1}{2}\mathrm{Re}\int \mathbf{j} \cdot \mathbf{E}^* d^3r. \quad (2)$$

Here, the bar means time averaging, the asterisk denotes complex conjugation, and $\mathbf{j}$ is the eddy current. Let local Ohm's law be applied to obtain the current $\mathbf{j}$:

$$\mathbf{j} = \sum(\omega)\mathbf{E}; \quad \Sigma(\omega) = \frac{\sigma(0)}{1 - i\omega\tau}, \quad (3)$$

where $\Sigma(\omega)$ is the Drude conductivity [6, 13] and $\Sigma(0) = (e^2 n\tau)/m$ is the static conductivity of the metal. Then, dividing $\bar{Q}$ by the mean energy flux $cH_0^2/8\pi$ in the wave, we arrive at the classical relationship for the cross section σ_{cl} of electromagnetic radiation absorption by the particle [12]:

$$\sigma_{\mathrm{cl}} = \frac{\pi^2 e^2 n R^4 L}{2mc^3}\frac{\tau\omega^2}{1 + \omega^2\tau^2}, \quad (4)$$

where e, m, and n are the electron charge, electron mass, and density of conduction electrons, respectively, and τ is the relaxation time.

In this study, we assume that the particle radius R is comparable to, or lower than, the electron mean free

path Λ in the metal. In this case, Eq. (3) is inapplicable since the relationship between **E** and **j** becomes essentially nonlocal. In order to find this relationship, we apply the kinetic equation (in the relaxation time approximation) to the degenerate Fermi gas of conduction electrons in a cylindrical particle. For weak external fields **E**, this equation can be linearized in **E** and in small deviations from the equilibrium Fermi distribution function:

$$-i\omega f_1 + \mathbf{v}\cdot\frac{\partial f_1}{\partial \mathbf{r}} + e(\mathbf{v}\cdot\mathbf{E})\frac{\partial f_0}{\partial \varepsilon} = -\frac{f_1}{\tau}. \quad (5)$$

Here,

$$f(\mathbf{r},\mathbf{v}) = f_0(\varepsilon) + f_1(\mathbf{r},\mathbf{v}), \quad \varepsilon = \frac{mv^2}{2} \quad (6)$$

is the electron distribution function, and $f_0(\varepsilon)$ is the equilibrium Fermi distribution of electrons over energy. In what follows, we consider the quadratic dependence of the energy on the velocity, $mv^2/2$, and use a step approximation of the equilibrium function $f_0(\varepsilon)$ [13]

$$f_0(\varepsilon) = \theta(\varepsilon_F - \varepsilon) = \begin{cases} 1, & 0 \le \varepsilon \le \varepsilon_F, \\ 0, & \varepsilon_F < \varepsilon. \end{cases} \quad (7)$$

In (7), $\varepsilon_F = mv_F^2/2$ is the Fermi energy and $f_1(\mathbf{r},\mathbf{v})$ is a small field-induced deviation of f from the equilibrium value $f_0(\varepsilon)$, which generates the current

$$\mathbf{j} = en\langle\mathbf{v}\rangle = en\left[\int f_0 d^3v\right]^{-1}\int f_1\mathbf{v}d^3v. \quad (8)$$

The electron concentration n is determined from the standard formula

$$n = 2\frac{m^3}{h^3}\int f_0 d^3v = 2\frac{m^3}{h^3}\frac{4\pi v_F^3}{3}, \quad (9)$$

where h is the Planck constant and v_F is the Fermi velocity.

Substituting **E** in the form of (1) into Eq. (5), we find f_1 as a solution to Eq. (5). Next, from relationship (8), we find the current and absorption cross section

$$\sigma = \frac{8\pi\bar{Q}}{cH_0^2}. \quad (10)$$

In order to uniquely solve the problem posed, it is necessary to establish a boundary condition on the particle surface for the unknown function f_1. Physically, this means that if $R < \Lambda$, the energy absorption by the particle depends considerably on the interaction of conduction electrons with the particle boundary. Let the boundary condition be

$$f_1(\mathbf{r}_\perp,\mathbf{v}_\perp,\mathbf{v}_z) = qf_1(\mathbf{r}_\perp,\mathbf{v}'_\perp,\mathbf{v}_z) \quad \text{at} \quad \begin{cases} |r_\perp| = R \\ \mathbf{r}_\perp\cdot\mathbf{v}_\perp < 0, \end{cases} \quad (11)$$

where $\mathbf{r}_\perp$ and $\mathbf{v}_\perp$ are the respective projections of the radius vector **r** and velocity **v** of an electron onto the plane normal to the axis of the cylinder;

$$\mathbf{v}'_\perp = \mathbf{v}_\perp - \frac{2\mathbf{r}_\perp(\mathbf{r}_\perp\cdot\mathbf{v}_\perp)}{R^2} \quad (12)$$

is the velocity vector that transforms into the vector $\mathbf{v}_\perp$, being specularly reflected from the inner cylinder surface at the point $\mathbf{r}_\perp(|r_\perp| = R)$; $\mathbf{v}_z$ is the component of the electron velocity along the axis of the particle; and q is the probability of mirror reflection,

$$0 \le q \le 1. \quad (13)$$

At $q = 0$, we deal with purely diffuse scattering of conduction electrons; at $q = 1$, the reflection is purely specular. At $q \ne 0$ and $q \ne 1$, we have different kinds of mixed (mirror–diffuse) electron reflection.

DISTRIBUTION FUNCTION

Kinetic equation (5) is solved by the method of characteristics [14]. The variation of f_1 along the path (characteristic)

$$d\mathbf{r} = \mathbf{v}dt \quad (14)$$

is given by

$$df_1 = -\left(\nu f_1 + e(\mathbf{v}\cdot\mathbf{E})\frac{\partial f_0}{\partial\varepsilon}\right)dt, \quad (15)$$

where

$$\nu = \frac{1}{\tau} - i\omega \quad (16)$$

is the complex scattering frequency.

Boundary condition (10) enables us to keep track of f_1 along the mirror-reflecting trajectory. At the point of reflection $t = t_n$, the function $f_1(t)$ experiences a discontinuity:

$$f_1(t_n + 0) = qf_1(t_n - 0). \quad (17)$$

The sign +/– denotes the limit of the function f_1 at the point of reflection t_n on the right and left, respectively.

For mirror reflection, the angular momentum is conserved, $[\mathbf{r}_\perp\times\mathbf{v}_\perp] = [\mathbf{r}_\perp\times\mathbf{v}'_\perp]$; therefore, for the trajectory considered,

$$[\mathbf{r}_\perp\times\mathbf{v}_\perp] = \text{const}. \quad (18)$$

The difference $t_n - t_{n-1}$ does not depend on the number n of the point of reflection:

$$t_n = nT + \text{const}, \quad n \in Z, \quad (19)$$

where T is the transit time of an electron with a velocity

$\mathbf{v}_\perp$ from the point $\mathbf{r}_{n-1\perp}$ to the point $\mathbf{r}_{n\perp}$:

$$T = -\frac{2(\mathbf{v}_{n\perp}\cdot\mathbf{r}_{n\perp})}{v_\perp^2}. \tag{20}$$

The value of $\mathbf{v}\cdot\mathbf{E}$ also remains constant on the trajectory:

$$\mathbf{v}\cdot\mathbf{E} = \frac{\omega}{2ic}[\mathbf{r}\times\mathbf{H}]\cdot\mathbf{v} = \frac{i\omega}{2c}[\mathbf{r}\times\mathbf{v}]\cdot\mathbf{H} = \text{const}. \tag{21}$$

The general solution to Eq. (14) is the function

$$f_1 = C\exp(-\nu t) - \frac{A}{\nu}, \quad \text{where} \quad A = e(\mathbf{v}\cdot\mathbf{E})\frac{\partial f_0}{\partial\varepsilon}. \tag{22}$$

Let us solve this equation in the interval (t_{n-1}, t_n). At the initial time moment ($t = 0$),

$$f_1(t_{n-1}+0) = C - \frac{A}{\nu}. \tag{23}$$

Then, the value of the constant C is

$$C = \frac{A}{\nu} + f_1(t_{n-1}+0). \tag{24}$$

Now we can obtain a relationship between the initial values of the function f_1 in two adjacent segments of the trajectory. Since $t_n - 0 = t_{n-1} + T$, we have

$$\begin{aligned} f_1(t_n-0) &= \left(\frac{A}{\nu} + f_1(t_{n-1}+0)\right)\exp(-\nu T) - \frac{A}{\nu} \\ &= \frac{A}{\nu}(1-\exp(-\nu T)) + f_1(t_{n-1}+0)\exp(-\nu T). \end{aligned} \tag{25}$$

In view of condition (17),

$$\begin{aligned} f_1(t_n+0) = q\Big\{&-\frac{A}{\nu}(1-\exp(-\nu T)) \\ &+ f_1(t_{n-1}+0)\exp(-\nu T)\Big\}. \end{aligned} \tag{26}$$

Then, using this recurrence relation to express $f_1(t_{n-1}+0)$ through $f_1(t_{n-2}+0)$ etc., we come to the expression where $f_1(t_n+0)$ is represented as an infinite geometric progression with a ratio $q\exp(-\nu T)$. Its sum equals

$$f_1(t_n+0) = \frac{-qA(1-\exp(-\nu T))}{\nu(1-q\exp(-\nu T))}. \tag{27}$$

In order to find a final solution to Eq. (15), we use initial condition (27). When $t = 0$,

$$\frac{-qA(1-\exp(-\nu T))}{\nu(1-q\exp(-\nu T))} = C - \frac{A}{\nu}, \tag{28}$$

hence,

$$\begin{aligned} C &= \frac{A}{\nu}\left\{1 - \frac{q(1-\exp(-\nu T))}{1-q\exp(-\nu T)}\right\} \\ &= \frac{A}{\nu}\left\{\frac{1-q}{1-q\exp(-\nu T)}\right\}. \end{aligned} \tag{29}$$

Therefore,

$$\begin{aligned} f_1(t) &= \frac{A}{\nu}\left\{\frac{1-q}{1-q\exp(-\nu T)}\right\}\exp(-\nu t) - \frac{A}{\nu} \\ &= \frac{A}{\nu}\left\{\frac{(1-q)\exp(-\nu t)}{1-q\exp(-\nu T)} - 1\right\}. \end{aligned} \tag{30}$$

The parameters t and T can be related to the coordinates of the point $(\mathbf{r}_\perp, \mathbf{v}_\perp)$ in the phase space (at $n = 0$, $\mathbf{v}_{0\perp} = \mathbf{v}_\perp$) as

$$\begin{aligned} &\mathbf{r}_\perp = \mathbf{r}_{0\perp} + \mathbf{v}_\perp t; \quad \mathbf{v}_\perp\cdot\mathbf{r}_{0\perp} < 0; \\ &r_{0\perp}^2 = R^2; \quad T = -\frac{2(\mathbf{v}_\perp\cdot\mathbf{r}_{0\perp})}{v_\perp^2}, \end{aligned} \tag{31}$$

where $\mathbf{r}_{0\perp}$ is the projection of the electron radius vector at the instant of reflection from the particle boundary onto the plane normal to the cylinder axis. Excluding $\mathbf{r}_{0\perp}$, we obtain

$$t = \{\mathbf{r}_\perp\cdot\mathbf{v}_\perp + [(\mathbf{r}_\perp\cdot\mathbf{v}_\perp)^2 + (R^2 - r_\perp^2)\mathbf{v}_\perp^2]^{1/2}\}/v_\perp^2, \tag{32}$$

$$T = 2[(\mathbf{r}_\perp\cdot\mathbf{v}_\perp)^2 + (R^2 - \mathbf{r}_\perp^2)\mathbf{v}_\perp^2]^{1/2}/v_\perp^2. \tag{33}$$

Relationships (30), (32), and (33) define completely the function $f_1(\mathbf{r}_\perp, \mathbf{v}_\perp)$.

ABSORPTION CROSS SECTION

The distribution function obtained enables us to calculate the current (formula (8)) and average dissipated power (formula (2)), as well as the absorption cross section (formula (10)).

Integrals (8) and (2) are convenient to take in cylindrical coordinates both in the coordinate space ($r_\perp$, α, r_z, where the Z axis is the polar axis and the vector $\mathbf{H}_0$ is parallel to the Z axis), and in the velocity space ($v_\perp$, φ, v_z). The cylinder axis coincides with the Z axis. Field (1) in the cylindrical coordinates has only the φ component:

$$\mathbf{E} = E_\varphi\mathbf{e}_\varphi; \quad E_\varphi = \frac{i\omega}{2c}r_\perp H_0\exp(-i\omega t). \tag{34}$$

Correspondingly, current (8) also has the φ component alone (the current lines form closed circles cen-

tered on the Z axis in planes normal to the Z axis):

$$j_\varphi = 2e\left(\frac{m}{h}\right)^3\frac{1}{\nu}\int v_\varphi e(vE)\frac{\partial f_0}{\partial\varepsilon}\left\{\frac{(1-q)\exp(-\nu t)}{1-q\exp(-\nu T)}-1\right\}d^3v$$

$$= E_\varphi 2e^2\left(\frac{m}{h}\right)^3\frac{1}{\nu}\int v_\varphi^2\delta(\varepsilon-\varepsilon_f)\left\{1-\frac{(1-q)\exp(-\nu t)}{1-q\exp(-\nu T)}\right\}d^3v$$

$$= E_\varphi 2e^2\left(\frac{m}{h}\right)^3\frac{1}{\nu}\left(\frac{2}{m}\right)\int_0^{v_F}\int_0^{2\pi}\int_0^\infty v_\perp^2\sin^2\varphi\,\delta(v_z-\sqrt{v_F^2-v_z^2}) \tag{35}$$

$$\times\frac{1}{\sqrt{v_F^2-v_\perp^2}}\left\{1-\frac{(1-q)\exp(-\nu t)}{1-q\exp(-\nu T)}\right\}v_\perp dv_\perp d\varphi dv_z$$

$$= E_\varphi 2e^2\left(\frac{m}{h}\right)^3\frac{1}{\nu}\left(\frac{2}{m}\right)\int_0^{v_F}\int_0^{2\pi}\frac{v_\perp^3}{\sqrt{v_F^2-v_\perp^2}}$$

$$\times\left\{1-\frac{(1-q)\exp(-\nu t)}{1-q\exp(-\nu T)}\right\}\sin^2\varphi\,dv_\perp d\varphi.$$

Indeed, using the properties of the δ function, we obtain

$$\delta(\varepsilon-\varepsilon_F) = \frac{2}{m}\delta(v_z^2+v_\perp^2-v_F^2) = \frac{2}{m}\delta[v_z^2-(v_F^2-v_\perp^2)]$$

$$= \frac{2}{m}\delta[(v_z-\sqrt{v_F^2-v_\perp^2})(v_z+\sqrt{v_F^2-v_\perp^2})]$$

$$= \frac{1}{m\sqrt{v_F^2-v_\perp^2}}[\delta(v_z-\sqrt{v_F^2-v_\perp^2})+\delta(v_z+\sqrt{v_F^2-v_\perp^2})].$$

By virtue of the symmetry of the problem, integration over the whole range of velocities v_z is replaced by integration over the positive half-range and the result is doubled.

Putting $\xi = r_\perp/R$ and $\rho = v_\perp/v_f$ and taking into account that $\mathbf{r}_\perp\cdot\mathbf{v}_\perp = r_\perp v_\perp\cos\varphi$, we rearrange expressions (32) and (33) into the form

$$t = R(\xi\cos\varphi+\sqrt{1-\xi^2\sin^2\varphi})/v_\perp, \tag{36}$$

$$T = 2R\sqrt{1-\xi^2\sin^2\varphi}/v_\perp. \tag{37}$$

Let us introduce the new variable

$$z = \frac{R}{v_F}\left(\frac{1}{\tau}-i\omega\right) = \frac{R}{\Lambda}-i\frac{R\omega}{v_F} = x-iy = z(x,y). \tag{38}$$

Then, expression (35) takes the form

$$j_\varphi = 2e^2E_\varphi\left(\frac{m}{h}\right)^3\frac{R}{zv_F}\frac{2v_F^3}{m}\int_0^1\int_0^{2\pi}\frac{\rho^3}{\sqrt{1-\rho^2}} \tag{39}$$

$$\times\left\{1-\frac{(1-q)\exp(-\nu t)}{1-q\exp(-\nu T)}\right\}\sin^2\varphi\,d\rho\,d\varphi.$$

Using formulas (2) and (10), we calculate the absorption cross section

$$\sigma = \left(\frac{8\pi}{cH_0^2}\right)\frac{1}{2}\mathrm{Re}\int\mathbf{j}\cdot\mathbf{E}^*d^3r = \sigma_0F(x,y), \tag{40}$$

where

$$\sigma_0 = \frac{3\pi ne^2R^3Lv_F}{mc^3},$$

$$F(x,y) = y^2\mathrm{Re}\int_0^1\int_0^1\int_0^{2\pi}\xi^3d\xi\frac{\rho^3}{\sqrt{1-\rho^2}}\frac{1}{z} \tag{41}$$

$$\times\left\{1-\frac{(1-q)\exp(-\nu t)}{1-q\exp(-\nu T)}\right\}\sin^2\varphi\,d\rho\,d\varphi.$$

The triple integral is reduced to the double integral by changing the variables: $(\xi\cos\varphi,\ \xi\sin\varphi)\longrightarrow(u,\ w)$. Indeed, we have

$$F(x,y) = \frac{y^2}{z(x,y)}\int_0^1\int_{-1}^1\int_{-\sqrt{1-w^2}}^{\sqrt{1-w^2}}\frac{\rho^3}{\sqrt{1-\rho^2}}w^2$$

$$\times\left\{1-\frac{(1-q)\exp\left(-\dfrac{z(x,y)}{\rho}(u+\sqrt{1-w^2})\right)}{1-q\exp\left(-\dfrac{2z(x,y)}{\rho}\sqrt{1-w^2}\right)}\right\}d\rho\,dw\,du. \tag{42}$$

Integrating with respect to u yields the sum of three double integrals, which describes the dimensionless absorption cross section $F(x, y)$:

$$F(x,y) = \frac{y^2}{z(x,y)}\int_0^1\int_{-1}^1\frac{\rho^3}{\sqrt{1-\rho^2}}2w^2\sqrt{1-w^2}\,d\rho\,dw$$

$$+\frac{y^2}{z(x,y)^2}\int_0^1\int_{-1}^1\frac{\rho^4}{\sqrt{1-\rho^2}}w^2$$

$$\times\frac{(1-q)\exp\left(-\dfrac{2z(x,y)}{\rho}\sqrt{1-w^2}\right)}{1-q\exp\left(-\dfrac{2z(x,y)}{\rho}\sqrt{1-w^2}\right)}d\rho\,dw \tag{43}$$

$$-\frac{y^2}{z(x,y)^2}\int_0^1\int_{-1}^1\frac{\rho^4}{\sqrt{1-\rho^2}}\times\frac{(1-q)w^2}{1-q\exp\left(-\frac{2z(x,y)}{\rho}\sqrt{1-w^2}\right)}d\rho dw.$$

The last two integrals in sum (43) cannot be taken in elementary functions.

DISCUSSION

In the limit of purely mirror reflection ($q = 1$), we obtain the relationship for $F(x, y)$

$$F(x,y) = \frac{y^2}{z(x,y)}\times\int_0^1\int_{-1}^1\frac{\rho^3}{\sqrt{1-\rho^2}}2w^2\sqrt{1-w^2}\,d\rho dw = \frac{\pi y^2}{6z(x,y)}. \quad (44)$$

In view of notation (38) and (41), cross section (40) agrees completely with classical result (4), because the boundary does not affect the electron distribution function f at $q = 1$. The eddy current inside a mirror-reflecting extended cylinder (see (39)) meets local Ohm's law (3) at any relationship between the cylinder radius R and electron mean free path Λ. Thus, nonlocal (surface) effects are absent in the case of mirror reflection.

Irrespective of the character of reflection (at any q), as the particle size increases (at $x \gg 1$), we arrive at macroscopic asymptotics (44). As follows from (43) (where we neglect the last two integrals), the relative contribution of the surface effects decreases as $x^{-1}(|z| \sim x)$.

In the case of purely diffuse reflection ($q = 0$), integral (43) is simplified:

$$F(x,y) = \frac{y^2}{z(x,y)}\int_0^1\int_{-1}^1\frac{\rho^3}{\sqrt{1-\rho^2}}2w^2\sqrt{1-w^2}\,d\rho dw + \frac{y^2}{z(x,y)^2}\int_0^1\int_{-1}^1\frac{\rho^4}{\sqrt{1-\rho}}w^2\exp\left(-\frac{2z(x,y)}{\rho}\sqrt{1-w^2}\right)d\rho dw - \frac{y^2}{z(x,y)^2}\int_0^1\int_{-1}^1\frac{\rho^4 w^2}{\sqrt{1-\rho^2}}d\rho dw. \quad (45)$$

The detailed kinetic analysis made it possible to refine the applicability of the well-known approximate description of nonlocal kinetic effects in fine metal particles. The central idea of this approach is to modify the Drude formula (see above) and still retain formally local relation (3) between the current j and field E. The modification implies the substitution of the effective time of electron relaxation τ_{eff} for the relaxation time τ, $\tau \longrightarrow \tau_{\text{eff}}$, where τ_{eff} depends on the geometrical (R) and kinetic (q) parameters in much the same way as the relaxation frequency depends on the bulk and surface relaxation frequencies:

$$\tau^{-1} \longrightarrow \tau_{\text{eff}}^{-1} = \nu_{\text{eff}} = \tau^{-1} + (1-q)v_F/R. \quad (46)$$

In (38), (46) takes the form

$$x \longrightarrow x_{\text{eff}} = x + 1 - q. \quad (47)$$

In terms of the modified Drude theory (MD theory), the formula for the dimensionless absorption cross section $F(x, y)$ appears as

$$F_{\text{MD}}(x,y) = \frac{\pi}{6}\frac{(x+1-q)y^2}{(x+1-q)^2+y^2}. \quad (48)$$

In the limit of purely mirror reflection ($q = 1$), formula (48), as well as exact one (43), coincides with classical formula (44); however, at $q \neq 1$, (48) is an approximation to exact formula (43). The greatest difference between the exact kinetic calculation and MD theory arises in the case of purely diffuse electron reflection ($q = 0$). Thus, the MD approximation (i.e., the modification of Drude formula (44) by substituting (46)) approximates the exact kinetic calculation for a cylindrical particle with an accuracy of 50% or higher. It should be noted that the oscillatory frequency dependence of the dimensionless absorption cross section $F(x, y)$, which is the most noticeable for the diffuse reflection ($q = 0$) of small particles ($x \ll 1$), is basically impossible in the MD approximation.

The results obtained in this study are presented in Figs. 1–8.

Figures 1–3 show the dependences of the dimensionless absorption cross section F on the dimensionless frequency y of the external field. Figure 1 refers to small particles with $R \ll \Lambda$ ($x = 0$). The curves are plotted for different reflection coefficients q. The oscillatory frequency dependence can be explained by the fact that, for diffuse electron reflection from the particle surface ($q = 0$), the surface effects, which decay with an increase in the reflection coefficient q, are the most significant.

Figures 2 and 3 are plotted for a fixed value of the coefficient q. An increase in the particle radius smoothes out the oscillation in the frequency dependence in Fig. 2. With an increase in the reflection coefficient, the absorption cross section decreases because the contribution of the surface effects to the energy dissipation is reduced.

Figure 3 compares the results obtained with the kinetic approach with classical results (44) and (48). Here, the particle radius is equal to the electron mean free path ($x = 1$) and the reflection coefficient $q = 0.1$. When the dimensionless frequency y is small ($y < 2$), the adsorption cross section grows in proportion to y^2 and all the three formulas give close results. As y increases, the absorption rapidly tends toward saturation. The results obtained by the classical formulas

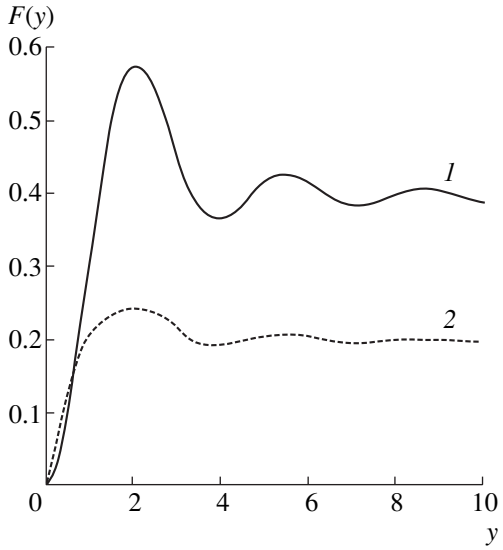

Fig. 1. Dimensionless absorption cross section F vs. dimensionless frequency y at the fixed dimensionless reciprocal mean free path $x = 0$. The reflection coefficient q is (*1*) 0, (*2*) 0.5, and (*3*) 1 (the last curve coincides with the y axis).

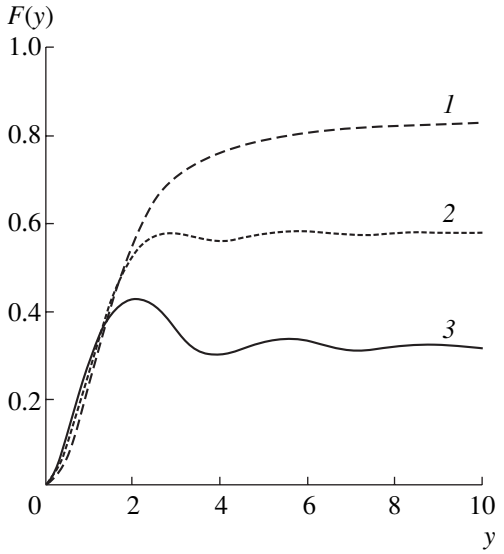

Fig. 2. The same as in Fig. 1 for $q = 0.2$ and $x = 1$ (*1*), 0.5 (*2*), and 0 (*3*).

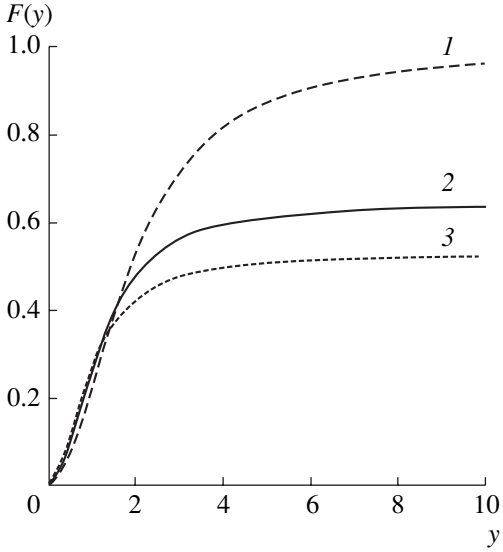

Fig. 3. The same as in Fig. 1 for $q = 0.1$ and $x = 1$: (*1*) modified Drude formula, (*2*) kinetic calculation, and (*3*) Drude formula.

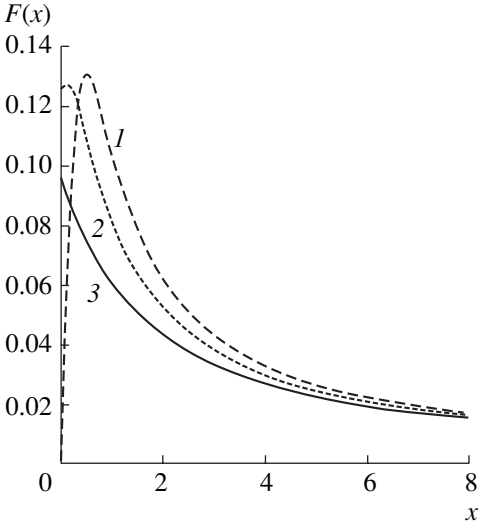

Fig. 4. Dimensionless absorption cross section F vs. dimensionless reciprocal mean free path x for the dimensionless frequency $y = 0.5$ and reflection coefficient $q = 1$ (*1*), 0.5 (*2*), and 0 (*3*).

asymptotically tend to $F_D(y) = \pi x/6$ and $F_{MD}(y) = \pi(x + 1 - q)/6$.

Figures 4–6 plot the dimensionless cross section F against the dimensionless reciprocal mean free path x. In Fig. 4, the dimensionless frequency y is fixed and the reflection coefficient q is varied. In this figure, the absorption cross section has the sharpest maximum at $q = 1$ (in agreement with the classical result), this curve emerging from the origin. At $q \neq 1$, the dimensionless absorption cross section is nonzero even at $x = 0$. With an increase in the particle radius, the curves merge, following the classical prediction. As the frequency grows, so does the absorption cross section, since the eddy electric field strength is proportional to the external field frequency.

Figure 5 shows how the absorption cross section varies with the dimensionless frequency y for a given reflection coefficient q; namely, the absorption cross section F increases with y.

With Fig. 6, the results obtained by the kinetic calculations and with the classical Drude theory can be

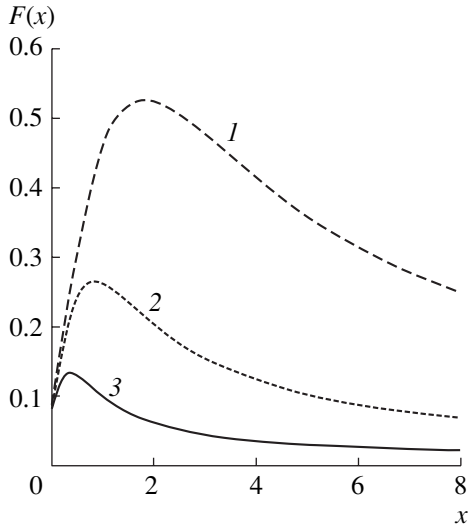

Fig. 5. The same as in Fig. 4 for $q = 0.8$ and $y = 2$ (*1*), 1 (*2*), and 0.5 (*3*).

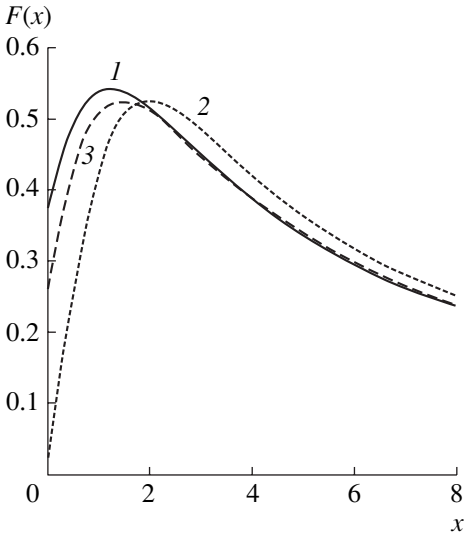

Fig. 6. The same as in Fig. 4 for $q = 0.3$ and $y = 2$. (*1*) Kinetic calculation, (*2*) Drude formula, and (*3*) modified Drude formula.

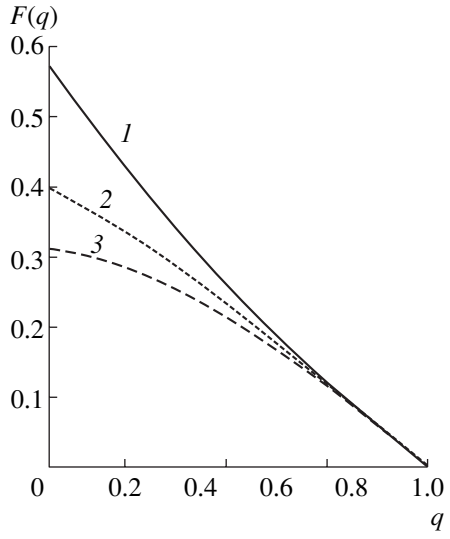

Fig. 7. Dimensionlessabsorption cross section F vs. reflection coefficient q at the fixed dimensionless reciprocal mean free path $x = 0$. $y = 2$ (*1*), 1 (*2*), and 0.5 (*3*).

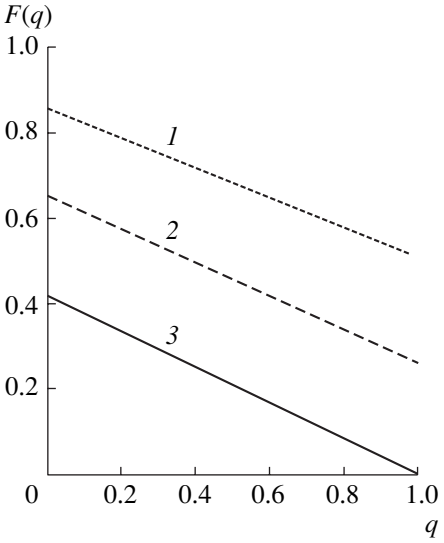

Fig. 8. The same as in Fig. 7 for $y = 5$ and dimensionless reciprocal mean free path $x = 1$ (*1*), 0.5 (*2*), and 0 (*3*).

compared. At high x, they are practically identical. Classical formulas (44) and (48) have the asymptotes $F_D(x) = \pi y^2/6x$ and $F_{MD}(x) = \pi y^2/6(x + 1 - q)$, respectively.

The effect of the reflection coefficient q on the absorption cross section F can be clarified from Figs. 7 and 8. It is evident from Fig. 7 that, in the absence of volume electron scattering, the absorption increases with dimensionless frequency y. In this case, the absorption cross section tends to zero at any y if the reflection of electrons is purely mirror ($q = 1$). The reason is that the absorption cross section is approximately proportional to the sum of the volume and surface scattering frequencies at large y (see (48)). At a given frequency, the absorption cross section decreases with growing reflection coefficient (Fig. 8).

REFERENCES

1. Yu. I. Petrov, *Physics of Small Particles* (Nauka, Moscow, 1984), Chap. 7.
2. I. D. Morokhov, V. I. Petinov, L. I. Trusov, *et al.*, Usp. Fiz. Nauk **133**, 653 (1981) [Sov. Phys. Usp. **24**, 295 (1981)].
3. M. Born and E. Wolf, *Principles of Optics*, 4th ed. (Pergamon, Oxford, 1969; Nauka, Moscow, 1973), Chap. 13.
4. H. J. Trodahl, Phys. Rev. B **19**, 1316 (1979).

5. A. G. Lesskis, V. E. Pasternak, and A. A. Yushkanov, Zh. Éksp. Teor. Fiz. **83**, 310 (1982) [Sov. Phys. JETP **56**, 170 (1982)].
6. J. M. Ziman, *Electrons and Phonons* (Clarendon, Oxford, 1960; IL, Moscow, 1962), Chap. 11.
7. H. J. Trodahl, J. Phys. C **15**, 7245 (1982).
8. A. G. Mal'shukov, Solid State Commun. **44**, 1257 (1982).
9. A. G. Mal'shukov, Zh. Éksp. Teor. Fiz. **85**, 700 (1983) [Sov. Phys. JETP **58**, 409 (1983)].
10. A. G. Lesskis, A. A. Yushkanov, and Yu. I. Yalamov, Poverkhnost, No. 11, 115 (1987).
11. É. V. Zavitaev, A. A. Yushkanov, and Yu. I. Yalamov, Zh. Tekh. Fiz. **71** (11), 114 (2001) [Tech. Phys. **46**, 1460 (2001)].
12. L. D. Landau and E. M. Lifshitz, *Course of Theoretical Physics*, Vol. 8: *Electrodynamics of Continuous Media* (Nauka, Moscow, 1992; Pergamon, New York, 1984).
13. W. A. Harrison, *Solid State Theory* (McGraw-Hill, New York, 1970; Mir, Moscow, 1972).
14. R. Courant and D. Hilbert, *Methods of Mathematical Physics*, Vol. 2: *Partial Differential Equations* (Interscience, New York, 1962; Mir, Moscow, 1964).

Translated by M. Lebedev

Technical Physics, Vol. 48, No. 3, 2003, pp. 298–302. Translated from Zhurnal Tekhnicheskoĭ Fiziki, Vol. 73, No. 3, 2003, pp. 23–27.

THEORETICAL AND MATHEMATICAL PHYSICS

On the Effect of Longitude-Dependent Fields on Convection in Stellar Atmospheres

Yu. V. Vandakurov

Ioffe Physicotechnical Institute, Russian Academy of Sciences, Politekhnicheskaya ul. 26, St. Petersburg, 194021 Russia

Received September 17, 2002

Abstract—In rotating stellar convective zones, heat transfer is shown to be associated with unbalanced azimuth forces arising in the radially ascending (heated) or descending (cold) matter. The presence of a longitude-dependent magnetic field generates additional azimuth forces, hence, new ways of compensating for the unbalanced forces. Generally speaking, this magnetic field is variable but may be nearly static in layers where convective equilibrium is replaced by radiative equilibrium. The condition for the coexistence of the static and usual fields is derived. To this end, an axisymmetric azimuth magnetic field of energy comparable to the energy of rotation should be introduced into models under consideration. In such configurations, conditions for magnetic field generation, as in the Sun, may appear. © *2003 MAIK "Nauka/Interperiodica".*

INTRODUCTION

The conventional model of the convective zone around a rotating star is based on the assumption that the effective turbulent viscosity of the medium plays a crucial role, as it is responsible for the differential rotation and magnetic field generation (see, e.g., [1]). However, many attempts to construct an appropriate theoretical model of differential rotation and solar activity heretofore have failed. Moreover, the very fact that viscous forces spontaneously sustain the rigid rotation of the medium comes into conflict with the laws of thermodynamics, as was noted in [2].

Therefore, models that are based on the minimal dissipation principle and ignore the turbulent viscosity of the medium [3] seem to be more substantiated. Yet these models, too, do not remove the contradictions between the theory and observations. In particular, differential rotation as in the Sun does form spontaneously in terms of the minimum dissipation models [3], but the latitude differentiation far exceeds that due to the Sun's rotation. In addition, in these models, a great role is allocated to latitude differentiation described by higher order modes, which has also not found experimental support.

It is not improbable that the problem should be treated with allowance for convective heat transfer in the presence of the Coriolis force. With this in mind, it should be noted that any radially moving convective element of a rotating medium is subjected to an unbalanced azimuth force, which has not been considered up to now in constructing the models.

The azimuth balance condition in a nonviscous rotating magnetized medium is given by

$$\frac{\partial v_\varphi}{\partial t} + \left[(\mathrm{curl}\mathbf{v})\times\mathbf{v} - \frac{1}{4\pi\rho}(\mathrm{curl}\mathbf{B})\times\mathbf{B}\right]\mathbf{i}_\varphi = 0, \quad (1)$$

where $\mathbf{v}$ is the velocity, $\mathbf{B}$ is the magnetic field, ρ is the density of the medium (which is assumed to be spherically symmetric), t is time, φ is the azimuth angle, and $\mathbf{i}_\varphi$ is the azimuth unit vector.

In a rigidly rotating (with an angular velocity Ω) medium, $\mathrm{curl}\mathbf{v} = \mathbf{i}_z 2\Omega$, where the z axis is parallel to the axis of rotation; therefore, for a radially moving (with a velocity v_r) convective element, the Coriolis force in Eq. (1) is azimuth. This force is nonzero not only at the poles. It is obvious that such an azimuth force arises at any differential rotation of the medium.

The velocity of convection in stellar atmospheres is not low. According to Spruit's estimates [4], the radial velocity v_r in the lower layers of the solar convective zone is on the order of 10^3–10^4 cm/s. Substituting these values into (1) yields characteristic times of variation of v_φ from one year to one month if $v_\varphi \approx 2$ km/s as in the Sun. Certainly, here we are actually dealing with an azimuth force arising in ascending (heated) or descending (cold) flows of matter; yet the unbalanced side force may markedly disturb the radial motion of convective elements and, hence, cause random variations of the velocity of rotation, which make convective heat transfer difficult. Thus, processes that regularize convective heat transfer in stellar atmospheres may be of crucial importance.

In the presence of longitude-dependent velocity and magnetic fields, the force balance must include additional azimuth forces. If these additional forces prevail,

1063-7842/03/4803-0298$24.00

new ways of compensating for the small unbalance mentioned above appear. As will be shown later, the additional forces are usually variable, which may be related to solar activity. The problem discussed here is also of interest for the theory of differential rotation of the Sun and also for the theory of nonrigid rotation of convective cores in stars.

Initially, it would be reasonable to study the static model in order to perceive more fully difficulties associated with the construction of a general theory. Specifically, one can expect that the static condition will be valid for equilibrium in transition layers between the convective and radiative zones of stars. In Sect. 1, we consider the basic condition for azimuth equilibrium in the steady state, bearing in mind that relationships derived in this section are a prerequisite for going to a more general nonstationary problem. The discussion of the results is given in Sect. 2.

1. AZIMUTH EQUILIBRIUM

The equilibrium problem for a magnetized rotating gravitating medium can be solved by using the quantum-mechanical apparatus for expanding vector fields in orthogonal spherical vector harmonics $Y_{JM}^{(\lambda)}$, where $\lambda = 0$ or ± 1, $J \geq 0$ is an integer, and $M = -J, -J+1, \ldots, J$. (For detailed derivation of all basic relationships, see [5].) It is important here that radius–time and angular variables in general nonlinear equations are separated without loss of generality. The reduction of the basic relationships to a form convenient for astrophysical applications is carried out in [6, 7]. It is also significant that there may arise difficulties associated with the nonexistence of a solution [7–9] because the equations of motion are nonlinear.

The disturbances of azimuth equilibrium (see Introduction) are nonaxisymmetric ($M \neq 0$). Then, a set of equations for longitude-dependent variable parameters includes Eq. (1) and a similar equation for the φ component of the induction. These fields with $M \neq 0$ will be imposed on rotational and magnetic structures symmetric about the axis of rotation.

With the relationships derived in [6] and negligibly small poloidal components of the fields, the basic equations after the separation of variables take the form

$$r\frac{\partial}{\partial t}v_{JM}^{(0)} = -\frac{M}{(2J+1)^{1/2}}\sum_{J_1J_2} T_{J_1J_2}^{J}(J_1 - J_2) \times (J_1 + J_2 + 1)(v_{J_1M}^{(0)} v_{J_20}^{(0)} - A_{J_1M}^{(0)} A_{J_20}^{(0)}), \quad (2)$$

$$r\frac{\partial}{\partial t}A_{JM}^{(0)} = \frac{MJ(J+1)}{(2J+1)^{1/2}} \times \sum_{J_1J_2} T_{J_1J_2}^{J}(v_{J_1M}^{(0)} A_{J_20}^{(0)} - A_{J_1M}^{(0)} v_{J_20}^{(0)}), \quad (3)$$

where $M \neq 0$, $A_{JM}^{(0)} = B_{JM}^{(0)}/(4\pi\rho)^{1/2}$ is the Alfvén velocity, $v_{J0}^{(0)}$ (or $B_{J0}^{(0)}$) is the coefficient in the formula for the rotation velocity (or axisymmetric azimuth magnetic field), $T_{J_1J_2}^{J} = C_{J_1MJ_20}^{JM}\Theta_{J_1J_2}^{J}/M$ is the numerical factor that will be discussed in the Appendix, and the sum $J + J_1 + J_2$ is odd.

We will study the longitude-dependent static fields with various subscripts M, assuming that the rotation velocity is symmetric about the equator (i.e., that the coefficients $v_{J0}^{(0)}$ have odd J) and the azimuth magnetic field is characterized by complementary symmetry (J is even). We also assume that the symmetry of the coefficients with $M \neq 0$ is complementary symmetry compared with the coefficients with $M = 0$. Finally, in what follows, the designations $u_J = u_{J0}^{(0)}/v_{10}^{(0)}$ and $a_L = A_{L0}^{(0)}/v_{10}^{(0)}$, where $J = 1, 3, 5, \ldots$ and $L = J + 1$, will be used.

In the general case, Eqs. (2) and (3) define the harmonic variations of the longitude-dependent fields. For the case of the rigid stationary rotation of a nonmagnetic medium, the former describes Rossby waves whose angular frequency divided by the angular velocity of rotation equals $-M(J-1)(J+2)/[J(J+1)]$ [10]. Note also that the generation of the longitude-dependent field should be studied in terms of more rigorous equations where the poloidal components of the fields are taken into account (see calculations in [11, 12]).

Nevertheless, a number of important conclusions can be drawn by studying the steady-state equilibrium state. In this case, the right-hand sides of Eqs. (2) and (3) represent a set of homogeneous linear equations for $v_{JM}^{(0)}$ and $A_{JM}^{(0)}$ with $M \neq 0$. Clearly, for solutions to these equations to exist, it is necessary that the parameters $v_{J0}^{(0)}$ and $A_{J0}^{(0)}$ (or u_J and a_L) satisfy the associated solubility condition, that is, that the determinant made up of the coefficients multiplying these parameters with $M \neq 0$ be equal to zero.

Below, it will be shown that a stationary single-mode model is of most interest. In this model, only the first coefficients u_1 and u_2 are essential in the expansions of the axisymmetric fields (u_1 is set equal to unity). If we put $M = \pm 1$ at once, Eqs. (2) and (3) take the form

$$\frac{(5)^{1/2}a_2}{J(2J-1)^{1/2}}v_{J-1,M}^{(0)} - \frac{(2J+1)^{1/2}}{J(J+1)}A_{JM}^{(0)} + \frac{(5)^{1/2}a_2}{(J+1)(2J+3)^{1/2}}v_{J+1,M}^{(0)} = 0; \quad J = 1, 3, \ldots, \quad (4)$$

$$\frac{(5)^{1/2}a_2(J-3)(J+2)}{J(2J-1)^{1/2}}A_{J-1,M}^{(0)}$$

$$-\frac{(J-1)(J+2)(2J+1)^{1/2}}{J(J+1)}v_{JM}^{(0)} \quad (5)$$

$$+\frac{(5)^{1/2}a_2(J-1)(J+4)}{(J+1)(2J+3)^{1/2}}A_{J+1,M}^{(0)} = 0, \quad J = 2, 4, \ldots,$$

where the first and last terms (with the subscripts $J - 1 = 0$ and $J + 1 > N$) in the first and last equations must be omitted. Here, N is the order of the determinant that follows from the solubility condition for the entire set of N variables. Note that N is an even number. Certainly, only solutions that depend on N insignificantly are of interest. The matrix corresponding to the left-hand sides of the last equations is tridiagonal: only the principle diagonal and two adjacent diagonals are filled.

Let us also give the solubility condition for the case when the first-order corrections to the latitude differentiation of rotation are taken into account. For $N = 4$ and $M = \pm 1$, this condition is reduced to

$$\begin{vmatrix} T_{11}^1 & -T_{22}^1 a_2 & T_{33}^1 u_3 & -T_{44}^1 a_4 \\ -4T_{12}^2 a_2 & -4T_{21}^2 + 6T_{23}^2 u_3 & 6T_{32}^2 a_2 - 8T_{34}^2 a_4 & -8T_{43}^2 u_3 \\ T_{13}^3 u_3 & -T_{22}^3 a_2 - T_{24}^3 a_4 & T_{31}^3 + T_{33}^3 u_3 & -T_{42}^3 a_2 - T_{44}^3 a_4 \\ -18T_{14}^4 a_4 & 6T_{23}^4 u_3 & 6T_{32}^4 a_2 - 8T_{34}^4 a_4 & -18T_{41}^4 - 8T_{43}^4 u_3 \end{vmatrix} = 0. \quad (6)$$

As was already noted, a solution to these equations is true when the parameters $v_{J0}^{(0)}$ and $A_{J0}^{(0)}$ found from them are virtually independent of N. Note in passing that a solution is absent if $N = 2$. Latitude differential rotation observed in the Sun roughly meets the condition $u_3 = v_{30}^{(0)}/v_{10}^{(0)} \approx -0.05$ [2, 7]. It appears that if $|u_3| < 0.1$ (with the same restriction imposed on the coefficients $u_5, u_7, \ldots, a_4, a_6, \ldots$), a solution to Eqs. (2) and (3) nearly coincides with that of (4) and (5) and becomes almost independent of both N and all the coefficients except u_1 (taken to be equal to unity) and a_2 provided that the maximal value of J, $J_{\max}$, is sufficiently large (e.g., $J_{\max} \geq 100$; i.e., $N \geq 100$). This solution specifies the first coefficient in the expansion of the azimuth Alfvén velocity:

$$a_2 = A_{20}^{(0)}/v_{10}^{(0)} \simeq \pm 0.449. \quad (7)$$

If $N = 4$, 8, or 12 and the correction coefficients u_3, a_4, etc., are negligibly small, $|a_2|$ equals 0.847, 0.525, and 0.482, respectively, and depends noticeably on the coefficients u_3, etc. For example, with $N = 4$, $a_4 = 0$, and $u_3 = -0.05$, we find from Eq. (6) the solution $a_2 = 0.814$. If $N = 4$ and $a_4 = u_3 = -0.05$, then $a_2 = 0.782$. Thus, in going from the very crude to exact solution, a_2 substantially decreases and becomes insensitive to the latitude variation of the fields.

In the case of the configuration with $|M| > 1$, all terms in basic equations (4) and (5) must be multiplied by M; also, the terms containing coefficients with the subscripts $J \pm 1$ and M must be additionally multiplied, respectively, by $\{[(J + I) - M^2]/[(J + I)^2 - 1]\}^{1/2}$, where $I = (1 \pm 1)/2$. It is easy to check that the above considerations are valid when M is not too large, i.e., when the ratio $|M|/J_{\max}$ is a small quantity.

It is seen that the stationary solution found describes fields that are virtually independent of the differential latitude rotation. If latitude differentiation is completely absent, the radius-dependent angular velocity,

$$\Omega = v_\varphi/(r\sin\vartheta) = i[3/(8\pi)]^{1/2}(v_{10}^{(0)}/r), \quad (8)$$

and the azimuth magnetic field,

$$B_\varphi = i[15/(32\pi)^{1/2}B_{20}^{(0)}\sin(2\vartheta)], \quad (9)$$

are related to each other as

$$B_\varphi = \pm 0.449(5\pi\rho)^{1/2}r\Omega\sin(2\vartheta). \quad (10)$$

For example, at the bottom of the solar convective zone, the linear rotation velocity $r\Omega$ is ≈2 km/s and the density $\rho \approx 0.1$ g/cm^3; then, if the condition under discussion is met, a maximal magnetic field of $B_\varphi \approx$ 110 kG is attained at a latitude of 45°.

The amplitudes of the longitude-dependent modes with the subscript M (M modes) can be found from (4) and (5) if the amplitude of the mode with the least subscript J is normalized. We will assume below that $w_J = A_{JM}^{(0)}$ (if J is odd) or $v_{JM}^{(0)}$ (if J is even). For $M = 1$, we put $A_{11}^{(0)} = 1$; for $M = 2$, $A_{12}^{(0)} = 0$ and $v_{22}^{(0)} = 1$. In the figure, the variation of the amplitudes for these two cases is depicted by the continuous and dotted curves. The amplitudes are seen to severely rotate when the subscript J changes. For example, with $J \geq 30$, the amplitude may exceed its initial value by more than three orders of magnitude.

2. DISCUSSION

The solution found indicates that the regularization of convective heat transfer in a rotating star is possible if both the axisymmetric azimuth magnetic field and

the longitude-dependent rotational and magnetic fields are present in the stellar atmosphere. At the bottom of the solar convective zone, this axisymmetric azimuth magnetic field equals about 110 kG irrespective of whether the latitude differentiation of the angular velocity takes place. This field can be compared with that defined by mechanical equilibrium. For the angular velocity of rotation depending on the radius r alone, these conditions were discussed in [11]. We will assume that at the bottom of the solar convective zone, the medium is stratified and quasi-adiabatic. First, only effects induced by axisymmetric fields will be discussed.

It is easy to show that the axisymmetric magnetic force that sustains the differential (in respect to the radius) rotation of the medium is described by a vector containing three spherical harmonics with the principal subscripts $J = 0$, 2, and 4. For $J = 0$, the equilibrium condition is met readily. With $J = 2$, equilibrium is established in the presence of the appropriate radial gradient of the angular velocity (see Eq. 42 in [11]). Under our conditions ($\rho \approx 0.1$ g/cm^3), equilibrium takes place when the angular velocity varies as $r^{0.38}$. Such a radial dependence of the angular velocity at the bottom of the solar convective zone may fit helioseismic data reported, e.g., in [13].

Difficulties arise in the case $J = 4$, when Eq. (26) in [11] is valid. In this case, the last term of this equation vanishes in an adiabatically stratified medium. This equation could be satisfied if the magnetic field decreased with increasing radius. This would mean that the angular velocity of rotation decreases with altitude. This, however, contradicts both the result obtained above and helioseismic data. In essence, we arrive at the conclusion that the equations of equilibrium cannot be solved for an adiabatically stratified medium if the standard conditions are considered (the fields are axisymmetric) and the angular velocity depends on the radius. This conclusion remains true irrespective of whether condition (10) of convective heat transfer regularization is taken into account or not. If the latitude differentiation of rotation is lacking, the situation becomes still more aggravated.

The conclusion that the equations of equilibrium are unsolvable is not related to any model concepts; therefore, here we are dealing with a fundamental problem of theoretical astrophysics. The fact is that, as applied to our nonlinear equilibrium problem, the number of coefficients to be found grows more slowly than the number of equations for these coefficients when one passes from one approximation to another (higher order) approximation. We believe that the only way to tackle this theoretical problem is to supplement the general equation for force balance with the averaged forces introduced by the longitude-dependent M modes. In this case, additional equations of equilibrium will certainly arise for layers between the convective and radiative zones (in the very convective zone, non-

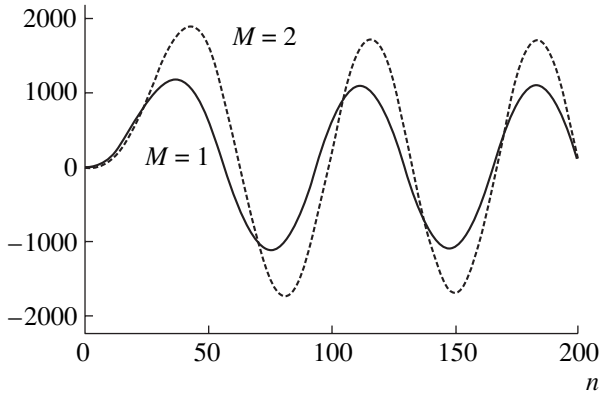

Amplitudes of the longitude-dependent Alfvén (if n is odd) and rotational (if n is even) velocities for $M = 1$ (continuous line) and $M = 2$ (dotted line) vs. mode number. The initial fragments of the curves are depicted.

stationary processes are expected to play a decisive role). These additional equations will probably be satisfied by exciting weak horizontal motions of the medium. Such a supposition is based on recent helioseismic data [14] indicating dynamic variations in the velocity of rotation of the Sun with periods of about a year in layers with relative radii of 0.63 and 0.72. These layers are below or near the convective zone boundary. It is also important here that the presence of the longitude-dependent fields makes it possible to regularize convective heat transfer.

Certainly, it seems unlikely that the amplitudes of the M modes be comparable with the amplitudes of the axisymmetric modes. However, the combined effect may arise from those large-amplitude M modes located near an extremum in the figure. For example, in the case of modes with amplitudes from $(2/3)(w_J)_{\max}$ to $(w_J)_{\max}$, where $(w_J)_{\max}$ is the largest amplitude corresponding to a given maximum, the force generated by these M modes will most likely be comparable to the standard force if the longitude-dependent field is one order of magnitude smaller than the axisymmetric field.

These results favor the opinion that convection in rotating stellar atmospheres is closely related to magnetic phenomena. We considered only the quasi-stationary situation, which occurs either at the bottom of the convective shell or at the top of the convective core. For the entire convective shell, as has been stated, nonstationary processes generating a longitude-dependent magnetic field are of great concern [11, 12, 15]. It should be stressed that this magnetic field is generated spontaneously in the presence of a rather weak meridional circulation of the medium. For example, the characteristic time of field generation in the Sun is about ten years if the circulation rate in the interior is as low as 10 cm/s. Relations between the magnetic field generation and convective heat transfer regularization call for special investigation.

APPENDIX

The numerical coefficients T^J_{KL} are determined with the equations given in [6]; however, the form of Eqs. (8), (9), (13), and (22)–(24) in [6] is inconvenient. In them, $\mathbf{v}_1$, $\mathbf{v}_2$, and $v^{(\lambda)}_{J_1M_1}$ should be replaced, respectively, by $\mathbf{u}$, $\mathbf{v}$, and $u^{(\lambda)}_{J_1M_1}$, where λ may stand for ±1, 0, or λ_1. The same substitutions should be made in Eqs. (34)–(37) in [7], where the last superscript in (36) should be –1.

Using the relationships given in [5], one can derive the following formulas for the numerical coefficients T^J_{KL} entering into Eqs. (2) and (3):

$$T^J_{K1} = -f\frac{(2J+1)^{1/2}}{J(J+1)}\delta(J,K),$$

$$T^J_{K2} = -f2(5)^{1/2}\frac{\delta(J,K+1)+\delta(J,K-1)}{(J+K+1)(2K+1)^{1/2}},$$

$$T^J_{K3} = -f\frac{(14)^{1/2}}{4}\left\{\frac{5[\delta(J,K+2)+\delta(J,K-2)]}{(J+K+1)(2K+1)^{1/2}}\right.$$

$$\left.+\frac{6(J-1)(J+2)(2J+1)^{1/2}}{J(J+1)(2J-1)(2J+3)}\delta(J,K)\right\},$$

$$T^J_{K4} = -f\frac{9(15)^{1/2}}{4[2(2K+1)]^{1/2}}$$

$$\times\left\{\frac{7(J+K+1)[\delta(J,K+3)+\delta(J,K-3)]}{(4J+2K+3)(2J+4K+3)}\right.$$

$$\left.+\frac{(J+K-3)(J+K+5)[\delta(J,K+1)+\delta(J,K-1)]}{(J+K+1)(J+K-2)(J+K+4)}\right\}.$$

Here, $f = [3/(8\pi)]^{1/2}$ and $\delta(J, K)$ equals unity for $J = K$ or otherwise zero.

ACKNOWLEDGMENTS

This work was financially supported by the Russian Foundation for Basic Research (project no. 00-02-16939).

REFERENCES

1. E. N. Parker, *Cosmical Magnetic Fields* (Clarendon, Oxford, 1979; Mir, Moscow, 1982).
2. Yu. V. Vandakurov, Pis'ma Astron. Zh. **25**, 868 (1999) [Astron. Lett. **25**, 758 (1999)].
3. Yu. V. Vandakurov, Pis'ma Astron. Zh. **28**, 633 (2002) [Astron. Lett. **28**, 560 (2002)].
4. H. C. Spruit, Sol. Phys. **34**, 277 (1974).
5. D. A. Varshalovich, A. N. Moskalev, and V. K. Khersonskii, *Quantum Theory of Angular Momentum* (Nauka, Leningrad, 1975; World Sci., Singapore, 1988).
6. Yu. V. Vandakurov, Astron. Zh. **76**, 29 (1999) [Astron. Rep. **43**, 24 (1999)].
7. Yu. V. Vandakurov, Astron. Zh. **78**, 253 (2001) [Astron. Rep. **45**, 216 (2001)].
8. Yu. V. Vandakurov, Pis'ma Astron. Zh. **25**, 143 (1999) [Astron. Lett. **25**, 111 (1999)].
9. Yu. V. Vandakurov, Zh. Tekh. Fiz. **71** (6), 1 (2001) [Tech. Phys. **46**, 645 (2001)].
10. Yu. V. Vandakurov, Astron. Zh. **74**, 115 (1997) [Astron. Rep. **41**, 106 (1997)].
11. Yu. V. Vandakurov, Pis'ma Astron. Zh. **27**, 700 (2001) [Astron. Lett. **27**, 596 (2001)].
12. Yu. V. Vandakurov, Izv. Vyssh. Uchebn. Zaved. Radiofiz. **44**, 735 (2001) [Radiophys. Quantum Electron. **44**, 678 (2001)].
13. J. Schou, H. M. Antia, S. Basu, *et al.*, Astrophys. J. **505**, 390 (1998).
14. R. Howe, J. Christensen-Dalsgaard, F. Hill, *et al.*, Science **287**, 2456 (2000).
15. Yu. V. Vandakurov, Pis'ma Zh. Tekh. Fiz. **27** (18), 29 (2001) [Tech. Phys. Lett. **27**, 769 (2001)].

Translated by V. Isaakyan

Technical Physics, Vol. 48, No. 3, 2003, pp. 303–310. Translated from Zhurnal Tekhnicheskoĭ Fiziki, Vol. 73, No. 3, 2003, pp. 28–35.

GASES AND LIQUIDS

Two-Dimensional Gas Motion in Nuclear-Pumped Laser Cells at Low Energy Deposits into the Gas

V. Yu. Mat'ev

AII-Russia Research Institute of Experimental Physics, Russian Federal Nuclear Center, Sarov, Nizhegorodsk oblast, 607190 Russia

Received April 29, 2002

Abstract—The distribution of the two-dimensional gas velocity inside ion-irradiated laser cells is considered for low ion energy deposits into the gas. It is shown that, if the energy deposit is smoothly nonuniform, the two-dimensional motion has two quasi-one-dimensional components: the longitudinal gas velocity is practically uniform across the cell and depends on the transversely averaged energy deposit, while the transverse velocity component depends on the difference between the local energy deposit and energy deposit averaged over the transverse direction. *© 2003 MAIK "Nauka/Interperiodica".*

INTRODUCTION

The basic principle behind nuclear-pumped laser operation is the production of inversely populated lasing levels in the gas medium via irradiation by ions that are products of nuclear reactions (usually, fission fragments from uranium layers; see review [1]). A nonuniform energy deposit from the ions into the gas leads to the redistribution of the gas density in the cell [2–7] and thereby adversely affects the lasing quality [2, 6]. One-dimensional calculations of the transverse gas motion in a gastight cell [2–6] and the numerical calculation of the two-dimensional gas density distribution over a flowing gas cell [7] have been carried out; however, the problem of two-dimensional distribution of the gas velocity has yet to be solved.

In this paper, the method of separation of variables is applied to analyze the two-dimensional gas motion inside a cell irradiated by fission fragments. The energy deposit from the fragments into the gas is assumed to be low (as compared with the internal gas energy). In this case, the gas velocity field is irrotational and is described by the scalar potential satisfying the Poisson equation [8].

BASIC PHYSICAL PROCESSES

A nuclear-pumped laser is a gas-filled (gastight or flowing-gas) cell with thin uranium layers on its inner surface that irradiate the gas (Fig. 1). Here, cells with plane layers inside are considered in the two-dimensional approximation. For gastight cells [5], the x axis is directed along the optical one (the length of such cells is $L \approx 1$ m); for flowing-gas cells [6], the x axis is aligned with the gas flow and runs transversely to the optical axis ($L \approx 0.1$ m). The width of either cell is $2h \approx 0.01$ m.

The key gasdynamic factor for such cells is the energy deposit from fusion fragments irradiating the gas from the uranium layers. The energy δQ of the fragments that is absorbed by a small gas volume δV for a time δt can be represented in the form [4, 5]

$$\frac{\delta Q}{\delta V \delta t} = \frac{\Theta P_0}{\gamma - 1}\frac{\rho(x, y, t)}{\rho_0}\psi(t)F(x, y, t), \qquad (1)$$

where $\rho(x, y, t)$ is the gas density; ρ_0 is the initial gas density; P_0 is the initial gas pressure; $\gamma \approx 5/3$ is the ratio of the specific heat at constant pressure to that at constant volume; $F(x, y, t)$ is the energy deposit function depending on the cell geometry, neutron flux distribution, and gas density ($F(x, y, t) \approx 1$) [9]; Θ is a dimensionless energy deposit parameter; and $\psi(t)$ is the time-dependent neutron flux profile such that its integral taken over the irradiation time τ is normalized to unity.

For gastight cells, τ is the duration of the neutron pulse ($\approx$1 ms); for flowing gas cells, τ is the characteristic time of the gas flow: $\tau = L/U_0 \approx 0.01$ s, where $U_0 \approx 10$ m/s is the gas velocity at the cell inlet ($x = 0$). The parameter Θ is introduced as a thermodynamic measure of the energy deposit [4]: it equals the ratio of the fission fragment energy absorbed by a homogeneous ideal gas with a density ρ_0 in the cell for a time τ to the internal energy of this gas. In practice, $\Theta < 1$ or $\Theta \approx 1.0$

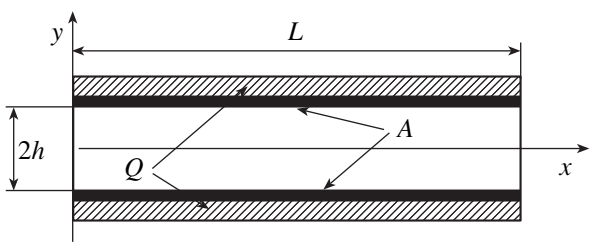

Fig. 1. Nuclear-pumped laser cell. *Q*, cell; *A*, uranium layer.

1063-7842/03/4803-0303$24.00 © 2003 MAIK "Nauka/Interperiodica"

[5, 6]. In this study, Θ is a small parameter: we assume that $\Theta \ll 1$.

The second small parameter is the Mach number M. In gastight cells, the transverse gas velocity is $w < h/\tau$ and the longitudinal velocity is $u < L/(2\tau)$; in flowing gas cells, $u \approx U_0$. For gases used in nuclear-pumped lasers (He or Ar at a pressure $P_0 \approx 1$ atm), the speed of sound $v_s \sim 10^3$ m/s; therefore, for gastight cells $w/v_s < 10^{-2}$ and $u/v_s < 0.5$, while for flowing gas cells $w/v_s < 10^{-3}$ and $u/v_s < 10^{-2}$. Thus, the gas pressure is practically uniform across the cell. Along flowing gas cells, the pressure is also uniform. However, for gastight cells, the longitudinal pressure can be considered to be uniform only if it is taken into account that $u \ll L/(2\tau)$ when $\Theta \ll 1$. The presence of considerable gas density differences at low Mach numbers, which is due to internal heat sources (see (1)), is a key feature of gas dynamics in nuclear-pumped lasers. Viscosity and heat conduction play a noticeable role only in the narrow near-wall layer. In most of the cell volume, their effect is negligibly small [2, 3, 6]. Under these conditions, the gas motion is virtually self-consistent thermal expansion over the cell volume; the self-consistency is conditioned by the pressure uniformity.

GASDYNAMIC MODEL

The gas is assumed to be ideal, inviscid, and nonheat-conducting, and the pressure is set equal to the cell-volume-averaged value:

$$p(x, y, t) \approx P(t) \approx \langle p(x, y, t)\rangle_V,$$

where $\langle\ldots\rangle_V$ means volume averaging.

The fission fragment energy ΔQ that is released in a gas volume element V raises the internal gas energy $E = PV/(\gamma - 1)$ and does the expansion work $P\Delta V$:

$$(\gamma - 1)\Delta Q = \gamma P\Delta V + V\Delta P.$$

In the limit $V \longrightarrow 0$ and in view of the mass conservation condition ($\Delta V/V \longrightarrow -d\rho/\rho$), we have

$$(\gamma - 1)\frac{\delta Q}{\delta V\delta t} = \frac{dP}{dt} - \frac{\gamma P}{\rho}\cdot\frac{d\rho}{dt} \qquad (2)$$

subject to the continuity equation

$$\frac{1}{\rho}\frac{d\rho}{dt} + \mathrm{div}\mathbf{v} = 0, \quad \mathbf{v} = (u, w),$$

where $\mathbf{v}$ is the gas velocity.

The neglect of heat removal in gastight cells yields

$$\frac{dP}{dt} = (\gamma - 1)\left\langle\frac{\delta Q}{\delta V\delta t}\right\rangle_V. \qquad (3)$$

In flowing gas cells, $P = P_0$ under steady-state gas flow conditions.

The set of Eqs. (1)–(3) was solved for one-dimensional transverse gas motion in a gastight cell [3, 4]. In this case, the energy deposit function can be assumed to be fixed in Lagrangian coordinates: $F(x, y, t) = F_0(y_0)$, where y_0 is the Lagrangian coordinate defined by the equation $\rho_0 dy_0 = \rho(y, t)dy$. In this case, the energy deposit is easily averaged and the gas pressure is determined at once. According to (1) and (3),

$$\frac{dP}{dt} = \Theta P_0\psi(t)\frac{1}{h}\int_0^h\frac{\rho(y, t)}{\rho_0}F_0(y_0)dy$$

$$= \Theta P_0\psi(t)\frac{1}{h}\int_0^h F_0(y_0)dy_0 = \Theta P_0\psi(t),$$

because the energy deposit function $F(x, y, t)$ is normalized so that [4, 5] its volume-averaged value in a cell containing an unperturbed gas with a density ρ_0 is equal to unity: $\langle F(x, y, 0)\rangle_V = 1$. Hence,

$$P(t) = \Theta P_0\int_0^t\psi(t')dt'.$$

At a specified gas pressure and energy deposit related to the Lagrangian coordinates, Eq. (2) is easily solved in the Lagrangian coordinates (y_0, t) [3, 4]; the return to the Eulerian coordinates can be accomplished through the continuity equation. Thus, for one-dimensional gas motion, Eqs. (2) and (3), which express the first law of thermodynamics, allow one to completely solve the gasdynamic problem. At low Mach numbers M, the solution obtained is practically exact [3] and even at $M \longrightarrow 1$ it well describes the dynamics of the smoothed density profile (on which, however, acoustic ripple is imposed [3]).

For two-dimensional flows, the situation is much more complicated. First, the energy deposit function is not fixed in the Lagrangian coordinates. Second, even if the gas density distribution is known, it is impossible, generally speaking, to describe the two-dimensional flow using the continuity equation alone: one must also invoke the Euler equation and consider the nonuniform pressure $p(x, y, t)$. Nevertheless, at low energy deposits, Eqs. (2) and (3) still make it possible to obtain an approximate two-dimensional distribution of the gas velocity. According to the Helmholtz theorem, a vector field is defined by its divergence and curl (up to a constant vector). The velocity field divergence is given by (2) and (3), while the velocity curl is given by the Friedmann equation [10], which in the two-dimensional case takes the form

$$\frac{d\omega}{dt} + \omega\mathrm{div}\mathbf{v} = \frac{1}{\rho^2}|\nabla\rho\times\nabla p|, \quad \omega = |\mathrm{curl}\mathbf{v}|.$$

At low energy deposits ($\Theta \ll 1$), the differences in the gas velocities and densities (and, consequently, the pressure difference) are first-order perturbations in Θ,

as is the time integral of the divergence. Therefore,

$$\omega(t) = \exp\left(-\int_0^t \mathrm{div}\mathbf{v}\,dt'\right)$$
$$\times\left\{\omega(0) + \int_0^t \exp\left(\int_0^{t'} \mathrm{div}\mathbf{v}\,dt''\right)|\nabla\rho\times\nabla p|\frac{dt'}{d\rho^2}\right\}$$
$$\approx \omega(0)\left(1-\int_0^t \mathrm{div}\mathbf{v}\,dt'\right) + \int_0^t |\nabla\rho\times\nabla p|\frac{dt'}{\rho^2}, \quad \Theta \ll 1.$$

If the gas is initially at rest or executes irrotational motion, the curl of the velocity is of higher order of smallness in Θ than the divergence of the velocity. Thus, at low energy deposits (and at high deposits at the initial stage), the gas flow can be assumed to be vortex-free [8] and one can introduce a scalar potential $\Phi(x, y, t)$:

$$\mathbf{v} = \nabla\Phi, \quad \mathrm{div}\mathbf{v} = \Delta\Phi = \frac{1}{\rho}\frac{d\rho}{dt},$$

which satisfies, according to (2), the Poisson equation [8]

$$\Delta\Phi = G(x, y, t),$$
$$G(x, y, t) = \frac{1}{\gamma P}\left\{(\gamma-1)\left(\frac{\delta Q}{\delta V\delta t}\right) - \frac{dP}{dt}\right\}. \quad (4)$$

Here, Δ is Laplacian.

At small Θ, energy deposit (1) can be calculated for a gas with an unperturbed density: $\rho(x, y, t) = \rho_0$ (in this case, $F(x, y, t) = F_0(x, y)$ is a known function [9]). In the first order of smallness in Θ for gastight cells, we have, subject to (3),

$$G(x, y, t) = \frac{\gamma-1}{\gamma P}\left\{\left(\frac{\delta Q}{\delta V\delta t}\right) - \left\langle\frac{\delta Q}{\delta V\delta t}\right\rangle_V\right\} \quad (5)$$
$$\approx \frac{\Theta}{\gamma}\psi(t)\{F_0(x, y) - \langle F_0(x, y)\rangle_V\}, \quad \Theta \ll 1;$$

for flowing gas cells under steady-state flow conditions, when $\psi(t) = 1/\tau = U_0/L$,

$$G(x, y) = \frac{\gamma-1}{\gamma P_0}\left(\frac{\delta Q}{\delta V\delta t}\right) \approx \frac{\Theta}{\gamma}\frac{U_0}{L}F_0(x, y), \quad \Theta \ll 1. \quad (6)$$

Time does not appear explicitly in Eq. (4) for the potential. The velocity distribution is quasi-stationary in the sense that at each time instant the velocity field is related to the gas pressure and energy-deposit distribution that are present at this instant and varies simultaneously with them in time. The time dependence of the velocity is virtually parametric. Hereafter, the argument t will be omitted.

GENERAL SOLUTION FOR THE VELOCITY POTENTIAL

Equation (4) can be solved by the method of separation of variables. For the transverse velocity $w(x, y)$, the boundary conditions in gastight and flowing gas cells are the same:

$$w(x, 0) = \frac{\partial\Phi}{\partial y}(x, 0) = 0, \quad w(x, \pm h) = \frac{\partial\Phi}{\partial y}(x, \pm h) = 0.$$

They correspond to symmetric eigenfunctions $\chi_n(y) = \cos(\pi n y/h)$ of the homogeneous equation $\Delta\Phi = 0$. The potential $\Phi(x, y)$ and function $G(x, y)$ can be expanded into series in these functions:

$$\Phi(x, y) = \frac{\varphi_0(x)}{2} + \sum_{n=1}^{\infty}\varphi_n(x)\cos(a_n y),$$
$$\varphi_n(x) = \frac{2}{h}\int_0^h \Phi(x, y)\cos(a_n y)\,dy, \quad (7)$$
$$G(x, y) = \frac{g_0(x)}{2} + \sum_{n=1}^{\infty} g_n(x)\cos(a_n y),$$
$$g_n(x) = \frac{2}{h}\int_0^h G(x, y)\cos(a_n y)\,dy, \quad (8)$$

where

$$a_n = \frac{\pi n}{h}, \quad \frac{g_0(x)}{2} = \langle G(x, y)\rangle_y,$$

and $\langle\ldots\rangle_y$ means averaging across a cell.

From (4), (7), and (8), it is seen that the zero-order potential $\varphi_0(x)/2$ specifies the longitudinal velocity $U(x)$, for which

$$\frac{dU}{dx} = \frac{1}{2}\frac{d^2\varphi_0}{dx^2} = \frac{g_0(x)}{2} = \langle G(x, y)\rangle_y,$$
$$U(x) = \int_0^x \langle G(\xi, y)\rangle_y d\xi + U_0. \quad (9)$$

For flowing gas cells, U_0 is the gas flow velocity; for gastight cells, $U_0 = 0$ and $U(L) = 0$, according to (5). From (4) and (9), it follows that the zero-order potential $\varphi_0(x)/2$ corresponds to the problem with transverse averaging, that is, describes the longitudinal gas motion in the one-dimensional approximation.

For the expansion coefficients of first and higher orders $\varphi(x)$, it follows from (4), (7), and (8) that

$$\frac{d^2\varphi_n}{dx^2} - a_n^2\varphi_n(x) = g_n(x), \quad (10)$$

$$\varphi_n(x) = \frac{\exp(a_n x)}{2a_n}\left\{A_n + \int_0^x g_n(\xi)\exp(-a_n\xi)d\xi\right\} - \frac{\exp(-a_n x)}{2a_n}\left\{B_n + \int_0^x g_n(\xi)\exp(a_n\xi)d\xi\right\}. \quad (11)$$

Thus, in the general case, the gas velocity components are given by

$$u(x, y) = \frac{\partial\Phi}{\partial x} = U(x) + \sum_{n=1}^{\infty} v_n(x)\cos(a_n y), \quad (12)$$

$$v_n(x) = \frac{d\varphi_n}{dx} = \frac{\exp(a_n x)}{2}\left\{A_n + \int_0^x g_n(\xi)\exp(-a_n\xi)d\xi\right\} + \frac{\exp(-a_n x)}{2}\left\{B_n + \int_0^x g_n(\xi)\exp(a_n\xi)d\xi\right\}, \quad (13)$$

$$w(x, y) = \frac{\partial\Phi}{\partial y} = \sum_{n=1}^{\infty}[-a_n\varphi_n(x)]\sin(a_n y). \quad (14)$$

The coefficients A_n and B_n are defined by the boundary conditions for the longitudinal velocity $u(x, y)$. Since these conditions for gastight and flowing gas cells are different, the two cases should be considered separately.

GASTIGHT CELLS

In gastight cells, the boundary conditions for the longitudinal velocity $u(x, y)$ are the same as for the transverse one: $u(0, y) = u(L, y) = 0$. Substituting these conditions into (12) gives the general solution to the problem:

$$B_n = -A_n = \frac{1}{\sinh(a_n L)}\int_0^L g_n(\xi)\cosh[a_n(L-\xi)]d\xi,$$

$$\varphi_n(x) = \frac{1}{a_n}\left\{\int_0^x g_n(\xi)\sinh[a_n(x-\xi)]d\xi - \frac{\cosh(a_n x)}{\sinh(a_n L)}\int_0^L g_n(\xi)\cosh[a_n(L-\xi)]d\xi\right\}, \quad (15)$$

$$v_n(x) = \int_0^x g_n(\xi)\cosh[a_n(x-\xi)]d\xi - \frac{\sinh(a_n x)}{\sinh(a_n L)}\int_0^L g_n(\xi)\cosh[a_n(L-\xi)]d\xi. \quad (16)$$

If the energy deposit is transversely uniform, that is, $F = F(x)$, then $g_n = 0$, $v_n = \varphi_n = 0$, and the solution is reduced to one-dimensional longitudinal motion (9). If the energy deposit is uniform in the longitudinal direction ($F = F(y)$), the solution is reduced to one-dimensional transverse motions [3, 4]. In this case, according to (5), $G = G(y)$, $\langle G\rangle_y = \langle G\rangle_V = 0$, transversely averaged velocity (9) is equal to zero, and the expansion coefficients g_n do not depend on x. According to (15) and (16),

$$B_n = -A_n = \frac{g_n}{a_n}, \quad \varphi_n = -\frac{g_n}{a_n^2}, \quad v_n = 0,$$

that is, the longitudinal velocity is equal to zero and the transverse velocity, according to (14), is given by

$$w(y) = \sum_{n=1}^{\infty}\frac{g_n}{a_n}\sin(a_n)y,$$

$$\frac{dw}{dy} = \sum_{n=1}^{\infty} g_n\cos(a_n y) = G(y) - \langle G\rangle_y = G(y).$$

In view of (4), this corresponds to (2) for one-dimensional transverse motions. Thus, the obtained distribution of the two-dimensional velocity covers, as particular cases, both longitudinal ($G = G(x)$, $g_n = 0$) and transverse ($G = G(y)$, $\langle G\rangle_y = 0$, and g_n does not depend on x) one-dimensional flows.

The general solution, given by (12)–(16), has a rather complicated form; however, in practically important cases, it can be simplified considerably. Usually, the energy deposit is smoothly nonuniform along the cell: $G(x, y,)$ and, accordingly, $g_n(x)$ vary considerably with x over distances $\sim L \gg h$, whereas the exponential functions under the integral sign in the general solution vary steeply over distances $\sim h$ even at $n \approx 1$. Therefore, with a good accuracy, the function $g_n(x)$ can be set equal to its value at the maximums of the decay exponentials. Then, for the longitudinal velocity it follows from (16) that

$$v_n(x) \approx \int_0^x \frac{g_n(\xi)}{2}\exp\{-a_n(x-\xi)\}d\xi - \int_x^L \frac{g_n(\xi)}{2}\exp\{-a_n(\xi-x)\}d\xi + \int_0^L \frac{g_n(\xi)}{2}\exp\{-a_n(\xi+x)\}d\xi - \int_0^L \frac{g_n(\xi)}{2}\exp\{-a_n(2L-\xi-x)\}d\xi$$

$$\approx \frac{g_n(0) - g_n(x)}{2a_n} \exp\{-a_n x\}$$

$$+ \frac{g_x(x) - g_n(L)}{2a_n} \exp\{-a_n(L - x)\},$$

with other exponential terms being small. The rest of the terms are equally small everywhere except narrow regions near the cell ends (the longitudinal size of these regions is on the order of h). Thus, in most of the cell, the longitudinal velocity can be replaced by its transversely averaged value (see (9)). Analogously, for the transverse velocity given by (15), we have

$$\varphi_n(x) \approx -\frac{g_n(x)}{a_n^2} - \Omega(x),$$

$$\Omega(x) = \frac{g_n(0) - g_n(x)}{2a_n^2} \exp\{-a_n x\} \tag{17}$$

$$+ \frac{g_n(L) - g_n(x)}{2a_n^2} \exp\{-a_n(L - x)\},$$

with the addition $\Omega(x)$ being exponentially small everywhere except the same end regions. Outside these regions, according to (14),

$$w(x, y) \approx \sum_{n=1}^{\infty} \frac{g_n(x)}{a_n} \sin(a_n y); \tag{18}$$

that is, the transverse velocity component satisfies the equation

$$\frac{\partial w}{\partial y} \approx \sum_{n=1}^{\infty} g_n(x) \cos(a_n y) = G(x, y) - \langle G(x, y) \rangle_y. \tag{19}$$

Result (17) can also be obtained directly from (10) by passing to the dimensionless longitudinal coordinate $X = x/L$ and recasting (10) in the form

$$\mu \frac{d^2 \varphi_n}{dX^2} - \varphi_n = \frac{g_n(X)}{a_n^2}, \quad \mu = \left(\frac{h}{\pi n L}\right)^2 \ll 1.$$

This is a typical singularly disturbed equation (with a small factor outside the derivative), and its solution away from the cell ends can be immediately written as

$$\varphi_n(X) \approx -\frac{g_n(X)}{a_n^2},$$

because the term with the second derivative is negligibly small everywhere except the end regions, where it must provide fulfillment of the boundary conditions.

Thus, if the energy deposit is smoothly nonuniform along the cell, the longitudinal gas velocity in most of the cell volume (except the narrow regions near the cell ends) depends on the transversely averaged energy deposit, while the transverse component depends on the difference between the local energy deposit and transversely averaged energy deposit.

The two-dimensionality of the problem can be demonstrated with a model cell with a step energy deposit:

$$F_0(x, y) = \begin{cases} f(y), & 0 < x < l \\ 0, & l < x < L, \end{cases}$$

$$\langle F_0(x, y) \rangle_V = f_0 \frac{l}{L}, \quad f_0 = \langle f(y) \rangle_y, \tag{20}$$

with the section $x = l$ of energy deposit discontinuity being located not too close to the cell ends. Physically, such a problem corresponds to a laser cell with a large buffer volume where the gas can flow (Fig. 2). Here, we disregard the narrow area near the edge of the uranium layer, where the energy deposit smoothly decays to zero (the longitudinal size of this area does not exceed the doubled range of fission fragments in the gas: $2R_0 \ll L$). If the energy deposit parameter Θ is normalized to the volume of the active (irradiated) part of the cell $0 < x < l$, then $f_0 = 1$ [4, 5].

According to (5), (9), and (20), we have

$$\langle G(x, y) \rangle_y = \begin{cases} \frac{\Theta}{\gamma} \psi(t) \left(1 - \frac{l}{L}\right) \\ \frac{\Theta}{\gamma} \psi(t) \left(-\frac{l}{L}\right), \end{cases}$$

$$g_n(x) = \begin{cases} g_n, & 0 < x < l, \\ 0, & l < x < L, \end{cases} \tag{21}$$

$$U(x) = \begin{cases} \frac{\Theta}{\gamma} \psi(t) \left(1 - \frac{l}{L}\right) x, & 0 < x < l \\ \frac{\Theta}{\gamma} \psi(t) l \left(1 - \frac{x}{L}\right), & l < x < L. \end{cases}$$

The longitudinal gas velocity averaged over the transverse direction linearly grows in the active part of the cell beginning from its end, reaches a maximum at the end of the active layer (at $x = l$), and then linearly

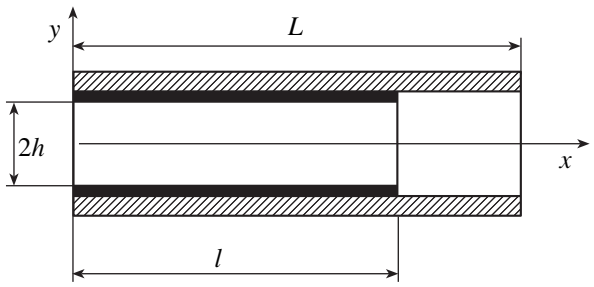

Fig. 2. Gastight laser cell with a buffer volume.

decays to zero at the other end (in the buffer volume). The expressions for the expansion coefficients of the longitudinal velocity in (16) are

$$v_n(x) = \frac{g_n}{a_n}\frac{\sinh(a_n x)}{\sinh(a_n L)}\sinh[a_n(L-l)]$$

$$\approx \frac{g_n}{2a_n}\exp\{-a_n(l-x)\},$$

$$0 < x < l, \qquad (22)$$

$$v_n(x) = \frac{g_n}{a_n}\left\{\frac{\sinh(a_n x)}{\sinh(a_n L)}\sinh[a_n(L-l)] + \sinh[a_n(l-x)]\right\}$$

$$\approx \frac{g_n}{2a_n}\exp\{-a_n(x-l)\}, \quad l < x < L$$

up to exponentially small terms. It is seen that, even if the energy deposit is discontinuous (see (20)), the longitudinal gas velocity is almost equal to its transversely averaged value given by (21) in both the active part and the buffer volume. Only in the region of discontinuity, the longitudinal velocity is essentially two-dimensional; the dimensions of this region are roughly equal to the cell width h. For the transverse velocity component, according to (15), one has

$$\varphi_n(x) = -\frac{g_n}{a_n^2}\left\{1 - \frac{\cosh(a_n x)}{\sinh(a_n L)}\sinh[a_n(L-l)]\right\}$$

$$\approx -\frac{g_n}{a_n^2}\left\{1 - \frac{1}{2}\exp[-a_n(l-x)]\right\}, \quad 0 < x < l,$$

$$\varphi_n(x) = -\frac{g_n}{a_n^2}\left\{\cosh[a_n(x-l)] - \frac{\cosh(a_n x)}{\sinh(a_n L)}\sinh[a_n(L-l)]\right\} \qquad (23)$$

$$\approx -\frac{g_n}{2a_n^2}\exp\{-a_n(x-l)\}, \quad l < x < L$$

up to exponentially small terms. As before, the two-dimensional effects are concentrated in the same narrow region near the discontinuity. Beyond this region, the transverse motion is absent, while in the active part of the cell, it is quasi-one-dimensional: according to (14) and (23), the transverse velocity in the active cell part has the same form (18) as for a smoothly nonuniform energy deposit given by Eq. (19). At the place of the discontinuity ($x = l$), the transverse velocity, according to (14) and (23), is half that in the active part (see (18)).

Note, however, that the velocity distribution obtained for the two-dimensional domain has a purely model character, because the step approximation of the energy deposit is especially crude just within this domain.

The cases of smoothly nonuniform and discontinuous energy deposits considered above allow us to reach a general conclusion for two-dimensional gas flows in gastight cells at low energy deposits. In those regions of the cell where the longitudinal profile of the energy deposit is smoothly nonuniform (varies considerably over a length far exceeding the cell width), the two-dimensional flow can be represented as the superposition of two quasi-one-dimensional motions: the longitudinal velocity is practically uniform across the cell and depends on the energy deposit averaged over the transverse direction according to (9), whereas the transverse component depends on the difference between the local energy deposit and the transversely averaged deposit according to (19). In this case, initial equation (2) splits into two equations [8]:

$$\gamma P\frac{\partial u}{\partial x} = (\gamma - 1)\left\langle\frac{\delta Q}{\delta V \delta t}\right\rangle_y - \frac{dP}{dt}, \qquad (24)$$

$$\gamma P\frac{\partial w}{\partial y} = (\gamma - 1)\left\{\left(\frac{\delta Q}{\delta V \delta t}\right) - \left\langle\frac{\delta Q}{\delta V \delta t}\right\rangle_y\right\}. \qquad (25)$$

Near the cell ends and in the transition regions between the smoothly nonuniform regions (in the former, the energy deposit is substantially nonuniform, considerably varying over a length on the order of the cell width), the velocity distribution switches from one quasi-one-dimensional form to another. The dimensions of the transition regions, where the gas motion is essentially two-dimensional, are approximately equal to the cell width.

The above consideration was carried out for cells with plane uranium layers. It seems, however, that the basic result given by (24) and (25) is also valid for cylindrical cells.

FLOWING GAS CELLS

General laws of velocity field formation in flowing gas cells (Fig. 1) are the same as in gastight ones. However, because of the absence of the end faces, boundary conditions here are more sophisticated. If we merely required the gas velocity to be transversely uniform and equal to U_0 at the cell inlet, (11) and (13) would yield "zero" boundary conditions

$$\varphi_n(0) = v_n(0) = 0, \quad A_n = B_n = 0, \qquad (26)$$

which cause the solution to diverge away from the inlet. The fact is that, in the case of a subsonic flow, any disturbances of flow conditions inside a channel (and the energy deposit greatly affects the flow conditions) are "discerned" upstream from the channel and, accordingly, the velocity distribution is modified upstream from the cell inlet. Therefore, one should establish the zero conditions not at the inlet (at $x = 0$) but away from it (formally at $x \longrightarrow -\infty$) and solve the conjugate prob-

lem. Since $g_n = 0$ at $x < 0$, from (11), (13), and zero boundary conditions (26) it follows at $x \longrightarrow -\infty$ that

$$\varphi_n(x) = \frac{C_n}{2a_n}\exp(a_n x), \quad v_n(x) = \frac{C_n}{2}\exp(a_n x), \quad x < 0. \tag{27}$$

From (27), (11), and (13) at $x = 0$, we find the coefficients B_n and C_n:

$$C_n = A_n \quad \text{and} \quad B_n = 0.$$

Downstream from the cell, the gas velocity must be finite at any distance $x \gg L$. From this condition in view of (11) and (13), we find A_n:

$$A_n = -\int_0^L g_n(\xi)\exp(-a_n\xi)d\xi. \tag{28}$$

This coefficient is seen to be virtually the same as for gastight cells.

Thus, the coefficients of expansions (11) and (13) for flowing gas cells have the form

$$\begin{aligned}\varphi_n(x) &= -\frac{1}{2a_n}\left\{\int_0^x g_n(\xi)\exp[a_n(\xi - x)]d\xi \right.\\ &\left. + \int_x^L g_n(\xi)\exp[a_n(x-\xi)]d\xi\right\},\\ v_n(x) &= \frac{1}{2}\left\{\int_0^x g_n(\xi)\exp[a_n(\xi - x)]d\xi \right.\\ &\left. - \int_x^L g_n(\xi)\exp[a_n(x-\xi)]d\xi\right\}.\end{aligned} \tag{29}$$

When deriving (27)–(29), we assumed that the energy deposit has an effect only within the cell, $0 < x < L$. In the general case, distinct bounds of energy deposit action may be absent. To avoid the need for considering two conjugate domains, one can impose limits on the gas velocity throughout the longitudinal axis and find from (11) and (13)

$$\begin{aligned}\varphi_n(x) &= -\frac{1}{2a_n}\left\{\int_{-\infty}^x g_n(\xi)\exp[a_n(\xi - x)]d\xi \right.\\ &\left. + \int_x^\infty g_n(\xi)\exp[a_n(x-\xi)]d\xi\right\},\\ v_n(x) &= \frac{1}{2}\left\{\int_{-\infty}^x g_n(\xi)\exp[a_n(\xi - x)]d\xi \right.\\ &\left. - \int_x^\infty g_n(\xi)\exp[a_n(x-\xi)]d\xi\right\},\end{aligned} \tag{30}$$

which virtually coincides with (29). Similarly to (28), we have in this case

$$A_n = -\int_{-\infty}^\infty g_n(\xi)\exp(-a_n\xi)d\xi, \quad B_n = 0.$$

For a smoothly nonuniform energy deposit ($g_n(x)$ are smooth functions), it follows from (29) that

$$\begin{aligned}\varphi_n(x) &\approx -\frac{g_n(x)}{a_n^2} + \frac{g_n(x)}{2a_n^2}\{\exp[-a_n x] + \exp[-a_n(L-x)]\},\\ v_n(x) &\approx -\frac{g_n(x)}{2a_n}\{\exp[-a_n x] - \exp[-a_n(L-x)]\}.\end{aligned} \tag{31}$$

In flowing gas cells, the same pattern as in gastight ones is observed: at a distance on the order of the cell width from the inlet (that is, from the energy deposit discontinuity), the difference between the actual longitudinal velocity and its averaged value becomes negligible; the transverse velocity takes form (18), satisfying Eq. (19); and the problem is reduced to the set of Eqs. (24) and (25) (split equation (2)).

Near the inlet in the initial part of the energy deposit area (at $x \longrightarrow 0$ but $x > 0$), we find from (29) subject to (9), (12), and (14) that

$$\begin{aligned}\frac{\partial u}{\partial x} - \frac{dU}{dx} &\approx \frac{\partial w}{\partial y} \approx \sum_{n=1}^\infty \frac{g_n(0)}{2}\cos(a_n y)\\ &= \frac{1}{2}\{G(0,y) - \langle G(0,y)\rangle_y\}, \quad 0 < x \longrightarrow 0.\end{aligned}$$

It is seen that in regions where the local energy deposit is higher than the deposit averaged over the cross section, the gas expands across the cell and its longitudinal expansion is larger than the expansion averaged over the cross section. In those regions where the local energy deposit is lower than the section-averaged value, the gas is compressed across the cell and its longitudinal expansion is less than that averaged over the cross section. For $x \longrightarrow 0$ on the other side of the cell inlet (where the energy deposit is yet absent), from (27) and (28) subject to (12) and (14) it follows that

$$\begin{aligned}u(x,y) &\approx -\sum_{n=1}^\infty \frac{g_n(0)}{2a_n}\exp(a_n x)\cos(a_n y),\\ \frac{\partial u}{\partial x} &\approx -\frac{1}{2}\{G(0,y) - \langle G(0,y)\rangle_y\},\\ w(x,y) &\approx \sum_{n=1}^\infty \frac{g_n(0)}{2a_n}\exp(a_n x)\sin(a_n y),\\ \frac{\partial w}{\partial y} &\approx \frac{1}{2}\{G(0,y) - \langle G(0,y)\rangle_y\}, \quad 0 > x \longrightarrow 0.\end{aligned}$$

Certainly, $\partial u/\partial x + \partial w/\partial y = 0$ at $x < 0$.

Thus, the gas to be entered into the region with a high energy deposit starts expanding across the cell and

for this reason it is compressed (decelerated) in the longitudinal direction. The gas to be entered into the region with a low energy deposit conversely starts being compressed across the cell beforehand and, therefore, expands (accelerates) in the longitudinal direction.

The two-dimensional gas velocity distribution in flowing gas cells (see (12), (14), and (29)) has been obtained in the form of infinite series. Using the well-known formulas [11]

$$2\sum_{n=1}^{\infty} e^{-nt}\sin(nz) = \frac{\sin z}{\cosh t - \cos z},$$

$$2\sum_{n=1}^{\infty} e^{-nt}\cos(nz) = \frac{\sinh t}{\cosh t - \cos z} - 1$$

and taking into consideration (8) and (9), one can represent this distribution in the form of double quadratures:

$$u(x, y) = \frac{1}{4h}\int_0^L\int_0^h \Xi(x, y, \xi, \eta)G(\xi, \eta)d\eta d\xi + U_0,$$

$$w(x, y) = \frac{1}{4h}\int_0^L\int_0^h \Psi(x, y, \xi, \eta)G(\xi, \eta)d\eta d\xi,$$

$$\Xi(x, y, \xi, \eta) = \frac{\sinh Z(x, \xi)}{\cosh Z(x, \xi) - \cos S(y, \eta)} + \frac{\sinh Z(x, \xi)}{\cosh Z(x, \xi) - \cos R(y, \eta)} + 2,$$

$$\Psi(x, y, \xi, \eta) = \frac{\sin S(y, \eta)}{\cosh Z(x, \xi) - \cos S(y, \eta)} + \frac{\sin R(y, \eta)}{\cosh Z(x, \xi) - \cos R(y, \eta)}, \quad (32)$$

$$Z(x, \xi) = \pi\frac{x - \xi}{h}, \quad S(y, \eta) = \pi\frac{y + \eta}{h},$$

$$R(y, \eta) = \pi\frac{y - \eta}{h}.$$

Such a representation of the gas velocity distribution is more convenient for numerical calculations, although makes qualitative analysis somewhat difficult. Similar formulas can also be derived for gastight cells.

CONCLUSIONS

A two-dimensional gas velocity distribution in low-velocity subsonic gas flows through gastight and flowing gas laser cells with an internal low-power heat source has been constructed. It has been shown that, at a smoothly nonuniform energy deposit, the two-dimensional gas flow splits into two quasi-one-dimensional flows because of different longitudinal and transverse scales of the process: the longitudinal gas velocity is practically uniform across the cell and depends on the transversely averaged energy deposit, while the transverse velocity depends on the difference between the local energy deposit and transversely averaged one.

The split of the two-dimensional motion into two quasi-one-dimensional flows allows one to approximately calculate the gas density distribution in laser cells without applying complicated two-dimensional gasdynamic computer programs (such as those used in [7]). This greatly simplifies the analysis of optical nonuniformities in nuclear-pumped lasers.

The set of Eqs. (24) and (25) (split equation (2)) of gas motion remains valid for near-axial regions of the cell even with allowance for the viscous thermal boundary layer if the gas pressure is calculated subject to heat removal onto the wall [4, 5].

In the framework of the model stated by (24) and (25), the transverse gas motion at very large energy deposits ($\Theta \longrightarrow \infty$) would lead to the formation of a transverse density profile that is the reciprocal of the transverse energy deposit profile, $\rho(y) \propto 1/F(y)$, in the limit $x \longrightarrow \infty$ for flowing gas cells and in the limit $t \longrightarrow \infty$ for gastight ones, similarly to the case of one-dimensional transverse motion [3, 4]. However, at large energy deposits, the split model, generally speaking, is incorrect [8].

REFERENCES

1. R. T. Schneider and F. Hohl, *Advances in Nuclear Science and Technology* (Plenum, New York, 1984), Vol. 16, pp. 123–287.
2. A. N. Sizov and Yu. N. Deryugin, Zh. Tekh. Fiz. **62** (9), 107 (1992) [Sov. Phys. Tech. Phys. **37**, 734 (1992)].
3. J. R. Torczynski, J. Fluid Mech. **201**, 167 (1989).
4. V. Yu. Mat'ev, in *Proceedings of the 2nd Conference on Nuclear-Excited Plasma and Problems of Nuclear-Pumped Lasers, Arzamas 16* (VNIIÉF, 1995), Vol. 1, pp. 410–420.
5. V. Yu. Mat'ev, V. V. Borovkov, and S. P. Mel'nikov, Zh. Tekh. Fiz. **71**, 79 (2001) [Tech. Phys. **46**, 76 (2001)].
6. V. V. Borovkov, B. V. Lazhentsev, V. A. Nor-Arevyan, *et al.*, Kvantovaya Élektron. (Moscow) **22**, 1187 (1995).
7. L. M. Montierth, W. A. Neuman, D. W. Nigg, *et al.*, J. Appl. Phys. **69**, 6776 (1991).
8. V. Yu. Mat'ev, in *Proceedings of the 2nd Conference on Nuclear-Excited Plasma and Problems of Nuclear-Pumped Lasers, Arzamas 16* (VNIIÉF, 1995), Vol. 1, pp. 430–442.
9. V. Yu. Mat'ev, Zh. Tekh. Fiz. **71**, 72 (2001) [Tech. Phys. **46**, 68 (2001)].
10. N. E. Kochin, I. A. Kibel', and N. V. Roze, *Theoretical Hydromechanics* (GITTL, Moscow, 1955), Chap. 1.
11. I. S. Gradshteĭn and I. M. Ryzhik, *Table of Integrals, Sums, Series, and Products* (Nauka, Moscow, 1971).

Translated by N. Mende

Technical Physics, Vol. 48, No. 3, 2003, pp. 311–316. Translated from Zhurnal Tekhnicheskoĭ Fiziki, Vol. 73, No. 3, 2003, pp. 36–41.

GAS DISCHARGES, PLASMA

Nonmonotonic Potential Distribution in a Grid Mesh of a Plasma Switch

A. N. Andronov, S. A. Voronin, A. M. Martsinovsky, I. I. Stolyarov, and V. K. Shigalev

St. Petersburg State Technical University, Politekhnicheskaya ul. 29, St. Petersburg, 195251 Russia

Ioffe Physicotechnical Institute, Russian Academy of Sciences, Politekhnicheskaya ul. 26, St. Petersburg, 194021 Russia

Received September 24, 2001; in final form, January 29, 2002

Abstract—The electrical transparency of the grid and the passing current are determined from probe measurements of the discharge plasma parameters when a plasma switch with a developed cathode is in the steady conductive state. To eliminate discrepancies between the analysis and experiment, it is assumed that the potential (virtual cathode) distribution in a grid mesh is nonmonotonic in the direction of current transfer. *© 2003 MAIK "Nauka/Interperiodica".*

INTRODUCTION

Current passage through a grid placed in a plasma and, accordingly, the dependence of the "electrical transparency" of a grid mesh on the grid potential and plasma properties are key issues in the problem of grid control of the current in plasma switches. Obviously, both characteristics are specified by the potential distribution in a mesh of the grid near its turns. It is also apparent, however, that usually neither the potential distribution can be directly measured nor ion kinetics can be adequately studied in the 3D case. Therefore, indirect data gained from the study of the general laws of grid control in plasma switches are used. Probe measurements of the plasma parameters in the cathode and anode regions of the discharge are the most informative. Based on certain assumptions, they allow one to determine the electrical transparency of the grid, establish the current balance in the grid plane, and judge the potential distribution near grid turns by comparing analytical results with direct current measurements.

MODEL OF ELECTRICAL TRANSPARENCY

Early progress toward an understanding of the current transfer mechanism is associated with the model of electrical transparency [1–3]. According to this model, a negative voltage applied to the grid increases the radius r_L of Langmuir layers near its turns, thereby decreasing its transparency

$$\delta = (1 - 2r_L/h)^2, \quad (1)$$

where h is the grid pitch. In this case, the current diminishes and may eventually vanish. In a low-voltage Knudsen cesium arc, where grid control is very efficient, the potentials φ_1 and φ_2 (Figs. 1b, 1c), the plasma concentrations n_1 and n_2, and the electron temperatures T_1 and T_2 were found [3] to vary insignificantly within the cathode–grid and grid–anode gaps, respectively. At the same time, there appears a potential step $\varphi_{12} = \varphi_1 - \varphi_2$ in the grid plane (hereafter, by the potential we conventionally mean the potential energy of an electron divided by the elementary charge). Under these conditions, the current density in the conducting path of a grid mesh is given by

$$j = qn_1\sqrt{\frac{kT_1}{2\pi m}}\exp\left\{\frac{q\varphi_{12}}{kT_1}\right\} - qn_2\sqrt{\frac{kT_2}{2\pi m}}, \quad \varphi_{12} < 0, \quad (2)$$

$$j = qn_1\sqrt{\frac{kT_1}{2\pi m}} - qn_2\sqrt{\frac{kT_2}{2\pi m}}\exp\left\{\frac{-q\varphi_{12}}{kT_2}\right\}, \quad \varphi_{12} > 0 \quad (2')$$

(where m is the mass of an electron, q is the elementary charge, and k is the Boltzmann constant), and the discharge (anode) current density is expressed as

$$j_a = \delta j. \quad (3)$$

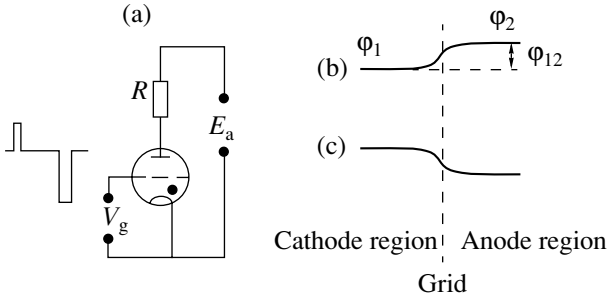

Fig. 1. (a) Connection diagram of a plasma switch and (b, c) longitudinal potential distribution along the central line of the meshes for the conductive state according to the generally accepted concepts.

1063-7842/03/4803-0311$24.00 © 2003 MAIK "Nauka/Interperiodica"

When steep (with a rise time of <100 ns) control pulses are applied to the grid, the plasma concentration has no time to change and the grid transparency decreases. Concurrently, the step φ_{12} changes. Experiments show [4–6] that if the amplitude of the grid pulse is small, the discharge current remains constant and the decrease in the transparency is compensated for by increasing the current density in the channel owing to the change in φ_{12}. Specifically, in the initially conductive state with $\varphi_{12} < 0$ (the potential step slows down the electron flow from the cathode toward the anode) and $n_1 \gg n_2$, the current density in the channel will grow up to the value $j \cong qn_1(kT_1/2\pi m)^{1/2}$, at which φ_{12} becomes larger than zero. This means that when a negative pulse is applied to the grid, the current starts decreasing after the current density in the transparent area of the mesh reaches the density of the stochastic current of plasma electrons near the cathode.

The model of electrical transparency made it possible to theoretically explain processes occurring in cesium switches in the conductive state and upon discharge quenching [3, 7]. However, the subsequent detailed experimental studies of the switches showed that this model does not necessarily fit probe measurements with which one can calculate the transparency, establish the current balance in the grid channel, and compare the analytical and experimental values of the passing current. The discrepancies are commonly explained by the low accuracy of probe measurements and the partial transfer of the discharge current by the cathodic electron beam.

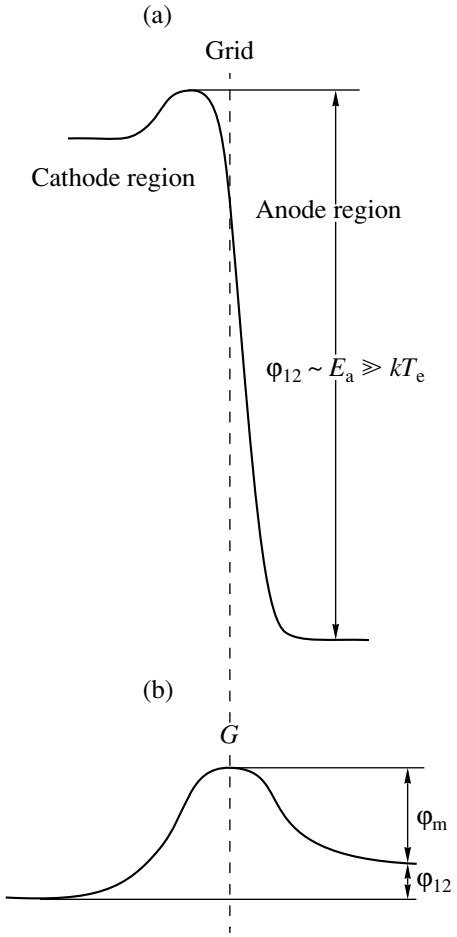

Fig. 2. (a) Potential distribution for the partially blocked state and (b) actual potential distribution in the conductive state.

DEPENDENCE OF INITIAL CURRENT BLOCKING ON E_a

If a grid pulse has a large amplitude and can partially block the current, the conditions for current passage change drastically as compared with those in the conductive state [8]. In conventional modulation circuits (Fig. 2a), the supply voltage E_a in the conductive state exceeds the anode voltage V_a many times. If a control grid pulse is sufficiently high and partially decreases the current from its initial value I_a to the residual value I_{res} (Fig. 2b), the voltage at the switch anode rises substantially by a value $\Delta V_a = -(R(I_{res} - I_a) + LdI_a/dt)$, where R is the anode load (resistance) and L is the stray inductance of the anode circuit. It was shown [4] that this voltage increment almost completely drops across the grid barrier; that is, $\varphi_{12} \approx \Delta V_a \gg kT_2$. In other words, the electric double (space-charge) layer (Fig. 2c) must form in the electrically transparent area of the mesh. Irrespective of the value of φ_{12},

$$j_e = j_i\sqrt{\frac{M}{m}}, \tag{4}$$

where M is the mass of an ion, j_e is the electron current density in the electrically transparent area of a mesh, and

$$j_i = 0.61qn_2\sqrt{\frac{kT_2}{M}}$$

is the saturation ion current density.

If the density of the stochastic current of plasma electrons near the cathode exceeds the value given by (4), a virtual cathode, which partially blocks this current, appears before the electric double layer. Under these conditions, the passing (anode) current density depends on the plasma parameters in the anode region of the discharge:

$$j_a = 0.61qn_2\sqrt{\frac{kT_2}{m}}\delta. \tag{5}$$

On the other hand, if the anode is short-circuited to the anode voltage supply, the current can be blocked by a grid pulse with the anode potential remaining unchanged. In this case, the electric double layer in a mesh does not form and the residual passing current at $n_1 \gg n_2$ is defined by expressions (2) and (3) irrespective of the initial blocking $\Delta I_a = I_a - I_{res}$. Since current blocking already takes place, $\varphi_{12} > 0$ and the current

density in the conducting channel equals that of the stochastic current of the near-cathode plasma; therefore, the anode current density is $j_a \cong qn_1(kT_1/2\pi m)^{1/2}\delta$. Comparing this formula with (5) implies that, in the cases considered, the values of the residual current I_{res} must differ substantially for the same value of the transparency and, hence, V_g under typical conditions with $n_1 \gg n_2$. The relative initial blocking is expected to be much larger in the presence of the load R_a than in its absence ($R_a = 0$), since the residual current ratio is $j_{res}(R_a \neq 0)/j_{res}(R_a = 0) \approx n_2/n_1$.

In real experiments, the condition $V_a = E_a$ is impossible to provide when current blocking is fast (≈0.1 μs) because of the inductance of wires connecting the anode to the voltage supply. This causes an appreciable spike of the anode voltage. However, since in the presence of R_a it is necessary that E_a far exceed V_a ($E_a - V_a \gg kT^2$) for the virtual cathode to appear and condition (5) to be valid, one can anticipate that, in the presence of the inductive spike when E_a grows, the relative blocking must also increase noticeably, especially at low E_a. This supposition is in conflict with the practical use of cesium plasma switches, according to which the discharge is the easier to quench, the higher the initial current blocking, and the harder to quench, the greater E_a (all other things being equal). Therefore, the E_a dependence of the initial current blocking needed careful experimental verification.

During the measurements, we suppressed the inductive spike as much as possible (to 5–10 V) by minimizing the connected wire length and using a low-induction anode load.[1] As in early studies [9], the dependence $\Delta I/I_0(E_a)$ was weak and the reproducibility of the results, poor. The reason for the latter fact turned out to be the inaccurate recovery of the initial conductive state of the switch after E_a and anode load had been changed. Only when the anode voltage V_a and the anode current I_0 were stabilized within 0.1–0.2% (the current was stabilized by regulating the cathode temperature) did the reproducibility of $\Delta I/I_0$ at different E_a become good. It turned out [10] that the initial blocking $\Delta I/I_0$ is almost independent of E_a or decreases (rather than increases) insignificantly with increasing E_a (Fig. 3).

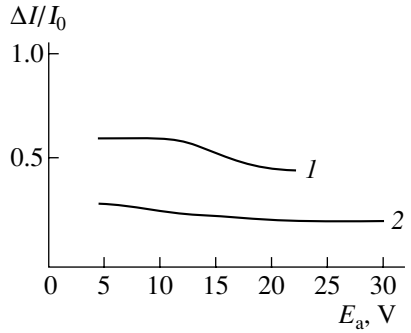

Fig. 3. Initial current blocking vs. anode supply voltage for $P_{Cs} = 10^{-2}$ torr and $T_e = 1130$ K. (*1*) $j_a = 1.5$ A/cm^2, $V_a = 2.3$ V, $V_g = -20$ V and (*2*) $j_a = 3.8$ A/cm^2, $V_a = 3.0$ V, $V_g = -30$ V.

NONMONOTONIC POTENTIAL DISTRIBUTION IN THE CURRENT CHANNEL AND CURRENT BALANCE IN THE GRID PLANE

It is logical to assume that the potential hump also exists in the steady conductive state with V_g close to zero. Such an assumption eliminates the discrepancy in calculating the current balance in the conducting channel that usually arises when the plasma parameters measured with a probe near the cathode and anode regions of the discharge are substituted into Eqs. (2). Earlier, this discrepancy was explained by experimental errors (see Introduction) and no significance was attached to it. Therefore, it was of interest to perform special experiments from which necessary discharge parameters would be extracted in the most reliable way. In these experiments, we used a device with a developed cathode [11], where the electron beam from the cathode is negligibly small and cannot influence the current balance. Accordingly, probe measurements in the absence of the beam can be interpreted more reliably.

Current values obtained with the model of electrical transparency are convenient to compare with experimental findings as follows. For the values of n_1, n_2, T_1, T_2, and the plasma potentials φ_1 and φ_2 measured with a probe and for the discharge current density j_a obtained from (2) and (3), one determines δ and then r_L from (1). The dimensionless (in terms of kT/q) potential drop η_L across the Langmuir layer for the Debye radius $r_D = (kT/4\pi q^2 n)^{1/2}$ was found [6] by integrating the equation

$$\frac{d^2\eta}{d\xi^2} + \frac{1}{\xi}\frac{d\eta}{d\xi} = \left(\frac{r_L}{r_D}\right)^2 \frac{1}{\sqrt{e}}\left(\frac{1}{\xi\sqrt{1+2\eta}} - \exp\{-\eta\}\right) \quad (6)$$

from $\xi = 1$ to a/r_L (where a is the radius of the grid wire) with the boundary conditions

$$\eta(1) = \left.\frac{d\eta}{d\xi}\right|_{\xi=1} = 0. \quad (6')$$

The values of η_L thus obtained were compared with those (η_L') found experimentally:

$$\eta_L' = -q(V_g + \varphi_{pl})/kT - 1/2. \quad (7)$$

Note that we used two values of the plasma potential φ_{pl}, as well as T and n, which also enter into the Debye radius in Eq. (6). These values were measured in the cathode and anode regions, respectively (see table). Both result in a considerable disagreement with η_L obtained from (6). Sometimes (especially for high plasma concentrations and $n_1 \gg n_2$), the disagreement is particularly large. It can be eliminated if we suppose

[1] A *U*-shaped Nichrome resistor with a wire spacing of ≈1 mm.

Table

T_e, K	J_a, A/cm^2	Calculation using (10)		Calculation using (10')	
		η	η'	η	η'
1100	0.635	118	5.3	17	4.9
	1.27	231	6.1	96	7.8
	1.9	275	6.7	155	9.0
	2.54	253	8.0	205	10.5
	3.17	205	9.4	215	12.7
1120	1.27	100	5.3	25	5.1
	2.54	134	5.9	51	6.6
	3.81	203	6.3	108	6.6
	5.08	278	6.6	213	8.3
	6.35	219	7.4	233	9.2

that the plasma concentration is measured inaccurately. However, the errors in this case seem to be unwarrantedly too large (several hundreds of percent).[2] At the same time, the anode current calculated from the experimental values of n_2, T_2, φ_2, and U_a deviates from the measured value insignificantly (by less than 30%), indicating that probe measurements are sufficiently accurate. Assuming that the discrepancies in the current balance on the grid as a whole are due to the potential hump in a mesh, one can determine the maximum value φ_m of the potential that eliminates them. The largest value among φ_1 and φ_2 (φ_1, $\varphi_2 < 0$) was taken as φ_m. The measurements were carried out over a wide range of plasma parameters. The calculation was performed as follows.

The current density in the grid channel is

$$j = qn_1\sqrt{\frac{kT_1}{2\pi m}}\exp\left\{\frac{-q(\varphi_m-\varphi_{12})}{kT_1}\right\} - qn_2\sqrt{\frac{kT_2}{2\pi m}}\exp\left\{\frac{-q\varphi_m}{kT_2}\right\},\quad \varphi_{12}<0, \tag{8}$$

$$j = qn_1\sqrt{\frac{kT_1}{2\pi m}}\exp\left\{\frac{-q\varphi_m}{kT_1}\right\} - qn_2\sqrt{\frac{kT_2}{2\pi m}}\exp\left\{\frac{-q(\varphi_m+\varphi_{12})}{kT_2}\right\},\quad \varphi_{12}>0. \tag{8'}$$

The transparency and the Langmuir radius were found from (3) and (1). The dimensionless potential η_L across the Langmuir layer was determined by integrating (6) subject to boundary conditions (6') with r_D calculated for the concentration n determined in the "neck" of the current channel:

$$n = \frac{1}{2}\left[n_1\exp\left\{\frac{-q(\varphi_m-\varphi_{12})}{kT_1}\right\} + n_2\exp\left\{\frac{-q\varphi_m}{kT_2}\right\}\right],\quad \varphi_{12}<0, \tag{9}$$

$$n = \frac{1}{2}\left[n_1\exp\left\{\frac{-q\varphi_m}{kT_1}\right\} + n_2\exp\left\{\frac{-q(\varphi_m+\varphi_{12})}{kT_2}\right\}\right],\quad \varphi_{12}>0. \tag{9'}$$

The value of V_g was found twofold:

$$V_g = -kT_1/q(1/2+\eta_L) - \varphi_1, \tag{10}$$

$$V_g = -kT_2/q(1/2+\eta_L) - \varphi_2, \tag{10'}$$

and the result of choice was that providing the least value of φ_m when the set of Eqs. (1), (3), (6), and (8)–(10) was solved for the unknowns j, r_L, δ, n, η_L, and φ_m. In either of the two schemes, we used the corresponding value of T when calculating the Debye radius entering into (6), although this circumstance is clearly of minor importance. Typical results of calculation are depicted in Figs. 4 and 5. In all the cases, φ_m is other than zero. Data measured under many other conditions gave similar results. It should be mentioned that taking into account the presence of the virtual cathode also reconciles the current balance in our earlier measurements on various devices, yielding quite reasonable values of φ_m (on the order of kT/q).

DISCUSSION

The presence of the potential hump in the steady conductive state in no way follows from the previous concepts, which imply the fulfillment of the balance equations and the validity of the model of electrical transparency [7]. To find reasons for the existence of the hump, it is first necessary to answer the question as to whether the potential hump (its height, as is seen, may markedly exceed kT/q) is a virtual cathode in the conventional meaning of this term (when the potential drop is localized within a short distance on the order of the Langmuir length where the space charge forms) or whether it is an extended feature in a quasi-neutral plasma. In the former case, the hump influences the current balance only in the grid plane without affecting the ion motion; in the latter, the potential hump must have a decisive effect on the ion motion, since electric fields in this case are strong for ions ($kT_e \gg kT_i$).

Although the overall potential drop $\varphi_{12} + \varphi_m$ may be very high (see above), we guess that potential steps in the current channel between the cathode and anode regions of the discharge are absent and a quasi-neutral plasma exists throughout the channel.

[2] If $n_1 \approx n_2$ and both terms on the right of Eq. (6) are of the same order of magnitude, the assumption of moderate errors (less than a factor of 2) involved in the plasma concentrations leads to agreement for the current balance in the grid plane.

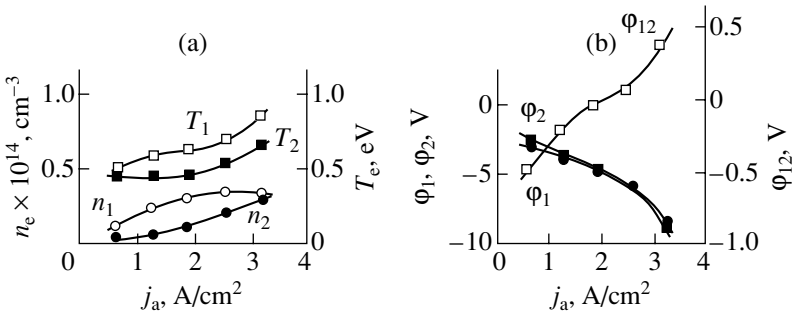

Fig. 4. Plasma parameters and potential drop φ_{12} vs. anode current density for $P_{Cs} = 10^{-2}$ Torr and $T_e = 1100$ K.

In fact, strictly speaking, the presence of an extended potential "hill" with a height of at least $kT/2q$ with a maximum near the grid is obligatory. Under typical operating conditions of the switch, the ion free path in terms of scattering by atoms (as well as the ionization length) far exceeds the entire interelectrode gap [12]; hence, the gap is essentially a set of near-electrode layers. If the grid in a Knudsen arc is absent, a potential minimum for electrons appears at the center of the gap and a potential drop of about $kT/2q$ between this minimum and the space charge boundary at the cathode and anode arises in the plasma volume. This drop is associated with ion transfer toward the electrodes. In the presence of the grid in the gap, the total surface area of its turns is close to the surface area of the cathode and anode (even for thin woven meshes of high, 0.6–0.8, transparency) and the ion currents to the plane electrodes and grid approach each other. Therefore, a potential minimum of the same nature must appear at the centers of the cathode–grid and grid–anode spaces, as well as a potential drop of about $kT/2q$ near either of the electrodes. The potential minima on both sides of the grid specify a maximum in the grid plane. Moreover, at a distance on the order of the mesh size from the grid, the ion motion becomes nonplanar: the trajectories of ions forming space-charge layers near those surfaces of the turns facing the mesh center move apart when approaching the quasi-neutrality boundary. Such a separation of the ion trajectories, which decreases the concentration because of the geometry of the collecting electrode, must cause an additional rise in the potential along the discharge axis at the mesh center and, thereby, an extended potential hill of much greater height.

This point of view is substantiated by the kinetic consideration of the high-field region in a quasi-neutral plasma for the cases when the plasma boundary admits an exact solution. Specifically, Langmuir and Tonks [13] analyzed the ion kinetics in a confined plasma in the presence of direct ionization and ballistic ion transfer toward the plasma boundary for the 1D case. The equation for potential distribution had the form

$$e^{-\eta} - \frac{1}{s^k}\int_0^s \frac{e^{-\eta'} s'^k}{\sqrt{\eta - \eta'}} ds' = 0; \quad k = 0, 1, 2,$$

where s is the dimensionless spatial coordinate and k = 0, 1, or 2 for the planar, cylindrical, and spherical boundaries, respectively. They obtained solutions for $k = 0$ and 1 in the form of series. The values of s_0 and η_0 corresponding to the quasi-neutrality boundary were found from the condition that the electric field at the plasma boundary is infinitely high: $ds/d\eta = 0$. In this case, $\eta_0 = 0.85$ and 1.15 for $k = 0$ and 1, respectively. Our solution for $k = 2$ is

$$s = 4/\pi(1 - 0.1428571428\eta - 0.0177228786\eta^2 - 0.00438904201\eta^3 - 0.00132569418\eta^4 - 0.00044099572\eta^5 - 0.00015537689\eta^6 - \ldots),$$

with $\eta_0 = 1.42$.

As follows from the above example, the additional reason for the ion concentration decrease near the plasma boundary (along with the acceleration of ions in the electric field because of the nonplanar motion) leads to a much greater potential drop across the quasi-neutrality region for the cylindrical and especially spherical boundaries in comparison with the planar one. The potential drop for the sphere is the greatest for any 1D case, since in this situation the rate of fall of the ion

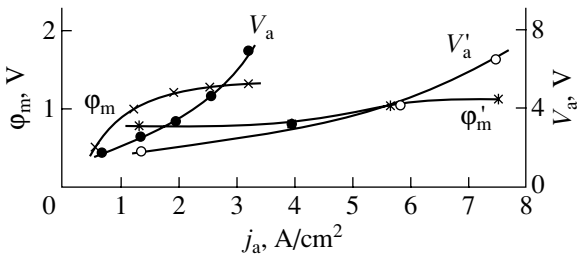

Fig. 5. Anode voltage and calculated maximal potential j_m vs. anode current density for $P_{Cs} = 10^{-2}$ Torr and $T_e = 1100$ and 1120 K.

concentration is the highest when the ion trajectories move apart when approaching the boundary. However, the potential drop for the spherical boundary cannot be considered as ultimate: it may be even higher in the case of a more complex non-one-dimensional geometry such as that in a grid mesh of a plasma switch.

In [14], a switch with a thick (cellular) grid was investigated. The grid was made in the form of "bottom-free" cells. Its thickness was 1 mm, and the cell size was 0.2 mm. For the thin and thick grids of the same transparency, the discharge parameters greatly differ. In the latter case, the plasma concentration in both the cathode and anode regions is high even at a low current density ($\approx$1 A/cm^2), with the concentration near the anode always exceeding that at the cathode. The rate of ion generation in the channel of the thick grid is low, and the quasi-neutral plasma inside its cells is provided by ions penetrating from the cathode and anode regions. It was supposed that a nonmonotonic longitudinal potential distribution with a maximum estimated as several kT/q exists in a cell of the thick grid. Our study of current transfer through thin grids can be considered as a validation of the assumptions used and conclusions drawn in [14]. This is important since the simplified calculations performed in [14] may provoke certain objections.

Thus, one can infer that the presence of a distinct peak in the potential distribution within the current channel is common for the conductive state of plasma switches with grid-controlled current.

It should also be noted that the existence of the potential hump offers a clearer view of why the Maxwell electron distributions with different electron temperatures are observed in the cathode and anode regions at low φ_{12} and high electrical transparencies (when unobstructed electron exchange between the discharge regions takes place).

REFERENCES

1. H. Fetz, Ann. Phys. (Leipzig) **37**, 1 (1940).
2. E. O. Johnson, J. Olmstead, and W. H. Webster, Proc. IRE **42**, 1350 (1954).
3. F. G. Baksht, V. B. Kaplan, A. A. Kostin, *et al.*, Zh. Tekh. Fiz. **48**, 2273 (1978) [Sov. Phys. Tech. Phys. **23**, 1301 (1978)].
4. V. B. Kaplan, A. N. Makarov, A. M. Martsinovsky, *et al.*, Zh. Tekh. Fiz. **47**, 274 (1977) [Sov. Phys. Tech. Phys. **22** (2), 159 (1977)].
5. F. G. Baksht, A. M. Martsinovsky, and V. G. Yur'ev, in *Proceedings of the XIV International Conference on Phenomena in Ionized Gases (ICPIG-XIV), Grenoble, 1979*, J. Phys. Suppl. (Paris), No. 7, 497.
6. V. B. Kaplan, A. M. Martsinovsky, F. N. Rasulov, *et al.*, in *Proceedings of the XIV International Conference on Phenomena in Ionized Gases (ICPIG-XIV), Grenoble, 1979*, J. Phys. Suppl. (Paris), No. 7, 495.
7. F. G. Baksht, B. I. Kolosov, A. A. Kostin, *et al.*, *Mathematical Simulation of Processes in Low-Voltage Plasma-Beam Discharge* (Énergoatomizdat, Moscow, 1990).
8. F. G. Baksht and A. A. Kostin, Fiz. Plazmy **9**, 628 (1983) [Sov. J. Plasma Phys. **9**, 366 (1983)].
9. F. N. Rasulov, Dissertation.
10. A. N. Andronov, A. M. Martsinovsky, V. K. Shigalev, *et al.*, in *Proceedings of Space Technology and Application International Forum (STAIF-99), E18 Termionic Technology and Application-II* (Albuquerque, 1999).
11. A. N. Andronov, A. M. Martsinovsky, F. N. Rasulov, *et al.*, in *Proceedings of Space Technology and Application International Forum (STAIF-99), E18 Thermionic Technology and Application-II* (Albuquerque, 1999).
12. F. G. Baksht, G. A. Dyuzhev, V. B. Kaplan, *et al.*, Zh. Tekh. Fiz. **47**, 263 (1977) [Sov. Phys. Tech. Phys. **22** (2), 153 (1977)].
13. L. Langmuir and L. Tonks, Phys. Rev. **34**, 867 (1929).
14. N. I. Alekseev, V. B. Kaplan, and A. M. Martsinovsky, Zh. Tekh. Fiz. **66**, 56 (1996) [Tech. Phys. **41**, 551 (1996)].

Translated by V. Isaakyan

Technical Physics, Vol. 48, No. 3, 2003, pp. 317–328. Translated from Zhurnal Tekhnicheskoĭ Fiziki, Vol. 73, No. 3, 2003, pp. 42–53.

SOLIDS

Dielectric Dispersion of Three- and Four-Component Matrix Media

Yu. P. Emets

Institute of Electrodynamics, National Academy of Sciences of Ukraine, Kiev, 03680 Ukraine

e-mail: emets@irpen.kiev.ua

Received August 27, 2002

Abstract—The dielectric dispersion of heterogeneous matrices containing dissimilar cylindrical inclusions is studied. Conditions for the dispersion in multicomponent media are found and explained from the physical standpoint. It is shown that the effective loss factor may have several maxima with their number depending on the number of dissimilar inclusions in the composite. Effective permittivity diagrams in the complex plane are constructed. For media with a low inclusion concentration, an approximate method for finding the frequency of the maxima is suggested. © *2003 MAIK "Nauka/Interperiodica".*

INTRODUCTION

In studying the transport properties of inhomogeneous materials, dielectric dispersion analysis is of crucial importance. For piecewise homogeneous matrix systems, Maxwell–Wagner polarization is the basic polarization mechanism [1, 2]. This polarization is macroscopic, or surface, polarization (it is also called interlayer, space-charge, interfacial, etc.). It is related to the formation of charged surface layers at the interface between dissimilar media when free charges move within separate phases of a composite subjected to an external variable electric field.

Although dielectric dispersion in heterogeneous media is finding wide application in many areas of physics, biology, and chemistry [3, 4], its theoretical study faces a number of difficulties. First, the analytical calculation of the effective parameters of multicomponent systems, which is of independent interest and makes an integral part of the theory of dispersion in inhomogeneous insulators, is a complex mathematical problem that is solvable only in specific cases. Second, in the case of multicomponent materials, the number of parameters and dimensionless quantities that characterize the behavior of an inhomogeneous system in a variable electric field greatly increases: to the parameters describing the geometrical structure of a composite, as well as its conductive and insulating properties, frequency parameters and characteristic times for each phase of the system are added. This complicates the electrical spectroscopy of inhomogeneous materials.

The most significant results have been obtained for two-dimensional two-component media with a doubly periodic distribution of inclusions. Using highly efficient techniques from the theory of functions of complex variable, researchers have succeeded in calculating the mean electrophysical characteristics of composites whose composition varies over a wide range up to the critical one at which the metal–insulator transition takes place [5–10]. Also, general symmetry transformations and reciprocity relations have been established that allow one to check the validity and accuracy of the effective parameters irrespective of the inhomogeneous system structure [11–14].

The mechanism of Maxwell–Wagner polarization is of orientation type, because inclusions within which charge carriers move behave as macroscopic objects with image dipoles. In fact, in calculations of an electric field outside spherical bodies and cylindrical inclusions of circular cross section, the field is usually represented as the infinite sum of image dipoles [15, 16]. Relaxation processes in such systems are described in terms of the Debye classical theory [17]. This is confirmed by the configuration of the Coal–Coal plot, which, in the case of a low inclusion concentration, has the shape of a semi-circle according to the Debye equations.

The frequency dependences of the effective permittivity and dielectric loss factor are sensitive to relationships between the electrophysical parameters of the disperse phase and matrix, as well as to the shape of inclusions and their orientation in an external electric field. These properties of the effective parameters were discovered in early works on the electroscopy of inhomogeneous materials [1, 2, 18]. Subsequently, the self-consistent models of heterogeneous media worked out by Wiener, Bruggeman, Wagner, and others made it possible to refine the effect of different factors on the dielectric dispersion of inhomogeneous materials [4]. The majority of available data concerns two-component systems.

Multicomponent systems have a wider variety of properties and a larger number of possible structure configurations than two-component ones. The matrix of a multicomponent system has several, rather than one, inclusions that differ in properties, size, and mutual

1063-7842/03/4803-0317$24.00

arrangement. In this work, we found conditions under which the permittivity of a multicomponent system has a dispersion and studied the relaxation spectrum in specific media where the polarizations of dissimilar phases are compensated for [19]. We theoretically supported experimental findings that relaxation processes in a piecewise homogeneous material have two and three relaxation times and depend on the number of its constituents.

Calculations were carried out in the quasi-steady-state approximation described in [20], which assumes that the wavelength of a variable electric field is much larger than the characteristic sizes of the system and, hence, the interfacial polarization process has time to respond to a field variation. It is also assumed that polarizations of other types contribute to the system's overall polarization insignificantly.

THREE-COMPONENT MEDIA

The analysis of the permittivity dispersion in heterogeneous systems with Maxwell–Wagner polarization is convenient to begin with simple doubly and singly periodic models, of which the latter acquires anisotropic properties on averaging.

Matrix system. Consider a model three-component dielectric system consisting of a matrix with a permittivity ε_1 where two types of circular cylindrical inclusions alternate. The radii and permittivities of the inclusions are r_1, r_2 and ε_2, ε_3, respectively (Fig. 1). The long cylindrical bodies run in the same direction, forming a 2D doubly periodic lattice with square cells of side h. In the plane normal to the axes of the cylindrical bodies, the electric field in such a system is two-dimensional and can be calculated with techniques from the theory of analytical functions [15, 19].

In such a system, field averaging over a period makes it possible to evaluate its effective electrical characteristics. On average, the structure is isotropic. If the inclusion concentration is not too high (relevant estimates will be given below), the effective permittivity of such a material is given by

$$\varepsilon_{\text{eff}} = \varepsilon_1 \frac{1 - s_1\Delta_{\varepsilon 12}/2 - s_2\Delta_{\varepsilon 13}/2 + A_1\Delta_{\varepsilon 12}^2 + A_2\Delta_{\varepsilon 13}^2 + (B_1 + B_2)\Delta_{\varepsilon 12}\Delta_{\varepsilon 13}}{1 + s_1\Delta_{\varepsilon 12}/2 + s_2\Delta_{\varepsilon 13}/2 + A_1\Delta_{\varepsilon 12}^2 + A_2\Delta_{\varepsilon 13}^2 + (B_1 + B_2)\Delta_{\varepsilon 12}\Delta_{\varepsilon 13}}. \quad (1)$$

Here,

$$s_k = \frac{\pi r_k^2}{h^2} = \pi r_{k*}^2, \quad r_{k*} = \frac{r_k}{h} \quad (k = 1, 2) \quad (2)$$

are the concentrations of inclusions with the permittivities ε_2 and ε_3, respectively, and

$$\Delta_{\varepsilon 12} = \frac{\varepsilon_1 - \varepsilon_2}{\varepsilon_1 + \varepsilon_2}, \quad \Delta_{\varepsilon 13} = \frac{\varepsilon_1 - \varepsilon_3}{\varepsilon_1 + \varepsilon_3} \quad (3)$$
$$(-1 \le \Delta_{\varepsilon 12}, \Delta_{\varepsilon 13} \le 1)$$

are the relative permittivities of the inclusions. The parameters A_k and B_k ($k = 1, 2$) appearing in formula (1) depend on the radii as

$$A_k = 2r_k^2\left\{2r_k^3\sum_{m=1}^{\infty}\frac{1}{r_k^4 - 16m^4} + \sum_{n=1}^{\infty}\sum_{m=1}^{\infty}\left[\frac{r_k - 2m}{(r_k - 2m)^2 + 4n^2} + \frac{r_k + 2m}{(r_k + 2m)^2 + 4n^2} + \frac{r_k - 2m + 1}{(r_k - 2m + 1)^2 + (2n - 1)^2} + \frac{r_k + 2m - 1}{(r_k + 2m - 1)^2 + (2n - 1)^2}\right]\right\},$$

$$B_k = 2r_{3-k}^2\left\{2r_k^3\sum_{m=1}^{\infty}\frac{1}{r_k^4 - (2m - 1)^4} + \sum_{n=1}^{\infty}\sum_{m=1}^{\infty}\left[\frac{r_k - 2m}{(r_k - 2m)^2 + (2n - 1)^2}\right.\right. \quad (4)$$

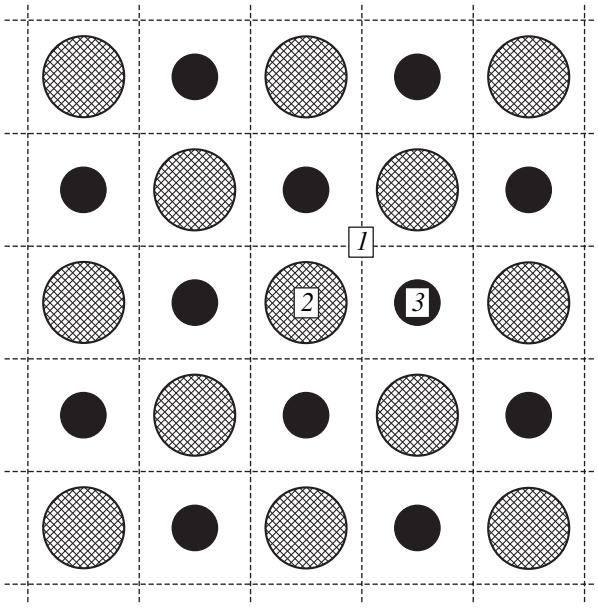

Fig. 1. Fragment of a three-component insulator with cylindrical inclusions.

$$+\frac{r_k+2m}{(r_k+2m)^2+(2n-1)^2}+\frac{r_k-2m+1}{(r_k-2m+1)^2+4n^2}$$
$$+\frac{r_k+2m-1}{(r_k+2m-1)^2+4n^2}\Bigg]\Bigg\}. \quad (4)$$

In (4), the inclusion radii r_k are given in relative units (see formula (2)). The asterisks are omitted for brevity.

Formula (1) was derived under the assumption that the concentration of inclusions is low and, hence, their interaction in the system is well described by an approximate multidipole representation of electric field where only the first-order (principal) image dipoles located at the centers of the inclusions are considered [16]. Higher order dipoles, whose moments decline rapidly with increasing order $\lambda = 2, 3, \ldots$, as $(s_k\Delta_{\varepsilon 12}\Delta_{\varepsilon 13})^\lambda$, contribute insignificantly under these conditions. The parameters $\Delta_{\varepsilon 1m}$ ($m = 2, 3$), whose magnitudes are usually less than unity, and concentrations s_k ($k = 1, 2$) appear in the expression for effective permittivity in multiplicatively; therefore, (1) is valid even if $|\Delta_{\varepsilon 1m}| \ll 1$ and s_k is finite or $s_k \ll 1$ and $|\Delta_{\varepsilon 1m}|$ is finite. The accuracy of formula (1) obtained asymptotically is the higher, the smaller are $|\Delta_{\varepsilon 1m}|$ and s_k.

Formula (1) defines the effective permittivity of a composite made up of perfect insulators. Real insulators are to a certain extent conductive. The electrical properties of such materials exposed to a harmonic electric field $\hat{\mathbf{E}} = \hat{\mathbf{E}}_0 \exp(i\omega t)$ are described by the complex permittivity

$$\hat{\varepsilon}(\omega) = \varepsilon - i\frac{\sigma}{\varepsilon_0\omega}, \quad (5)$$

where ε is the relative permittivity, σ is the electrical conductivity, ω is the circular frequency, and ε_0 is the permittivity of vacuum. The parameters σ and ε do not depend on the frequency ω of the electric field.

In the quasi-steady-state approximation, formula (1) with the complex permittivities $\hat{\varepsilon}_j(\omega)$ ($j = 1, 2, 3$) takes the form

$$\hat{\varepsilon}_{\text{eff}}(\omega) = \varepsilon'_{\text{eff}}(\omega) - i\varepsilon''_{\text{eff}}(\omega) = \hat{\varepsilon}_1(\omega)$$
$$\times\frac{1 - s_1\hat{\Delta}_{12}(\omega)/2 - s_2\hat{\Delta}_{13}(\omega)/2 + A_1\hat{\Delta}_{12}^2(\omega) + A_2\hat{\Delta}_{13}^2(\omega) + (B_1+B_2)\hat{\Delta}_{12}(\omega)\hat{\Delta}_{13}(\omega)}{1 + s_1\hat{\Delta}_{12}(\omega)/2 + s_2\hat{\Delta}_{13}(\omega)/2 + A_1\hat{\Delta}_{12}^2(\omega) + A_2\hat{\Delta}_{13}^2(\omega) + (B_1+B_2)\hat{\Delta}_{12}(\omega)\hat{\Delta}_{13}(\omega)}. \quad (6)$$

Here,

$$\hat{\Delta}_{1m}(\omega) = \Delta'_{1m}(\omega) + i\Delta''_{1m}(\omega) \quad (m = 2, 3) \quad (7)$$

are complex parameters with the components given by

$$\Delta'_{1m}(\omega) = \frac{\Delta_{\varepsilon 1m}(1-\Delta_{\sigma 1m})^2 + \Gamma_m^2(\omega)\Delta_{\sigma 1m}(1-\Delta_{\varepsilon 1m})^2}{(1-\Delta_{\sigma 1m})^2 + \Gamma_m^2(\omega)(1-\Delta_{\varepsilon 1m})^2}, \quad (8)$$
$$\Delta''_{1m}(\omega) = \frac{\Gamma_m(\omega)(\Delta_{\varepsilon 1p} - \Delta_{\sigma 1m})(1-\Delta_{\sigma 1m})(1-\Delta_{\varepsilon 1m})}{(1-\Delta_{\sigma 1m})^2 + \Gamma_m^2(\omega)(1-\Delta_{\varepsilon 1m})^2},$$

where

$$\Delta_{\sigma 1m} = \frac{\sigma_1 - \sigma_m}{\sigma_1 + \sigma_m} \quad (-1 \le \Delta_{\sigma 1m} \le 1) \quad (9)$$

is the relative conductivity.

Expressions (6)–(8) involve three frequency parameters:

$$\Gamma_j(\omega) = \frac{\omega_{0j}}{\omega} = \frac{\sigma_j}{\varepsilon_0\varepsilon_j\omega} \quad (0 \le \Gamma_j \le \infty); \quad j = 1, 2, 3, \quad (10)$$

which are the ratios of the Maxwellian frequencies $\omega_{0j} = \sigma_j/\varepsilon_0\varepsilon_j$ to the angular frequency ω. In terms of energy, they define the dielectric loss tangents in the components of a composite material. The parameters Γ_j are linearly related to each other as

$$\Gamma_1(\omega) = \frac{\varepsilon_2\sigma_1}{\varepsilon_1\sigma_2}\Gamma_2(\omega) = \frac{\varepsilon_3\sigma_1}{\varepsilon_1\sigma_3}\Gamma_3(\omega) \quad (11)$$

or, in terms of $\Delta_{\varepsilon 1m}$ and $\Delta_{\sigma 1m}$ ($m = 2, 3$), as

$$\Gamma_1(\omega) = \frac{(1-\Delta_{\varepsilon 12})(1+\Delta_{\sigma 12})}{(1+\Delta_{\varepsilon 12})(1-\Delta_{\sigma 12})}\Gamma_2(\omega)$$
$$= \frac{(1-\Delta_{\varepsilon 13})(1+\Delta_{\sigma 13})}{(1+\Delta_{\varepsilon 13})(1-\Delta_{\sigma 13})}\Gamma_3(\omega). \quad (12)$$

For subsequent analysis, it is convenient to introduce the relative frequency $\Delta_{\omega j}$:

$$\Delta_{\omega j} = \frac{\omega}{\omega_{0j} + \omega} \quad (0 \le \Delta_{\omega j} < 1). \quad (13)$$

As the angular frequency ω runs continuously from 0 to ∞, $\Delta_{\omega j}$ runs from 0 to 1.

Now expression (6) can be represented in the form

$$\hat{\varepsilon}_{\text{eff}}(\omega) = \varepsilon'_{\text{eff}}(\omega) - i\varepsilon''_{\text{eff}}(\omega)$$
$$= \varepsilon_1[1 - i\Gamma_1(\omega)]\frac{U^-(\omega) + iV^+(\omega)}{U^+(\omega) + iV^-(\omega)}. \quad (14)$$

Here, the real functions $U^{\pm}(\omega)$ and $V^{\pm}(\omega)$ are given by

$$U^{\pm}(\omega) = 1 \pm s_1\Delta'_{12}(\omega)/2 \pm s_2\Delta'_{13}(\omega)/2 + A_1[\Delta'^2_{12}(\omega) - \Delta''^2_{12}(\omega)] + A_2[\Delta'^2_{13}(\omega) - \Delta''^2_{13}(\omega)] + (B_1 + B_2)[\Delta'_{12}(\omega)\Delta'_{13}(\omega) - \Delta''_{12}(\omega)\Delta''_{13}(\omega)],$$
$$V^{\pm}(\omega) = \pm s_1\Delta''_{12}(\omega)/2 \pm s_2\Delta''_{13}(\omega)/2 - 2A_1\Delta'_{12}(\omega)\Delta''_{12}(\omega) - 2A_2\Delta'_{13}(\omega)\Delta''_{13}(\omega) - (B_1 + B_2)[\Delta'_{12}(\omega)\Delta''_{13}(\omega) + \Delta'_{13}(\omega)\Delta''_{12}(\omega)]. \quad (15)$$

Estimates show that if the radii of the cylindrical inclusions are small and, hence, their concentrations are low, the terms quadratic in $\Delta'_{12}(\omega)$, $\Delta''_{12}(\omega)$, $\Delta'_{13}(\omega)$, and $\Delta''_{13}(\omega)$ in (15) can be neglected. This also can be done if the material inhomogeneity is small: $|\Delta_{\varepsilon 1m}| \ll 1$ and $|\Delta_{\delta 1m}| \ll 1$. Then, formula (14) becomes

$$\hat{\varepsilon}_{\text{eff}}(\omega) = \varepsilon'_{\text{eff}}(\omega) - i\varepsilon''_{\text{eff}}(\omega) = \varepsilon_1[1 - i\Gamma_1(\omega)] \times \frac{1 - s_1\Delta'_{12}(\omega)/2 - s_2\Delta'_{13}(\omega)/2 + i[s_1\Delta''_{12}(\omega)/2 + s_2\Delta''_{13}(\omega)/2]}{1 + s_1\Delta'_{12}(\omega)/2 + s_2\Delta'_{13}(\omega)/2 - i[s_1\Delta''_{12}(\omega)/2 + s_2\Delta''_{13}(\omega)/2]}. \quad (16)$$

From (8), it directly follows that with

$$\Delta_{\varepsilon 12} = \Delta_{\sigma 12}, \quad \Delta_{\varepsilon 13} = \Delta_{\sigma 13}, \quad (17)$$

or, otherwise,

$$\varepsilon_1\sigma_2 = \varepsilon_2\sigma_1, \quad \varepsilon_1\sigma_3 = \varepsilon_3\sigma_1, \quad (18)$$

we have

$$\Delta'_{12}(\omega) = \Delta_{\varepsilon 12}, \quad \Delta'_{13}(\omega) = \Delta_{\varepsilon 13}, \quad \Delta''_{12}(\omega) = \Delta''_{13}(\omega) = 0. \quad (19)$$

Under these conditions, a three-component medium has the single frequency parameter

$$\Gamma_1(\omega) = \Gamma_2(\omega) = \Gamma_3(\omega). \quad (20)$$

Substituting (19) into (14) and (15) yields

$$\varepsilon'_{\text{eff}} = \varepsilon_1\frac{1 - s_1\Delta'_{\varepsilon 12}/2 - s_2\Delta'_{\varepsilon 13}/2 + A_1\Delta'^2_{\varepsilon 12} + A_2\Delta'^2_{\varepsilon 13} + (B_1 + B_2)\Delta'_{\varepsilon 12}\Delta'_{\varepsilon 13}}{1 + s_1\Delta'_{\varepsilon 12}/2 + s_2\Delta'_{\varepsilon 13}/2 + A_1\Delta'^2_{\varepsilon 12} + A_2\Delta'^2_{\varepsilon 13} + (B_1 + B_2)\Delta'_{\varepsilon 12}\Delta'_{\varepsilon 13}}, \quad \varepsilon''_{\text{eff}}(\omega) = \varepsilon'_{\text{eff}}\Gamma_1(\omega). \quad (21)$$

As follows from the first expression in (21), the effective permittivity $\varepsilon'_{\text{eff}}$ does not depend on the frequency. Thus, relationships (18) specify the condition under which the dispersion of a three-component matrix composite is absent. Unlike a two-component inhomogeneous material, for which either of two relationships (17) and (18) is fulfilled, in a three-component system, both must be fulfilled simultaneously.

The dielectric loss factor $\varepsilon''_{\text{eff}}$ in this case depends on the frequency, and its frequency dependence is given by the function $\Gamma_1(\omega)$ alone.

If the concentrations of inclusions of two sorts in a composite are the same ($s_1 = s_2$) and the permittivities of the inclusions satisfy the relationship

$$\varepsilon_1 = \sqrt{\varepsilon_2\varepsilon_3} \quad (\Delta_{\varepsilon 12} = -\Delta_{\varepsilon 13}), \quad (22)$$

the effective permittivity equals the permittivity of the matrix: $\varepsilon_{\text{eff}} = \varepsilon_1$. Relationships (22) outline the class of so-called characteristic media [19]. Their specific feature is that the polarizations in dissimilar inclusions are in opposition to each other and thus cancel each other out.

To find the effective permittivity values in limiting cases, we will take advantage of approximate expression (16). In this expression, as well as in the others, one must first fix one of the three frequency parameters $\Gamma_j(\omega)$ ($j = 1, 2, 3$) for which calculations will be performed. The choice of the parameter is of no principal significance: it must be merely convenient for analysis. For definiteness, the calculation will hereafter be performed for $\Gamma_2(\omega)$, unless otherwise stated. This parameter is assigned to phase 2, which has the electrophysical parameters ε_2 and σ_2 and Maxwellian frequency $\omega_{02} = \sigma_2/\varepsilon_0\varepsilon_2$. Accordingly, the relative frequency $\Delta_{\omega 2}$ will be used as a variable (see formulas (10)–(13)).

In the limit $\omega \longrightarrow 0$ ($\Gamma_2(\omega) \longrightarrow \infty$, $\Delta_{\omega 2} \longrightarrow 0$), we have from expression (16)

$$\varepsilon'_{\text{eff}}(0) = \varepsilon_1\left\{\frac{1 - s_1\Delta_{\varepsilon 12}/2 - s_2\Delta_{\varepsilon 13}/2}{1 + s_1\Delta_{\varepsilon 12}/2 + s_2\Delta_{\varepsilon 13}/2} + \frac{1}{1 + s_1\Delta_{\varepsilon 12}/2 + s_2\Delta_{\varepsilon 13}/2}\left[s_1(\Delta_{\sigma 12} - \Delta_{\varepsilon 12})\frac{1 + \Delta_{\sigma 12}}{1 + \Delta_{\varepsilon 12}}\right.\right. \quad (23)$$

$$+ s_2(\Delta_{\sigma 13} - \Delta_{\varepsilon 13})\frac{1+\Delta_{\sigma 13}}{1+\Delta_{\varepsilon 13}}\Big]\Big\}.$$

The static value of the permittivity $\varepsilon'_{\text{eff}}(0)$ is seen to be dependent on the inclusion concentration and all the electrophysical parameters of the system. The loss factor in this case has a singularity of type $1/\omega$:

$$\varepsilon''_{\text{eff}}(0) = \varepsilon_1\Gamma_2(0) \times \frac{(1-\Delta_{\varepsilon 12})(1+\Delta_{\sigma 12})(1-s_1\Delta_{\varepsilon 12}/2 - s_2\Delta_{\varepsilon 13}/2)}{(1+\Delta_{\varepsilon 12})(1-\Delta_{\sigma 12})(1+s_1\Delta_{\varepsilon 12}/2 + s_2\Delta_{\varepsilon 13}/2)}. \quad (24)$$

The infinite growth of $\varepsilon''_{\text{eff}}(0)$ at $\omega \longrightarrow 0$ is due to the bulk conductivity of the composite.

In the other limit, $\omega \longrightarrow \infty$ ($\Gamma_2(\omega) \longrightarrow 0$, $\Delta_{\omega 2} \longrightarrow 1$), the optical values of the effective permittivity and loss factor are expressed as

$$\varepsilon'_{\text{eff}}(\infty) = \varepsilon_1\frac{1 - s_1\Delta_{\varepsilon 12}/2 - s_2\Delta_{\varepsilon 13}/2}{1 + s_1\Delta_{\varepsilon 12}/2 + s_2\Delta_{\varepsilon 13}/2}, \quad \varepsilon''_{\text{eff}}(\infty) = 0. \quad (25)$$

At high frequencies, $\varepsilon''_{\text{eff}}(\infty)$ depends only on the inclusion concentration and permittivity of the material constituents. Under these conditions, losses in the composite are absent.

The frequency dependences of the complex effective permittivity become clearer if the inclusions are conductive and the matrix is a perfect insulator; that is,

$$\sigma_1 = 0 \quad (\Delta_{\sigma 12} = \Delta_{\sigma 13} = -1); \quad \sigma_2, \sigma_3 \neq 0. \quad (26)$$

Then, the parameters $\Delta'_{1m}(\omega)$ and $\Delta''_{1m}(\omega)$ ($m = 2, 3$), which are given by (8), will take the form

$$\Delta'_{1m}(\omega) = \frac{4\Delta_{\varepsilon 1m} - \Gamma_m^2(\omega)(1-\Delta_{\varepsilon 1m})^2}{4 + \Gamma_m^2(\omega)(1-\Delta_{\varepsilon 1m})^2},$$
$$\Delta''_{1m}(\omega) = \frac{2\Gamma_m(\omega)(1-\Delta_{\varepsilon 1m}^2)}{4 + \Gamma_m^2(\omega)(1-\Delta_{\varepsilon 1m})^2}. \quad (27)$$

Now, to find the limiting values of the complex effective permittivity, we will proceed from general expression (14).

For $\omega \longrightarrow 0$ ($\Gamma_2(\omega) \longrightarrow \infty$, $\Delta_{\omega 2} \longrightarrow 0$), the effective values $\varepsilon'_{\text{eff}}(0)$ and $\varepsilon''_{\text{eff}}(0)$ are given by

$$\varepsilon'_{\text{eff}}(0) = \varepsilon_1\frac{1 + s_1/2 + s_2/2 + A_1 + A_2 + B_1 + B_2}{1 - s_1/2 - s_2/2 + A_1 + A_2 + B_1 + B_2}, \quad (28)$$
$$\varepsilon''_{\text{eff}}(0) = 0.$$

For $\omega \longrightarrow \infty$ ($\Gamma_2(\omega) \longrightarrow 0$, $\Delta_{\omega 2} \longrightarrow 1$), the optical values of the effective permittivity $\varepsilon'_{\text{eff}}(\infty)$ and loss factor $\varepsilon''_{\text{eff}}(\infty)$ are expressed as

$$\varepsilon'_{\text{eff}}(\infty) = \varepsilon_1\frac{1 - s_1\Delta_{\varepsilon 12}/2 - s_2\Delta_{\varepsilon 13}/2 + A_1\Delta_{\varepsilon 12}^2 + A_2\Delta_{\varepsilon 13}^2 + (B_1 + B_2)\Delta_{\varepsilon 12}\Delta_{\varepsilon 13}}{1 + s_1\Delta_{\varepsilon 12}/2 + s_2\Delta_{\varepsilon 13}/2 + A_1\Delta_{\varepsilon 12}^2 + A_2\Delta_{\varepsilon 13}^2 + (B_1 + B_2)\Delta_{\varepsilon 12}\Delta_{\varepsilon 13}}, \quad (29)$$
$$\varepsilon''_{\text{eff}}(\infty) = 0.$$

In our material, the effective static value of the permittivity $\varepsilon'_{\text{eff}}(0)$ depends on the permittivity of the matrix with a proportionality coefficient (>1) that is a function only of the system's geometrical parameters. In the limits $\omega \longrightarrow 0$ and $\omega \longrightarrow \infty$, the effective loss factor of the composite vanishes; therefore, the frequency dependence $\varepsilon''_{\text{eff}}(0)$ has at least one maximum in the interval $0 \le \omega < \infty$. Actually, as follows from investigations, the function $\varepsilon''_{\text{eff}}(\omega)$ for a three-component system may have two (and no more) maxima under certain relationships between the electrophysical parameters.

Such behavior of the static value of the complex effective permittivity is observed in inhomogeneous matrix systems where the matrix is nonconductive and, thus, bulk conduction is absent. This follows from comparison of (28) and (29) with expressions (23)–(25) for a material with a conductive matrix, in which $\varepsilon''_{\text{eff}}(\omega) \longrightarrow \infty$ at $\omega \longrightarrow 0$.

With $\omega \longrightarrow \infty$, the effective permittivity $\varepsilon'_{\text{eff}}(\omega)$ depends only on the permittivities of the components and geometrical parameters of the system for both $\sigma_1 \neq 0$ and $\sigma_1 = 0$. Thus, $\varepsilon'_{\text{eff}}(\infty)$ is independent of the conductive properties of the inclusions.

The aforesaid is illustrated in Fig. 2, where the effective permittivity $\varepsilon'_{\text{eff}}(\Delta_{\omega 2})$, effective loss factor $\varepsilon'_{\text{eff}}(\Delta_{\omega 2})$, and effective loss tangent $\tan\delta_{\text{eff}}(\Delta_{\omega 2})$ are plotted against relative frequency $\Delta_{\omega 2}$ using formulas (28) and (29). The dimensionless parameters are as follows: $s_1 = 0.25$, $s_2 = 0.20$, $\varepsilon_1 = 12$, $\varepsilon_2 = 4$, $\varepsilon_3 = 2$, $\sigma_1 = 0$, $\sigma_2 = 1$, and $\sigma_3 = 100$ ($\Delta_{\varepsilon 12} = 0.5$, $\Delta_{\varepsilon 13} = 0.714$, and $\Delta_{\sigma 12} = \Delta_{\sigma 13} = -1$). The plots are constructed for the relative values $\varepsilon'_{\text{eff}*} = \varepsilon'_{\text{eff}}/\varepsilon_1$ and $\varepsilon''_{\text{eff}*} = \varepsilon''_{\text{eff}}/\varepsilon_1$ (the asterisks are omitted). For the conditions under consideration, Fig. 3 shows the complex permittivity diagram in the form of two semicircles, which intersect at the point where the effective loss factor has a local minimum between two maxima.

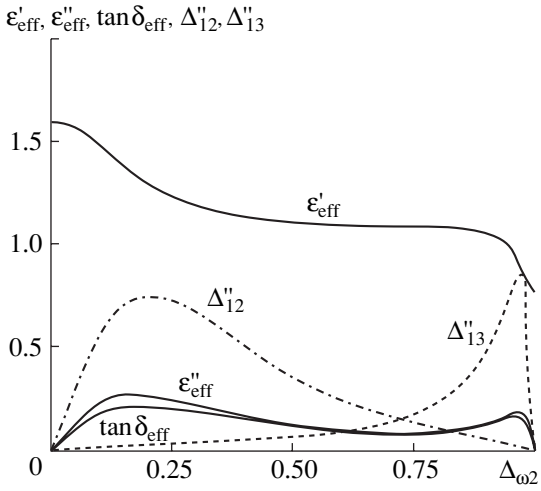

Fig. 2. Effective permittivity, effective loss factor, effective loss tangent, and parameters Δ''_{12} and Δ''_{13} vs. relative frequency $\Delta_{\omega 2}$ for the inclusion concentrations $s_1 = 0.25$ and $s_2 = 0.20$ and $\Delta_{\varepsilon 12} = 0.5$, $\Delta_{\varepsilon 13} = 0.714$, and $\Delta_{\sigma 12} = \Delta_{\sigma 13} = -1$.

The curves $\varepsilon''_{\text{eff}}(\Delta_{\omega 2})$ and $\varepsilon''_{\text{eff}}(\varepsilon'_{\text{eff}})$ (Figs. 2, 3) have two peaks. In terms of the Debye theory [17], this means that the system has two relaxation times under the conditions adopted. The peaks of the dependence $\varepsilon''_{\text{eff}}(\Delta_{\omega 2})$ coincide with the inflection points of the dependence $\varepsilon'_{\text{eff}}(\Delta_{\omega 2})$.

The direct use of expressions (14) and (15) to find the frequencies at which the function $\varepsilon''_{\text{eff}}(\Delta_{\omega 2})$ takes extremum values yields very awkward and hard-to-perceive results. Therefore, it would be appropriate to make an approximate estimate in order to cut the body of calculation and represent the final results in a physically meaningful form. The mathematical prerequisite for such estimates is as follows.

From expressions (14) and (15) for $\sigma_1 = 0$ ($\Delta_{\sigma 12} = -1$), the effective loss factor can be represented as

$$\varepsilon''_{\text{eff}}(\Delta_{\omega 2}) = \frac{-s_1\Delta''_{12}(\Delta_{\omega 2}) - s_2\Delta''_{13}(\Delta_{\omega 2}) + \ldots}{1 + s_1\Delta'_{12}(\Delta_{\omega 2}) + s_2\Delta'_{13}(\Delta_{\omega 2}) + \ldots}, \quad (30)$$

where the dots in the numerator and denominator imply two-term products like $\Delta'^2_{12}(\Delta_{\omega 2})$, $\Delta''^2_{12}(\Delta_{\omega 2})$, $\Delta'_{12}(\Delta_{\omega 2})\Delta''_{12}(\Delta_{\omega 2})$, etc. Here, the parameters $\Delta'_{1m}(\Delta_{\omega 2})$ and $\Delta''_{1m}(\Delta_{\omega 2})$ ($m = 2, 3$) are defined by formulas (27). In (30), the absolute values of all subsequent terms are always smaller than those of the first two shown. The difference between them is the greater, the smaller the nonuniformity of the electrophysical parameters of the material and the smaller the concentrations of inclusions of either type. Thus, it can be concluded that the first two terms of the numerator in (30), which contain the parameters $\Delta''_{12}(\Delta_{\omega 2})$ and $\Delta''_{13}(\Delta_{\omega 2})$ in the first power, make a major contribution to the effective loss factor. Since these parameters as functions of the relative frequency $\Delta_{\omega 2}$ have maxima, one can expect that these maxima define those of the function $\varepsilon''_{\text{eff}}(\Delta_{\omega 2})$. This supposition is confirmed by many particular calculations. As applied to the case under consideration, the results of calculation are graphically depicted in Fig. 2. It is seen that the maxima of the effective loss factor $\varepsilon''_{\text{eff}}(\Delta_{\omega 2})$ do roughly coincide with the extrema of the functions $\Delta''_{12}(\Delta_{\omega 2})$ and $\Delta''_{13}(\Delta_{\omega 2})$, the coincidence being more accurate at high frequencies and less accurate at low ones. Thus, the qualitative analysis of the effective loss factor spectrum $\varepsilon''_{\text{eff}}(\Delta_{\omega 2})$ can be performed by studying the frequency dependences of $\Delta''_{12}(\Delta_{\omega 2})$ and $\Delta''_{13}(\Delta_{\omega 2})$.

The parameter $\Delta''_{12}(\Delta_{\omega 2})$ reaches a maximum at

$$\Delta^{(1)}_{\omega 2} = \frac{1 - \Delta_{\varepsilon 12}}{3 - \Delta_{\varepsilon 12}} = \frac{\varepsilon_2}{\varepsilon_1 + 2\varepsilon_2}. \quad (31)$$

Theoretically, the frequency $\Delta^{(1)}_{\omega 2}$ may take values from the interval $0 \le \Delta^{(1)}_{\omega 2} \le 1/2$.

The other parameter, $\Delta''_{13}(\Delta_{\omega 2})$, has an extremum at

$$\Delta^{(2)}_{\omega 2} = \frac{1 - \Delta_{\varepsilon 13}}{1 + 2\varepsilon_3\sigma_2/\varepsilon_2\sigma_3 - \Delta_{\varepsilon 13}} = \frac{\varepsilon_2\sigma_3}{\varepsilon_2\sigma_3 + \sigma_2(\varepsilon_1 + \varepsilon_3)}, \quad (32)$$

in this case, the range of the frequency $\Delta^{(2)}_{\omega 2}$ is not limited by the interval $0 \le \Delta^{(2)}_{\omega 2} \le 1$.

The frequencies $\Delta^{(1)}_{\omega 2}$ and $\Delta^{(2)}_{\omega 2}$, at which the effective loss factor $\varepsilon''_{\text{eff}}(\Delta_{\omega 2})$ takes maximal values, are found by conventional techniques of mathematical analysis. The general extremum condition follows from the second expression of (27):

$$\Gamma^{(m-1)}_m = \frac{2}{1 - \Delta_{\varepsilon 1m}} \quad (m = 2, 3). \quad (33)$$

Hence, using formulas (10) and (13) in view of relationships (11), we arrive at expressions (31) and (32).

For the maxima of the effective loss factor $\varepsilon''_{\text{eff}}(\Delta_{\omega 2})$ to be distinguishable and not to overlap, the frequency spacing between them must be sufficiently wide. This requirement can be provided if the frequency $\Delta^{(1)}_{\omega 2}$ of the first maximum is shifted, for example, to low frequencies and the frequency $\Delta^{(2)}_{\omega 2}$ of the second maximum, to high frequencies. According to formulas (31) and (32), such conditions are met when the electrophysical parameters of the composite satisfy the relationships

$$\varepsilon_1 \gg \varepsilon_2 \quad (\Delta_{\varepsilon 12} \longrightarrow 1), \quad \varepsilon_2\sigma_3 \gg \varepsilon_3\sigma_2. \quad (34)$$

Note that the parameters used in constructing the graphical dependences in Figs. 2 and 3 satisfy relationships (34).

Stratified system. Studying the spectral characteristics of an inhomogeneous medium composed of doubly periodically alternating cylindrical inclusions of two types, we have found conditions when the permittivity dispersion is absent. It has been shown that the effective loss factor in a three-component system may have two maxima. The natural question arises: To what extent do these results apply to nonmatrix systems? To tackle the question, one should study the frequency dependence of the complex permittivities of variously textured inhomogeneous systems. Below, as a simple inhomogeneous system of this type, we consider a stratified material consisting of three dissimilar alternating layers of equal size. As a whole, such a system acquires anisotropic properties, and its effective permittivity tensor has the components

$$\varepsilon_{\text{eff},\,xx} = \frac{3\varepsilon_1\varepsilon_2\varepsilon_3}{\varepsilon_1\varepsilon_2 + \varepsilon_1\varepsilon_3 + \varepsilon_2\varepsilon_3},$$
$$\varepsilon_{\text{eff},\,yy} = \frac{1}{3}(\varepsilon_1 + \varepsilon_2 + \varepsilon_3). \tag{35}$$

It is assumed that the x axis is directed normally to the layers.

For a medium whose constituents have complex permittivity of form (5), expressions (35) written in terms of the complex parameters $\hat{\Delta}_{1m}(\omega)$ (m = 2, 3) become

$$\hat{\varepsilon}_{\text{eff},\,xx}(\omega) = 3\hat{\varepsilon}_1(\omega)\frac{F^-(\omega)}{G^-(\omega)},$$
$$\hat{\varepsilon}_{\text{eff},\,yy}(\omega) = \frac{1}{3}\hat{\varepsilon}_1(\omega)\frac{G^+(\omega)}{F^+(\omega)}. \tag{36}$$

Here,

$$F^{\pm}(\omega) = [\pm\hat{\Delta}_{12}(\omega)][1 \pm \hat{\Delta}_{13}(\omega)],$$
$$G^{\pm}(\omega) = [\pm\hat{\Delta}_{12}(\omega)][1 \mp \hat{\Delta}_{13}(\omega)] \tag{37}$$
$$+ [1 \mp \hat{\Delta}_{12}(\omega)][1 \pm \hat{\Delta}_{13}(\omega)] + [1 \pm \hat{\Delta}_{12}(\omega)][1 \pm \hat{\Delta}_{13}(\omega)].$$

In expanded form, expressions (36) and (37) take the form

$$\hat{\varepsilon}_{\text{eff},\,xx}(\omega) = 3\hat{\varepsilon}_1(\omega)\frac{X^-(\omega) + iY^-(\omega)}{Z^-(\omega) + iY^+(\omega)},$$
$$\hat{\varepsilon}_{\text{eff},\,yy}(\omega) = \frac{\hat{\varepsilon}_1(\omega)}{3}\frac{Z^+(\omega) - iY^-(\omega)}{X^+(\omega) - iY^+(\omega)}, \tag{38}$$

where the functions $X^{\pm}(\omega)$, $Y^{\pm}(\omega)$, and $Z^{\pm}(\omega)$ are given

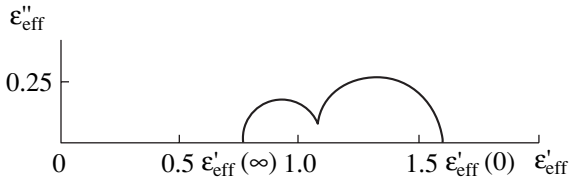

Fig. 3. Diagram of the effective complex permittivity of the three-component insulator with the same parameters as in Fig. 2.

by

$$X^{\pm}(\omega) = 1 \pm \Delta'_{12}(\omega) \pm \Delta'_{13}(\omega)$$
$$+ \Delta'_{12}(\omega)\Delta'_{13}(\omega) - \Delta''_{12}(\omega)\Delta''_{13}(\omega),$$
$$Y^{\pm}(\omega) = \Delta''_{12}(\omega)[1 \pm \Delta'_{13}(\omega)] + \Delta''_{13}(\omega)[1 \pm \Delta'_{12}(\omega)], \tag{39}$$
$$Z^{\pm}(\omega) = 3 \pm \Delta'_{12}(\omega) \pm \Delta'_{13}(\omega)$$
$$- \Delta'_{12}(\omega)\Delta'_{13}(\omega) + \Delta''_{12}(\omega)\Delta''_{13}(\omega).$$

With conditions (17) and (18) met, relationships (19) are valid and the system is characterized by single frequency parameter (20). Then, from expressions (38) and (39), we find that the real parts of the effective permittivity tensor, $\varepsilon'_{\text{eff},\,xx}$ and $\varepsilon'_{\text{eff},\,yy}$, retain their constant values, while the imaginary parts vary with frequency as the parameter $\Gamma_1(\omega)$:

$$\varepsilon'_{\text{eff},\,xx} = 3\varepsilon_1\frac{1 - \Delta_{\varepsilon12} - \Delta_{\varepsilon13} + \Delta_{\varepsilon12}\Delta_{\varepsilon13}}{3 - \Delta_{\varepsilon12} - \Delta_{\varepsilon13} - \Delta_{\varepsilon12}\Delta_{\varepsilon13}},$$
$$\varepsilon''_{\text{eff},\,xx}(\omega) = \varepsilon'_{\text{eff},\,xx}\Gamma_1(\omega);$$
$$\varepsilon'_{\text{eff},\,yy} = \frac{\varepsilon_1}{3}\frac{3 + \Delta_{\varepsilon12} + \Delta_{\varepsilon13} - \Delta_{\varepsilon12}\Delta_{\varepsilon13}}{1 + \Delta_{\varepsilon12} + \Delta_{\varepsilon13} + \Delta_{\varepsilon12}\Delta_{\varepsilon13}}, \tag{40}$$
$$\varepsilon''_{\text{eff},\,yy}(\omega) = \varepsilon'_{\text{eff},\,yy}\Gamma_1(\omega).$$

Relationships (18) thus define the conditions under which the permittivity dispersion is also absent in the case of a one-period system.

The expressions for $\varepsilon''_{\text{eff},\,xx}$ and $\varepsilon'_{\text{eff},\,yy}$ coincide with respective formulas (35), which is easy to check by substituting formulas (3) for $\Delta_{\varepsilon12}$ and $\Delta_{\varepsilon13}$ into (40).

Let one of the layers (e.g., layer 1) be nonconducting; that is, $\sigma_1 = 0$ ($\Delta_{\sigma12} = \Delta_{\sigma13} = -1$). Then, in the limiting cases (as for the matrix system, the relative frequency $\Delta_{\omega2}$ and the frequency parameter $\Gamma_2(\Delta_{\omega2})$ assigned to phase 2 are taken as variable parameters), we have the following expressions:

for $\omega \longrightarrow 0$ ($\Gamma_2(\omega) \longrightarrow \infty$, $\Delta_{\omega2} \longrightarrow 0$),

$$\varepsilon'_{\text{eff},\,xx}(0) = 3\varepsilon_1, \quad \varepsilon''_{\text{eff},\,xx}(0) = 0;$$

$$\varepsilon''_{\text{eff},\,yy}(0) = \frac{\varepsilon_1}{3}\frac{3+\Delta_{\varepsilon12}+\Delta_{\varepsilon13}-\Delta_{\varepsilon12}\Delta_{\varepsilon13}}{1+\Delta_{\varepsilon12}+\Delta_{\varepsilon13}+\Delta_{\varepsilon12}\Delta_{\varepsilon13}}, \quad (41)$$

$$\varepsilon''_{\text{eff},\,yy}(0) = \frac{1}{3}\varepsilon_1\Gamma_2(0)\left(1+\frac{\sigma_3}{\sigma_2}\right)\frac{1-\Delta_{\varepsilon12}}{1+\Delta_{\varepsilon12}};$$

for $\omega \longrightarrow \infty$ ($\Gamma_2(\omega) \longrightarrow 0$, $\Delta_{\omega2} \longrightarrow 1$),

$$\varepsilon'_{\text{eff},\,xx}(\infty) = 3\varepsilon_1\frac{1-\Delta_{\varepsilon12}-\Delta_{\varepsilon13}+\Delta_{\varepsilon12}\Delta_{\varepsilon13}}{3-\Delta_{\varepsilon12}-\Delta_{\varepsilon13}-\Delta_{\varepsilon12}\Delta_{\varepsilon13}},$$

$$\varepsilon''_{\text{eff},\,xx}(\infty) = 0; \quad (42)$$

$$\varepsilon'_{\text{eff},\,yy}(\infty) = \frac{\varepsilon_1}{3}\frac{3+\Delta_{\varepsilon12}+\Delta_{\varepsilon13}-\Delta_{\varepsilon12}\Delta_{\varepsilon13}}{1+\Delta_{\varepsilon12}+\Delta_{\varepsilon13}+\Delta_{\varepsilon12}\Delta_{\varepsilon13}},$$

$$\varepsilon''_{\text{eff},\,yy}(\infty) = 0.$$

From (41) and (42), it follows that the electrostatic and optical components of the effective permittivity tensor differ substantially. There are at least two distinguishing features. First, at $\omega \longrightarrow 0$, the effective longitudinal loss factor $\varepsilon''_{\text{eff},\,yy}(0)$ has a singularity. It is noteworthy that this singularity exists even if two layers of the three are nonconducting. In fact, setting $\sigma_3 = 0$ in formula (41) for $\varepsilon''_{\text{eff},\,yy}(0)$ does not change the character of the singularity. This is because for the longitudinal component of the effective permittivity tensor (unlike the transverse component), bulk conduction exists if at least one of the layers is conducting. Second, the effective longitudinal permittivity $\varepsilon'_{\text{eff},\,yy}$ does not depend on the frequency; hence, the dispersion of this permittivity component is absent under any conditions.

For the component $\hat{\varepsilon}_{\text{eff},\,xx}(\omega)$, the dielectric spectrum of the stratified material is the same as for the doubly periodic matrix structure with circular inclusions that was considered in the previous section. This can be visualized by comparing Figs. 2 and 4.

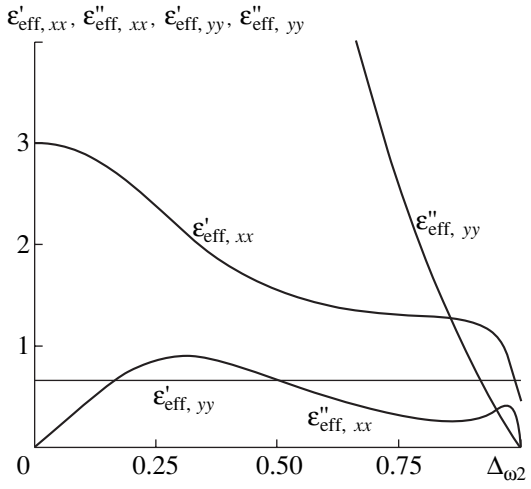

Fig. 4. Frequency dependences of the effective permittivity of the stratified medium with $\Delta_{\varepsilon12} = 0.333$, $\Delta_{\varepsilon13} = 0.6$, and $\Delta_{\sigma12} = \Delta_{\sigma13} = -1$.

Thus, a singly periodic structure and a doubly periodic structure with a low concentration of inclusions have the same frequency characteristics of the transverse permittivity component. The associated dielectric spectra are described based on similar theoretical statements.

FOUR-COMPONENT MEDIUM WITH A HEXAGONAL STRUCTURE

The simplest model of such a medium is represented by a matrix with a permittivity ε_1 in which three types of circular cylindrical unidirectional inclusions with permittivities ε_2, ε_3, and ε_4 and radii r_1, r_2, and r_3, respectively, are embedded (Fig. 5). The inclusions are doubly periodically arranged at the centers of hexagonal cells, continuously covering the plane. Geometrically, this structure has a hexagonal axis. On averaging, the structure acquires anisotropic properties and its electrophysical parameters in the transverse direction are described by the effective permittivity tensor $\tilde{\varepsilon}_{\text{eff}}$, which has two components when reduced to the principal axes: $\tilde{\varepsilon}_{\text{eff}} = \{\varepsilon_{\text{eff},\,xx}, \varepsilon_{\text{eff},\,yy}\}$. The four-component system under consideration has a matrix structure, like the former of the two analyzed above, and is anisotropic as a whole like the latter.

To find the basic features of the dielectric spectrum of such structures, it is sufficient to analyze the case when the total concentration of the inclusions is low ($s_1 + s_2 + s_3 \le 0.5$). Under the conditions adopted, the components of the effective permittivity tensor are given by [21]

$$\varepsilon_{\text{eff},\,xx} = \varepsilon_1\frac{1-\alpha(s_1\Delta_{\varepsilon12}+s_2\Delta_{\varepsilon13}+s_3\Delta_{\varepsilon14})}{1+\beta(s_1\Delta_{\varepsilon12}+s_2\Delta_{\varepsilon13}+s_3\Delta_{\varepsilon14})},$$

$$\varepsilon_{\text{eff},\,yy} = \varepsilon_1\frac{1-\beta(s_1\Delta_{\varepsilon12}+s_2\Delta_{\varepsilon13}+s_3\Delta_{\varepsilon14})}{1+\alpha(s_1\Delta_{\varepsilon12}+s_2\Delta_{\varepsilon13}+s_3\Delta_{\varepsilon14})}. \quad (43)$$

Here, α and β are numerical coefficients reflecting the system's anisotropy ($\alpha = 4/3$ and $\alpha + \beta = 2$) and the parameters $\Delta_{\varepsilon1g}$ ($g = 2, 3, 4$) are given by formulas (3) with an obvious complement. The components of the tensor $\tilde{\varepsilon}_{\text{eff}}$ satisfy the reciprocity relations

$$\varepsilon_{\text{eff},\,xx}(\Delta_{\varepsilon12}, \Delta_{\varepsilon13}, \Delta_{\varepsilon14})\varepsilon_{\text{eff},\,yy}(\Delta_{\varepsilon21}, \Delta_{\varepsilon31}, \Delta_{\varepsilon41}) = \varepsilon_1^2; \quad (44)$$

therefore, it is sufficient to analyze the properties of only one of the components. Let this component be $\varepsilon_{\text{eff},\,xx}$ for the sake of definiteness.

Then, for the complex permittivity given by (5), the first expression in (43) can be rearranged into

$$\hat{\varepsilon}_{\text{eff},\,xx}(\omega) = \hat{\varepsilon}_1 \frac{1-\alpha[s_1\hat{\Delta}_{12}(\omega)+s_2\hat{\Delta}_{13}(\omega)+s_3\hat{\Delta}_{14}(\omega)]}{1+\beta[s_1\hat{\Delta}_{12}(\omega)+s_2\hat{\Delta}_{13}(\omega)+s_3\hat{\Delta}_{14}(\omega)]}, \quad (45)$$

where the complex parameters $\hat{\Delta}_{14}(\omega)$ are given by expressions (7)–(10) as before with the subscripts m replaced by g.

Now these expressions contain four frequency parameters $\Gamma_\nu(\omega)$ ($\nu = 1, \ldots, 4$), which are linearly related to each other:

$$\Gamma_1(\omega) = \frac{\varepsilon_2\sigma_1}{\varepsilon_1\sigma_2}\Gamma_2(\omega) = \frac{\varepsilon_3\sigma_1}{\varepsilon_1\sigma_3}\Gamma_3(\omega) = \frac{\varepsilon_4\sigma_1}{\varepsilon_1\sigma_4}\Gamma_4(\omega). \quad (46)$$

With formulas (3) and (9), relationships (46) can be rearranged into

$$\Gamma_1(\omega) = \frac{(1-\Delta_{\varepsilon 12})(1+\Delta_{\sigma 12})}{(1+\Delta_{\varepsilon 12})(1-\Delta_{\sigma 12})}\Gamma_2(\omega) = \frac{(1-\Delta_{\varepsilon 13})(1+\Delta_{\sigma 13})}{(1+\Delta_{\varepsilon 13})(1-\Delta_{\sigma 13})}\Gamma_3(\omega) = \frac{(1-\Delta_{\varepsilon 14})(1+\Delta_{\sigma 14})}{(1+\Delta_{\varepsilon 14})(1-\Delta_{\sigma 14})}\Gamma_4(\omega). \quad (47)$$

Relationships (46) and (47) generalize equalities (11) and (12) for the case of a four-component medium.

Separating the real and imaginary parts of complex expression (45), we obtain

$$\varepsilon'_{\text{eff},\,xx}(\omega) = \varepsilon_1 \frac{1-(\alpha-\beta)\Delta' - \alpha\beta(\Delta'+\Delta'') + (\alpha+\beta)\Gamma_1(\omega)\Delta''}{(1+\beta\Delta')^2+(\beta\Delta'')^2},$$
$$\varepsilon''_{\text{eff},\,xx}(\omega) = \varepsilon_1 \times \frac{\Gamma_1(\omega)[1-(\alpha-\beta)\Delta' - \alpha\beta(\Delta'+\Delta'')] - (\alpha+\beta)(\omega)\Delta''}{(1+\beta\Delta')^2+(\beta\Delta'')^2}, \quad (48)$$

where

$$\Delta' = s_1\Delta'_{12} + s_2\Delta'_{13} + s_3\Delta'_{14},$$
$$\Delta'' = s_1\Delta''_{12} + s_2\Delta''_{13} + s_3\Delta''_{14}. \quad (49)$$

From expressions (48) and (49) in view of formulas (7)–(10), it follows that if the three conditions

$$\Delta_{\varepsilon 12} = \Delta_{\sigma 12}, \quad \Delta_{\varepsilon 13} = \Delta_{\sigma 13}, \quad \Delta_{\varepsilon 14} = \Delta_{\sigma 14} \quad (50)$$

or, which is the same,

$$\varepsilon_1\sigma_2 = \varepsilon_2\sigma_1, \quad \varepsilon_1\sigma_3 = \varepsilon_3\sigma_1, \quad \varepsilon_1\sigma_4 = \varepsilon_4\sigma_1, \quad (51)$$

are satisfied, the real part of the component $\hat{\varepsilon}_{\text{eff},\,xx}(\omega)$ does not depend on frequency,

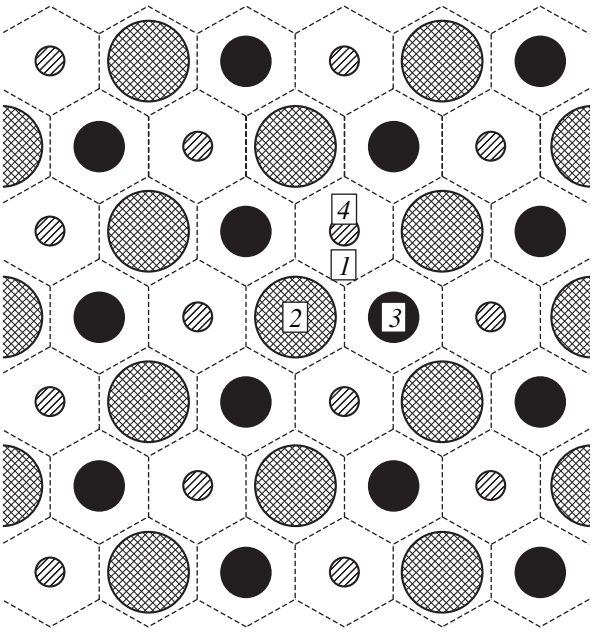

Fig. 5. Fragment of a four-component medium with a hexagonal structure.

$$\varepsilon'_{\text{eff},\,xx} = \varepsilon_1 \frac{1-\alpha(s_1\Delta_{\varepsilon 12}+s_2\Delta_{\varepsilon 13}+s_3\Delta_{\varepsilon 14})}{1+\beta(s_1\Delta_{\varepsilon 12}+s_2\Delta_{\varepsilon 13}+s_3\Delta_{\varepsilon 14})}, \quad (52)$$

and takes electrostatic value (43). The imaginary part varies as the frequency parameter $\Gamma_1(\omega)$:

$$\varepsilon''_{\text{eff},\,xx}(\omega) = \varepsilon'_{\text{eff},\,xx}\Gamma_1(\omega). \quad (53)$$

Relationships (50) or (51), like similar expressions in the previous cases, specify no-dispersion conditions. Note that relationships (51) can be derived from the boundary conditions in the absence of free charges. As compared with the previous systems, here the number of governing equations increases by one and becomes equal to the number of inclusion types in a matrix composite. According to (46), the material in this case is characterized by the single frequency parameter

$$\Gamma_1(\omega) = \Gamma_2(\omega) = \Gamma_3(\omega) = \Gamma_4(\omega). \quad (54)$$

In the general case, when conditions (50) fail, the effective parameter $\hat{\varepsilon}_{\text{eff},\,xx}(\omega)$ with $\omega \longrightarrow 0$ ($\Gamma_2(\omega) \longrightarrow \infty$, $\Delta_{\omega 2} \longrightarrow 0$) takes the following electrostatic values (as before, $\Gamma_2(\omega)$ and $\Delta_{\omega 2}$ are variables):

$$\varepsilon'_{\text{eff},\,xx}(0) = \varepsilon_1 \frac{1-\alpha(s_1\Delta_{\sigma 12}+s_2\Delta_{\sigma 13}+s_3\Delta_{\sigma 14})}{1+\beta(s_1\Delta_{\sigma 12}+s_2\Delta_{\sigma 13}+s_3\Delta_{\sigma 14})} + \frac{2\varepsilon_1}{[1+\beta(s_1\Delta_{\varepsilon 12}+s_2\Delta_{\varepsilon 13}+s_3\Delta_{\varepsilon 14})]^2}$$

$$\times\left[s_1(\Delta_{\sigma 12}-\Delta_{\varepsilon 12})\frac{1+\Delta_{\sigma 12}}{1+\Delta_{\varepsilon 12}}+s_2(\Delta_{\sigma 13}-\Delta_{\varepsilon 13})\frac{1+\Delta_{\sigma 13}}{1+\Delta_{\varepsilon 13}}\right.$$
$$\left.+\,s_3(\Delta_{\sigma 14}-\Delta_{\varepsilon 14})\frac{1+\Delta_{\sigma 14}}{1+\Delta_{\varepsilon 14}}\right],$$

$$\varepsilon''_{\text{eff},\,xx}(0)=\varepsilon_1\Gamma_2(0)$$
$$\times\frac{(1-\Delta_{\varepsilon 12})(1+\Delta_{\sigma 12})[1-\alpha(s_1\Delta_{\sigma 12}+s_2\Delta_{\sigma 13}+s_3\Delta_{\sigma 14})]}{(1+\Delta_{\varepsilon 12})(1-\Delta_{\sigma 12})[1+\beta(s_1\Delta_{\sigma 12}+s_2\Delta_{\sigma 13}+s_3\Delta_{\sigma 14})]}. \quad (55)$$

At low frequencies, the effective parameters of the medium are seen to depend considerably on the conductivity of the components.

From the second formula of (55), it follows that the effective dielectric loss factor has a singularity at $\omega \longrightarrow 0$. The infinite growth of $\varepsilon''_{\text{eff},\,xx}(0)$ (as $1/\omega$) is associated with the conductivity of the matrix phase and, consequently, with the bulk conductivity of the composite.

At high frequencies, $\omega \longrightarrow \infty$ ($\Gamma_2(\omega) \longrightarrow 0$, $\Delta_{\omega 2} \longrightarrow 1$), the effective parameters of the medium (we everywhere mean the component $\hat{\varepsilon}_{\text{eff},\,xx}(\omega)$ of the tensor $\tilde{\varepsilon}_{\text{eff},\,xx}(\omega)$) take the values

$$\varepsilon'_{\text{eff},\,xx}(\infty)=\varepsilon_1\frac{1-\alpha(s_1\Delta_{\varepsilon 12}+s_2\Delta_{\varepsilon 13}+s_3\Delta_{\varepsilon 14})}{1+\beta(s_1\Delta_{\varepsilon 12}+s_2\Delta_{\varepsilon 13}+s_3\Delta_{\varepsilon 14})}, \quad (56)$$
$$\varepsilon''_{\text{eff},\,xx}(\infty)=0.$$

Formulas (56) describe Maxwell–Wagner polarization at high frequencies.

As before, it is convenient to consider the frequency dependences when the matrix is a perfect insulator:

$$\hat{\varepsilon}_1=\varepsilon_1, \quad \sigma_1=0 \quad (\Delta_{\sigma 12}=\Delta_{\sigma 13}=\Delta_{\sigma 14}=-1). \quad (57)$$

The electrostatic parameters of such a system are derived from general expression (45) at $\omega \longrightarrow 0$ ($\Gamma_2(\omega) \longrightarrow \infty$, $\Delta_{\omega 2} \longrightarrow 0$):

$$\varepsilon'_{\text{eff},\,xx}(0)=\varepsilon_1\frac{1+\alpha(s_1+s_2+s_3)}{1-\beta(s_1+s_2+s_3)}, \quad \varepsilon''_{\text{eff},\,xx}(0)=0. \quad (58)$$

Formulas (58) can also be obtained from (55) in view of condition (57).

With $\omega \longrightarrow \infty$ ($\Gamma_2(\omega) \longrightarrow 0$, $\Delta_{\omega 2} \longrightarrow 1$), the expressions for $\varepsilon'_{\text{eff},\,xx}(\infty)$ and $\varepsilon''_{\text{eff},\,xx}(\infty)$ completely coincide with (56). Thus, at high frequencies, the system's behavior does not depend on the component conductivity.

Comparing these expressions with similar expressions obtained previously, one can note that in the limiting cases, the parameters of the four-component system qualitatively behave in the same manner as those of the three-component composite. The quantitative difference is due to the different compositions of the systems and anisotropy, which arises in the four-component hexagonal structure upon averaging its parameters.

A more significant difference between the systems results from the fact that the number of the extrema of the function $\varepsilon''_{\text{eff},\,xx}(\omega)$ grows in proportion to the number of components (the number of the extrema depends on certain relationships between local parameters of the components).

By way of example, Fig. 6 shows the frequency dependences of the effective permittivity, dielectric loss factor, and dielectric loss tangent. The diagram of the complex effective permittivity for this case is constructed in Fig. 7. The system has the following relative parameters: $s_1 = 0.1$, $s_2 = 0.15$, $s_3 = 0.2$, $\varepsilon_1 = 19$, $\varepsilon_2 = 9$, $\varepsilon_3 = 4$, $\varepsilon_4 = 2$, $\sigma_1 = 0$, $\sigma_2 = 1$, $\sigma_3 = 30$, and $\sigma_4 = 1500$ ($\Delta_{\varepsilon 12} = 0.357$, $\Delta_{\varepsilon 13} = 0.652$, $\Delta_{\varepsilon 14} = 0.810$, $\Delta_{\sigma 12} = \Delta_{\sigma 13} = \Delta_{\sigma 14} = -1$). With these parameters, the dependence $\varepsilon''_{\text{eff},\,xx}(\Delta_{\omega 2})$ has three peaks, one of which (near $\Delta_{\omega 2} \longrightarrow 1$) is not clearly seen in Fig. 6. These three peaks are well defined in the diagram of the complex permittivity (Fig. 7), which means that the complex diagram is a convenient tool for permittivity dispersion analysis. For the parameters listed above, this diagram consists of circular arcs with their centers below the abscissa axis.

The peak of the curve $\varepsilon''_{\text{eff},\,xx}(\Delta_{\omega 2})$ at $\Delta_{\omega 2} \longrightarrow 1$ ($\omega \longrightarrow 1$) is distinctly seen in Fig. 8, where the frequency dependences of the permittivity components are shown on an enlarged scale in the range $0.95 \le \Delta_{\omega 2} \le 1.0$.

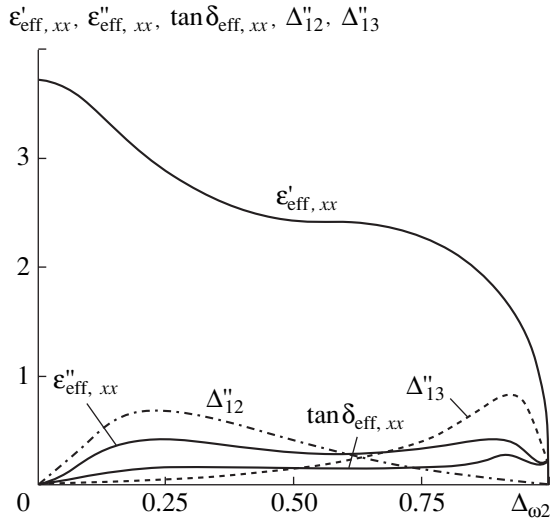

Fig. 6. The same as in Fig. 2 for $s_1 = 0.25$, $s_2 = 0.20$, $s_3 = 0.20$, $\Delta_{\varepsilon 12} = 0.5$, $\Delta_{\varepsilon 13} = 0.714$, $\Delta_{\varepsilon 14} = 0.714$, and $\Delta_{\sigma 12} = \Delta_{\sigma 13} = \Delta_{\sigma 14} = -1$.

The direct application of analytical methods to find the frequencies of the peaks of $\varepsilon''_{\text{eff},\,xx}(\Delta_{\omega 2})$ is cumbersome; therefore, as before, the frequencies of effective loss factor extrema are approximately found from the frequencies where the parameters $\Delta''_{1g}(\Delta_{\omega 2})$ ($g = 2, 3, 4$). This greatly simplifies calculations.

In order of increasing frequency (more exactly, the parameter $\Delta_{\omega 2}$), the frequencies of the first two maxima, $\Delta^{(1)}_{\omega 2}$ and $\Delta^{(2)}_{\omega 2}$, are given by formulas (31) and (32), while the third frequency is found from the expression

$$\Delta^{(3)}_{\omega 2} = \frac{1 - \Delta_{\varepsilon 14}}{1 + 2\varepsilon_4\sigma_2/\varepsilon_2\sigma_4 - \Delta_{\varepsilon 14}} = \frac{\varepsilon_2\sigma_4}{\varepsilon_2\sigma_4 + \sigma_2(\varepsilon_1 + \varepsilon_4)}. \quad (59)$$

The dependences of the parameters Δ''_{1g} ($g = 2, 3, 4$) on the relative frequency $\Delta_{\omega 2}$ are shown by the dash-and-dot and dotted lines in Figs. 6 and 8. It is seen that the frequencies $\Delta^{(j)}_{\omega 2}$ ($j = 1, 2, 3$) do specify the maxima of the function $\varepsilon''_{\text{eff},\,xx}(\Delta_{\omega 2})$ with a high accuracy (the error is about 1%). It should be noted in this respect that the maxima of $\Delta''_{1g}(\Delta_{\omega 2})$ and $\varepsilon''_{\text{eff},\,xx}(\Delta_{\omega 2})$ correlate only at low and moderate concentrations of the inclusions ($s_1 + s_2 + s_3 \le 0.5$). Under these conditions, the complex permittivity depends essentially on the complex parameters $\hat{\Delta}_{1g}(\Delta_{\omega 2})$.

To summarize, we note that complex parameters (7) are of great importance in the theory of permittivity dispersion in heterogeneous media. They depend on frequency, conductivity, and permittivity. It is convenient to analyze them in the complex plane. By eliminating the frequency parameter $\Gamma_m(\omega)$ from expressions (8), we arrive at the equation of circle in the complex plane:

$$\left[\Delta'_{1m}(\omega) - \frac{1}{2}(\Delta_{\varepsilon 1m} + \Delta_{\sigma 1m})\right]^2 + \Delta''^2_{1m}(\omega) = \frac{1}{4}(\Delta_{\varepsilon 1m} - \Delta_{\sigma 1m})^2. \quad (60)$$

The circle has a radius $|\Delta_{\varepsilon 1m} - \Delta_{\sigma 1m}|/2$ and is centered at the point $(\Delta_{\varepsilon 1m} + \Delta_{\sigma 1m})/2$ on the x axis.

For the limiting values of the frequency, $\omega \longrightarrow 0$ ($\Gamma_m(\omega) \longrightarrow \infty$) and $\omega \longrightarrow \infty$ ($\Gamma_m(\omega) \longrightarrow 0$), the real part of the complex parameter $\hat{\Delta}_{1m}(\omega)$ takes the respective values

$$\Delta'_{1m}(0) = \Delta_{\sigma 1m}, \quad \Delta'_{1m}(\infty) = \Delta_{\varepsilon 1m}; \quad (61)$$

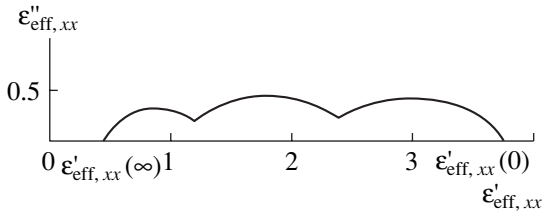

Fig. 7. Diagram of the effective complex permittivity of the four-component medium (the parameters are the same as in Fig. 6).

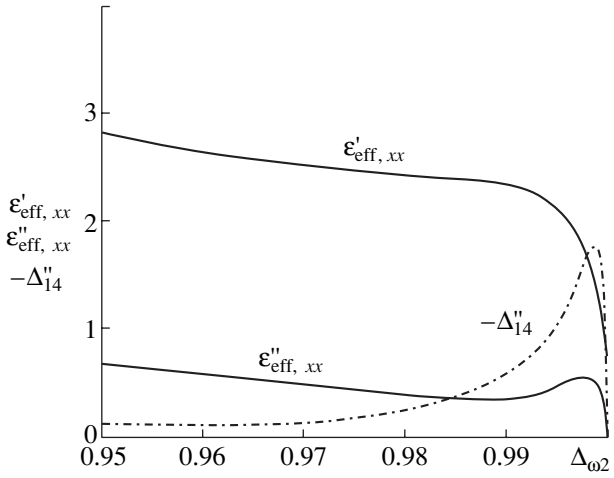

Fig. 8. Effective permittivity, effective loss factor, and the parameter $-\Delta''_{14}$ vs. relative frequency $\Delta_{\omega 2}$ at high frequencies (the parameters are the same as in Fig. 6).

therefore, relationship (60) can be represented as

$$\left[\Delta'_{1m}(\omega) - \frac{1}{2}(\Delta'_{1m}(\infty) + \Delta'_{1m}(0))\right]^2 + \Delta''^2_{1m}(\omega) = \frac{1}{4}(\Delta'_{1m}(\infty) - \Delta'_{1m}(0))^2. \quad (62)$$

Only the semicircle in the upper (at $\Delta_{\varepsilon 1m} > \Delta_{\sigma 1m}$) or lower ($\Delta_{\varepsilon 1m} < \Delta_{\sigma 1m}$) half-plane, rather than the complete circle, has a physical meaning.

CONCLUSION

Some general comments in conclusion.

If a matrix composite contains several types of dissimilar inclusions, the frequency dependences of the effective complex permittivity components become more complicated; namely, the effective loss factor may have several, rather than one, maxima. Hence, there is a set of relaxation times associated with Maxwell–Wagner polarization. The effective permittivity diagram in the complex plane is composed of successively connected circular arcs. The greatest number of

the maxima of the imaginary part of the complex effective permittivity equals the number of inclusion types.

Heterogeneous materials for which the complex diagram shows several maxima are some polymers, silica gels, and polycondensation resins (ionites). For example, AB-18 multipurpose ionite is an insulating matrix with two types of high-conductivity inclusions (grains) [4]. The complex diagram of this material exhibits two maxima, each of which corresponds to its own type of inhomogeneity.

Since calculations for multiphase media are very awkward because of the great number of relevant parameters, we analyzed matrix systems with a low concentration of inclusions. It seems, however, that this simplification cannot significantly affect the conclusions drawn in this paper about the dielectric dispersion in heterogeneous materials. For nonmatrix multicomponent systems, the situation remains unclear and calls for special investigation. This applies, in particular, to totally inhomogeneous systems with the symmetry of color mosaics or parquetry, where each color is associated with a certain property of the components. The study of the effective parameters of such systems is greatly complicated by the need to solve boundary-value problems concerned with the formation of physical fields in the structure's constituents.

REFERENCES

1. J. C. Maxwell, *A Treatise on Electricity and Magnetism*, 3rd ed. (Clarendon, Oxford, 1892; Nauka, Moscow, 1989), Vol. 1.
2. K. W. Wagner, *Die Isolierstoffe der Electrotechnik* (Springer, Berlin, 1924).
3. T. L. Chelidze, A. I. Derevyanko, and O. D. Kurilenko, *Electrospectroscopy of Heterogeneous Systems* (Naukova Dumka, Kiev, 1977).
4. Yu. V. Gorokhovatskiĭ and G. A. Bordovskiĭ, *Thermoactivation Current Spectroscopy of High-Resistance Semiconductors and Insulators* (Nauka, Moscow, 1991).
5. B. Ya. Balagurov and V. A. Kashin, Zh. Éksp. Teor. Fiz. **117**, 978 (2000) [JETP **90**, 850 (2000)].
6. Y. V. Obnosov, SIAM J. Appl. Math. **59**, 1267 (1999).
7. B. Ya. Balagurov, Zh. Éksp. Teor. Fiz. **120**, 668 (2001) [JETP **93**, 586 (2001)].
8. Y. V. Obnosov, Proc. R. Soc. London, Ser. A **452**, 2423 (1996).
9. Yu. P. Emets, Zh. Éksp. Teor. Fiz. **121**, 1339 (2002) [JETP **94**, 1149 (2002)].
10. Yu. P. Emets, *Electrical Characteristics of Composite Materials* (Naukova Dumka, Kiev, 1986).
11. J. B. Keller, J. Math. Phys. **5**, 548 (1964).
12. A. G. Fokin, Usp. Fiz. Nauk **166**, 1071 (1996) [Phys. Usp. **39**, 1009 (1996)].
13. K. S. Mendelson, J. Appl. Phys. **46**, 4740 (1975).
14. Yu. P. Emets, Zh. Éksp. Teor. Fiz. **118**, 1207 (2000) [JETP **91**, 1046 (2000)].
15. B. Ya. Balagurov, Zh. Éksp. Teor. Fiz. **119**, 142 (2001) [JETP **92**, 123 (2001)].
16. Yu. P. Emets and Yu. P. Onofrichuk, IEEE Trans. Dielectr. Electr. Insul. **3**, 87 (1996).
17. P. Debye, *Polar Molecules* (Chemical Catalogue Co., New York, 1929; GNTI, Moscow, 1931).
18. R. W. Sillars, J. Inst. Electr. Eng. **80**, 378 (1937).
19. Yu. P. Emets, Zh. Éksp. Teor. Fiz. **114**, 1121 (1998) [JETP **87**, 612 (1998)].
20. L. D. Landau and E. M. Lifshitz, *Course of Theoretical Physics*, Vol. 8: *Electrodynamics of Continuous Media* (Nauka, Moscow, 1982; Pergamon, New York, 1984).
21. Yu. P. Emets, Zh. Tekh. Fiz. **72**, 51 (2002) [Tech. Phys. **47**, 49 (2002)].

Translated by V. Isaakyan

Technical Physics, Vol. 48, No. 3, 2003, pp. 329–333. Translated from Zhurnal Tekhnicheskoĭ Fiziki, Vol. 73, No. 3, 2003, pp. 54–58.

SOLIDS

Martensite-Induced Stress Relaxation and Deformation Effects in Membranes Made of Shape Memory Materials

G. A. Malygin

Ioffe Physicotechnical Institute, Russian Academy of Sciences, Politekhnicheskaya ul. 26, St. Petersburg, 194021 Russia

e-mail: malygin.ga@mail.ioffe.ru

Received September 9, 2002

Abstract—The theory of diffuse martensitic transitions is used to analyze martensitic transformation and stress relaxation in a planar round membrane made of a shape memory material under a constant pressure. The plastic flexure of the membrane is found as a function of the temperature and applied pressure. © *2003 MAIK "Nauka/Interperiodica".*

INTRODUCTION

Metallic shape memory alloys (SMAs) have unique deformation properties; namely, they can undergo reversible plastic deformation and recover their initial (prior to deformation) shape [1–3]. Owing to these properties, they are applied in orthopedic medicine [4] and various devices [5]. Recently, SMAs have become considered as candidates for active elements in microsensors and microactuators [6–9], e.g., in microelectromechanical systems (MEMSs) [10].

The intriguing properties of shape memory materials are caused by structural martensitic transformations, which are sensitive to temperature and mechanical stresses. To evaluate the functional characteristics of devices and elements made of shape memory materials, it is necessary to know the relationship between the material strain and applied stress at various temperatures. This relationship can be obtained empirically or by using a relevant theory of structural martensitic transformation. Since these transformations are first-order phase transitions, for which a complete theory has yet to be developed, the performance of devices with the shape memory effect is usually evaluated based on semi-empirical models [11].

In this work, we calculate martensite-induced stress relaxation and reversible plastic strain (flexure) in shape memory membranes under a constant pressure in terms of the recently developed phenomenological theory of diffuse martensitic transitions in such materials [12–14]. This theory considers martensitic transformation in terms of thermodynamics, namely, as a sequence of phase equilibria depending on temperature and applied mechanical stress. Such an approach makes it possible to find the volume fraction of martensite and the plastic strain as a function of temperature and stress over the whole range, including the case of nonuniform stress distribution in the material. Using the theory of diffuse martensitic transformations, we analyze the plastic flexure of the membrane as a function of its radius, temperature, and pressure.

ELASTIC FLEXURE OF A MEMBRANE

Consider a round membrane of thickness h and radius $R \gg h$ that is circumferentially clamped. The equation for the angle of rotation ω_e of its plane sections upon elastic bending under a constant pressure P has the form [15, 16]

$$\frac{d}{dr}\left[\frac{1}{r}\frac{d}{dr}(\omega_e r)\right] = -\frac{r}{2D}P, \quad D = \frac{Eh^3}{12(1-\nu^2)}, \qquad (1)$$

where r is the distance from the center of the membrane, E is the modulus of elasticity, and ν is Poisson's ratio.

Integrating Eq. (1) twice, we find the dependence of the angle of rotation on the radius:

$$\omega_e(r) = C_1 r + C_2 r^{-1} - \frac{r^3}{16D}P = \frac{P}{16D}r(R^2 - r^2). \qquad (2)$$

Here, $C_1 = PR^2/16D$ and $C_2 = 0$ are constants of integration that are determined from the conditions $\omega_e(0) = \omega_e(R) = 0$. Since $\omega_e = dw_e/dr$, the elastic flexure of the membrane is

$$w_e(r) = C_3 + \int \omega_e dr = -\frac{P}{64D}(R^2 - r^2)^2. \qquad (3)$$

The constant of integration $C_3 = -PR^4/64D$ is found from the condition $w_e(R) = 0$.

1063-7842/03/4803-0329$24.00

Taking into account the expressions for the radial and tangential strains in the membrane,

$$\varepsilon_r = (d\omega_e/dr)z = -\frac{3(1-\nu^2)P}{4E}\left(\frac{R}{h}\right)^2\left[1-3\frac{r^2}{R^2}\right]\frac{z}{h},$$
$$\varepsilon_t = (\omega_e/r)z = -\frac{3(1-\nu^2)P}{4E}\left(\frac{R}{h}\right)^2\left[1-\frac{r^2}{R^2}\right]\frac{z}{h}, \quad (4)$$

where z is the distance from the neutral plane of the membrane, we obtain the corresponding stress distributions [16]

$$\sigma_r = \frac{E}{1-\nu^2}(\varepsilon_r + \nu\varepsilon_t)$$
$$= -\frac{3}{4}P\left(\frac{R}{h}\right)^2\left[1+\nu-(3+\nu)\frac{r^2}{R^2}\right]\frac{z}{h},$$
$$\sigma_t = \frac{E}{1-\nu^2}(\varepsilon_t + \nu\varepsilon_r) \quad (5)$$
$$= -\frac{3}{4}P\left(\frac{R}{h}\right)^2\left[1+\nu-(1+3\nu)\frac{r^2}{R^2}\right]\frac{z}{h}.$$

Figure 1a shows the distributions of the radial (curve *1*) and tangential (curve *2*) stresses in the lower surface layer of the membrane ($z = -h/2$) in the $\sigma_r/E_* - r/R$ coordinates at $h/R = 0.1$, $P/E_* = 10^{-2}$, and $\nu = 0.3$, where $E_* = (h/R)^2E$ is the effective modulus of elasticity of the membrane. Since pressure is applied along the negative z direction, the central part of the lower surface is extended and the peripheral part is compressed. Equations (1)–(5) are derived based on the hypotheses of plane sections and bending strain dominance, which imply that the flexure of the membrane must be significantly smaller than its thickness, $w_e(R) \ll h$. This condition specifies the range of applied pressures: $P \ll (16/3)(h/R)^2E_*$. At $h/R = 0.1$, we have $P/E_* \ll 5 \times 10^{-2}$ or $P/E \ll 5 \times 10^{-4}$.

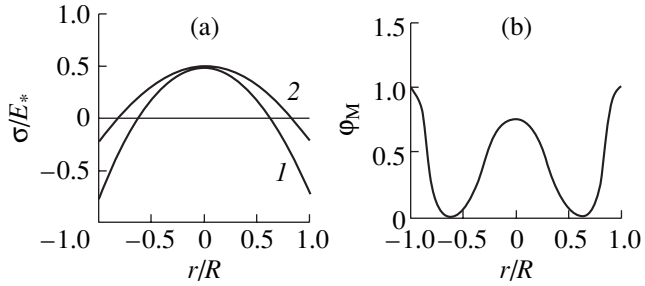

Fig. 1. (a) Distributions of (*1*) radial and (*2*) tangential bending stresses and (b) martensite distribution in the lower surface layer of the loaded membrane.

MARTENSITE-INDUCED STRESS RELAXATION IN THE MEMBRANE

For the membrane made of a shape memory alloy, the applied pressure P in the temperature range of martensitic transformation leads to elastic stress relaxation and causes a plastic strain, i.e., an additional (but reversible) plastic flexure. The problem is to find the variation of this flexure with the membrane radius. To this end, it is necessary to know the relation between the plastic strain of the membrane and the applied stress (pressure).

According to the theory of diffuse martensitic transitions [12–14], this relation follows from the law of phase equilibrium

$$\varphi_M(T, \tau) = \left[1 + \exp\left(\frac{\Delta U}{kT}\right)\right]^{-1}. \quad (6)$$

Here, φ_M is the volume fraction of martensite in the material that undergoes martensitic transformation; $\Delta U = \omega\Delta u$ is the change in the internal energy of the material when its elementary volume ω passes from the austenitic to martensitic state; k is the Boltzmann constant; and

$$\Delta u = q\frac{T - T_c}{T_c} - \xi_{ik}\tau_{ik} \quad (7)$$

is the change in the internal energy of the elementary volume of the membrane material due to this transformation, where q is the heat of transformation, T is temperature, T_c is the critical (characteristic) temperature of martensitic transformation in the absence of mechanical stress τ_{ik}; and ξ_{ik} are the spontaneous shear strains of the lattice that appear during its reconstruction. Assuming that plastic (martensitic) stress relaxation in the membrane is specified by the maximum shear stresses $\tau = (\sigma_1 - \sigma_3)/2$, where $\sigma_1 = \sigma_r$, $\sigma_2 = \sigma_t$, and $\sigma_3 = \sigma_z = 0$ are principal stresses, we obtain the martensite distribution in the membrane (for one dominating type of martensite $\xi_{ik} \equiv \xi$)

$$\varphi_M(r, z, P, T)$$
$$= \left\{1 + \exp\left[B\left(\frac{T - T_c}{T_c} - \frac{m\xi|\sigma_r(r, z, P)|}{2q}\right)\right]\right\}^{-1}, \quad (8)$$

where $B = \omega q/kT \approx \omega q/kT_c$ and m is the orientation factor, which depends on the angle the plane and direction of the shear ξ make with the normal to the plane of the stress σ_r. In Eq. (8), we took into account expressions (5)–(7).

For further calculation, it is convenient to recast (8) in dimensionless variables:

$$\varphi_M(\bar{r}, \bar{z}, p, t) = \{1 + \exp[B(t - 1 - ma|S_r(\bar{r}, \bar{z}, p)|)]\}^{-1},$$

$$\bar{r} = \frac{r}{R}, \quad \bar{z} = \frac{z}{h}, \quad p = \frac{P}{E_*}, \quad t = \frac{T}{T_c}, \quad a = \frac{\xi E_*}{2q}, \quad (9)$$

$$\frac{\sigma_r}{E_*} = S_r(\bar{r}, \bar{z}, p) = -\frac{3}{4}p\left(\frac{R}{h}\right)^2[1 + \nu - (3 + \nu)\bar{r}^2]z.$$

Figure 1b shows the radial distribution of martensite in the surface layer of the membrane ($z/h = -0.5$) according to (9) ($B = 50$, $a = 1$, $m = 0.5$, $t = 1.1$, $p = 10^{-2}$, and $h/R = 0.1$). The corresponding distribution of radial stresses is given in Fig. 1a. Martensite is seen to form at sites of maximum stresses at the center of the membrane and at its periphery, where it is clamped. Figures 2a and 2b show the martensite distribution in the radial section of the membrane at the given parameters and two temperatures ($T = 1.1T_c$ and $1.05T_c$). Contours *1* and *2* in these figures correspond to the martensite volume fractions $\varphi_M = 0.67$ and 0.33. Obviously, a decrease in the temperature and an increase in the pressure raise the martensite volume fraction.

PLASTIC FLEXURE OF THE MEMBRANE

The local plastic strain of the membrane related to the formation of martensite is given by

$$\varepsilon_r^m(r, z, P, T) = [m\xi\varphi_M(r, z, P, T, m) - m\xi\varphi_M(r, z, P, T, -m)]\,\mathrm{sgn}(\sigma_r). \quad (10)$$

Formula (10) takes into account the fact that the membrane does not have plastic strain in the absence of stress (pressure) despite the formation of martensite in it, since martensite is in a twinned state. According to (10), the applied stress leads to detwining the martensite; i.e., the fraction of martensite with orientation m grows and the martensite phase with orientation $-m$ eventually disappears. As a result, a plastic strain appears in the membrane in addition to its elastic strain.

Curve *1* in Fig. 3 shows the dependence of the elastic strain ε_r^e on the radius r in the membrane surface layer ($z = -h/2$) according to (4) at the parameters given above. Curves *2–4* illustrate the distributions of plastic strains in the surface layer according to (10) at various temperatures and $\xi = 0.1$. The plastic strains are maximal at the sites where radial stresses are maximal, namely, at the center of the membrane and at its periphery. As follows from (10), the plastic strain of the membrane is limited by the value $m\xi = 0.05$. Figure 3 shows that this limiting value is reached at these sites at a pressure $P = 10^{-2}E_*$ and temperature $T = 1.05T_c$ and significantly exceeds the elastic strain of the membrane there.

To find the plastic flexure of the entire membrane, we will average the radial strains over the membrane thickness. Using the notation in (9) and integrating, we find

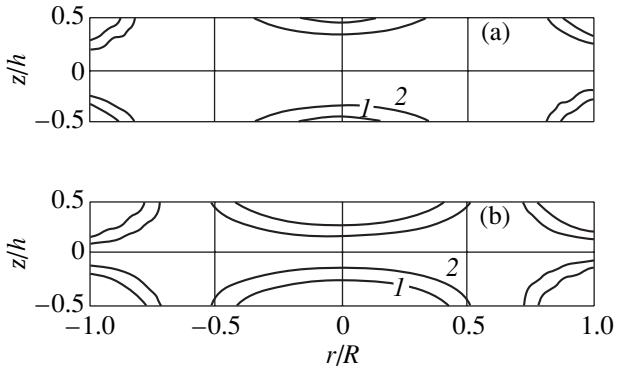

Fig. 2. Martensite distribution in the radial section of the membrane for $T = 1.1T_c$ (a) and $1.05T_c$ (b) at $P = 10^{-2}E_*$. The section is shown for the ratio $h/R = 0.2$.

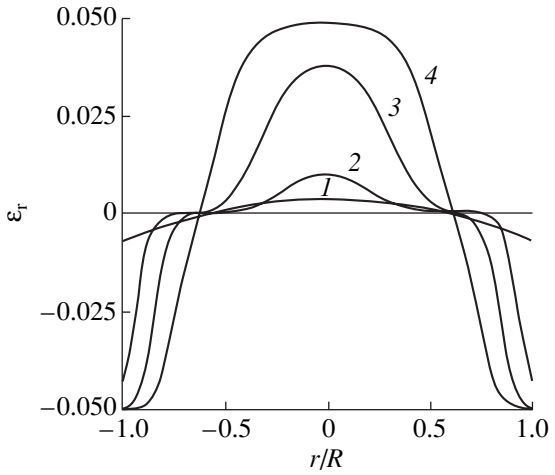

Fig. 3. Dependences of the (*1*) elastic and (*2–4*) plastic radial strains in the lower surface layer of the membrane on the radius at $T = 1.1T_c$ (*2*), $1.05T_c$ (*3*), and T_c (*4*).

$$\varepsilon_r^m(\bar{r}, p, t) = 2\int_0^{1/2}\varepsilon_r^m(\bar{r}, \bar{z}, p, t)d\bar{z} = \frac{2\xi}{aB|S_r(\bar{r}, p)|} \times \ln\left[1 + \left(\frac{\sinh(maB|S_r(\bar{r}, p)|/4)}{\cosh(B(t-1)/2)}\right)^2\right]\mathrm{sgn}(\sigma_r). \quad (11)$$

Then, using the relationship between the rotation of the membrane sections and the radial strains, $\xi_r^m(\bar{r}, p, t) = (h/2)d\omega_m/dr$, we arrive at the dependence of the angle of plastic rotation ω_m on the membrane radius:

$$\omega_m(\bar{r}, p, t) = \frac{R}{h}\int_0^{\bar{r}}\varepsilon_r^m(\bar{r}, p, t)d\bar{r}. \quad (12)$$

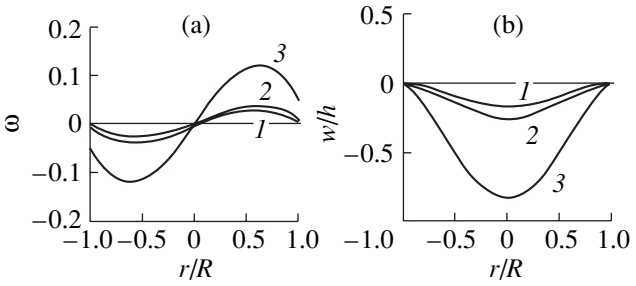

Fig. 4. Dependences of the (*1*) elastic and (*2*, *3*) plastic (a) rotations of sections and (b) membrane flexures at $T = 1.1T_c$ (*2*) and $1.05T_c$ (*3*).

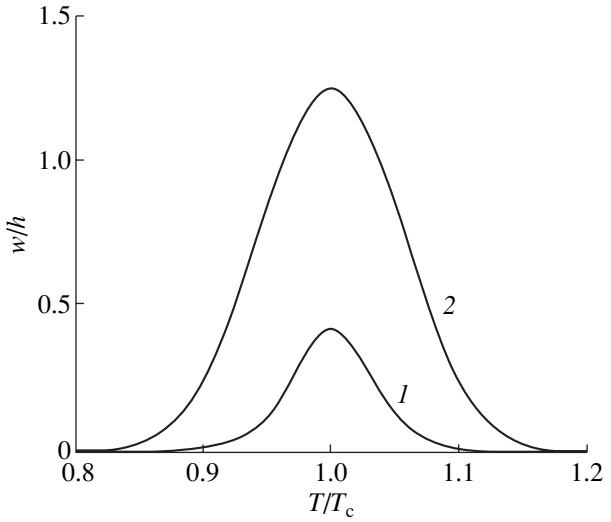

Fig. 5. Temperature dependences of the plastic flexures of the membrane at $P = 10^{-3}E_*$ (*1*) and $10^{-2}E_*$ (*2*).

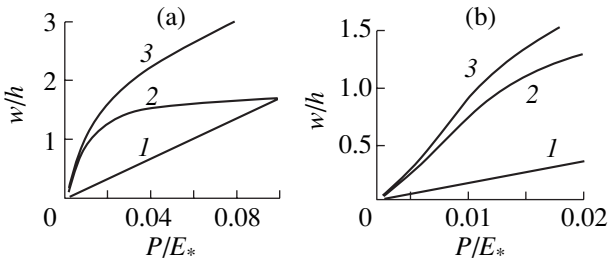

Fig. 6. (a) Pressure dependences of the (*1*) elastic, (*2*) plastic, and (*3*) total flexures of the membrane for $T = 1.05T_c$. (b) The initial segments of curves (*1–3*).

Expression (12) uses the boundary condition $\omega_m = 0$ at $r = 0$. Figure 4a illustrates the dependences $\omega_m(\bar{r})$ for two temperatures ($T = 1.1T_c$ and $1.05T_c$) at a pressure $P = 10^{-2}E_*$. Curve *1* demonstrates the dependence of the angle of elastic rotation on the radius $\omega_e(\bar{r})$ (see (2)) at the given pressure. Unlike the elastic rotation, the plastic rotation at the periphery of the membrane is nonzero, since a plastic hinge forms at the edges owing to the martensitic transformation.

Since $\omega_m = dw_m/dr$, the dependence of the plastic flexure of the membrane w_m on its radius is given by

$$\bar{w}_m(\bar{r}, p, t) = \frac{w_m(\bar{r}, p, t)}{h} = \frac{R}{h}\int_0^{\bar{r}} \omega_m(\bar{r}, p, t)d\bar{r}. \quad (13)$$

Here, it is taken into account that $w_m = 0$ at the periphery. Figure 4b shows the dependences $\omega_m(r)$ corresponding to the radial dependences of the angles of plastic rotation in Fig. 4a. For comparison we also show the radial dependence of the elastic flexure described by Eq. (3) (curve *1*).

The formation of the plastic hinge at the membrane circumference significantly (several times) increases the flexure of the central part in comparison with the elastic flexure at the periphery. Therefore, it is of interest to compare the maximum plastic flexure of the center of the membrane $w_m^{max} = \bar{w}(0, p, t)h$ with its maximum elastic flexure when the edges of the membrane are mounted on a hinged support. Calculation [15] shows that the elastic flexure of the hinged membrane is greater than the maximum elastic flexure of the clamped membrane, w_e^{max}, by a factor of $(5 + \nu)/(1 + \nu) \approx 4$. This figure is comparable with the flexure ratios $w_m^{max}/w_e^{max} = 1.5$ and 4.9 in Fig. 4b. It was shown that more than half the material of the membrane passes to the martensitic state at $T = T_c$ and $P = 10^{-2}E_*$. Under these conditions, $w_m^{max}/w_e^{max} = 7.4$.

STRAIN CHARACTERISTICS OF THE MEMBRANE

The membrane plastic flexure depends not only on the applied stress but also on the temperature. Figure 5 shows the temperature dependences of the relative plastic flexure w_m^{max}/h described by (13) at pressures $P = 2 \times 10^{-3}E_*$ (curve *1*) and $10^{-2}E_*$ (curve *2*). The flexure is maximum at the critical temperature T_c and approaches zero as the material turns into a purely martensitic or purely austenitic state.

Figure 6a illustrates the pressure dependences of the maximum elastic (curve *1*) and plastic (curve *2*), as well as of the total (curve *3*), flexures of the membrane at $1.05T_c$. The initial (low-pressure) segments of the curves are shown in Fig. 6b. As follows from Fig. 6a, the plastic flexure tends toward saturation at pressures over $0.03E_*$ and then becomes pressure-independent. The computed results given in Fig. 6b evidence that, at near-critical temperatures, the plastic flexure exceeds the elastic flexure at indefinitely small pressures.

Another specific feature of plastic flexure is its nonlinear pressure dependence and a large value at a rela-

tively small pressure. Figures 4b, 5, and 6 indicate that the plastic flexures at near-critical temperatures become comparable to the membrane thickness. At such flexures, radial tensile stresses, which depend on the membrane flexure, appear along with bending stresses [15–17]. This circumstance significantly (nonlinearly) affects the pressure dependence of the elastic flexures of the membrane and requires special calculation. This remark is also true for large plastic flexures of shape memory membranes.

Thus, the theory of diffuse martensitic transitions allows one to completely calculate the strain characteristics of a shape memory membrane and find their temperature and pressure dependences.

REFERENCES

1. K. Shimizu and K. Otsuka, *Shape Memory Effects in Alloys* (Translated from Japanese) (Nauka, Moscow, 1979).
2. V. A. Likhachev, S. L. Kuzmin, and Z. P. Kamentseva, *Memory Shape Effect* (Leningr. Gos. Univ., Leningrad, 1987).
3. V. G. Pushin, V. V. Kondrat'ev, and V. N. Khachin, *Titanium Nickelide* (Nauka, Moscow, 1992).
4. *Shape Memory Effects in Medicine*, Ed. by V. R. Gyunter (Nauka, Novosibirsk, 1992).
5. *Shape Memory Alloys*, Ed. by H. Funakabo (Gordon and Breach, New York, 1984), Vols. 1, 2.
6. *Materials for Smart Systems II*, Ed. by E. P. George, R. Gotthardt, K. Otsuka, *et al.* (MRS, Pittsburgh, 1997), Vol. 459.
7. A. L. Roytburd, T. A. Kim, Q. Su, *et al.*, Acta Mater. **46**, 5095 (2000).
8. G. A. Malygin, Fiz. Tverd. Tela (St. Petersburg) **43**, 1286 (2001) [Phys. Solid State **43**, 1339 (2001)].
9. G. A. Malygin, Zh. Tekh. Fiz. **71** (9), 33 (2001) [Tech. Phys. **46**, 1101 (2001)].
10. S. M. Spearing, Acta Mater. **48**, 179 (2000).
11. A. E. Volkov, M. E. Evard, L. N. Kurzeneva, *et al.*, Zh. Tekh. Fiz. **71** (9), 3 (1996) [Tech. Phys. **41**, 1084 (1996)].
12. G. A. Malygin, Fiz. Tverd. Tela (St. Petersburg) **36**, 1489 (1994) [Phys. Solid State **36**, 815 (1994)].
13. G. A. Malygin, Zh. Tekh. Fiz. **71** (9), 112 (1996) [Tech. Phys. **41**, 1145 (1996)].
14. G. A. Malygin, Usp. Fiz. Nauk **171** (2), 187 (2001) [Phys. Usp. **44**, 173 (2001)].
15. V. I. Fedoseev, *Resistance of Materials* (Nauka, Moscow, 1972).
16. L. E. Andreeva, *Elastic Elements of Devices* (Mashinostroenie, Moscow, 1981).
17. A. S. Vol'mir, *Stability of Deformable Systems* (Nauka, Moscow, 1967).

Translated by K. Shakhlevich

Technical Physics, Vol. 48, No. 3, 2003, pp. 334–343. Translated from Zhurnal Tekhnicheskoĭ Fiziki, Vol. 73, No. 3, 2003, pp. 59–68.

OPTICS, QUANTUM ELECTRONICS

Kinetic Mechanisms of Initiating Hydrogen–Oxygen Mixture Combustion through the Excitation of Electronic Degrees of Freedom of Molecular Oxygen by Laser Radiation

A. M. Starik and N. S. Titova

Baranov Central Institute of Aviation Motors, Moscow, 111116 Russia

e-mail: star@ciam.ru

Received July 2, 2002

Abstract—Kinetic mechanisms resulting in the enhancement of combustion of $H_2 + O_2$ mixtures when O_2 molecules are excited to the $a^1\Delta_g$ and $b^1\Sigma_g^+$ states with laser radiation (λ = 1.268 and 0.762 μm) are analyzed. It is shown that the excitation of O_2 molecules by the laser radiation leads to the appearance of new O, H, and OH formation channels; promotes the ignition of the starting mixture; and reduces the self-ignition temperature. With initial pressures in the range $P_0 = 10^3$–10^4 Pa, the self-ignition temperature can be reduced to 300 K even at relatively low energies of the laser radiation with λ = 0.762 μm. *© 2003 MAIK "Nauka/Interperiodica".*

INTRODUCTION

The intensification of combustion of reactive gas mixtures by initiating plasma-chemical reactions involving excited atoms and molecules has long been discussed in the literature [1–5]. In particular, it has been shown that the pre-excitation of the initial molecular reagents accelerates the formation of reactive radicals and lowers the self-ignition threshold, thereby facilitating combustion [5, 6].

This is generally associated with the reduction of the barrier for endoergic reactions with the participation of vibrationally excited molecules. The excitation of the electronic degrees of freedom of reacting molecules must cause a further reduction of the barrier, because electron states have a much higher energy than vibrational states. However, detailed information on mechanisms initiating combustion when the electronic states of reagents are excited is lacking. This is primarily due to the absence of adequate kinetic models that describe processes in reactive mixtures with the participation of electronically excited molecules.

$H_2 + O_2$ mixtures, where O_2 molecules can be excited to the $a^1\Delta_g$ and $b^1\Sigma_g^+$ states, are the simplest to analyze theoretically. This excitation can be accomplished with either an electrical discharge [7] or resonant laser radiation [8]. Recent analysis [9] has shown that even a small fraction (≈1%) of electronically excited O_2 molecules $O_2(a^1\Delta_g)$ present in the mixture may substantially intensify the chain mechanism of combustion and cause the self-ignition of a $H_2 + O_2$ mixture even at an initial temperature $T_0 \approx 400$ K. $O_2(b^1\Sigma_g^+)$ molecules should overcome endoergic reaction barriers more easily than $O_2(a^1\Delta_g)$. Moreover, $O_2(b^1\Sigma_g^+)$ molecules are much easier to produce than $O_2(a^1\Delta_g)$ when molecular oxygen is excited by laser radiation.

In this work, we analyze the self-ignition dynamics of an $H_2 + O_2$ mixture when O_2 molecules are excited into the $a^1\Delta_g$ and $b^1\Sigma_g^+$ states by laser radiation.

KINETIC MODEL

The elaboration of a kinetic scheme that allows one to correctly describe the basic characteristics of combustion and analyze ignition mechanisms is the most important and, at the same time, most complex stage in treating elementary events in reactive systems. We will consider a stirred $H_2 + O_2$ mixture placed in an adiabatic reactor where $O_2(a^1\Delta_g)$ and $O_2(b^1\Sigma_g^+)$ excited molecules may be present. It is assumed that translational, rotational, and vibrational degrees of freedom are in thermodynamic equilibrium, which does not break during chemical reactions.

It is known that the ignition of a simple $H_2 + O_2$ mixture in a wide range of initial temperatures and pressures is described by a branched kinetic scheme involving 29 reactions with the participation of H, O, OH, H_2O, H_2, O_2, HO_2, H_2O_2, and O_3 even if electronically excited O_2 molecules are absent. The reactions and associated reaction rates are given in [9, 10]. The presence of excited $O_2(a^1\Delta_g)$ and $O_2(b^1\Sigma_g^+)$ molecules in the reactive mixture necessitates the introduction of additional reaction channels not only for these molecules but also for $O(^1D)$ atoms that are generated by reactions

1063-7842/03/4803-0334$24.00

involving $O_2(a^1\Delta_g)$ and $O_2(b^1\Sigma_g^+)$ [8]. Reactions included in the kinetic scheme are listed in the table.

The excitation of vibrational and electronic degrees of freedom of reacting molecules increases the reaction cross section and lowers the barrier for endoergic reactions [11]. The rate constant for an endoergic reaction is represented in the usual form

$$k_{\text{ex},\,q} = A_q T_n^{n_q} \exp\left(-\frac{E_{aq}^e}{T}\right), \qquad (1)$$

where E_{aq}^e is the energy of activation of a qth exchange reaction involving an excited molecule. Figure 1 shows the energy diagram of an exothermal exchange reaction $AB + C = A + BC$ for the cases when the AB molecule is in a ground electronic state and in excited state e (the latter will be hereafter designated as $AB(e)$). Here, ΔH is the thermal effect of the reaction and E_a^0 is the energy of activation of the reaction when the AB molecule is not excited. According to [11], the potential energy surfaces for the forward and backward reactions when the AB molecule is unexcited are given by

$$U_1(r) = \Delta H + E_a^0 \exp(r/r_1),$$

$$U_2(r) = (\Delta H + E_a^0)\exp(-r/r_2).$$

The potential energy surface for the forward reaction with the AB molecule excited to state e with an energy E_e is expressed as

$$U_1^e = \Delta H + E_e + E_a^0 \exp(r/r_1),$$

where r_1 and r_2 are the exchange force ranges for the reagents and reaction products, respectively. For many reactions, $r_1 \approx r_2$ [11]. In this case, at the point of intersection of the potential surfaces U_1^e and U_2, we have

$$E_a^0 t^2 + (\Delta H + E_e)t - (\Delta H + E_a^0) = 0,$$

where $t = \exp(r/r_1)$.

Then, the energy of E_a^e is given by

$$E_a^e = \frac{1}{2}\left(\sqrt{(\Delta H + E_e)^2 + 4E_a^0(\Delta H + E_a^0)} - (\Delta H + E_e)\right). \qquad (2)$$

From relationships (1) and (2), we calculated the rate constants for forward reactions 4, 5, 16, 17, 27, 28, 32, 33, 46, and 47 (see table) and backward reactions 41, 42, 52, 53, 55, and 56.

For barrier-free and low-barrier ($E_a^0 \approx 0$) reactions, which produce O_2 in various electronic states ($X^3\Sigma_g^-$, $a^1\Delta_g$, and $b^1\Sigma_g^+$) according to [12], it was assumed that the probability of producing $O_2(X^3\Sigma_g^-)$, $O_2(a^1\Delta_g)$, and $O_2(b^1\Sigma_g^+)$ is proportional to the degeneracy multiplicity of these states $q_X = 0.5$, $q_a = 0.33$, and $q_b = 0.17$. The channels of the associated reactions are numbered 18–20, 34–36, 61–63, and 65–67. The rate constants of the overall processes are taken to be the same as in [13].

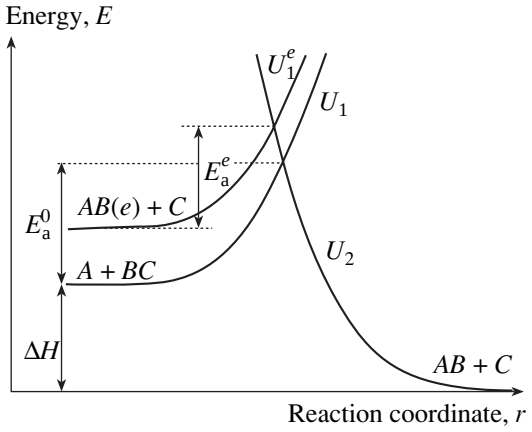

Fig. 1. Energy diagram of an exothermal exchange reaction $AB + C = A + BC$ with the participation of an unexcited molecule AB and excited molecule $AB(e)$.

The rate constants for chain reactions 10 and 22, which involve $O_2(a^1\Delta_g)$, were taken from [14], and the rate constants for similar reactions with the participation of $O_2(b^1\Sigma_g^+)$ (reactions 11 and 23) were calculated by formulas (1) and (2). Here, it was assumed that in (2) the thermal effect ΔH and the energy of activation E_a^0 correspond to reactions 10 and 22, while $E_e = \Delta E_{ba}$, where ΔE_{ba} is the difference between the energies of the states $b^1\Sigma_g^+$ and $a^1\Delta_g$ of an O_2 molecule with a zero vibrational quantum number ($E_{ba} = 7593$ K).

The rate constants of reactions that involve excited atoms $O(^1D)$ (reactions 8, 13, 25, 57–60, 73–76) were taken according to recommendations in [8, 12, 15] and those of electronic–electronic (E–E) exchange and electronic–translational (E–T) relaxation (reactions 70–72) were taken from [16]. The rate constants of forward reactions 34–36, 41, 42, 52, 53, 55, and 56 and of backward reactions 4, 5, 8, 11, 13, 16, 17, 23, 25, 27, 28, 32, 33, 46, 47, 49, 50, 57–60, and 62–76 were found by the detailed balance principle.

STATEMENT OF THE PROBLEM AND BASIC EQUATIONS

Let us consider a stationary homogeneous $H_2 + O_2$ gas mixture exposed to a laser pulse with a duration τ_p and frequency that is in resonance with the frequency of the center of the $m(e', v', j', K') \longrightarrow n(e'', v'', j'', K'')$ electronic–vibrational transition, where $e' = X^3\Sigma_g^-$; $e'' = a^1\Delta_g$ or $b^1\Sigma_g^+$; v' and v'' are the vibrational quantum numbers; and j', K' and j'', K'' are the rotational quantum

Reactions involved in the kinetic scheme

No.	Reaction	No.	Reaction
1	$H_2O + M = OH + H + M$	32	$OH + O_2(a^1\Delta_g) = O(^3P) + HO_2$
2	$H_2 + M = 2H + M$	33	$OH + O_2(b^1\Sigma_g^+) = O(^3P) + HO_2$
3	$O_2(X^3\Sigma_g^-) + M = O(^3P) + O(^3P) + M$	34	$OH + O_2(X^3\Sigma_g^-) = O(^1D) + HO_2$
4	$O_2(a^1\Delta_g) + M = O(^3P) + O(^3P) + M$	35	$OH + O_2(a^1\Delta_g) = O(^1D) + HO_2$
5	$O_2(b^1\Sigma_g^+) + M = O(^3P) + O(^3P) + M$	36	$OH + O_2(b^1\Sigma_g^+) = O(^1D) + HO_2$
6	$OH + M = O(^3P) + H + M$	37	$H_2O_2 + M = 2OH + M$
7	$H_2 + O(^3P) = OH + H$	38	$H + H_2O_2 = H_2 + HO_2$
8	$H_2 + O(^1D) = OH + H$	39	$H + H_2O_2 = H_2O + OH$
9	$O_2(X^3\Sigma_g^-) + H = OH + O(^3P)$	40	$2HO_2 = H_2O_2 + O_2(X^3\Sigma_g^-)$
10	$O_2(a^1\Delta_g) + H = OH + O(^3P)$	41	$2HO_2 = H_2O_2 + O_2(a^1\Delta_g)$
11	$O_2(b^1\Sigma_g^+) + H = OH + O(^3P)$	42	$2HO_2 = H_2O_2 + O_2(b^1\Sigma_g^+)$
12	$H_2O + O(^3P) = 2OH$	43	$HO_2 + H_2O = H_2O_2 + OH$
13	$H_2O + O(^1D) = 2OH$	44	$OH + HO_2 = H_2O_2 + O(^3P)$
14	$H_2O + H = OH + H_2$	45	$H_2O + O_2(X^3\Sigma_g^-) = H_2O_2 + O(^3P)$
15	$H_2 + O_2(X^3\Sigma_g^-) = 2OH$	46	$H_2O + O_2(a^1\Delta_g) = H_2O_2 + O(^3P)$
16	$H_2 + O_2(a^1\Delta_g) = 2OH$	47	$H_2O + O_2(b^1\Sigma_g^+) = H_2O_2 + O(^3P)$
17	$H_2 + O_2(b^1\Sigma_g^+) = 2OH$	48	$O_3 + M = O(^3P) + O_2(X^3\Sigma_g^-) + M$
18	$HO_2 + M = O_2(X^3\Sigma_g^-) + H + M$	49	$O_3 + M = O(^3P) + O_2(a^1\Delta_g) + M$
19	$HO_2 + M = O_2(a^1\Delta_g) + H + M$	50	$O_3 + M = O(^3P) + O_2(b^1\Sigma_g^+) + M$
20	$HO_2 + M = O_2(b^1\Sigma_g^+) + H + M$	51	$O_3 + H = OH + O_2(X^3\Sigma_g^-)$
21	$H_2 + O_2(X^3\Sigma_g^-) = H + HO_2$	52	$O_3 + H = OH + O_2(a^1\Delta_g)$
22	$H_2 + O_2(a^1\Delta_g) = H + HO_2$	53	$O_3 + H = OH + O_2(b^1\Sigma_g^+)$
23	$H_2 + O_2(b^1\Sigma_g^+) = H + HO_2$	54	$O_3 + O(^3P) = 2O_2(X^3\Sigma_g^-)$
24	$H_2O + O(^3P) = H + HO_2$	55	$O_3 + O(^3P) = O_2(X^3\Sigma_g^-) + O_2(a^1\Delta_g)$
25	$H_2O + O(^1D) = H_2 + O_2(X^3\Sigma_g^-)$	56	$O_3 + O(^3P) = O_2(X^3\Sigma_g^-) + O_2(b^1\Sigma_g^+)$
26	$H_2O + O_2(X^3\Sigma_g^-) = OH + HO_2$	57	$O_3 + O(^1D) = 2O_2(X^3\Sigma_g^-)$
27	$H_2O + O_2(a^1\Delta_g) = OH + HO_2$	58	$O_3 + O(^1D) = O_2(X^3\Sigma_g^-) + O_2(a^1\Delta_g)$
28	$H_2O + O_2(b^1\Sigma_g^+) = OH + HO_2$	59	$O_3 + O(^1D) = O_2(X^3\Sigma_g^-) + O_2(b^1\Sigma_g^+)$
29	$H_2O + OH = H_2 + HO_2$	60	$O_3 + O(^1D) = O_2(X^3\Sigma_g^-) + O(^3P) + O(^3P)$
30	$2OH = H + HO_2$	61	$O_3 + OH = HO_2 + O_2(X^3\Sigma_g^-)$
31	$OH + O_2(X^3\Sigma_g^-) = O(^3P) + HO_2$	62	$O_3 + OH = HO_2 + O_2(a^1\Delta_g)$

Table. (Contd.)

No.	Reaction	No.	Reaction
63	$O_3 + OH = HO_2 + O_2(b^1\Sigma_g^+)$	70	$2O_2(a^1\Delta_g) = O_2(b^1\Sigma_g^+) + O_2(X^3\Sigma_g^-)$
64	$O_3 + H_2 = OH + HO_2$	71	$O_2(a^1\Delta_g) + M = O_2(X^3\Sigma_g^-) + M$
65	$O_3 + HO_2 = OH + 2O_2(X^3\Sigma_g^-)$	72	$O_2(b^1\Delta_g) + M = O_2(a^1\Delta_g) + M$
66	$O_3 + HO_2 = OH + O_2(X^3\Sigma_g^-) + O_2(a^1\Delta_g)$	73	$O(^1D) + O_2(X^3\Sigma_g^-) = O(^3P) + O_2(a^1\Delta_g)$
67	$O_3 + HO_2 = OH + O_2(X^3\Sigma_g^-) + O_2(b^1\Sigma_g^+)$	74	$O(^1D) + O_2(X^3\Sigma_g^-) = O(^3P) + O_2(b^1\Sigma_g^+)$
68	$O_3 + O_2(a^1\Delta_g) = 2O_2(X^3\Sigma_g^-) + O(^3P)$	75	$O(^1D) + O_2(a^1\Delta_g) = O(^3P) + O_2(b^1\Sigma_g^+)$
69	$O_3 + O_2(b^1\Sigma_g^+) = 2O_2(X^3\Sigma_g^-) + O(^3P)$	76	$O(^1D) + M = O(^3P) + M$

numbers in the ground, $X^3\Sigma_g^-$, and excited, $a^1\Delta_g$ or $b^1\Sigma_g^+$, states of an O_2 molecule. We will analyze the case $\tau_I \gg \tau_R, \tau_V$. Here, τ_I is the induced transition time, and τ_R and τ_V are the characteristic times of rotational and vibrational relaxations. Electronically excited molecules $O_2(a^1\Delta_g)$ and $O_2(b^1\Sigma_g^+)$, as well as atoms $O(^1D)$, will be treated as separate chemical components with their own enthalpy of formation. In this case, *E–E* exchange and *E–T* relaxation can be considered as usual chemical reactions. With the above assumptions, the equations describing processes in a reactive gas mixture where O_2 molecules are excited to the $a^1\Delta_g$ or $b^1\Sigma_g^+$ states by laser radiation are given by

$$\frac{\partial N_i}{\partial t} + \nabla[N_i(V_i + u)] = G_i + q_I^i + q_{sp}^i, \tag{3}$$

$$\rho\frac{\partial u}{\partial t} + \rho(u\nabla)u + \nabla P = \sum_{i=1}^{M} N_i X_i, \tag{4}$$

$$\frac{\partial}{\partial t}\left[\rho\left(E + \frac{u^2}{2}\right)\right] + \nabla\left[\rho u\left(E + \frac{P}{\rho} + \frac{u^2}{2}\right) + q_e\right]$$
$$= Q_I - \rho\sum_{i=1}^{M}\frac{h_{0i}}{N}(G_i + q_I^i + q_{sp}^i) + \sum_{i=1}^{M} N_i X_i (V_i + u),$$

$$G_i = \sum_{q=1}^{M_1} S_{iq}, \quad S_{iq} = (\alpha_{iq}^- - \alpha_{iq}^+)[R_q^+ - R_q^-],$$

$$R_q^{+(-)} = k_{+(-)q}\prod_{j=1}^{n_q^{+(-)}} N_j^{\alpha_{jq}^{+(-)}},$$

$$q_{sp}^i = \sum_{q=1}^{3}(A_{qi}^s N_q - A_{iq}^s N_i),$$

$$q_I^i = l_{Ii} W_I\left(\frac{g_n}{g_m}N_m - N_n\right), \quad W_I = \sigma_{mn} I/h\nu_I,$$

$$\sigma_{mn} = \frac{\lambda_{mn}^2}{4\pi b_D} A_{mn}\sqrt{\frac{\ln 2}{\pi}}H(x, a), \quad P = \frac{\rho RT}{\mu},$$

$$Q_I = k_\nu I, \quad k_\nu = \sigma_{mn}\left(\frac{g_n}{g_m}N_m - N_n\right),$$

$$q_e = \rho T\sum_{i=1}^{M} C_{VT}^i V_i - \lambda_T \nabla T + \frac{k_B T}{N}\sum_{i\neq j}\frac{D_i^T N_i}{m_i D_{ij}}(V_i - V_j), \tag{5}$$

$$V_i = \frac{N^2}{N_i\rho}\sum_{j=1}^{M} m_j D_{ij} d_j - \frac{1}{m_i N_i} D_i^T \nabla \ln T,$$

$$E = \sum_{i=1}^{M} C_{VT}^i T,$$

$$d_j = \nabla\frac{N_j}{N} + \left(\frac{N_j}{N} + \frac{N_j m_j}{\rho}\right)\nabla \ln P + \frac{N_j m_j}{\rho P}\sum_{i=1}^{M} N_i X_i - \frac{N_j X_j}{\rho},$$

$$\gamma_i = N_i/N,$$

$$C_{VT}^i = \frac{R}{\mu}\gamma_i\left(\frac{3}{2} + C_R^i + C_V^i\right),$$

$$C_V^i = \sum_{l=1}^{L_i}\left(\frac{\Theta_{il}}{T}\right)^2 \frac{\exp(\Theta_{il}/T)}{[\exp(\Theta_{il}/T) - 1]^2},$$

$$\mu = \sum_{i=1}^{M}\mu_i\gamma_i, \quad N = \sum_{i=1}^{M} N_i.$$

Here, ρ, T, P, and u are the density, temperature, pressure, and velocity of the gas, respectively; N_i is the concentration of molecules of an ith sort ($i = 1, \ldots, M$); m_i is the mass of a molecule of an ith sort; h_{0i} is the enthalpy of formation of an ith component at $T = 298$ K; μ_i is its molar mass ($i = 1$, 2, or 3 for $O_2(X^3\Sigma_g^-)$, $O_2(a^1\Delta_g)$, and $O_2(b^1\Sigma_g^+)$, respectively); α_{iq}^+ and α_{iq}^- are the stoichiometric coefficients of a qth reaction; $k_{+(-)q}$ are the rate constants of a qth reaction proceeding in the forward and backward directions; $n_q^{+(-)}$ is the number of components involved in this reaction; M_1 is the number of reactions causing the decomposition (production) of an ith component; D_i^T and D_{ij} are the coefficients of thermal diffusion of an ith component and of multicomponent diffusion; λ_T is the thermal conductivity; R is the gas constant; k_B is the Boltzmann constant; h is the Planck constant; l_{li} is the number of quanta lost (or acquired) by a molecule of an ith sort under induced transitions; $C_R^i = 0$ (for atoms), 1 (for linear molecules), or 1.5 (for nonlinear molecules); Θ_{il} is the characteristic temperature of vibrations of l type in an ith molecule; L_i is the total number of vibration types in this molecule; ν_I is the frequency of laser radiation; I is its intensity; A_{qi}^s is the decomposition rate for a molecule of qth sort and the formation rate for a molecule of ith sort under spontaneous transitions; λ_{mn} is the wavelength corresponding to the center of the $m \longrightarrow n$ transition; A_{mn} is the Einstein coefficient for this transition; g_n and g_m are the degeneracy multiplicities of the states m and n, respectively; N_n and N_m are the populations of these states; and X_i is the electromagnetic field force acting on a molecule of the ith sort.

In the general case, the expression for X_i has the form [17]

$$X_i = f_{ig} l_r + (f_{iA} + f_{ip}) l_z,$$

$$f_{ig} = \alpha_i \frac{2\pi}{c n_0} \frac{\partial I}{\partial r}, \quad f_{ip} = \frac{k_\nu I}{N_i c},$$

$$f_{iA} = \frac{4\pi\alpha_i}{c^2} \frac{\partial I}{\partial t} + \frac{4\pi I}{c^2} \frac{\partial \mathrm{Re}\,\alpha_i}{\partial t}.$$

Here, f_{ig} is the so-called gradient (or striction) force, f_{ip} is the light pressure force, f_{iA} is the Abraham force, l_z and l_r are the unit vectors along the beam and in the radial direction; α_i is the polarizability of molecules of the ith sort, c is the velocity of light in free space, and n_0 is the refractive index of the undisturbed mixture at $t = 0$. Below, we consider conditions under which the parameters f_A and f_p can be ignored.

Specific analysis will be performed for radiation absorption at the center of the spectral line for the transitions $X^3\Sigma_g^- \longrightarrow a^1\Delta_g$ and $X^3\Sigma_g^- \longrightarrow b^1\Sigma_g^+$ with $v' = v'' = 0$, $j' = 9$, and $j'' = K' = K'' = 8$ (with such rotational numbers at $T_0 = 300$ K, the absorption coefficient is maximal). To the transition $X^3\Sigma_g^- \longrightarrow a^1\Delta_g$ with the given v', j', K', v'', j'', and K'', there corresponds the wavelength $\lambda = 1.268$ μm; to the transition $X^3\Sigma_g^- \longrightarrow b^1\Sigma_g^+$, $\lambda = 0.762$ μm. The Einstein coefficients depend on the rotational quantum number only slightly and for the given transitions for the branch $^QP(9)$ were taken to be equal to 2.58×10^{-4} and 8.5×10^{-2} s^{-1} [8]. When calculating the Voigt function $H(x, a)$ (at the center of the line $x = 0$), we assumed that the cross sections of the collisional broadening of the spectral line are equal to the gas-kinetic cross sections. The rotational energies of an O_2 molecule in the states m and n were calculated in view of the fact that the level j' in the state $X^3\Sigma_g^-$ is split into three components: $j' = K' + 1$, $j' = K'$, and $j' = K' - 1$ [18].

Consider the ignition of a combustible mixture in a laser beam with the radial Gaussian distribution of intensity: $I(r, t) = I_0(t)\exp(-r^2/R_a^2)$, where R_a is the characteristic beam radius and $I_0(t) = I_0$ (for $0 < t \le \tau_p$) or 0 (for $t > \tau_p$). Let $R_a \ll k_\nu^{-1}$; then, the variation of the parameters in the longitudinal direction is negligibly small as compared with the radial direction and it is appropriate to consider an optically thin gaseous layer where the parameters of the medium vary only along the beam radius. By introducing the dimensionless coordinates $r' = r/R_a$ and $t' = t/\tau_p$ and passing to the dimensionless variables $\tilde{N}_i = N_i/N_0$, $\tilde{\rho} = \rho/\rho_0$, $\tilde{u} = u(\tau_p/R_a)$, $\tilde{P} = P/N_0 k_B T_0$, $\tilde{T} = T/T_0$, $\tilde{V}_i = V_i \tau_p/R_a$, $\tilde{k}_\nu = k_\nu/k_\nu^0$, $\tilde{I} = I/I_0$, $\tilde{X}_i = f_{ig}/f_g^0$, and $f_g^0 = 2\pi\alpha_{10} I_0 N_{10}/c n_0 R_a$ (the index 0 refers to the time instant $t = 0$), we reduce system (3)–(5) to the dimensionless form (primes and tildes are omitted)

$$\frac{\partial N_i}{\partial t} = \sum_{q=1}^{M_1} S_{iq} \frac{\tau_p}{\tau_{iq}^{ch}}$$

$$- \nabla \left[N_i \left(\tau_p \sum_k \frac{N_0 m_k N^2 d_k}{\rho_0 N_i \rho \tau_D^{ik}} - \frac{\tau_p}{\tau_{Ti}} \frac{\nabla \ln T}{N_i} + u \right) \right] \qquad (6)$$

$$+ l_{Ii} k_\nu I \gamma_{10} \frac{\tau_p}{\tau_I} + \sum_{q=1}^{3} \left(N_q \frac{\tau_p}{\tau_{qi}^s} - N_i \frac{\tau_p}{\tau_{iq}^s} \right),$$

$$\rho \frac{\partial u}{\partial t} + \rho (u\nabla) u = - \frac{\nabla P}{\chi} \left(\frac{\tau_p}{\tau_a} \right)^2 + \left(\frac{\tau_p}{\tau_F} \right)^2 \sum_{i=1}^{M} N_i f_{ig}, \qquad (7)$$

$$\rho\frac{\partial E}{\partial t}+\rho(u\nabla)E = k_\nu I\delta_I-\frac{\rho}{N}\Bigg[\sum_{i=1}^{3}\Bigg(k_\nu I l_{Ii}\gamma_{10}\frac{\tau_\mathrm{p}}{\tau_I}+\sum_{q=1}^{3}\Big(\frac{N_q}{\tau^\mathrm{s}_{qi}}-\frac{N_i}{\tau^\mathrm{s}_{iq}}\Big)\tau_\mathrm{p}\Bigg)\frac{h_{0i}}{C^0_\mathrm{VT}T_0}+\sum_{i=1}^{M}\frac{\tau_\mathrm{p}}{\tau^\mathrm{ch}_i}G_i\frac{h_{0i}}{C^0_\mathrm{VT}T_0}\Bigg]$$
$$-(\chi-1)\Bigg[P\nabla u-\chi\Big(\frac{\tau_a}{\tau_F}\Big)^2\sum_{i=1}^{M}N_i f_{ig}V_i\Bigg]$$
$$-\nabla\Bigg[\frac{\rho T}{C^0_\mathrm{VT}}\sum_{i=1}^{M}C^i_\mathrm{VT}V_i-\frac{\tau_\mathrm{p}}{\tau_\lambda}\nabla T$$
$$+(\chi-1)\frac{T}{N}\sum_{i\neq j}(V_i-V_j)\frac{\tau^{ij}_\mathrm{D}N_i}{\tau_{\mathrm{T}i}}\Bigg], \qquad (8)$$

$$V_i = -\frac{\tau_\mathrm{p}}{\tau_{\mathrm{T}i}}\frac{\nabla\ln T}{N_i}-\frac{\tau_\mathrm{p}}{\tau^i_\mathrm{D}}\sum_j\nabla d_j\frac{N_0 m_j}{\rho_0\gamma_i\rho},$$

$$\chi = 1+\Big(C^0_\mathrm{VT}\frac{\mu_0}{R}\Big)^{-1},$$

$$d_k = \gamma_{k0}\nabla(\gamma_k)+\gamma_{k0}\Big(\gamma_k-\frac{N_k m_k N_0}{\rho\rho_0}\Big)\nabla\ln P$$
$$+\frac{\chi\gamma_{k0}\tau_a^2}{P\tau_F^2}\Bigg[\frac{N_k m_k}{\rho\gamma_{10}}\sum_{i=1}^{M}N_i f_{ig}-N_k f_{kg}\Bigg].$$

Here, $\tau_a = R_a/\sqrt{\chi P_0/\rho_0}$ is the time of acoustic wave propagation across the beam; $\tau^{ij}_\mathrm{D} = R_a^2/D_{ij}$ and $\tau_{\mathrm{T}i} = R_a^2 m_i N_0/D_i^\mathrm{T}$ are, respectively, the times of multicomponent diffusion and thermal diffusion; $\tau_\lambda = \rho_0 R_a^2 C^0_\mathrm{VT}/\lambda_T$ is the heat conduction time; $\tau^\mathrm{ch}_{iq} = N_0(S^0_{iq})^{-1}$ is the characteristic time of a qth reaction producing an ith component; $\tau_I = N_{10}h\nu_I/k^0_\nu I_0$ is the induced transition time; $\tau^\mathrm{s}_{qi} = (A^\mathrm{s}_{qi})^{-1}$ is the time of the radiation decomposition of the O_2 excited states (i = 1, 2, 3) due to spontaneous transitions; $\tau_\mathrm{F} = \sqrt{\rho_0 R_a/f^0_g N_0}$ is the time of change of a mixture state under the action of the striction force; and $\delta_\mathrm{I} = k^0_\nu I_0\tau_\mathrm{p}/\rho_0 C^0_\mathrm{VT}T_0$.

Now let us numerically estimate the characteristic times when the stoichiometric $2H_2 + O_2$ mixture is exposed to laser radiation with $\lambda = 0.762$ μm for I_0 = 1–10 kW/cm^2, R_a = 10 cm, $P_0 = 10^3$–10^4 Pa, T_0 = 300–700 K. The hierarchy of these times to a great extent determines the influence of various processes on the evolution of the components within the range and, hence, ignition process. With the given conditions of numerical experiment, $\tau_\mathrm{I} = 2\times10^{-1}$–$4\times10^{-3}$ s, $\tau_a \approx 2\times10^{-4}$ s, $\tau_\mathrm{D} \approx \tau_{\mathrm{T}i} \approx \tau_\lambda$ = 0.3–10 s, and τ_F = 1–10 s. For the transition $a^1\Delta_g \longrightarrow X^3\Sigma^-_g$, $\tau^\mathrm{s}_{21} = 3.87\times10^3$ s; for the transition $b^1\Sigma^+_g \longrightarrow X^3\Sigma^-_g$, $\tau^\mathrm{s}_{31} = 1.18\times10^1$ s. We will consider the case in which $\tau_a \ll \tau_\mathrm{p} \sim \tau_I \leq \tau_\mathrm{in} \ll \tau_\mathrm{D}$, where τ_in is the characteristic time of ignition (induction time).

In this case, one can neglect macrotransfer processes and spontaneous emission within the interval $[0, \tau_\mathrm{in}]$ and assume that the motion of the gas across the beam is insignificant at $u(t = 0) = 0$. Then, Eqs. (6)–(8) can be represented as

$$\frac{\partial N_i}{\partial t} = \sum_{q=1}^{M_1}S_{iq}\frac{\tau_\mathrm{p}}{\tau^\mathrm{ch}_{iq}}+l_{Ii}k_\nu I\gamma_{i0}\frac{\tau_\mathrm{p}}{\tau_I}, \qquad (9)$$

$$\nabla P = 0, \qquad (10)$$

$$\rho\frac{\partial E}{\partial t} = k_\nu I\Bigg(\delta_I-\frac{\rho}{N}\sum_{i=1}^{3}\frac{h_{0i}}{C^0_\mathrm{VT}T_0}l_{Ii}\gamma_{10}\frac{\tau_\mathrm{p}}{\tau_I}\Bigg)$$
$$-\frac{\rho}{N}\sum_{i=1}^{M}\frac{h_{0i}}{C^0_\mathrm{VT}T_0}\frac{\tau_\mathrm{p}}{\tau^\mathrm{ch}_i}G_i. \qquad (11)$$

Equation (10) has the simple solution $P(r) = P_a$, where P_a is the pressure in the undisturbed gas ($P_a = P_0$). Equations like (9) for $i = O_2(X^3\Sigma^+_g)$, $O_2(a^1\Delta_g)$, $O_2(b^1\Sigma^+_g)$, H_2, H_2O, OH, HO_2, H_2O_2, O_3, $O(^3P)$, $O(^1D)$, and H, as well as Eq. (11), were solved numerically in the second approximation with the implicit difference scheme.

IGNITION OF THE $H_2 + O_2$ MIXTURE WITH O_2 MOLECULES EXCITED TO THE $a^1\Delta_g$ AND $b^1\Sigma^+_g$ STATES

It is known that the ignition of hydrogen–air mixtures implies chain reactions involving reactive O and H atoms and OH radicals. These atoms and radicals are produced by chemical reactions, which have characteristic reaction times τ^ch_{iq}. A set of these times defines the induction period τ_in (or the delay time of ignition). Active radicals are lost in chain-termination reactions and leave the reaction zone by diffusion. Self-ignition takes place if $\tau^\mathrm{ch}_{iq} \sim \tau_\mathrm{in} \leq \tau^i_\mathrm{D}$. In $H_2 + O_2$ mixtures, τ^i_D coincides with the diffusion time of the lightest participant of the chain mechanism, i.e., hydrogen atoms ($\tau^\mathrm{H}_\mathrm{D}$).

Figure 2 demonstrates the dependence of the induction period τ_in and atomic hydrogen diffusion time $\tau^\mathrm{H}_\mathrm{D}$ on the initial temperature T_0 of the H_2/O_2 = 2/1 mixture

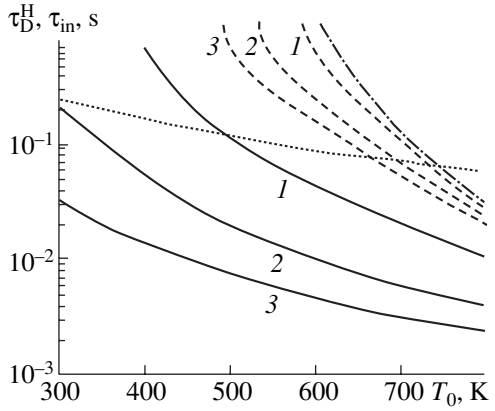

Fig. 2. Dependences $\tau_D^H(T_0)$ (dotted line) and $\tau_{in}(T_0)$ for the radiation wavelengths $\lambda = 0.762$ (solid lines) and 1.268 μm (dashed lines) and intensities I_0 = (*1*) 1, (*2*) 5, and (*3*) 10 kW/cm^2. The dash-and-dot line depicts the dependence $\tau_{in}(T_0)$ for $I_0 = 0$.

for $P_0 = 10^3$ Pa; radiation wavelengths $\lambda = 1.286$ and 0.762 μm; $\tau_p = 10^{-3}$ s; and $I_0 = 1$, 5, and 10 kW/cm^2. For the given I_0, τ_p, and parameters of the medium, the laser energy absorbed by an O_2 molecule is 0.017, 0.082, and 0.15 eV/mol at $\lambda = 0.762$ μm and 2.4×10^{-4}, 1.2×10^{-3}, and 2.4×10^{-3} eV/mol at $\lambda = 1.268$ μm. One can see that the radiation with $\lambda = 0.762$ μm decreases τ_{in} and accordingly the self-ignition temperature to a greater extent than the radiation with $\lambda = 1.268$ μm. In the first approximation, the self-ignition temperature can found from the equality $\tau_{in}(T, I_0) = \tau_D^H(T)$. For radiation with $\lambda = 0.762$ μm with an input energy $E_{inp} = I_0\tau_p \geq 5$ J/cm^2, the self-ignition temperature can be decreased to T_{ign} = 300 K. Note that even with such E_{inp}, the energy spent on the excitation of one O_2 molecule to the state $b^1\Sigma_g^+$ is as low as 0.15 eV, while the photodissociation of an O_2 molecule that is derived from the ground state (this process initiates the chain mechanism of the ignition of the $H_2 + O_2$ mixture via atomic oxygen production) requires 5.8 eV. Moreover, at low temperatures ($T_0 \leq$ 600 K), O atoms recombine rather quickly, which also reduces the efficiency of the photochemical ignition method [19], which is based on molecule dissociation by laser radiation.

A decrease in τ_{in} upon exciting O_2 molecules to the state $a^1\Delta_g$ ($\lambda = 1.268$ μm) or $b^1\Sigma_g^+$ ($\lambda = 0.762$ μm) is related to a change in the production kinetics of reactive O and H atoms and OH radicals. This is illustrated in Fig. 3, which shows the time evolution of the species concentration (mole fractions) without laser radiation and with the radiation at $\lambda = 1.268$ and 0.762 μm. When O_2 molecules are excited to the state $a^1\Delta_g$ ($\lambda = 1.268$ μm)

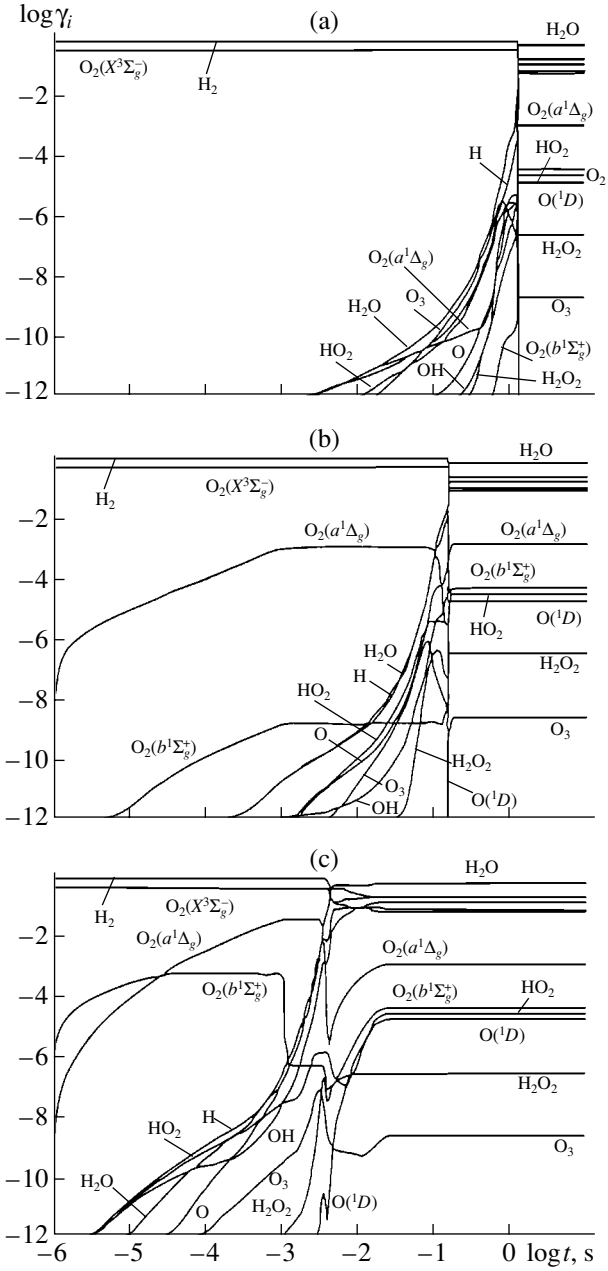

Fig. 3. Time evolution of the component concentrations upon ignition of the H_2/O_2 mixture at $T_0 = 600$ K and $P_0 = 10^3$ Pa (a) without and (b) in the presence of laser radiation with λ = (b) 1.268 and (c) 0.762 μm. $I_0 = 10$ kW/cm^2.

or $b^1\Sigma_g^+$ ($\lambda = 0.762$ μm), not only τ_{in} but also the dynamics of the species concentration within the interval [0, τ_{in}] changes. It is of interest that when O_2 molecules are excited to the $b^1\Sigma_g^+$ state, the concentration of $O_2(a^1\Delta_g)$ molecules also grows because of *E–T* collisional relaxation by reaction 72 (see table). In this case, the concentration of $O_2(a^1\Delta_g)$ molecules due to the irradiation by 0.762-μm radiation under $t = \tau_p$ is much (by a factor of

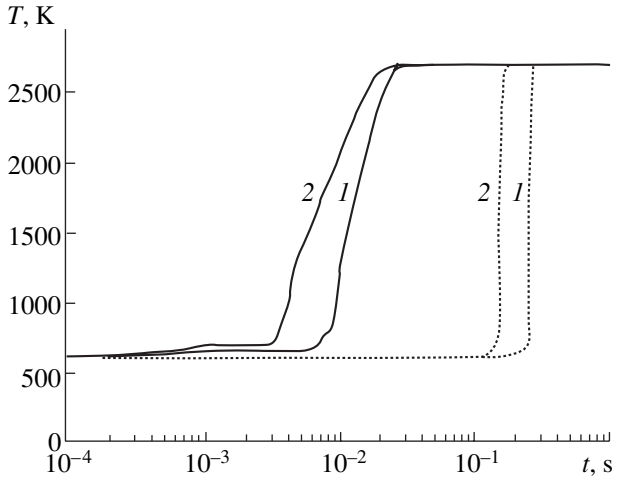

Fig. 4. Time evolution of the temperature when the mixture was ignited by laser radiation with $\lambda = 1.268$ (dotted lines) and 0.762 μm (solid lines) at $T_0 = 600$ K and $I_0 = (1)$ 5 and (2) 10 kW/cm^2.

about 50) higher than the concentration of O_2 molecules directly excited to the $a^1\Delta_g$ state by the 1.268-μm radiation. This is caused by the fact that for given I_0 and parameters of the medium, the rate of the induced $X^3\Sigma_g^- \longrightarrow b^1\Sigma_g^+$ transitions is much (by a factor of 40–75) greater than that for the $X^3\Sigma_g^- \longrightarrow a^1\Delta_g$ transitions.

The intense collisional quenching of the $b^1\Sigma_g^+$ state for the given parameters of the medium not only increases the concentration of $O_2(a^1\Delta_g)$ but also slightly raises the temperature in the interval $[0, \tau_{in}]$. At the same time, when O_2 molecules are directly excited by laser radiation to the $a^1\Delta_g$ state, T does not grow since the quenching rate of the state $a^1\Delta_g$ (reaction 73) is much slower. This is illustrated in Fig. 4, where the gas temperature is plotted versus time when the $H_2/O_2 = 2/1$ mixture with $T_0 = 600$ K and $P_0 = 10^3$ Pa is exposed to the radiations with $\lambda = 1.268$ and 0.762 μm, $I_0 = 5$ and 10 kW/cm^2, and $\tau_p = 10^{-3}$ s. For $\lambda = 0.762$ μm and the two given values of I_0, the temperature in the interval $[0, \tau_p]$ varies from 600 to 647 and 688 K, respectively. The respective values of τ_{in} in this case equal 9.8×10^{-3} and 4.6×10^{-3} s. It should be noted that the combustion time τ_c (its value was determined at the instant the temperature reaches $0.99T_e$, where T_e is the equilibrium temperature of combustion products) varies less significantly when I_0 changes from 5 to 10 kW/cm^2.

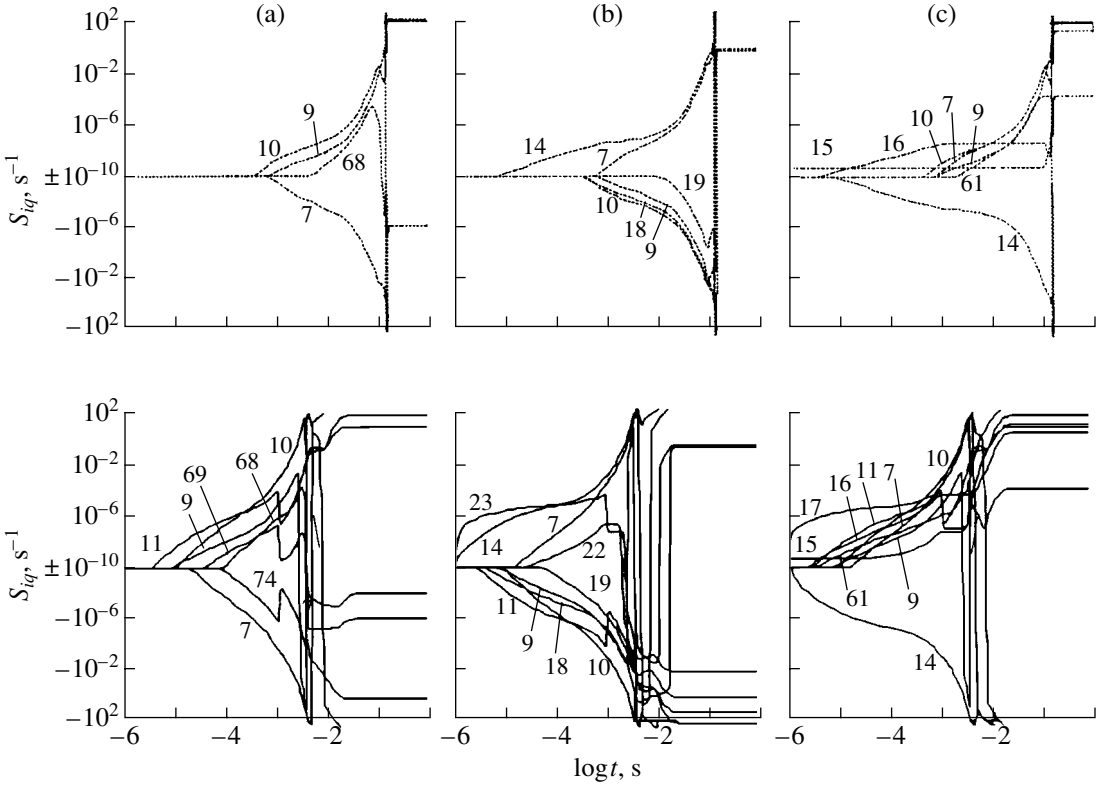

Fig. 5. Rates S_{iq} of (+) formation and (–) loss of (a) O, (b) H, and (c) OH vs. time when the mixture was ignited by the radiation with $\lambda = 1.268$ (dotted lines) and 0.762 μm (solid curves). $I_0 = 10$ kW/cm^2.

The reduction of the ignition delay time is associated mainly with the appearance of new channels for the formation of reactive O and H atoms and OH radicals rather than with a temperature increase due to the absorption of the 0.762-μm radiation. This is clearly seen from Fig. 5, where the time evolution of the rates S_q of (+) formation and (–) loss of (a) O and (b) H atoms, as well as (c) OH radicals, is shown for λ = 1.268 (dashed lines) and 0.762 μm (solid lines). Recall that in the absence of $O_2(a^1\Delta_g)$ and $O_2(b^1\Sigma_g^+)$ molecules in the mixture, the basic reaction initiating the ignition of the $H_2 + O_2$ mixture in air at low temperatures ($T_0 <$ 800 K) is $H_2 + O_2 = 2OH$ (reaction 15). Then, the chain propagation reaction $H_2 + OH = H_2O + H$ produces H atoms, which react with O_2 molecules to form O and OH (branching reaction 9). The chain mechanism is closed by the reaction $H_2 + O = OH + H$ (reaction 7).

When O_2 molecules are excited by the laser radiation with λ = 1.268 μm, the basic reaction triggering the chain mechanism is reaction 16, which involves $O_2(a^1\Delta_g)$. Hydrogen atoms form, as in the absence of excited $O_2(a^1\Delta_g)$ molecules, by reaction 14, which proceeds in the back direction. Here, reaction 10 becomes the key one in the formation of O atoms. Moreover, even if a small amount of $O_2(a^1\Delta_g)$ molecules is present in the mixture (for I_0 = 10 kW/cm^2 and $\tau_p = 10^{-3}$ s, their relative content in the mixture does not exceed 0.1%), reaction 68, involving O_3 and $O_2(a^1\Delta_g)$ molecules, also becomes an efficient source of O atoms. Both processes are much faster than the associated reactions with the participation of unexcited O_2 molecules. Therefore, even if $O_2(a^1\Delta_g)$ molecules are present in small amounts (≈0.1%), τ_{in} decreases significantly (more than tenfold at T_0 = 600 K, $P_0 = 10^3$ Pa, and I_0 = 10 kW/cm^2).

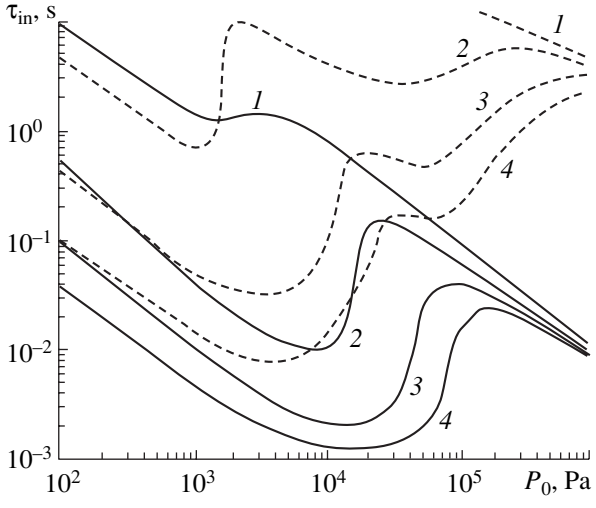

Fig. 6. τ_{in} vs. P_0 dependence when the mixture at T_0 = 400 (dashed lines) and 600 K (solid lines) is irradiated by 0.762-μm radiation with I_0 = (*1*) 0, (*2*) 1, (*3*) 5, and (*4*) 10 kW/cm^2.

When $O_2(b^1\Sigma_g^+)$ molecules are excited, reactions 17 and 23, which involve $O_2(b^1\Sigma_g^+)$, become the basic chain-initiating reactions. In reaction 17, OH radicals are produced; and reaction 23, hydrogen atoms. Since the radiation with λ = 0.762 μm produces not only $O_2(b^1\Sigma_g^+)$ but also $O_2(a^1\Delta_g)$ molecules, O atoms appear early in the process mainly by branching reactions 11 and 10. Such new intense reaction paths generate additional components taking part in the chain mechanism of ignition, thus accelerating the chain reactions and cutting τ_{in}. If the thermal mechanism of ignition alone occurred under the evolution radiation of the mixture at λ = 0.762 μm, the induction period at T_0 = 688 K (the temperature that is reached at $t = \tau_p = 10^{-3}$ s for I_0 = 10 kW/cm^2) would equal 1.4×10^{-1} s. This value is 30 times that obtained with allowance for the chain reaction intensification due to the presence of $O_2(a^1\Delta_g)$ and $O_2(b^1\Sigma_g^+)$ molecules in the mixture. If the radiation energy were spent only on heating the gas, the temperature of the mixture for $t = \tau_p$ and the parameters given above would be 806 K and $\tau_{in} = 2 \times 10^{-2}$ s. The latter value is by a factor of 4.4 greater than τ_{in} that is observed when O_2 molecules are excited to the $b^1\Sigma_g^+$ state. With lower T_0 and higher P_0, the difference is still larger. For example, with T_0 = 400 K, $P_0 = 10^4$ Pa, I_0 = 10 kW/cm^2, and $\tau_p = 10^{-3}$ s, the induction period in the case of O_2 molecules excited to the $b^1\Sigma_g^+$ state more than 60 times exceeds that for the purely thermal action of the radiation with λ = 0.762 μm.

The effect of the initial pressure in the $2H_2 + O_2$ mixture on the ignition delay time when O_2 molecules are excited to the $b^1\Sigma_g^+$ state by the 0.762-μm radiation for T_0 = 400 and 600 K and various values of I_0 is illustrated in Fig. 6. For each of the values of I_0 and T_0, there are three characteristic ranges of P_0. In the first range, τ_{in} decreases with increasing P_0; in the second range, it increases; and in the third range, it decreases again. The excitation of O_2 molecules with the 0.762-μm radiation not only substantially cuts τ_{in} (e.g., for I_0 = 10 kW/cm^2 and $P_0 = 10^4$ Pa, the value of τ_{in} is by a factor of 600 smaller than without the radiation) but also increases the boundary values of P_0 separating these ranges. The higher I_0, the higher P_0 at which the run of the dependence $\tau_{in}(P_0)$ changes. For I_0 = 0 and T_0 = 600 K, the boundary value of P_0, P_{b0}, separating the first and second ranges, equals 10^3 Pa; for I_0 = 10 kW/cm^2, it equals 2×10^4 Pa. The presence of the characteristic ranges is explained by the fact that at sufficiently low T_0 and $P_0 > P_{b0}$, the intense formation of chemically inactive H_2O_2

molecules takes place, while the formation of O and H atoms, as well as OH radicals, slows down. When combined, these two trends increase the ignition delay [13]. From the dependences $\tau_{in}(P_0)$ shown in Fig. 6, it follows that there exists the third range of P_0, $P_0 > P_{0c} = f(I_0, T_0)$, where the radiation has an insignificant effect on τ_{in}. For example, at $T_0 = 600$ K and $I_0 = 10$ kW/cm^2, $P_{0c} = 2 \times 10^5$ Pa. At lower mixture temperatures, the value of P_{0c} at the same I_0 grows.

CONCLUSION

The excitation of O_2 molecules to the $b^1\Sigma_g^+$ state by resonant laser radiation with $\lambda = 0.762$ μm generates electronically excited $O_2(b^1\Sigma_g^+)$ molecules and $O_2(a^1\Delta_g)$ metastable molecules in the mixture via *E–E* and *E–T* transitions. In this case, the concentration of $O_2(a^1\Delta_g)$ molecules in the mixture is even higher (≈50 times) than when O_2 molecules are directly excited to the $a^1\Delta_g$ state by laser radiation with $\lambda = 1.268$ μm of the same intensity. The presence of $O_2(a^1\Delta_g)$ and $O_2(b^1\Sigma_g^+)$ excited molecules in the mixture produces new paths for the formation of reactive O and H atoms and OH radicals, stimulating ignition by the chain mechanism. This allows a decrease in the induction period and ignition temperature. Even if the energy density of the 0.762-μm radiation is low, $E_{inp} = 5$ J/cm^2, the self-ignition temperature can be reduced to 300 K. In terms of the influence on the combustion process, the excitation of O_2 molecules into the $b^1\Sigma_g^+$ state by resonant laser radiation is much more (several tens of times) efficient than the direct laser heating of the medium. Since molecular oxygen serves as an oxidant in the combustion of most organic and inorganic fuels, one can expect that the given method of intensifying chain reactions will also be efficient for other combustible mixtures.

ACKNOWLEDGMENTS

This work was financially supported by the Russian Foundation for Basic Research (projects no. 02-01-00703 and 02-02-16915).

REFERENCES

1. *Advanced Combustion Methods*, Ed. by F. J. Weinberg (Academic, London, 1986).
2. D. Lucas, D. Dunn-Rankin, K. Hom, *et al.*, Combust. Flame **69**, 171 (1987).
3. R. A. Morris, A. A. Viggiano, S. T. Arnold, *et al.*, in *WIP Abstracts of the 27th International Symposium on Combustion* (Boulder, Colorado, 1998), p. 343.
4. V. Ya. Basevich and S. M. Kogarko, Kinet. Katal. **7**, 393 (1966).
5. A. M. Starik and N. G. Dautov, Dokl. Akad. Nauk **336**, 617 (1994) [Dokl. Phys. **39**, 424 (1994)].
6. A. M. Starik and N. S. Titova, Dokl. Akad. Nauk **370**, 38 (2000) [Dokl. Phys. **45**, 5 (2000)].
7. A. I. Zakharov, K. S. Klopovskiĭ, A. P. Osipov, *et al.*, Fiz. Plazmy **14**, 327 (1988) [Sov. J. Plasma Phys. **14**, 191 (1988)].
8. A. M. Starik and O. V. Taranov, Khim. Fiz. **18** (3), 15 (1999).
9. A. M. Starik and N. S. Titova, Khim. Fiz. **20** (5), 17 (2001).
10. E. P. Dougherty and H. Rabitz, J. Chem. Phys. **72**, 6571 (1980).
11. V. D. Rusanov and A. A. Fridman, *Physics of Chemically Active Plasma* (Nauka, Moscow, 1984).
12. A. S. Biryukov, S. A. Reshetnyak, and L. A. Shelepin, Tr. Fiz. Inst. Akad. Nauk SSSR **107**, 179 (1979).
13. A. M. Starik and N. S. Titova, Khim. Fiz. **19** (9), 61 (2000).
14. V. Ya. Basevich and A. A. Belyaev, Khim. Fiz. **8**, 1124 (1989).
15. R. Atkinson, D. L. Baulch, R. A. Cox, *et al.*, J. Phys. Chem. Ref. Data **21**, 1125 (1992).
16. Yu. A. Kulagin, L. A. Shelepin, and V. I. Yarygina, Tr. Fiz. Inst. Akad. Nauk SSSR **212**, 166 (1994).
17. V. I. Grabovskiĭ and A. M. Starik, Kvantovaya Élektron. (Moscow) **21**, 365 (1994).
18. L. D. Landau and E. M. Lifshitz, *Course of Theoretical Physics*, Vol. 3: *Quantum Mechanics: Non-Relativistic Theory* (Nauka, Moscow, 1989; Pergamon, New York, 1977).
19. M. S. Chou, F. E. Fendell, and H. W. Behrens, Proc. SPIE **1862**, 45 (1993).

Translated by V. Isaakyan

Technical Physics, Vol. 48, No. 3, 2003, pp. 344–348. Translated from Zhurnal Tekhnicheskoĭ Fiziki, Vol. 73, No. 3, 2003, pp. 69–74.

OPTICS, QUANTUM ELECTRONICS

Hysteretic Behavior of Spectral Components of a Femtosecond Pulse Passing through a Nonlinear Layer

D. K. Skripov and V. A. Trofimov

Moscow State University, Vorob'evy gory, Moscow, 119992 Russia

e-mail: vatro@cs.msu.su

Received September 18, 2002

Abstract—The variation of the frequency at which the spectral intensity is maximal within a given time interval with the amplitude of an applied femtosecond pulse is simulated. The computer simulation is performed in the model of an optically thin layer for a medium with cubic nonlinearity and saturable restoring force. It is shown that the hysteretic dependence of the spectral line frequency on the applied pulse amplitude may take place for both one and several simultaneously generated harmonics. *© 2003 MAIK "Nauka/Interperiodica".*

INTRODUCTION

When passing through a medium, a femtosecond optical pulse is known to cause various nonlinear optical phenomena, such as plasma formation and generation of optical harmonics and supercontinuum, depending on the pulse intensity. Also, there appears the possibility of controlling ultrafast chemical reactions, etc. (see, e.g., [1–8]). Therefore, the study of femtosecond pulse propagation is of great importance for many applications.

It has been discovered recently [8, 9] that the femtosecond pulse spectrum in the bulk of a nonlinear medium depends on the absolute phase of the pulse at the entrance to the medium and that the pulse generates a train of subpulses with various spatial and frequency characteristics. Computer experiments revealed the asymmetry of the spectral distribution of the pulse near local maxima under certain relationships between pulse parameters. Such behavior can be explained, for example, if one takes into account the nonlinear dependence of the resonance frequency on the applied pulse amplitude. From the vibration theory it is known [10] that when a pulse of sufficient duration and amplitude exceeding some critical value is applied to a medium with cubic nonlinearity, the dependence of the steady-state oscillation amplitude on the detuning of the frequency of the applied harmonic signal from the resonance frequency of a linear oscillator shows hysteresis. Obviously, with a femtosecond pulse applied, the interaction pattern becomes more complicated, because the process is basically non-steady-state in this case and nonlinearities of different orders come into play simultaneously. Therefore, obtaining the hysteretic dependence, e.g., of the frequency at which the amplitude is maximal in a given spectral band, on the femtosecond pulse amplitude at the entrance to a medium where the pulse propagates is a challenge. This point is discussed in this work (see also [11]), where this effect is shown to be possible within the model of an optically thin layer.

Note that the presence of hysteretic phenomena, first, opens up the fundamental possibility of realizing ultrafast all-optical bistable elements where radiations with different frequencies play the role of "zero" and "unity." Second, the bistable dependence of the frequency at which the spectral intensity has a local maximum in the spectral distribution on the input amplitude of a wave packet propagating in the medium allows for the control of chemical reactions [2] with a single input pulse generating a train of subpulses with various frequencies.

BASIC EQUATIONS

In this work, we consider the propagation of a light pulse through an optically thin layer. The situation is described either by the Duffing dimensionless equation with cubic nonlinearity

$$\frac{d^2P}{dt^2} + \delta\frac{dP}{dt} + P + \beta P^3 = \alpha E \qquad (1')$$

or by the equation with the saturable potential of the restoring force

$$\frac{d^2P}{dt^2} + \delta\frac{dP}{dt} + \frac{P}{1+P^4} = \alpha E,\ 0 < t \le L_t,$$

$$D = E + 4\pi P \qquad (1'')$$

with the initial conditions

$$P|_{t=0} = \left.\frac{dP}{dt}\right|_{t=0} = 0$$

corresponding to the undisturbed medium. The acting

pulse is either triangular,

$$E(t) = E_0(t)\cos(\omega(t - L_t/2)),$$
$$E_0(t) = E_0(1 - |1 - 2t/L_t|), \quad (2')$$

or trapezoidal,

$$E(t) = E_0(t)\cos(\omega(t - L_t/2)),$$
$$E_0(t) = 2E_0(1 - |t/L_t - 0.25| - |t/L_t - 0.75|). \quad (2'')$$

These shapes meet the purpose of this work: they highlight the dependences responsible for optical bistability and are therefore widely used in the relevant literature.

In the formulas given above, t is dimensionless time, L_t is its maximal value, E_0 is the maximal amplitude of the pulse, δ characterizes the polarization attenuation in the medium, α is the quantity proportional to the dipole moment of an atom or molecule, and ω is the frequency of the pulse. The normalization of the variables is such that the linear oscillator frequency equals unity. The sign of β in (1) specifies the contribution of anharmonicity to the potential energy of an atom. With $\beta > 0$, the potential energy grows; i.e., the atom is disturbed (compressed) near the equilibrium state. The negative value of β refers to the heavily disturbed system (far from equilibrium), when electron–ion coupling loosens, that is, describes the state of the atom immediately before ionization.

For a medium with cubic nonlinearity, the parameters used in the simulation were

$$\alpha = 0.9, \ \omega = 1.4, \ \delta = 10^{-4}, \ \beta = 0.1. \quad (3)$$

These values were taken for the following reasons. For the attenuation factor $\delta = 10^{-4}$, the absorption of the medium has a minor effect on the nonlinear propagation of a femtosecond pulse [9]. The other parameters had the same values as in [6–9, 11], where the associated linear and nonlinear effects were clearly demonstrated.

The amplitude of the applied pulse and its duration were varied to trace the spectral response of the medium in a given time interval. To this end, the time of pulse action $[0, L_t]$ is split into M equal intervals of width T ($t_k = kT$, $k = 0\ldots M$, $L_t = MT$), at each of which $[t_k, t_{k+1}]$ the Fourier transformation of the electric induction was carried out:

$$D_k(\omega) = \frac{1}{T}\int_{t_k}^{t_k + T} D(t)e^{-i\omega(t - t_k)}dt, \ k = 0\ldots(M-1). \quad (4)$$

Accordingly, the inverse Fourier transform has the form

$$D(t) = \int_{-\infty}^{\infty} D_k(\omega)e^{i\omega(t - t_k)}d\omega, \quad t \in [t_k, t_{k+1}]. \quad (5)$$

Note that in numerical experiments, the fast discrete Fourier transform is used instead of (4). The intensity of a spectral mode is defined in the standard manner, i.e., as the squared magnitude of the amplitude of the associated harmonic:

$$I_k(\omega) = |D_k(\omega)|^2. \quad (6)$$

RESULTS OF COMPUTER SIMULATION

Clearly, because of the nonlinearity of the system, new spectral lines generated are of different intensity. Consequently, in each of the time intervals, there exist several spectral lines with center frequencies $\omega_{k,m}$ (the subscript k denotes the corresponding time interval, and m refers to a local spectral maximum in this interval). In going from one time interval to another, these spectral maxima may shift or disappear and their amplitudes may vary. Because of this, the frequency at which the maximum of the spectral intensity is observed in a given time interval also varies. Therefore, in numerical experiments, the frequency of choice is that providing the maximal spectral intensity in most of the time intervals (i.e., that corresponding to the "global" spectral maximum). In those several intervals where the spectral maxima are observed at other (greatly differing) frequencies, the frequency of another "global" maximum is looked for. In the figures that follow, the results of simulation are depicted as the dependences of the frequency

$$\omega_k = \max_{\omega} I_k(\omega), \quad k = 0\ldots(M-1) \quad (7)$$

(in view of the remark made above) on the averaged (over a given interval) amplitude of the external action

$$A_{\text{ext}} = \frac{(E_0(t_{k+1}) + E_0(t_k))}{2}. \quad (8)$$

For convenience, the arrows indicate the direction of time variation. The beginning and end of the lines near $A_{\text{ext}} \approx 0$ correspond to the appearing or disappearing amplitudes of related spectral harmonics. However, the amplitudes may also disappear near the peak of the signal (Fig. 2b, curve *4*), which means that a given harmonic is absent. In a number of the figures, the number of intervals into which the pulse is split and their widths (the first and second number, respectively, in the parentheses) are shown for clarity. Note also that an increase (decrease) in A_{ext} corresponds to the leading (trailing) edge of the pulse.

To answer the question as to whether the frequency of the harmonic with the maximal amplitude can exhibit the hysteretic dependence on the applied field, the simulation is carried out in two steps. First, the feasibility of such a dependence was studied for the variable maximal amplitude E_0 of the pulse with its width fixed. In this case, as E_0 grows, the width of the elementary time interval is made narrower to keep the acting momentum roughly the same. Another splitting crite-

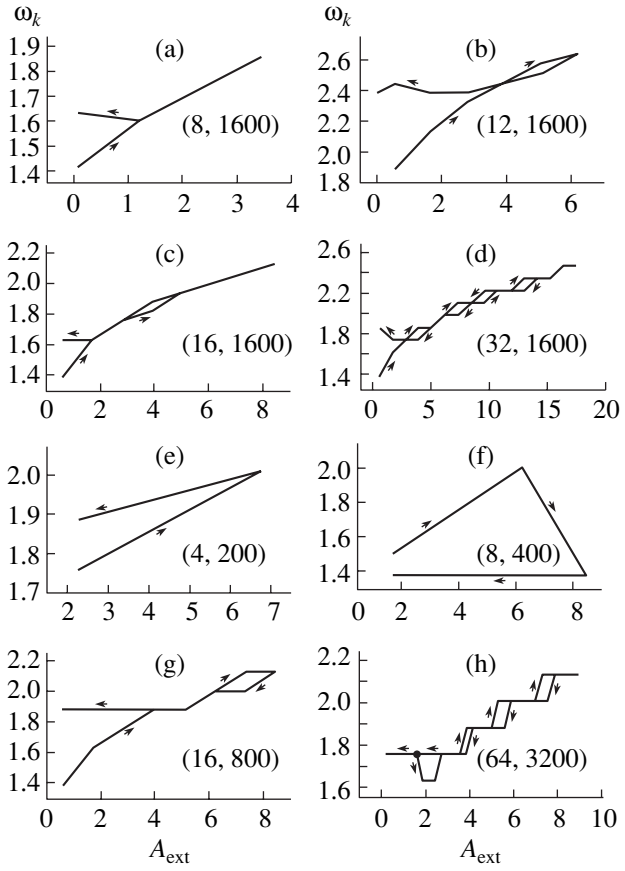

Fig. 1. (a–d) Frequency of the most intense harmonic vs. averaged amplitude of the triangular pulse for L_t = 1600, α = 0.9, ω = 1.4, $\delta = 10^{-4}$, β = 0.1, and fixed product E_0T. (E_0; T) = (5; 200) (a), (7.5; 133) (b), (10; 100) (c), and (20; 50) (d). (e–h) Frequency of the most intense harmonic vs. duration of the triangular pulse for E_0 = 10, α = 0.9, ω = 1.4, $\delta = 10^{-4}$, β = 0.1, and L_t = 200 (e), 400 (f), 800 (g), and 3200 (h). The elementary time interval is T = 50.

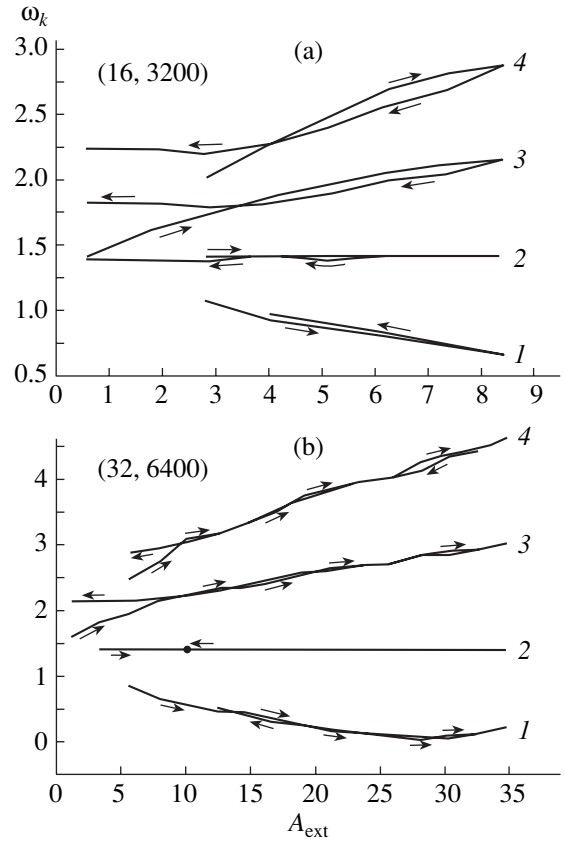

Fig. 2. Time evolution for four frequencies at which the spectral amplitudes are maximal under the action of the triangular pulse with α = 0.9, ω = 1.4, $\delta = 10^{-4}$, and β = 0.1. E_0 = 10 (a) and 40 (b). L_t = 3200 (a) and 6400 (b). The elementary time interval is T = 200.

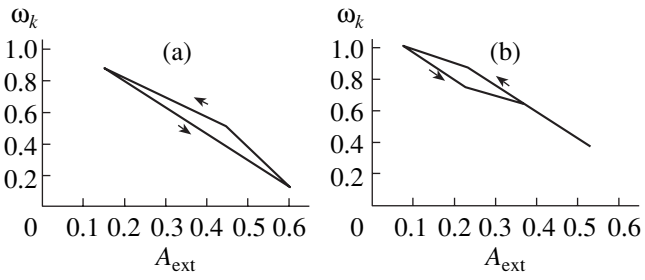

Fig. 3. Center frequency of the spectral line whose intensity is 5% of the highest intensity harmonic vs. amplitude of the (a) trapezoidal and (b) triangular pulses. E_0 = 1, L_t = 400, α = 0.6, ω = 1.4, $\delta = 10^{-4}$, and β = –4.485 (a) and –4.536 (b).

rion is to keep the quantity $E_0^2 T$ roughly the same in order to conserve the pulse energy over the interval T.

Then, the feasibility of the hysteretic dependence is studied for the case when the amplitude of the acting pulse and elementary time interval T are fixed and the total width of the pulse is varied. The simulation of this type is widely used in studying optical bistability.

Medium with cubic nonlinearity. As follows from Fig. 1, the hysteretic dependence of the frequency of the highest intensity harmonic on the applied pulse amplitude appears in both cases (when the amplitude of the pulse grows with its width remaining fixed, Figs. 1a–1d, and vice versa, Figs. 1e–1h). Many local hysteresis loops are noteworthy (Figs. 1d, 1h). Thus, Fig. 1 demonstrates the bistable dependence of the frequency of the highest intensity harmonic on the amplitude of the pulse applied. This is one more reason why the spectral composition of the response near several spectral lines is different at the leading and trailing edges of the pulse.

It should also be emphasized that hysteresis may be observed at a number of frequencies (see Fig. 2 for illustration). However, the amplitudes of these harmonics may differ dramatically: from almost coincident to differing by several tens of times. For example, over the interval the nearest to the center of the pulse (Fig. 2),

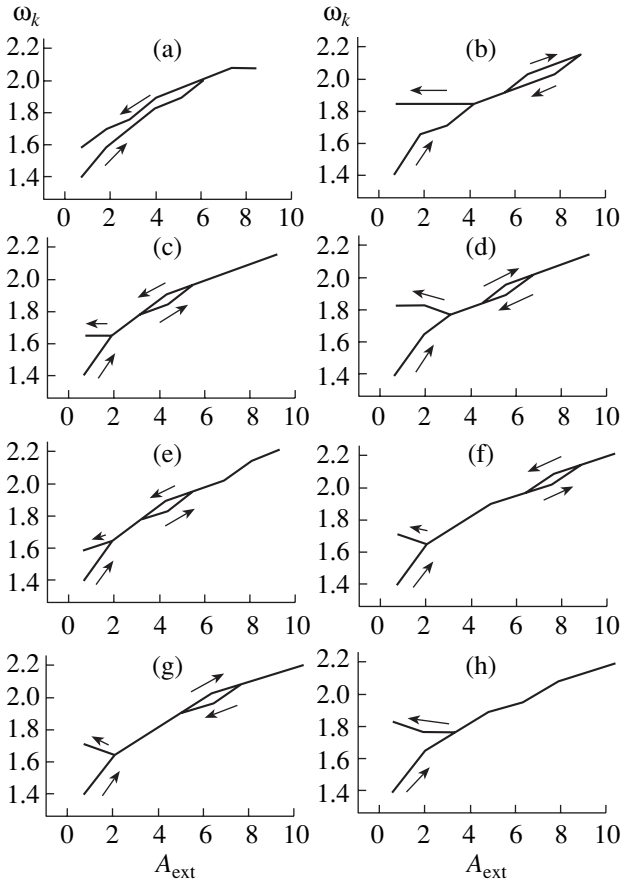

Fig. 4. Frequency of the most-intense harmonic vs. amplitude of the triangular pulse for $\alpha = 0.9$, $\delta = 10^{-4}$, $L_t = 1600$, $\omega = 1.4$, $\beta = 0.1$, and $T = 100$. $E_0 = 9$ (a), 9.5 (b), 9.8 (c), 9.85 (d), 9.9 (e), 11.0 (f), 11.25 (g), and 11.5 (h).

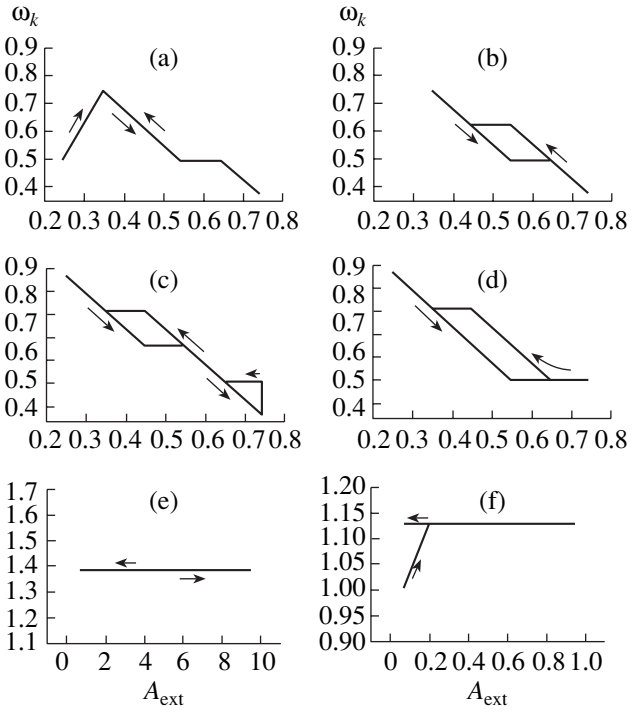

Fig. 5. (a–d) Hysteresis loops for one frequency of the electric induction that appear when the triangular pulse is applied to the medium with saturable potential for $\alpha = 0.79$, $\delta = 10^{-4}$, $L_t = 800$, and (E_0; T) = (1; 50); $\omega = 1.098$ (a), 1.1 (b), 1.12 (c), and 1.13 (d). (e, f) Single frequency of the response vs. triangular pulse amplitude in the case of a linear medium for the same parameters as in Figs. 1g and 5b, respectively.

harmonic *3* is the highest. The intensities of harmonics *1*, *2*, and *4* amount to 7, 28, and 3% (Fig. 2a) and 10, 80, and 1% (Fig. 2b), respectively, relative to that of harmonic *3*.

The hysteretic dependences in Fig. 2 are of two types. Some of them form closed contours (when the curves intersect), while others contain well-defined portions of standard hysteretic loops. It should be noted that if the response of a medium is nonstationary, nonself-intersecting curves may also be observed in a linear medium. However, these curves will appear only at the center (carrier) frequency of the pulse, since new frequencies will not be generated because of the linear propagation. Also, in a linear medium, it is impossible to obtain the hysteretic dependence of the frequency of the highest intensity harmonic on the pulse amplitude, because the resonance frequency does not exhibit such a dependence. Figure 2 illustrates that the interaction nonlinearity is of great concern in the appearance of hysteretic dependence of the frequency of the highest intensity harmonic on the amplitude of the applied pulse. Additional evidence can be gained from Figs. 5e and 5f.

The run of the curves discussed above is independent of the pulse shape and sign of β. Figures 3a and 3b demonstrate the time evolution of the frequency of one harmonic under the action of a trapezoidal (Eq. (2")) and triangular (Eq. (2')) pulse, respectively, for negative β. During most of the pulse, the spectral intensity of this harmonic is 2–5% relative to the most intense harmonic generated at a hysteresis-free frequency. By the end of the pulse, its intensity grows to 10% or more relative to the highest intensity. Hysteresis is pronounced in both cases. For the trapezoidal pulse (Fig. 3a), the extreme point (at $A_{ext} \approx 0.62$) is as if extended: the frequency of the harmonic studied remained unchanged for a time because the pulse amplitude was constant.

Obviously, the appearance and disappearance of the hysteresis at a fixed elementary time interval must also depend on the maximal amplitude of the pulse, since it specifies the shift of the frequency of nonlinear resonance. By way of example, Fig. 4 demonstrates the ω_k vs. A_{ext} dependence when the maximal amplitude of the pulse grows. The initial value is $E_0 = 9$, at which the hysteresis is absent (Fig. 4a) and the shape of the pulse transmitted is essentially asymmetric (see also Fig. 5).

As the maximal amplitude of the pulse grows, the curves close at smaller A_{ext} and a hysteresis loop appears (Fig. 4b). With a further increase in E_0 to 11.25, the hysteresis loop shifts nonmonotonically along the abscissa axis; accordingly, the frequency at which the spectral amplitude is maximal also varies. Finally, at $E_0 = 11.5$, the hysteresis dependence of ω on the pulse amplitude disappears (Fig. 4h). This is because the scale of hysteresis development becomes less than the elementary time interval used ($T = 100$).

Medium with saturable restoring force. In this case (Eq. (1")), the dependences are similar, as illustrated in Fig. 5, where the curves are calculated for several frequencies of the applied signal. Here, the nonlinear response of the medium is more complicated and the hysteresis phenomena depend on the frequency mismatch between the pulse and nonlinear resonance much more strongly. For example, at $\omega = 1.098$, the frequency of the locally maximal spectral amplitude becomes dependent on the pulse amplitude (Fig. 5a). At higher frequencies of the optical pulse, a hysteresis loop appears (Fig. 5b) and is retained up to $\omega = 1.13$ (Figs. 5c, 5d). With $\omega = 1.14$, the hysteresis loop disappears.

CONCLUSION

Thus, under the nonlinear action of a femtosecond pulse, the frequency at which the spectral intensity is maximal may exhibit the hysteretic dependence on the pulse amplitude. This means that the hysteretic dependence of this frequency on time takes place near the center frequency of one or several harmonics generated.

The effect discovered apparently opens a new class of all-optical switches where light waves of certain frequencies are assigned to various states. The obvious advantages of these switches are the insignificant attenuation of the optical energy, the feasibility of realizing many hysteretic dependences simultaneously, as well as the fact that switching times fall into the femtosecond range.

Note once again that these hysteresis phenomena stem from the nonlinearity of the process. The non-stationary response of the medium to a femtosecond pulse is known to render the shape of the pulse transmitted asymmetric. In the spectral analysis of the pulse carried out in this work, its nonsymmetry shows up in the bifurcation of the curves $\omega(A_{ext})$. As an example, Figs. 5e and 5f illustrate the variation of the most intense harmonic with the amplitude of the triangular pulse passing through a linear medium with a nonstationary response. If the action on the medium is sufficiently strong (the effect of polarization is significant), the shape of the pulse deforms and the curve $\omega_k(A_{ext})$ bifurcates (Figs. 5c and 5d). It is the nonstationarity of the process and the high excitation of the medium that are responsible for the bisecting of the curves $\omega_k(A_{ext})$ in previous figures.

ACKNOWLEDGMENTS

This work was partially supported by the Russian Foundation for Basic Research (grant no. 02-01-727).

REFERENCES

1. S. M. Gladkov and N. I. Koroteev, Usp. Fiz. Nauk **160** (7), 105 (1990) [Sov. Phys. Usp. **33**, 554 (1990)].
2. M. V. Korolkov, J. Manz, and G. K. Paramonov, Chem. Phys. **217**, 341 (1997).
3. A. I. Maĭmistov, Kvantovaya Élektron. (Moscow) **30**, 287 (2000).
4. I. R. Shen, *Principles of Nonlinear Optics* (Wiley, New York, 1984; Nauka, Moscow, 1989).
5. A. V. Andreev and A. B. Kozlov, in *Proceedings on Ultrafast Phenomena and Interaction of Superstrong Laser Fields with Matter: Nonlinear Optics and High-Field Physics*, Ed. by M. V. Fedotov *et al.*, Proc. SPIE **3735**, 75 (1998).
6. D. K. Skripov and V. A. Trofimov, in *Laser Physics and Spectroscopy*, Ed. by V. L. Derbov, L. A. Melnikov, and V. P. Ryabukho, Proc. SPIE **4002**, 34 (2000).
7. D. K. Skripov and V. A. Trofimov, Tr. UNTs Volok.-Opt. Mater. Ustr., No. 3, 83 (2000).
8. D. K. Skripov and V. A. Trofimov, Pis'ma Zh. Tekh. Fiz. **27** (14), 6 (2001) [Tech. Phys. Lett. **27**, 575 (2001)].
9. D. K. Skripov and V. A. Trofimov, Opt. Spektrosk. (in press).
10. M. I. Rabinovich and D. I. Trubetskov, *An Introduction to the Theory of Vibrations and Waves* (NITs Regul. Khaot. Din., Izhevsk, 2000).
11. V. A. Trofimov and D. K. Skripov, in *Program and Abstracts of the Second Conference "Superstrong Fields in Plasmas," Varenna, Italy, 2001*, p. 8.

Translated by V. Isaakyan

Technical Physics, Vol. 48, No. 3, 2003, pp. 349–353. Translated from Zhurnal Tekhnicheskoĭ Fiziki, Vol. 73, No. 3, 2003, pp. 75–79.

**OPTICS,
QUANTUM ELECTRONICS**

Resolutions of Quantum Double-Resonance Frequency Discriminators of Two Types: Comparative Analysis

E. B. Aleksandrov and A. S. Pazgalev

*Vavilov State Optical Institute, All-Russia Research Center,
Birzhevaya Liniya 12, St. Petersburg, 199034 Russia*

e-mail: ealex@online.ru

Received September 2, 2002

Abstract—The resolutions of quantum frequency discriminators of two types are compared with analytical and numerical calculations. It is shown that a double-coherent-field device does not offer significant advantages over a conventional double-resonance device for frequency discrimination. © *2003 MAIK "Nauka/Interperiodica".*

INTRODUCTION

A quantum frequency discriminator (QFD) is a quantum (two-level in the simplest case) device that resonantly responds to a variable probe field. In this way, the probe field frequency is compared with the natural frequency of the system. QFDs are widely used in frequency meters, time counters, and magnetometers. Discriminators are characterized by their resolution, i.e., the least detectable (with a given degree of confidence) deviation of the probe field frequency from its rated value.

The necessary condition for QFD operation is a difference in the populations of combining states. More generally, the system's density matrix must be nonunit. This condition is fulfilled automatically, since relaxation processes excessively populate the lower energy sublevel. However, if the natural frequency of a discriminator is small compared with the thermal energy, the population difference (and, accordingly, the QFD efficiency) is also small. This trouble is obviated by means of "pumping." Such an expedient is applied to a multilevel system where at least one additional level with an energy far exceeding the energies of two operating levels is present. Specifically, if the energy of the third level is many times higher than the thermal energy and the level is empty in equilibrium, the pumping is efficient (so-called "optical pumping" [1]). The simplest scheme of optical pimping is depicted in Fig. 1. Operating levels *1* and *2* are assumed to be long-lived (the relaxation rate $\gamma = 2\pi T_1^{-1}$, where T_1 is the time of longitudinal relaxation), while high-lying level *3* is short-lived and decays spontaneously into states *1* and *2*. Using a pump field I_p to selectively excite, for example, the transition *1–3*, one can create an excess population of level *2*. Then, a probe field *V* at a frequency ω that is close to the frequency ω_{12} of the transition *1–2* will reduce the population of level *2* and cause the coherence ρ_{12}, which can be used as a resonant response. It is essential that this response can be observed in an optical pump channel with a high quantum yield. The approach described has been given the title Kastler–Brossel double radiooptical resonance. Shortly after its discovery, a modification of double resonance was suggested and demonstrated. This version is today variously known, since many researchers arrived at it independently (see review [2]). We will use the term "Λ resonance." This name is associated with the transition scheme (Fig. 2). Here, in a three-level system, two high-frequency transitions *1–3* and *2–3* are excited by

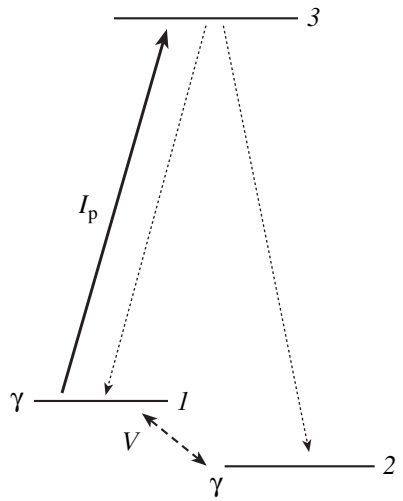

Fig. 1. Optical pumping in a three-level system.

1063-7842/03/4803-0349$24.00

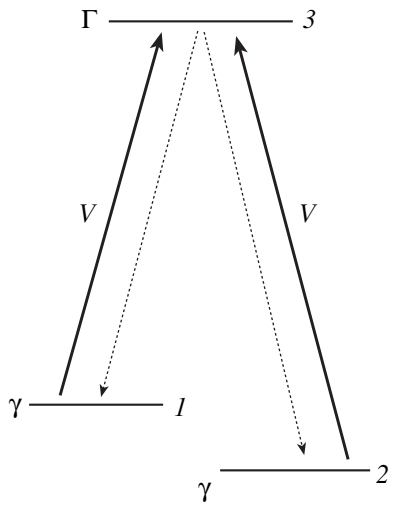

Fig. 2. Three-level △ scheme.

applying fields V with frequencies ω_1 and ω_2. Under conditions of double resonance, when the equalities $\omega_1 = \omega_{13}$ and $\omega_2 = \omega_{23}$ hold, the coherence ρ_{12} at the combination frequency $\omega_{12} = \omega_1 - \omega_2$ arises and the population of top level *3* is the least (hence, another name "dark resonance," since the luminescence intensity drops in this case). To date, many approaches to using △ resonance as a means for measuring the transition frequency ω_{12} have been suggested and implemented. It is assumed (explicitly or implicitly) that this method offers improved accuracy, since the field directly connecting states *1* and *2* is absent. The obvious disadvantage of the method is that the relatively low frequency ω_{12} is measured as a difference of the two high frequencies ω_1 and ω_2. However, the situation can be readily remedied if the frequency ω_2 is obtained by mixing the frequency ω_1 with a low reference frequency Ω in the vicinity of the desired combination frequency ω_{12}. If the widths of the high-frequency resonances at ω_{13} and ω_{23} are many times that of the Raman resonance at ω_{12}, the instability of the high frequency ω_1 will not affect the accuracy of ω_{12} measurements (such an approach was used in the early experimental demonstration of rubidium spin coherent precession excited by absorbing polarized light modulated at the precession frequency [3]).

Nevertheless, these basic advantages of the △ resonance method have not been proved until now. Our work is an attempt to quantitatively compare the two double-resonance approaches in terms of frequency discrimination efficiency. First, we considered an idealized three-level system and made sure that △ resonance basically can twice improve the resolution of a discriminator. Then, using the simplest real medium, ^{4}He atoms, we compared the calculated efficiencies for the two types of QFDs.

RESOLUTION ANALYSIS FOR △ AND RADIOOPTICAL RESONANCES IN A MODEL THREE-LEVEL SYSTEM

Let us turn back to Figs. 1 and 2. They can be analyzed by solving an equation for the density matrix ρ_{ik} subject to appropriate simplifications. In Fig. 1, the system can be viewed as a system of two levels (*1* and *2*) where optical pumping via channel *1–3* is a relaxation process with a rate I_p, which establishes a stationary population difference between levels *1* and *2* (initially equipopulated). The interaction with the coherent field of frequency ω for transition *1–2* will be considered in the conventional rotating-wave approximation. The coherence $\rho_{12}(t)$ will be used as a system's response. A set of equations for the density matrix has the form

$$id\rho_{11}/dt = -i\gamma(\rho_{11} - 1/2) - iI_p\rho_{11} + 1/2iI_p\rho_{11} + V(\rho_{21} - \rho_{12}),$$

$$id\rho_{22}/dt = -i\gamma(\rho_{22} - 1/2) + 1/2iI_p\rho_{11} + V(\rho_{12} - \rho_{21}),$$

$$id\rho_{12}/dt = +\delta\rho_{12} - i\Gamma_{12}\rho_{12} + V(\rho_{22} - \rho_{11}).$$

Under stationary conditions, the coherence oscillates with a frequency ω and its complex amplitude is given by

$$\rho_{12} = -\frac{VI_p}{2\Gamma_{12}}\frac{\delta + i\Gamma_{12}}{\delta^2 + \Gamma_{12}^2 + 4V^2}.$$

Here, V is the matrix element of coupling with a variable field (Rabi frequency), $\delta = \omega - \omega_{12}$ is the detuning of the resonance, $\Gamma_{12} = \gamma + I_p/2$ is the resonance halfwidth, I_p is the optical pumping rate, and γ is the population relaxation rate in the absence of pumping. It is assumed that level *3* decays into states *1* and *2* equiprobably. If the probabilities of spontaneous decay differ, the expression for the coherence takes the form

$$\rho_{12} = -V\kappa I_p\frac{\delta + i\Gamma_{12}}{(\delta^2 + \Gamma_{12}^2)(\gamma + \kappa I_p) + 4V^2\Gamma_{12}},$$

where κ is the probability of decay into state *2*.

A frequency discriminator is convenient to design so that the real part of the coherence is detected. The real part is a dispersion curve vanishing at the exact resonance frequency. The steepness S of the discriminator response in the vicinity of a resonance,

$$S = d(\mathrm{Re}\rho_{12})/d\delta|_{\delta = 0},$$

should be optimized in terms of the pumping rate I_p and field V. Its maximum, $(16\gamma)^{-1}$, is reached with $V = \gamma$, $\Gamma_{12} = 2\gamma$, and $I_p = 2\gamma$.

In the case of the △ resonance method, it is necessary to solve an equation for the density matrix when the system has three levels and two coherent fields at frequencies ω_1 and ω_2. The rotating wave approximation remains valid, so that the problem can be solved exactly. The general solution was repeatedly obtained

earlier. However, it is so awkward that only specific cases were published. We will also restrict our analysis to the specific case for the coherence ρ_{12} when the Rabi frequencies obey the equalities $V_{13} = V_{23} = V$. In addition, we will assume that the radiation width Γ of the top-most level *3* is many orders of magnitude greater than the width of pumping-undisturbed operating transition *1–2*. The associated set of equations is as follows:

$$id\rho_{11}/dt = V(\rho_{31} - \rho_{13}) - i\gamma(\rho_{11} - 1/2) + 1/2i\Gamma\rho_{33},$$

$$id\rho_{22}/dt = V(\rho_{23} - \rho_{32}) - i\gamma(\rho_{22} - 1/2) + 1/2i\Gamma\rho_{33},$$

$$id\rho_{33}/dt = V(\rho_{13} - \rho_{31} + \rho_{23} - \rho_{32}) - i\Gamma\rho_{33},$$

$$id\rho_{13}/dt = +\delta_{31}\rho_{13} - 1/2i\Gamma\rho_{13} + V(\rho_{33} - \rho_{11}) - V_{23}\rho_{12},$$

$$id\rho_{23}/dt = +\delta_{32}\rho_{23} - 1/2i\Gamma\rho_{23} + V(\rho_{33} - \rho_{22}) - V_{13}\rho_{21},$$

$$id\rho_{12}/dt = +\delta_{21}\rho_{12} - i\gamma\rho_{12} + V(\rho_{32} - \rho_{12}).$$

For the coherence ρ_{12} to occur, the fulfillment of the resonance condition $\omega_1 - \omega_2 = \omega_{12}$ is of prime importance, while resonances at the pumping frequencies take place automatically because level *3* is sufficiently wide. Introducing symmetric and equal detunings for the pump fields, $\delta_{31} = \omega_1 - \omega_{31} = -\delta_{32} = \omega_{32} - \omega_2 = \delta \gg \Gamma$, we arrive at the expression for the dispersion part y_{12} of the coherence $\rho_{12} = x_{12} + iy_{12}$

$$y_{12} = \delta V^2\Gamma^{-1}[\delta^2 + (\gamma/2 + 2V^2/\Gamma)^2]^{-1}.$$

The steepness of the discrimination curve $dy_{12}/d\delta$ in the absence of the detuning, $\delta = 0$, has the form

$$S(y_{12}) = V^2/\Gamma/(\gamma/2 + 2V^2/\Gamma)^2.$$

It is maximal when $V^2 = \Gamma\gamma/4$:

$$S(y_{12})_{\max} = 1/(4\gamma).$$

The extrema of the discrimination curve are found at $V^2 = \Gamma\gamma/4$ and $\delta = \pm\gamma$. They equal $(y_{13})^{\text{extr}} = \pm 1/8$, respectively.

When comparing the maximal steepness of a $\triangle$ discriminator with that of a discriminator designed as shown in Fig. 1, one should bear in mind that the equal-in-magnitude and opposite-in-sign detunings adopted above correspond to the doubled detuning of Raman resonance: $\delta_{12} = 2\delta$. Therefore, the maximal steepness of a $\triangle$ discriminator per single detuning of Raman resonance is halved and becomes equal to $1/(8\gamma)$.

Thus, all other things being equal, the optimized steepness of a $\triangle$ discriminator, which is proportional to the resolution, is twice as large as that of a discriminator based on double radiooptical resonance.

EFFICIENCY ANALYSIS FOR DISCRIMINATORS OF BOTH TYPES WITH CONSIDERATION FOR THE REAL ATOMIC LEVEL STRUCTURE

The above comparison was made for the model three-level system. However, any real structure is more complicated and includes no less than four levels. The simplest atomic system suitable for the method of double radiooptical resonance is a helium atom in the metastable triplet state. In a magnetic field, this state is split into three equidistant sublevels with the spin projections 0 and ±1. This effect is conventionally used in magnetometry. For the optical pumping of helium, the closely spaced lines of the triplet $2^3S_1 \rightleftharpoons 2^3P_{0,1,2}$ are usually used. By means of a laser, the line $2^3S_1 \rightleftharpoons 2^3P_0$ (D_0 line, 1.083 μm) can be selectively excited, allowing the realization of the simplest four-level system (Fig. 3).

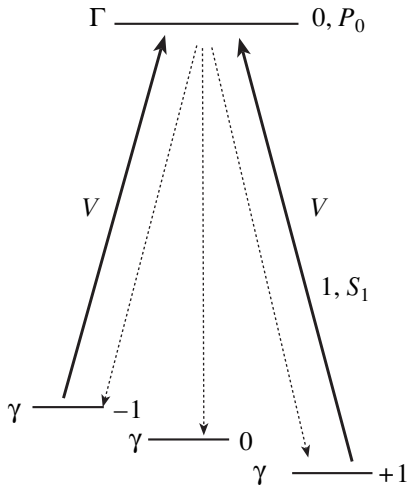

Fig. 3. Transitions between the 2^3S_1 and 2^3P_0 levels in a helium atom.

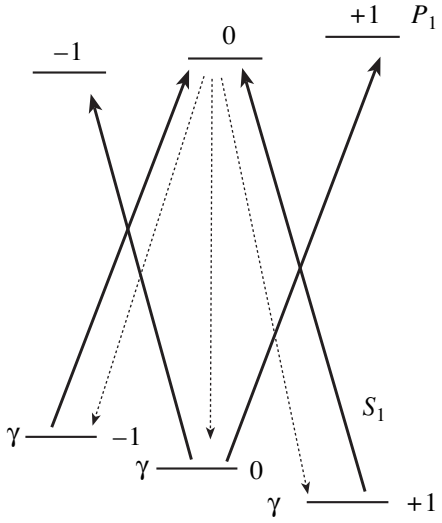

Fig. 4. $2^3S_1 \rightleftharpoons 2^3P_1$ transitions in a helium atom initiated by two pairs of coherent optical fields.

To achieve maximal magnetic sensitivity in the $\triangle$ version, the excited level 2^3P_0 must obviously be related to the $m = \pm 1$ sublevels of the state 2^3S_1 by two

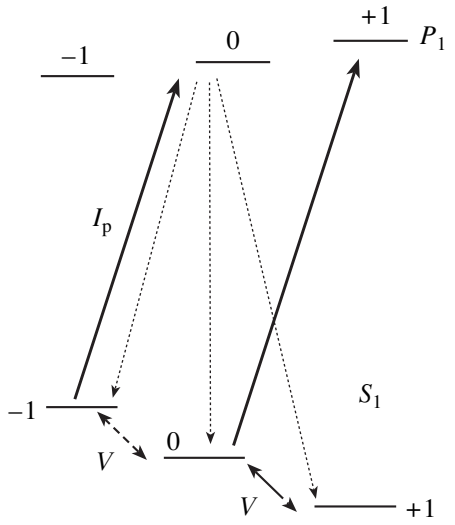

Fig. 5. $2^3S_1 \rightleftharpoons 2^3P_1$ transitions in a helium atom. Orientation due to pumping by incoherent light.

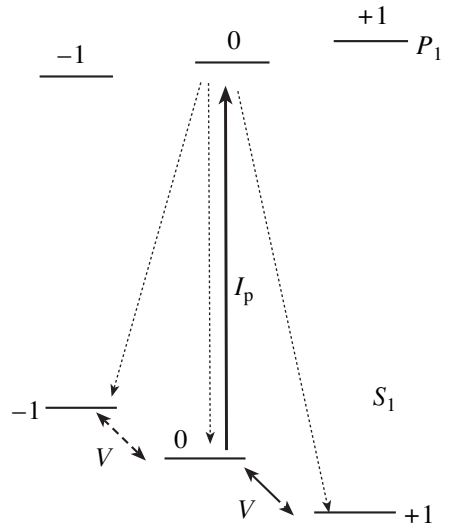

Fig. 6. Alignment due to the excitation of the 2^3S_1, $m = 0 \rightleftharpoons 2^3P_1$, $m = 0$ transition by linearly polarized light.

coherent optical harmonics with appropriate polarizations (Fig. 4). In practice, this can be done most conveniently by exciting metastable helium along the magnetic field by a radiation whose plane of polarization rotates with a frequency ω close to the Larmor frequency $\omega_{10} = \omega_{-10}$, which linearly depends on the field with a proportionality coefficient of ≈28 Hz/nT.

The calculation of the discrimination curve steepness optimized in terms of pumping radiation intensity yields $0.071\gamma^{-1}$. This value is almost half as high as that calculated for the idealized three-level system. The difference is due to the presence of the "idle" sublevel 2^3S_1, $m = 0$, especially if it is taken into account that its population increases because of the pumping and reaches 0.42. The "leakage" of the atoms to the idle sublevel can be suppressed in a more sophisticated scheme using the transition $2^3S_1 \rightleftharpoons 2^3P_1$ (D_1 line, 1.083 μm). Here, for the same type of optical excitation, the △ scheme coexists with the V scheme owing to the coherent excitation of the two transitions 2^3S_1, $m = 0 \rightleftharpoons 2^3P_1$, $m = \pm 1$. Since the excited state is wide, its magnetic splitting does not resonate with the V scheme; the role of the latter is to deplete the idle sublevel 2^3S_1, $m = 0$. The calculation of the discrimination curve steepness yields $\approx 0.105\gamma^{-1}$ in this case, which is close to the limiting value. The population of the idle level in resonance is 0.152.

In passing to the situation of usual radiooptical resonance in helium, it is necessary to separately consider the cases of optical alignment and orientation. When pumping along the field is accomplished by circularly polarized light (Fig. 5), the $m = -1$ sublevel is depleted, while the $m = 0$ and +1 sublevels of the S_1 state are enriched. This causes the effect of optical orientation. The orientation signal is observed at the frequency ω of the applied radio field *V*. The calculation shows that the coherence signal ρ_{0+1} between the sublevels $m = 0$ and +1 has the maximal discrimination steepness, $\approx 0.062\gamma^{-1}$.

When the optical transition 2^3S_1, $m = 0 \rightleftharpoons 2^3P_1$, $m = 0$ is initiated by linearly polarized light (Fig. 6), alignment takes place, which is characterized by the depletion of the $m = 0$ sublevel. The resonant rf field *V* with the frequency of the transition 2^3S_1, $m = 0 \rightleftharpoons m' = \pm 1$ partially restores the equilibrium populations and generates coherences at the field frequency and at the doubled frequency. The maximal discrimination steepness, $\approx 0.06\gamma^{-1}$, is observed at the doubled frequency. Longitudinal alignment of opposite sign appears at the incoherent pumping of the transitions 2^3S_1, $m = \pm 1 \rightleftharpoons 2^3P_0$, $m = 0$, which occurs, for example, when atoms are excited along the magnetic field by linearly polarized light. In this case, the coherence at the doubled frequency ρ_{-11} is also the coherence of choice, since it provides a maximal discrimination steepness of $\approx 0.038\gamma^{-1}$. Note that in this case, too, the steepness is lower than for the △ scheme ($\approx 0.071\gamma^{-1}$).

CONCLUSION

Our mathematical simulation shows that the △ scheme (double resonance using two coherent fields) does not have any distinct advantages over the conventional approach (double radiooptical resonance with a single coherent field) in terms of frequency discrimination. Therefore, in deciding on a particular method, one should take into consideration the real atomic level structure and also a number of experiment-related factors, such as optical pumping efficiency, quantum yield of a photodetector, and the relaxation characteristics of an operating transition and its frequency. As a rule,

magnetic resonance is easier to induce with an rf magnetic field rather than by producing two coherent harmonics. Sometimes, however, it is more convenient to do without an rf inductor. In this case, the all-optical △ scheme may appear to be preferable.

ACKNOWLEDGMENTS

This work was supported by the program "Fundamental Metrology" (grant no. 106-23(00)P).

REFERENCES

1. A. Kastler and C. Cohen-Tannoudji, Prog. Opt. **5**, 1 (1966).
2. E. Arimondo and E. Wolf, Prog. Opt. **35**, 257 (1966).
3. W. Bell and A. Bloom, Phys. Rev. Lett. **6**, 280 (1961).

Translated by V. Isaakyan

Technical Physics, Vol. 48, No. 3, 2003, pp. 354–360. Translated from Zhurnal Tekhnicheskoĭ Fiziki, Vol. 73, No. 3, 2003, pp. 80–86.

ACOUSTIC, ACOUSTOELECTRONICS

Efficiency of Shear Surface Wave Transformation by the Motion of the Confining Domain Wall

E. A. Vilkov*, V. G. Shavrov, and N. S. Shevyakhov***

** Institute of Radio Engineering and Electronics, Ul'yanovsk Division, Russian Academy of Sciences, Ul'yanovsk, 432011 Russia*

*** Institute of Radio Engineering and Electronics, Russian Academy of Sciences, Mokhovaya ul. 11, Moscow, 103907 Russia*

Received April 18, 2002

Abstract—The transformation of a shear surface magnetoelastic wave by the motion of the 180° confining domain wall in a ferromagnet is considered. Changes in the wave spectrum due to the motion of the wall are correlated with the variations of the energies of the elastic and magnetic subsystems. The efficiency of surface wave transformation by the domain wall motion is estimated in terms of energy. The frequency dependences of the mean energy density of the wave are found. It is shown that the energy density grows with wall velocity.

INTRODUCTION

Recently [1, 2], we considered (in the exchangeless magnetostatic approximation) the dispersive properties of a shear surface magnetoelastic wave (SSW) on a 180° geometrical domain wall moving with a nonrelativistic velocity in a cubic ferromagnet. The approach adopted in [1, 2] relies on the well-known fact in magnetodynamics [3–5] that a domain wall (DW) is fairly stable against weak perturbations introduced by the wave and control actions moving the wall. The subthreshold DW motion conditions and a low structural sensitivity of DWs to external effects (which is usually observed away from the phase transition [6]) make it possible to consider the motions of the wave and DW separately. The latter motion is included in the boundary conditions of the problem. Naturally, with such a statement, wave–wall interaction becomes incomplete and can be described as a parametric action on the system [7, 8] from an implicitly given source. In spite of the disadvantages of this approach, it seems to be promising (especially when combined with the small-signal approximation), since it allows one to avoid hard-to-perceive magnetodynamic solutions and leaves room for invoking analytical methods of Fourier spectroscopy.

The aim of this work is to consider the energy aspects of SSW transformation via DW motion, which were not covered in [1, 2]. First of all, it would be of interest to find a correlation between changes in the SSW spectrum (including in the frequency dependence of the factor of wave localization at the wall) and the wall-motion-induced variations of the energy of the elastic and magnetic subsystems. To estimate the efficiency of SSW parametric transformation by DW motion, it is useful to discuss the variation of the mean energy with DW velocity.

It is worth noting that, according to our approach [1, 2] to treating an SSW on a moving DW, the wave energy alone can be considered. Energy redistribution between the wave and moving DW is virtually postulated to be negligibly small. This does not mean that such issues as the stability of a DW and the adequacy of its geometrical (structureless) model are completely ignored. For example, a large increment of the SSW mean energy combined with a sharply enhanced localization of the wave at the wall can serve as a heuristic test for loss of the above properties.

A SHEAR SURFACE WAVE IN THE COORDINATE SYSTEM RELATED TO A MOVING DOMAIN WALL

In [1, 2], results were obtained for cubic ferromagnets with both a positive and negative magnetic anisotropy constant K_1. Accordingly, the appearance of internal magnetic fields $\mathbf{H}_i \parallel \tilde{z}$ in semi-infinite domains separated by the DW plane $\tilde{y} = 0$ ($\tilde{x}0\tilde{y}\tilde{z}$ is the frame of reference related to the moving DW) is associated with the effect of magnetic anisotropy. In other words, it is assumed that $H_i \equiv H_a$, where H_a is the field of magnetocrystalline anisotropy: $H_a = 2K_1/M_0$ if $K_1 > 0$ and $H_a = -4K_1/3M_0$ if $K_1 < 0$ [9] (M_0 is the spontaneous magnetization in the domains). The $\tilde{y}$ axis coincides with the direction of DW propagation and easy magnetic axis in a ferromagnet.

Thus, in the laboratory frame of reference $x0yz$, a DW is a (010)-oriented (if $K_1 > 0$) or a (111)-oriented ($K_1 < 0$) wall. The renormalization of the shear modulus

1063-7842/03/4803-0354$24.00 © 2003 MAIK "Nauka/Interperiodica"

λ and magnetoelastic coupling coefficient β, which is necessary in the latter case, is given in [10]. For an isolated 180° DW in a ferromagnet to be considered as geometrically thin and structureless, we impose the restriction $k_{sh}\Delta \ll 1$, where k_{sh} is the wavenumber of shear waves and Δ is the DW thickness. This restriction allows us to apply the exchangeless magnetostatic approximation up to the bottom of the frequency gap in the magnetoelastic wave spectrum [11, 12]. We also assume that the DW structure remains unchanged as the DW moves along the y axis. For bulk (nonfilm) ferromagnets like YIGs, this assumption is valid for DW velocities $V_D < c_{sh}$ (c_{sh} is the shear wave velocity in the absence of magnetoelastic coupling) [3] provided that the DW structure is not too sensitive to external effects near the phase transition [6].

To be definite, we assume that the magnetic anisotropy constant of a ferromagnet is positive. Then, aligning the easy magnetic axis with the crystallographic direction [001] $\parallel z$, one can relate the DW to the moving coordinate $y = y_D$ ($y_D = V_D t$, where t is time). Also, it can be assumed that shear waves travel in the plane (001) and that their displacements $u_j \parallel z$ are collinear with spontaneous magnetizations $\mathbf{M}_0^{(j)}$ in the domains ($\mathbf{M}_0^{(1)} \uparrow\downarrow \mathbf{M}_0^{(2)} \parallel [111]$, where $j = 1, 2$ is the domain number). Accordingly, the internal magnetic fields $\mathbf{H}_i^{(j)} \parallel z$ of the domains and the spontaneous magnetizations are given by

$$M_0^{(j)} = (-1)^{j+1} M_0, \quad H_i^{(j)} = (-1)^{j+1} H_a, \qquad (1)$$

where $j = 1$ at $y = y_D$ and $j = 2$ at $y < y_D$.

Since $V_D < c_{sh}$ and $c_{sh} \ll c$, where c is the velocity of light, the rest frame of the DW can be related to the laboratory frame by the Galilean transformation $\tilde{x} = x$, $\tilde{y} = y - V_D t$, $\tilde{z} = z$, $\tilde{t} = t$. Therefore, the transition to the rest frame of the DW is accomplished by replacing the differential operators: $\partial/\partial x \longrightarrow \partial/\partial\tilde{x}$, $\partial/\partial y \longrightarrow \partial/\partial\tilde{y}$, $\partial/\partial t \longrightarrow \partial/\partial\tilde{t} - V_D\partial/\partial\tilde{y}$. Then, the initial equations [1, 2] are represented in the form

$$\rho\left(\frac{\partial}{\partial\tilde{t}} - V_D\frac{\partial}{\partial\tilde{y}}\right)^2 u_j = \lambda\tilde{\nabla}^2 u_j + \frac{(-1)^{j+1}\beta}{4\pi M_0}\tilde{\nabla}^2\varphi_j,$$

$$\left[\left(\frac{\partial}{\partial\tilde{t}} - V_D\frac{\partial}{\partial\tilde{y}}\right)^2 + \omega_k^2\right]\tilde{\nabla}^2\varphi_j \qquad (2)$$

$$= -4\pi\gamma\beta\omega_0(-1)^{j+1}\tilde{\nabla}^2 u_j,$$

where $\tilde{\nabla}^2 = \partial^2/\partial\tilde{x}^2 + \partial^2/\partial\tilde{y}^2$, γ is the gyromagnetic ratio, ρ is the density, and φ_j is the potential of the dynamic part of the magnetic field.

Equations (2) are supplemented by the standard boundary conditions from the theory of ferrite magnetoacoustics [10, 11]. They imply that the potentials, tangential displacements, normal components of shear stresses, and dynamic component of the induction are continuous at the DW (i.e., for $\tilde{y}$).

It was shown [1, 2] that Eqs. (2) have the unique solution (in terms of field boundedness and SSW noncollinearity due to DW motion)

$$\varphi_j = \Phi_j - \frac{4\pi\gamma\beta\omega_0(-1)^{j+1}}{\omega_k^2 + [i(\Omega + pV_D) + s(-1)^j V_D]^2}u_j,$$

$$u_j = U_j \exp i(k\tilde{x} + p\tilde{y})\exp(-i\Omega\tilde{t})\exp[(-1)^j s\tilde{y}], \quad (3)$$

$$\Phi_j = F_j \exp[i(k\tilde{x} - \Omega\tilde{t})]\exp[(-1)^j k\tilde{y}],$$

where $\omega_0 = \gamma H_a$, $\omega_k^2 = \omega_0(\omega_0 + \omega_m)$, $\omega_m = 4\pi\gamma M_0$, and Ω is the SSW frequency in the rest frame of the DW.

The parameters p and s are the transverse component of the wave vector and the SSW amplitude decline factor. Schematically, the wave front pattern and the tangential displacement distribution in it (u_j given by (3)) are depicted in Fig. 1. From (3), it follows that the motion of the DW has an orienting effect on the SSW wave normal, which is deflected toward the vector $\mathbf{V}_D$ by an acute angle $\Theta = \arctan(p/k)$. Such a wind-vane effect indicates that the SSW wave vector $\mathbf{K} = \mathbf{k} + \mathbf{p}$ ($\mathbf{p} \parallel \mathbf{V}_D$, $pV_D > 0$) and the DW directrix are noncollinear; therefore, it can be said that we are dealing with a new class of boundary waves—noncollinear boundary waves [1, 2].

It has already been noted [2] that, according to (3), an SSW possesses a unidirectional continuous energy flux, which penetrates a DW; therefore, a DW cannot be considered as an energy source or sink. As a result, SSWs propagate along a moving DW in the steady regime, i.e., without amplification or damping: $\mathrm{Im}k = 0$ and $\Omega > 0$. It has also been mentioned that the transverse component of the energy flux (this component is nonuniform along the $\tilde{y}$ coordinate) is the energy of an SSW coupled with the DW via the magnetic poles (Fig. 1) (this energy component is transferred by the

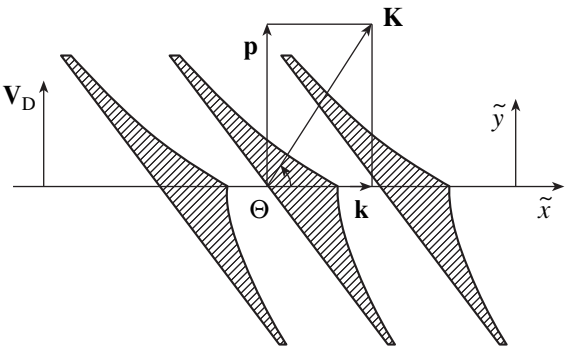

Fig. 1. Schematic pattern of a shear surface wave on a moving Bloch wall.

DW), while the longitudinal component characterizes energy transfer along the DW by the wave.

The SSW spectral parameters s, p, and Ω are related to k by the dispersion relation $\Omega = \Omega(k)$. It is obtained by substituting field representations (3) into the boundary conditions of the problem and equating the determinant of the resultant set of homogeneous algebraic equations to zero. In the laboratory frame of reference, ω is substituted for Ω,

$$\omega = \Omega + \mathbf{K}V_D = \Omega + pV_D, \tag{4}$$

and the dispersion relation $\omega = \omega(k)$ takes the form

$$s + \chi\omega_0\sigma\frac{G(\omega, V_D)}{1 + \chi\omega_0^2 F(\omega, V_D)}|k| = 0. \tag{5}$$

Here,

$$F(\omega, V_D) = \frac{(\omega^2 - s^2V_D^2 - \omega_k^2) - 2pV_D\omega}{(\omega^2 - s^2V_D^2 - \omega_k^2)^2 + 4s^2V_D^2\omega^2}, \tag{6}$$

$$G(\omega, V_D) = \frac{\omega^2 - s^2V_D^2 - \omega_k^2}{(\omega^2 - s^2V_D^2 - \omega_k^2)^2 + 4s^2V_D^2\omega^2}$$

$$\times\left[\omega - \frac{\omega_0\omega_m(\omega - \sigma\omega_0)}{(\omega - \sigma\omega_0)^2 + s^2V_D^2} + \frac{\sigma\omega_m s^2V_D^2}{(\omega - \sigma\omega_0)^2 + s^2V_D^2}\right.$$

$$\left.\times\frac{(\omega - \sigma\omega_0)^2 + s^2V_D^2 + \omega_0\omega_m}{(\omega - \sigma\omega_0)^2 + s^2V_D^2 - \sigma\omega_m(\omega - \sigma\omega_0)}\right] \tag{7}$$

$$+\frac{2s^2V_D^2\omega}{(\omega^2 - s^2V_D^2 - \omega_k^2)^2 + 4s^2V_D^2\omega^2}$$

$$\times\frac{(\omega - \sigma\omega_0)^2 + s^2V_D^2 + \omega_0\omega_m - 2\sigma\omega_m\omega}{(\omega - \sigma\omega_0)^2 + s^2V_D^2 - \sigma\omega_m(\omega - \sigma\omega_0)}.$$

In (5)–(7), χ is the magnetoelastic coupling constant and $\sigma = +1$, when the SSW propagates in the positive $\tilde{x}$ direction, or –1 when the SSW is directed oppositely.

ENERGY DENSITY OF A SHEAR SURFACE WAVE ON A MOVING DOMAIN WALL

In the rest frame of the DW, the efficiency of SSW transformation by the DW motion can be estimated by comparing the time-averaged energies per DW unit surface area at $V_D = 0$ and $V_D \neq 0$. The energies are found from the expression for the energy density of a ferromagnet [12, 13]

$$w_j = -\mathbf{m}_j \cdot \mathbf{h}_j + (-1)^{j+1}\frac{\beta}{M_0}(\mathbf{m} \cdot \nabla u_j) + \frac{\lambda}{2}(\nabla u_j)^2, \tag{8}$$

which includes the Zeeman term, the magnetoelastic energy density, and the elastic energy density. Here, $\mathbf{m}_j$ and $\mathbf{h}_j = -\nabla\varphi_j$ are the dynamic magnetic moment and magnetic field strength, respectively. The value of φ_j depends on Φ_j and u_j according to (3), and $\mathbf{m}_j$ is expressed through Φ_j and u_j from the equation of motion of magnetic moment:

$$m_x^{(j)} = \frac{\gamma\beta}{\Omega^2 - \omega_k^2}\left[-i\Omega\frac{\partial u_j}{\partial y} + (-1)^{j+1}\omega_0\frac{\partial u_j}{\partial x}\right]$$

$$+\frac{\omega_m}{4\pi(\Omega^2 - \omega_0^2)}\left[-(-1)^{j+1}i\Omega\frac{\partial\Phi_j}{\partial y} + \omega_0\frac{\partial\Phi_j}{\partial x}\right],$$

$$m_y^{(j)} = \frac{\gamma\beta}{\Omega^2 - \omega_k^2}\left[i\Omega\frac{\partial u_j}{\partial x} + (-1)^{j+1}\omega_0\frac{\partial u_j}{\partial y}\right] \tag{9}$$

$$+\frac{\omega_m}{4\pi(\Omega^2 - \omega_0^2)}\left[(-1)^{j+1}i\Omega\frac{\partial\Phi_j}{\partial x} + \omega_0\frac{\partial\Phi_j}{\partial y}\right].$$

In its turn, the amplitude factor of scattered field Φ_j, which appears in (3) and (9), depends on u_j through the boundary conditions. Certainly, formula (8) applies if the process is quasi-stationary. In our case, the quasi-stationarity means that the change in the SSW amplitude due to DW displacement is insignificant over the period T of the wave at any fixed point of the crystal; that is, $\exp(-sV_DT) \sim 1$ or $sV_D \ll \omega$. The inequality has been established to hold throughout the frequency range of the spectrum, which validates formula (8) for the SSW energy density in the rest frame of the DW.

Since expression (8) is quadratic in field, all its terms must be written in real form. To this end, the complex quantities are represented as the sum of complex and complex conjugate components and the expressions obtained are substituted into (8). Averaging ω_j over time and integrating over the $\tilde{y}$ coordinate in the first ($j = 1$) and second ($j = 2$) domains yields the time-averaged SSW energy per DW unit surface area:

$$W = \int_{-\infty}^{0} w_2 d\tilde{y} + \int_{0}^{\infty} w_1 d\tilde{y}, \tag{10}$$

Specifically, for $V_D = 0$, expression (10) takes the form

$$W_0 = W|_{V_D = 0}$$

$$= \lambda\left\{\frac{k^2 + s^2}{4s} + \chi\left[\frac{2\omega\omega_0 ks + \omega_0^2(k^2 + s^2)}{2s}\frac{(\omega^2 - \omega_0^2)}{(\omega^2 - \omega_k^2)^2}\right.\right. \tag{11}$$

$$\left.\left. - \frac{\omega_0^2\omega_m(\omega_0 + \omega)k}{(\omega^2 - \omega_k^2)^2}\left(2 - \frac{\omega_0\omega_m}{\omega^2 - \omega_0^2}\right)\right]\right\}U^2,$$

where U is the amplitude u_j in the first or second domain.

In the case of a moving DW, the energy density is the sum

$$W = W_e + W_m,$$

where

$$W_e = \frac{\lambda}{4}\frac{k^2 + p^2 + s^2}{s}U^2 \quad (12)$$

is the elastic energy density and

$$\begin{aligned} W_m = {} & \chi\lambda\{[(a_1^2 + a_2^2)\omega_m\omega\omega_0^{-2} + (a_1\omega + a_2V_Ds)\omega_0^{-1}]k \\ & + [(a_1^2 + a_2^2)\omega_m\omega_0^{-1} + a_1](k^2 + p^2 + s^2)(2s)^{-1} \\ & + b_1[k(k+s)f_1(\omega, k, V_D, s) - kpf_2(\omega, k, V_D, s)] \\ & + b_2[k(k+s)f_2(\omega, k, V_D, s) + kpf_1(\omega, k, V_D, s)] \\ & + \omega_0\omega_m^{-1}(\mathbf{l}^2 + f^2)k[a_3(\omega + \omega_0) + a_4V_Ds]\}U^2 \end{aligned} \quad (13)$$

is the magnetoelastic energy density. Here,

$$b_1 = \frac{\mathbf{l}(s+k)}{p^2 + (s+k)^2} - \frac{gp}{p^2 + (s+k)^2},$$

$$b_2 = \frac{g(s+k)}{p^2 + (s+k)^2} + \frac{\mathbf{l}p}{p^2 + (s+k)^2},$$

$$\begin{aligned} f_1(\omega, k, V_D, s) = {} & -\{(a_3a_1 + a_2a_4)(\omega + \omega_0) \\ & + (a_2a_3 - a_4a_1)V_Ds + \omega^{-1}(a_1\omega + a_2V_Ds) \\ & + a_1 + a_3\omega_0^2\omega_m^{-1} + \omega_0\omega_m^{-1}(a_3\omega + a_4V_Ds)\}, \end{aligned}$$

$$\begin{aligned} f_2(\omega, k, V_D, s) = {} & -\{(a_2a_3 + a_4a_1)(\omega + \omega_0) \\ & - (a_3a_1 + a_2a_4)V_Ds + \omega^{-1}(a_2\omega - a_1V_Ds) \\ & + a_2 - a_4\omega_0^2\omega_m^{-1} - \omega_0\omega_m^{-1}(a_4\omega - a_3V_Ds)\}, \end{aligned}$$

$$\mathbf{l} = \frac{(\omega^2 - V_D^2s^2 - \omega_k^2)\omega_0\omega_m}{\tau_1},$$

$$\begin{aligned} g = {} & -\omega_mV_Ds\frac{(\omega^2 + V_D^2s^2 + \omega_k^2)}{\tau_1} \\ & \times \frac{[(\omega - \omega_0)^2 + V_Ds^2]}{(\omega - \omega_0)^2 + V_D^2s^2 - \omega_m(\omega - \omega_0)} \\ & + \frac{\omega_m^2\omega_0V_Ds}{\tau_1}\frac{(\omega^2 - V_D^2s^2 - \omega_k^2)}{(\omega - \omega_0)^2 + V_D^2s^2 - \omega_m(\omega - \omega_0)}, \end{aligned}$$

$$a_1 = \frac{(\omega^2 - V_D^2s^2 - \omega_k^2)\omega_0^2}{\tau_1},$$

$$a_2 = \frac{2V_Ds\omega\omega_0^2}{\tau_1},$$

$$a_3 = \frac{(\omega^2 - V_D^2s^2 - \omega_0^2)\omega_m}{\tau_2},$$

$$a_4 = \frac{2V_Ds\omega\omega_m}{\tau_2},$$

$$\tau_1 = (\omega^2 - V_D^2s^2 - \omega_k^2)^2 + 4V_D^2s^2\omega^2,$$

$$\tau_2 = (\omega^2 - V_D^2s^2 - \omega_0^2)^2 + 4V_D^2s^2\omega^2.$$

The calculation of the energy densities for $V_D = 0$ and $V_D \neq 0$ by formulas (11)–(13) and the discussion of the results obtained are presented in the following section.

NUMERICAL RESULTS AND DISCUSSION

Substituting (3) into (2) and separating the real and imaginary parts gives

$$p = \frac{V_D}{c_{sh}}\frac{\omega}{c_{sh}}\frac{\omega_k^2 - 2\omega^2 - s^2c_{sh}^2(1 - 2V_D^2/c_{sh}^2) + K^2c_{sh}^2}{\omega_L^2 - \omega^2 + s^2V_D^2}, \quad (14)$$

$$\begin{aligned} K^2 = {} & (\omega_L^2 - \omega^2 + s^2V_D^2) \\ & \times \frac{(\omega_k^2 - \omega^2 + s^2V_D^2)\left[\frac{\omega^2}{c_{sh}^2} + s^2\left(1 - \frac{V_D^2}{c_{sh}^2}\right)\right] - \chi\omega_0^2s^2}{(\omega_L^2 - \omega^2 + s^2V_D^2)^2 + 4s^2\omega^2V_D^2} \\ & + 4s^2\omega^2\frac{V_D^2}{c_{sh}^2}\frac{\omega^2 - \chi\omega_0^2 + s^2c_{sh}^2(1 - V_D^2/c_{sh}^2)}{(\omega_L^2 - \omega^2 + s^2V_D^2)^2 + 4s^2\omega^2V_D^2}, \end{aligned} \quad (15)$$

where $K^2 = p^2 + k^2$ and $\omega_L^2 = \omega_k^2 - \chi\omega_0^2$.

Putting

$$|k| = \sqrt{K^2 - p^2} \quad (16)$$

in (5) and using (14) and (15), we can reduce the dispersion relation for SSWs to the form $\tilde{\mathcal{F}}(\omega, s) = 0$, which is suitable when one-dimensional nonlinear equations are solved by numerical methods [14, 15].

Numerical calculations have shown [1, 2] that the spectrum of backward-propagating SSWs ($\sigma = -1$) is affected by DW motion insignificantly. The weak nonresonant transformation of the backward-propagating SSWs shows up primarily as a change in the components of the total wavevector **K**. Therefore, we will restrict our analysis to the spectrum of forward-propagating SSWs ($\sigma = 1$).

Figure 2 shows typical spectra of forward-propagating SSWs (in the reduced spectral variables $\xi = \omega/\omega_0$ and $\eta = Kc_{sh}/\omega_0$) for DWs moving with various velocities in Y–Ga and Bi–Ca–V garnet ferrites (which have a low saturation magnetization at the usual degree of

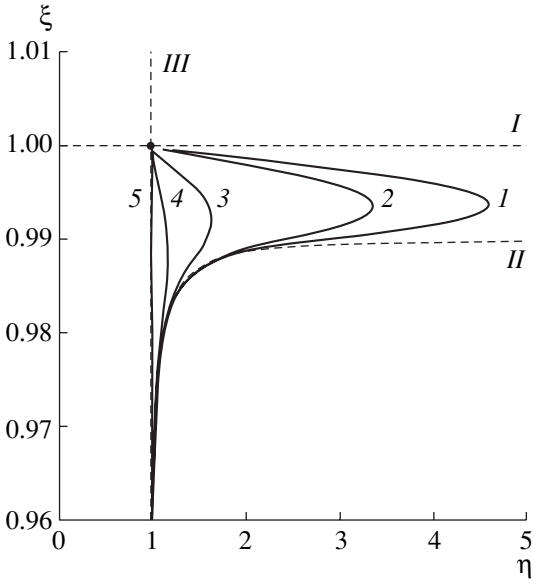

Fig. 2. Fragment of forward-propagating SSW spectrum on the moving DW. V_D/c_{sh} = 0.0007 (*1*), 0.001 (*2*), 0.003 (*3*), 0.01 (*4*), and 0.1 (*5*). Here and in Figs. 3–5, $\omega_m/\omega_0 = 0.5$ and $\chi = 0.01$.

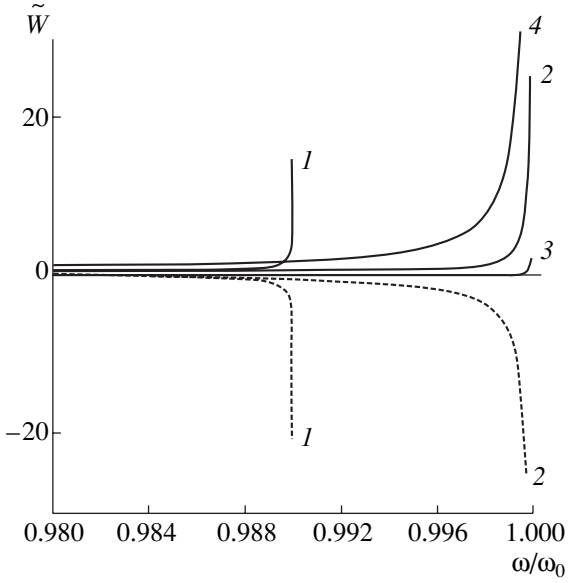

Fig. 3. Dimensionless energy density vs. reduced frequency. V_D/c_{sh} = 0 (*1*), 0.01 (*2*), 0.04 (*3*), and 0.1 (*4*).

magnetic anisotropy). Horizontal dashed line *I* represents the line of ferromagnetic resonance (FMR) ($\xi = 1$, $\omega = \omega_0$) for a static DW; dashed line *II*, the SSW spectrum branch that tends to the asymptote $\xi = 1 - \chi$ when $\eta \longrightarrow \infty$. Near-vertical dashed line *III* is a part of the spectrum of volume shear waves $k_{sh} = k_{sh}(\omega)$ in the $\chi - \eta$ representation.

The SSW dispersion spectra at $V_D \neq 0$ in Fig. 2 are loops of quasi-linear volume shear wave spectrum *III* that are cut off by FMR line *I*. In the frequency interval $1 - \chi < \xi < 1$, the loops are extended toward shorter wavelengths the stronger, the smaller V_D is. This fact was associated [1, 2] with the twofold local degeneracy of modes I and II [16] as a result of the DW motion. The similar degeneracy of the FMR spectral doublet, $\omega = \omega_0$ and $\omega = \omega_0 + \omega_m$, was also observed for magnetostatic surface waves on a moving DW [17].

Using the SSW parameters thus defined (ω, p, k, K, and s), we will calculate the mean energy density by formulas (12) and (13) and other relevant expressions. The results of calculation for the dispersion spectra in Fig. 2 are shown in Fig. 3 as the frequency dependences of the dimensionless energy density $\tilde{W} = Wc_{sh}/(\omega\lambda U^2)$ for a static DW moving with low and moderate velocities (dashed lines *1* and *2* and thin continuous lines *3* and *4*, respectively). It is seen that the SSW mean energy density grows with ω, infinitely increasing as ω approaches ω_0 at $V_D \neq 0$ (dashed curve *2* and curves *3* and *4*). As can be judged from the frequency dependences of the SSW localization coefficient in Fig. 4, this is explained by the coming delocalization of the wave ($s \longrightarrow 0$, $\omega \longrightarrow \omega_0$).

It is of interest that, in the static case and at low DW velocities, W may change sign from positive (see the initial portions of curves *1* and *2* in Fig. 3) to negative. The reason is that the negative energy W_m starts exceeding the always positive energy W_e of the elastic subsystem as the SSW spectrum for the static DW approaches its asymptote. Once can check this supposition most easily by turning to expression (11) for W_0, where the first term in the braces is the contribution to W_e. Note that the value of W_e at $V_D = 0$ is found from (12) with $p = 0$. Accordingly, the brackets in (11) will define the sign of W_m at $V_D = 0$; it is then easy to see that we actually have $W_m < 0$ with $\omega < \omega_0$.

In nonconservative energy-transferring systems, energy negativity is known [18, 19] to indicate the redistribution of the total kinetic energy among the system's constituents and instability development because of the excitation of negative-energy waves. From the standpoint of an observer moving together with the DW, the wave–wall system appears to be an energy-transferring system and seemingly can be treated in terms of the concepts put forward in [18, 19] in order to explain negative values of W ($W < 0$) at $V_D \neq 0$ (Fig. 3, dotted curve). However, the fact that W becomes positive as V_D increases (thin solid lines *3* and *4* in Fig. 3) casts some doubt on such an approach. Note also that our model of a geometrically thin and structureless DW virtually excludes the energy redistribution among the SSW and DW. To do this, it would be necessary to consider the internal degrees of freedom, i.e., virtually to pass to the problem of magnetodynamics [3–5].

This contradiction cannot be removed by introducing losses. For example, the replacement of ω by $\omega' - i\omega''$

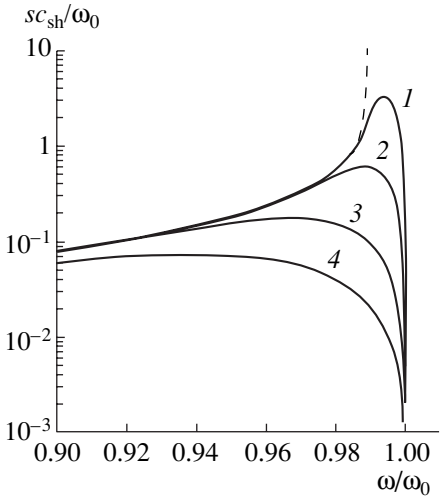

Fig. 4. Frequency dependence of the dimensionless localization factor. V_D/c_{sh} = 0.001 (*1*), 0.01 (*2*), 0.1 (*3*), and 0.5 (*4*).

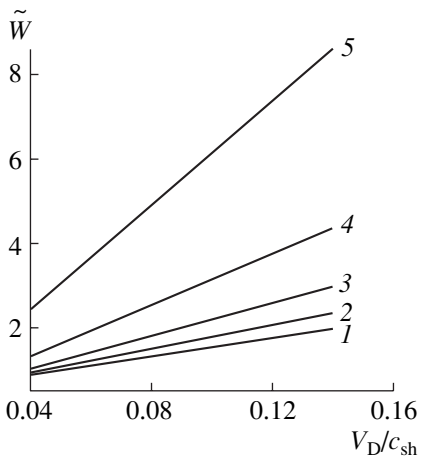

Fig. 5. Dimensionless energy density vs. reduced DW velocity. ω_m/ω_0 = 0.98 (*1*), 0.984 (*2*), 0.988 (*3*), 0.992 (*4*), and 0.996 (*5*).

($\omega''/\omega' \ll 1$) in (11) does not remove the negativity of W_0. Turning to dispersion spectrum *II* in Fig. 2, one can, however, note that W_0 changes sign exactly when the quasi-acoustic behavior of the SSW changes to magnetostatic. It is logical to assume that the exchangeless approximation, which is fairly accurate for the calculation of the SSW spectrum, turns out to be inadequate in determining the SSW mean energy. In a sense, the situation is akin to those encountered in acoustoelectronics [20, 21] when the conventional quasi-static description of electric fields in piezoelectrics, which well applies to treating solutions to boundary-value problems in the linear field statement, introduces almost 100% errors in energy characteristics that are quadratic in field (e.g., energy fluxes), whose correct finding requires exact electrodynamic analysis.

Supposing that the negativity of W in the static case and at low DW velocities is removed by taking into account exchange interaction, we will correct the results by substituting $\omega_0 + \alpha k^2$ for ω_0 in formulas (14) and (15) (α is the exchange constant and k is the SSW wavenumber corresponding to the exchangeless approximation). Essentially, such a correction is the iterative redefinition of the SSW spectral parameters by invoking formulas (5) and (6). Certainly, such a procedure does not change our approach, which, in essence, remains exchangeless.[1] It is therefore natural that this procedure does not significantly change the SSW spectrum in the transition region even at the first iteration. Nevertheless, the subsequent substitution of the SSW spectral characteristics thus corrected into (10)–(13) removes, as was expected, the negativity of W. This fact indirectly validates the above supposition that, in the presence of exchange interaction, the energy characteristics that are quadratic in field are more sensitive to the variation of the SSW spectrum than the spectra themselves. This is clearly illustrated in Fig. 3, which demonstrates the frequency dependences of $\tilde{W}$ (curves *1, 2*) obtained after the correction of $\tilde{W}$ (α = 0.1) corresponding to dashed lines *1* and *2*.

Figure 5 shows typical dependences of $\tilde{W}$ on the DW velocity for several frequency values with the correction procedure applied. It is seen that the motion of the DW always raises the SSW energy and has the most pronounced effect in the vicinity of the FMR frequency. Physically, an increase in the SSW energy due to DW motion, which shows up as a decrease in the wave localization strength and as a Doppler gain in the wave frequency, can be considered as the result of the work done on the parametrically transforming wave field during the motion of the confining DW.

The results given above were obtained for $\omega_m/\omega_0 < 1$. With $\omega_m/\omega_0 > 1$, the resonance frequencies ω_k and ω_0 will be separated still further in comparison with the case described. Qualitatively, the spectrum of SSWs on a moving wall will not change. The limiting cases $\omega_m/\omega_0 \ll 1$ ($\omega_m/\omega_0 = 0.01$, $\chi = 0.01$ and $\omega_m/\omega_0 = 0.01$, $\chi = 0.3$) were studied in [2]. In these cases, the SSW spectrum is severely modified: it is cut off by the dispersion curve of volume shear waves on the vicinity of magnetoacoustic resonance frequency lying below the FMR frequency. However, the frequency dependence of the energy density remains the same as for the SSW spectrum parameters in Fig. 2.

[1] Otherwise, it is necessary to include the exchange energy density in (8), introduce its associated terms into initial equations (2), and set additional boundary conditions.

CONCLUSION

We studied the energy efficiency of transforming SSWs by the motion of the confining DW. It was shown that the SSW transformation by DW motion is largely due to FMR appearing in scattered fields when the wave propagates in the forward direction. An increase in the DW velocity near the FMR frequency causes a substantial increase in the energy and phase velocity of the SSW compared with the same parameters for a static DW. The degree of delocalization of the wave also grows. It was demonstrated that negative values of the SSW energy, which are possible in the formally strict exchangeless approximation, can be removed by correcting the spectrum with allowance for exchange interaction.

REFERENCES

1. E. A. Vilkov, V. G. Shavrov, and N. S. Shevyakhov, Pis'ma Zh. Tekh. Fiz. **27** (17), 40 (2001) [Tech. Phys. Lett. **27**, 728 (2001)].
2. E. A. Vilkov, V. G. Shavrov, and N. S. Shevyakhov, Izv. Vyssh. Uchebn. Zaved. Radiofiz. **44**, 712 (2001).
3. V. G. Bar'yakhtar, B. A. Ivanov, and M. V. Chetkin, Usp. Fiz. Nauk **146**, 417 (1985) [Sov. Phys. Usp. **28**, 563 (1985)].
4. L. G. Potemina, Zh. Éksp. Teor. Fiz. **90**, 964 (1986) [Sov. Phys. JETP **63**, 562 (1986)].
5. F. G. Bass, I. N. Nasonov, and O. V. Naumenko, Zh. Tekh. Fiz. **58**, 1248 (1988) [Sov. Phys. Tech. Phys. **33**, 742 (1988)].
6. V. S. Gornakov, L. M. Dedukh, and Yu. P. Kabanov, Fiz. Tverd. Tela (Leningrad) **26**, 648 (1984) [Sov. Phys. Solid State **26,** 391 (1984)].
7. L. A. Ostrovskiĭ and N. S. Stepanov, Zh. Éksp. Teor. Fiz. **45**, 1473 (1963) [Sov. Phys. JETP **18**, 1018 (1964)].
8. V. N. Krasil'nikov, *Parametric Wave Effects in Classical Electrodynamics* (St. Peterb. Gos. Univ., St. Petersburg, 1996).
9. A. G. Gurevich, *Magnetic Resonance in Ferrites and Antiferromagnets* (Nauka, Moscow, 1973).
10. V. Strauss, *Physical Acoustics*, Ed. by W. P. Mason (Academic, New York, 1968; Mir, Moscow, 1970), Vol. 4, Part 6.
11. Yu. V. Gulyaev, I. E. Dikshteĭn, and V. G. Shavrov, Usp. Fiz. Nauk **167**, 735 (1997) [Phys. Usp. **40**, 701 (1997)].
12. A. I. Akhiezer, V. G. Bar'yakhtar, and S. V. Peletminskiĭ, *Spin Waves* (Nauka, Moscow, 1967).
13. G. A. Smolenskiĭ and V. V. Lemanov, *Ferrites and Their Technical Applications* (Nauka, Leningrad, 1975).
14. V. L. Zagustin, *Handbook of Numerical Methods for Solution of Equations* (GIFML, Moscow, 1960).
15. J. E. Dennis and R. Schnabel, *Numerical Methods for Unconstrained Optimization and Nonlinear Equations* (Prentice-Hall, Englewood Cliffs, New York, 1983; Mir, Moscow, 1988).
16. V. V. Shevchenko, Radiotekh. Élektron. (Moscow) **45**, 1157 (2000).
17. E. A. Vilkov, Pis'ma Zh. Tekh. Fiz. **26** (20), 28 (2000) [Tech. Phys. Lett. **26**, 907 (2000)].
18. M. V. Nezlin, Usp. Fiz. Nauk **120**, 481 (1976) [Sov. Phys. Usp. **19**, 946 (1976)].
19. L. A. Ostrovskiĭ, S. A. Rybak, and L. Sh. Tsimring, Usp. Fiz. Nauk **150**, 417 (1986) [Sov. Phys. Usp. **29**, 1040 (1986)].
20. M. K. Balakirev and I. A. Gilinskiĭ, *Waves in Piezoelectric Crystals* (Nauka, Novosibirsk, 1982).
21. T. N. Marysheva and N. S. Shevyakhov, Akust. Zh. **32**, 413 (1986) [Sov. Phys. Acoust. **32**, 259 (1986)].

Translated by V. Isaakyan

Technical Physics, Vol. 48, No. 3, 2003, pp. 361–369. Translated from Zhurnal Tekhnicheskoĭ Fiziki, Vol. 73, No. 3, 2003, pp. 87–95.

RADIOPHYSICS

Dispersion and Instability of Electromagnetic Waves in Layered Periodic Semiconductor Structures

A. A. Bulgakov and O. V. Shramkova

Institute of Radiophysics and Electronics, National Academy of Sciences of Ukraine, ul. Akad. Proskura 12, Kharkov, 61085 Ukraine

e-mail: bulgakov@ire.kharkov.ua

Received August 23, 2002

Abstract—The effect of carrier drift on the dispersive properties and instability of electromagnetic waves and plasma polaritons in infinite layered periodic semiconductors are considered. It is assumed that in similar semiconductor layers, carriers drift parallel to the interfaces. Drift waves are shown to have a specific band structure of the spectrum. The dispersive properties of collective plasma polaritons under drift are considered, the instability of the polaritons and drift waves is studied, and the instability increments are determined. © *2003 MAIK "Nauka/Interperiodica".*

INTRODUCTION

The production of millimeter- and sub-millimeter-wave devices faces a number of physical and technical difficulties. Millimeter lasers are bulky, and vacuum tubes lack efficient coupling between the electron flow and electrodynamic system. In solid-state (semiconductor) carrier-drift devices, one cannot provide Cerenkov interaction between drift and natural waves, since it is impossible to realize synchronism between the wave's drift and phase velocities. However, the creation of long-term-interaction semiconductor devices similar to TWTs is necessary for advancing solid-state technology into the millimeter- and sub-millimeter-wave range.

Physical phenomena that could serve as the basis for solid-state microwave amplifiers and oscillators have been sought for several decades [1, 2]. In [3, 4], the effect of beam instability was predicted. Later [5], beam instability due to wall losses in a metallic waveguide carrying an electron current was studied theoretically and experimentally. Resistive instability arising when an electron current passes through a channel in a germanium crystal was investigated in [6]. It was shown that instability increments predicted theoretically agree well with those found experimentally. The recent theoretical work [7] on the instability of waves in a beam propagating through a hole in a cylindrical semiconductor specimen also merits notice. It was demonstrated that colliding space-charge waves are unstable at any frequency if the thermal velocity of carriers in a semiconductor is ignored.

It was also shown [8–11] that the instability of drift waves in a two-component semiconductor plasma or in layers with drifting carriers is Buneman instability [8, 12]. Finally [11], the instability of a semiconductor superlattice with a period much smaller than the wavelength, as well as the instability of drift waves propagating along the drift direction in a superlattice with arbitrary thicknesses of the layers, was investigated. It turned out that Buneman instability may also occur in periodic structures. Conditions for instability development depending on the thermal velocity of carriers in different layers were found, and instability increments were determined.

In this work, we consider a layered periodic semiconductor structure (superlattice) whose period equals or exceeds the length of a natural electromagnetic wave propagating in the layered structure. It is assumed that the Debye radius and free path of carriers are much less than the thickness of the layers. This assumption simplifies the problem, allowing one to treat semiconductors in the hydrodynamic approximation. It is known that the hydrodynamic equations are valid at frequencies $\omega \gg \nu$ (collisionless plasma [13]) and $\omega \ll \nu$ (ν is the collision frequency) if only the collective behavior of particles is studied and effects like Landau damping are ignored [14]. The effect of thermal motion of carriers can also be included in the hydrodynamic approximation. As was shown [11], even at $\nu\lambda/2\pi v_{th} \geq 3$ (λ is the wavelength under study and v_{th} is the thermal velocity), the discrepancy between the hydrodynamic and kinematic descriptions is no more than 10%. With the plasma frequency $\omega_p = (4\pi e^2 n_0/m\varepsilon_0)^{1/2} = 10^{12}$–$10^{13}$ s^{-1}, effective mass $m = 10^{-28}$–10^{-29} g, and collision frequency $\nu = 5 \times 10^{10}$–10^{13} s^{-1}(typical values for semiconductors [15]), we have $v_{th} = 10^7$–10^8 cm/s, the Debye radius $R_D = v_{th}/\omega_p \approx 10^{-5}$ cm, and the free path $l = v_{th}/\nu \approx 10^{-4}$–$10^{-5}$ cm. Thus, we consider layers of thickness between 5×10^{-4}–10^{-1} cm and frequencies ranging from 1×10^{11} to 5×10^{13} s^{-1}. Landau damping is ignored, therefore, drift waves can be considered as

1063-7842/03/4803-0361$24.00

van Kampen waves [16]. In other words, we suppose that the drifting-carrier flow is modulated with the frequency ω. We show that the translational symmetry of the medium is responsible for a specific band structure of the spectrum of drift waves, which turn out to be stable when collisions are disregarded. Instability arises when collisions are taken into account; i.e., we deal with resistive instability. The effect of dissipation on the propagation of natural waves in the superlattice, collective plasma polaritons, is also studied.

1. STATEMENT OF THE PROBLEM AND BASIC RELATIONSHIPS

Consider an infinite periodic structure composed of alternating layers of different semiconductors with thicknesses d_1 and d_2. In our coordinate system, the 0z axis is directed normally to the interfaces and the 0x axis, parallel to them. We assume that all layers of semiconductor 1 are exposed to an electric field that is aligned with the 0x axis and causes carriers to drift with a velocity $\mathbf{v}_0 = (v_0, 0, 0)$. The associated set of equations includes the Maxwell equations, as well as the continuity equation and equation of motion of carriers:

$$\begin{aligned}\frac{\partial n_1}{\partial t} + \operatorname{div}(n_{01}\mathbf{v}_1 + n_1\mathbf{v}_0) &= 0,\\ \frac{\partial \mathbf{v}_1}{\partial t} + (\mathbf{v}_0\cdot\nabla)\mathbf{v}_1 + \nu_1\mathbf{v}_1 &= \frac{e}{m}\mathbf{E}_1,\end{aligned} \tag{1}$$

where n_{01} is the equilibrium carrier concentration in layers 1 and ν_1 is the collision frequency.

For layers of semiconductor 2, all equations have the same form except that $\mathbf{v}_0 = 0$ and $\nu_2 = 0$. Since the medium is homogeneous in the 0y direction, we will assume that $\partial/\partial y = 0$; then, the initial set of equations splits into two polarizations. In what follows, the polarization with the components E_x, E_z, and H_y is considered.

The initial set of equations must be complemented by boundary conditions. The feature of our situation is that drift in one of the layers causes interfacial currents. Assuming that the transition region thickness is much less than the wavelength (i.e., the interface is sharp), we can apply the boundary conditions from [17], which include a step in the normal components of the electric induction and the continuity of the tangential components of the electric field. For plane waves of form $\exp(-i\omega t + ik_x x + ik_{z1,2}z)$, we have

$$\begin{aligned}D_{z2} - D_{z1} &= -\frac{\omega_{L1}^2 k_x v_0}{(\omega - k_x v_0)^2\omega}E_{z1}\big|_{\text{at interface}},\\ E_{x1} &= E_{x2}\big|_{\text{at interface}}.\end{aligned} \tag{2}$$

Here,

$$k_{z1,2} = \sqrt{\frac{\omega^2}{c^2}\varepsilon_{s1,s2} - k_x^2},$$

$$\varepsilon_{s1} = \varepsilon_{01} - \frac{\omega_{L1}^2}{\omega(\omega - k_x v_0 + i\nu_1)}, \quad \varepsilon_{s2} = \varepsilon_{02} - \frac{\omega_{L2}^2}{\omega^2},$$

$\varepsilon_{01,02}$ are the lattice permittivities of the semiconductor, and $\omega_{L1,2}$ are the Langmuir frequencies.

To derive a dispersion relation, we take advantage of the method of transmission matrix [18, 19], which relates the fields at the beginning and end of the structure period ($d = d_1 + d_2$):

$$\begin{pmatrix}E_{x1}(0)\\ D_{z1}(0)\end{pmatrix} = \hat{M}\begin{pmatrix}E_{x2}(d)\\ D_{z2}(d)\end{pmatrix}. \tag{3}$$

The relationships for the matrix components can be found in [19]. Using the Floquet theorem

$$\begin{aligned}E_{x2}(d) &= E_{x1}(0)\exp(i\bar{k}d),\\ D_{z2}(d) &= D_{z1}(0)\exp(i\bar{k}d),\end{aligned}$$

where $\bar{k}$ is the Bloch wavenumber, we arrive at a dispersion relation, which relates the frequency ω to the wavenumbers k_x and $\bar{k}$:

$$\cos\bar{k}d = \frac{M_{11} + M_{22}}{2},$$

$$M_{11} = \cos k_{z1}d_1\cos k_{z2}d_2 - \frac{k_{z2}\varepsilon_1}{k_{z1}\varepsilon_2}\sin k_{z1}d_1\sin k_{z2}d_2, \tag{4}$$

$$M_{22} = \cos k_{z1}d_1\cos k_{z2}d_2 - \frac{k_{z1}\varepsilon_2}{k_{z2}\varepsilon_1}\sin k_{z1}d_1\sin k_{z2}d_2.$$

Here,

$$\varepsilon_1 = \varepsilon_{01} - \frac{\omega_{L1}^2}{(\omega - k_x v_0 + i\nu_1)(\omega - k_x v_0)},$$

$\varepsilon_2 = \varepsilon_{s2}$.

It is seen that $\bar{k}$ is the averaged wavenumber, which describes the structure periodicity instead of $k_{z1,2}$.

2. DRIFT WAVES IN THE SEMICONDUCTOR SUPERLATTICE

Relationship (4) will be studied for space-charge waves with $\omega \approx k_x v_0$. Let $\nu_1 = 0$. In this case, as follows from the formula for ε_{s1}, the transverse wavenumber k_{z1} may be infinitely large. If $\omega - k_x v_0 \geq 0$ and

$$\frac{\omega^2}{c^2}\frac{\omega_{L1}^2}{(\omega - k_x v_0)\omega} > \frac{\omega^2}{c^2}\varepsilon_{01} - k_x^2,$$

k_{z1} can be represented as

$$k_{z1} \approx i\frac{\omega_{L1}}{c}\sqrt{\frac{\omega}{\omega - k_x v_0}}.$$

In view of the fact that k_{z1} is an imaginary number, Eq. (4) can be recast in the same approximation:

$$\cos\bar{k}d \approx -\frac{1}{2}\frac{k_{z2}}{\varepsilon_2}\frac{\omega_{L1}c}{\sqrt{\omega(\omega - k_x v_0)^3}} \times \sinh\left(\frac{\omega_{L1}}{c}\sqrt{\frac{\omega}{\omega - k_x v_0}}d_1\right)\sin k_{z2}d_2. \quad (5)$$

The absolute value of the right-hand side of this relationship far exceeds unity; therefore, $\bar{k}$ must be imaginary. Consequently, the frequency range $\omega \geq k_x v_0$ is forbidden and fast drift waves do not propagate in the 0z direction (note that if $\sin k_{z2}d_2 \approx 0$, a transmission band for fast drift waves may exist).

If $\omega \leq k_x v_0$, k_{z1} is real. We represent it as

$$k_{z1} = \frac{n\pi}{d_1} + \delta k_z; \quad n = \pm 1, \pm 2, \ldots. \quad (6)$$

Let $\delta k_z \ll \pi/d_1$. Then, Eq. (5) takes the form

$$(-1)^n \cos\bar{k}d \approx \cos k_{z2}d_2 + \delta k_z d_1 \times \frac{k_{z2}}{2\varepsilon_2}\frac{c^4}{\omega_{L1}^2\omega^2}\left(\frac{n\pi}{d_1}\right)^3 \sin k_{z2}d_2. \quad (7)$$

This equation has many solutions for $\bar{k}d$ at given n. If the right-hand side is less than or equal to unity, $\bar{k}$ is a real number from the 0–π interval. Thus, in this case, the spectrum of drift waves has a band structure. The width of transmission bands is inversely proportional to n. Certainly, the frequency band width cannot be less than the collision frequency ν_1. This remark allows one to estimate the number of transmission zones from the condition $(\omega_{n+1} - \omega_n)/\nu_1 \approx 1$. Substituting ν_1 into the expression for ε_{s1} and assuming that $\omega_{L1} \gg \nu_1$, we get

$$n = \mathrm{Int}\left\{\frac{1}{2}\left[\left(\frac{\omega_{L1}d_1}{\pi c}\right)^2 - 1\right]\right\}.$$

From this formula, it follows that the formation of the band structure for drift waves depends significantly on the lattice parameters. If the Langmuir frequency ω_{L1} is low and the collision frequency ν_1 is high, the band structure may be absent.

Figure 1 shows the band structure in the presence and absence of drift. The dispersion relations are given for the following cases: (a) $v_0 = 0$; (b) $v_0 \neq 0$, $\omega_{p1} \ll \omega_{p2}$; (c) $v_0 \neq 0$, $\omega_{p1} \leq \omega_{p2}$; and (d) $v_0 \neq 0$, $\omega_{p1} \geq \omega_{p2}$. In the calculations, we used the following numerical values of the parameters: $\varepsilon_{01} = 17.8$, $\varepsilon_{02} = 10$, $d_1 = 0.006$ cm, and $d_2 = 0.002$ cm. In Fig. 1a ($\omega_{p1} = 2.5 \times 10^{12}$ s^{-1}, $\omega_{p2} = 3 \times 10^{12}$ s^{-1}), where drift is absent, one can see two dashed bands where natural waves, collective plasma polaritons, can propagate [19]. The symbol "+" corresponds to $\bar{k}d = \pi$; the symbol "○," to $\bar{k}d = 0$. Both transmission bands asymptotically tend to the line $\omega = \omega_{ps} = \sqrt{\omega_{ps1}^2 + \omega_{ps2}^2}$, where $\omega_{ps1,2} = \omega_{L1,2}(\varepsilon_{01} + \varepsilon_{02})^{-1/2}$ are the frequencies of interfacial plasmons propagating at the interface between the semiconductor layers. It should be noted that in the upper band, the group velocity of the waves is negative. The existence of polaritons of two types can be explained as follows. Let us write the expression for the power flux:

$$P_{x1,2} = -\frac{c}{4\pi}\mathrm{Re}(E_z H_y^*) = \frac{\omega}{4\pi}|E_{x1,2}|^2\frac{k_x}{|k_{z1,2}|}\mathrm{Re}\varepsilon_{1,2},$$
$$P_{z1,2} = \frac{c}{4\pi}\mathrm{Re}(E_x H_y^*) = \frac{\omega}{4\pi}\frac{|E_{x1,2}|^2}{|k_{z1,2}|^2}\mathrm{Re}k_{z1,2}^*\varepsilon_{1,2}. \quad (8)$$

From (8), it follows that the P_x component of the flux is other than zero and that its sign coincides with that of the permittivity. In the range of interest (between ω_{p1} and ω_{p2}), ε_1 is positive and ε_2, negative. In addition, $k_{z2}^2 < 0$ throughout the frequency range, while $k_{z1}^2 < 0$ if $k_x^2 > (\omega^2/c^2)\varepsilon_{s1}$. From (8), it also follows that the P_z component equals zero. The flux in layers 1 coincides with the positive 0x direction, while in layers 2 it is directed oppositely. Thus, in the lower transmission band, the major portion of the energy is transferred by layers 1, while in the upper band most of the energy concentrates in layers 2. This circumstance also defines the direction of the group velocity $v_g = d\omega/dk_x$.

When constructing Fig. 1b, we took the drift velocity $v_0 = 5 \times 10^9$ cm/s, $\omega_{p1} = 6 \times 10^{10}$ s^{-1}, and $\omega_{p2} = 3 \times 10^{12}$ s^{-1}. Here, the dashed line is given by the equation $\omega = k_x v_0$; that is, this line reflects the dispersion relation for a drift wave without considering the structure periodicity. The interaction between drift waves and plasma polaritons shows up in that the curves move apart at the points where this line crosses the dispersion lines of natural lattice waves. As a result, the allowed bands for plasma polaritons change their form and transmission bands appear near the line $\omega = k_x v_0$ (see inset). These bands have been mentioned in the analysis of Eqs. (6) and (7). Note that the equation for the boundary of these bands is $\omega = k_x v_0 + \mathrm{const}$. The bands are situated to the right of the dashed line and correspond to slow drift waves. To the left of this line, transmission bands are absent up to the transmission bands for plasma polaritons. Thus, fast drift waves fall into the forbidden band and are absent in layered semiconductors with translational symmetry.

In Fig. 1c, the range of drift waves is much wider than in Fig. 1b. In Fig. 1d, it is assumed that the waves

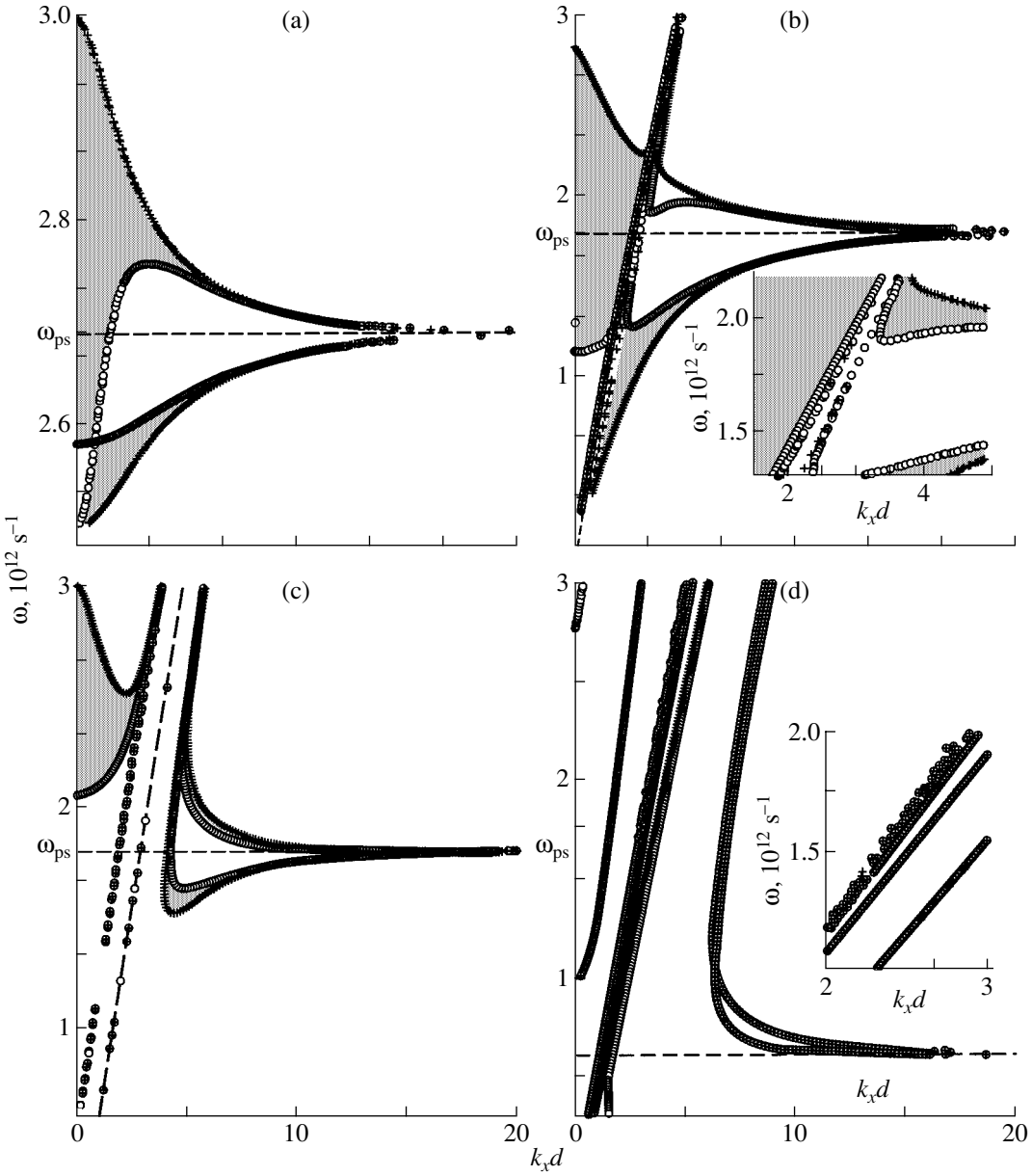

Fig. 1. Graphical representation of the dispersion relation.

drift in layers with a high carrier concentration; therefore, the range of drift waves is still wider. In this figure, the asymptote for $k_x d \longrightarrow \infty$ is the frequency ω_{ps2}, rather than ω_{ps} as in Figs. 1a–1c.

To obtain analytical results for the case $\omega \leq k_x v_0$, we assume that $\omega_{L1} \ll \omega_{L2}$ and represent Eq. (4) in the form

$$(\omega - k_x v_0)^2(\varepsilon_{01}\omega^2 + (\omega_{L2}^2 - \varepsilon_{02}\omega^2)F_{1,2}) = \omega_{L1}^2\omega^2, \quad (9)$$

$$F_{1,2} = \frac{n\pi}{d_1 k_{z2}}(A \mp \sqrt{A^2 - 1}),$$
$$A = \frac{1}{\delta k_z d_1}\frac{\cos k_{z2}d_2 - (-1)^n \cos \bar{k}d}{\sin k_{z2}d_2}. \quad (10)$$

Formula (10) was derived in view of relationship (6). For drift waves, (9) gives

$$\omega = k_z v_0 - \frac{\omega_{L1} k_z v_0}{\sqrt{\varepsilon_{01}(k_z v_0)^2 + [\omega_{L2}^2 - \varepsilon_{02}(k_z v_0)^2]F_{1,2}}} \quad (11)$$

(the plus sign outside the second term is absent, because the slow drift wave propagates in the structure as was indicated above). Since $\delta k_z d_1$ is small and $|A| \gg 1$, expanding the radicands in (9) in A^{-1} yields

$$F_{1,2} = \frac{n\pi}{d_1 k_{z2}}\begin{cases}(2A)^{-1}\\ 2A\end{cases}. \quad (12)$$

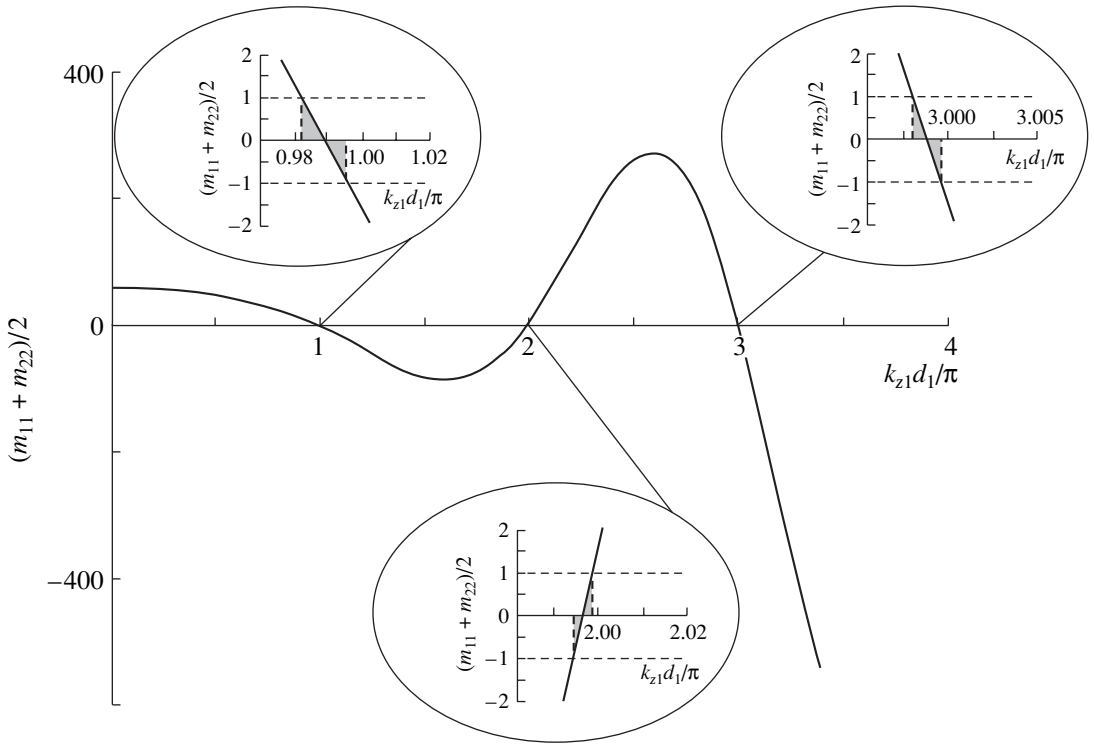

Fig. 2. $(m_{11} + m_{22})/2$ vs. $k_{z1}d_1/\pi$ for Fig. 1b.

In the frequency range under study, k_{z2} is an imaginary number and

$$A = \frac{-i}{\delta k_z d_1}\frac{\cosh k_{z2}d_2 - (-1)^n \cos \bar{k}d}{\sinh k_{z2}d_2} = \frac{-i}{\delta k_z d_1}\beta.$$

Then, F_1 is inversely proportional to the small quantity $|\delta k_z|d_1$. Therefore,

$$\omega \approx k_x v_0 - \omega_{p1}.$$

The value of F_2 is inversely proportional to $|\delta k_z|d_1$ and, hence, is large. In this case,

$$\omega \approx k_x v_0\left(1 - \frac{\omega_{L1}}{\omega_{L2}}\sqrt{-\frac{|k_{z2}|d_1}{2\beta n\pi}\delta k_z d_1}\right). \quad (13)$$

Consequently, at $\delta k_z < 0$, the slow drift wave is stable.

Let us define δk_z. To do this, we construct the dependence of $(m_{11} + m_{22})/2$ on $k_{z1}d_1/\pi$ (Fig. 2), from which it follows that $|(m_{11} + m_{22})|/2 \le 1$ at points where the argument is an integer number. As is seen from dispersion relation (4), this implies the presence of a transmission band. At the points $k_{z1}d_1/\pi = 1$, 2, and 3, the bands arise to the left of them and $\delta k_z d_1 < 0$; that is, the drift waves are stable. The negativity of $\delta k_z d_1$ can be shown analytically. From (7), we have for the right-hand side

$$\exp(|k_{z2}|d_2)\left|1 + \delta k_z d_1 \frac{|k_{z2}|}{2|\varepsilon_2|}\frac{c^4}{\omega_{L1}^2\omega^2}\left(\frac{d_1}{n\pi}\right)^3\right| < 1. \quad (14)$$

Here, we took into account that k_{z2} is imaginary and $\varepsilon_2 < 0$ in the range of interest. Thus, with dissipation not taken into consideration, drift waves in the periodic structure are stable.

3. THE EFFECT OF DRIFT ON PLASMA POLARITONS

Figure 1a shows the transmission bands for plasma polaritons without drift. In this section, we consider the numerical solution to the equation

$$\varepsilon_{01}\omega^2 + (\omega_{L2}^2 - \varepsilon_{02}\omega^2)F_{1,2} = 0 \quad (15)$$

in the presence of drift. In (15), ε_1 is large in magnitude at frequencies near $\omega \approx k_x v_0$; therefore, k_{z1} can be represented by formula (6) and $F_{1,2}$, by (10). Figure 3 demonstrates the solutions to (15) for two drift velocities. At the lower velocity (Fig. 3a), the transmission bands change in shape insignificantly as compared with Fig. 1a. The basic difference between Fig. 1a and Fig. 3a is that the asymptote to which the boundaries of the bands tend at $k_x d \longrightarrow \infty$ depends on the frequency of the surface plasmon in layer 2, and not on the hybrid frequency ω_{ps2}. In Fig. 3b, the band $\omega \approx k_x v_0$ is seen to

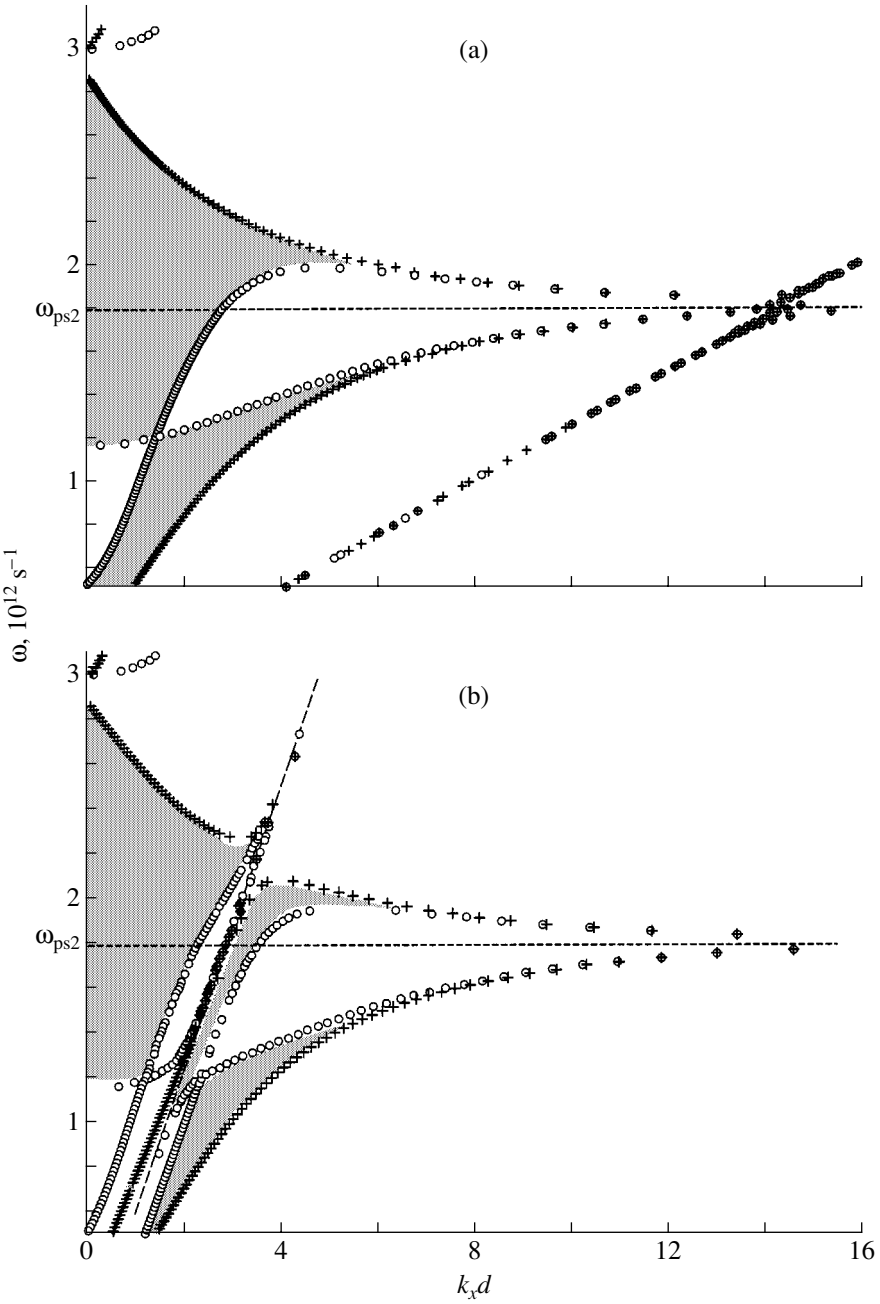

Fig. 3. Band structure of the plasma polariton spectrum in the presence of drift: $v_0 = 1 \times 10^9$ (a) and 5×10^9 cm/s (b).

be in the range of small $k_x d$. Also, the bands are noticeably extended along the line $\omega = k_x v_0$. It is of interest that the bands where plasma polaritons have a negative or positive group velocity are also retained in the presence of drift.

Now we will consider a solution to Eq. (9) for collective plasma polaritons. From (9), it follows that carrier drift does not cause the instability of natural waves but merely shifts the frequency by a small quantity on the order of $\omega_{L1}^2/(\omega_{ps2} - k_x v_0)^2$.

4. TAKING ACCOUNT OF DISSIPATION

The above results were obtained without considering losses, which are certainly present in any semiconductor. Dissipation is known to considerably affect wave dispersion and damping, conditions under which instability develops, etc. Specifically, it has been shown [20–22] that taking into account the collision frequency limits the maximal wavenumber and hence introduces some minimal value of the phase velocity of a wave $v_{ph} = \omega/(k_x)_{max}$. Because of this, the instability condition $(\omega/(k_x)_{max} < v_0)$ fails even in high-mobility semi-

conductors like InSb and PbTe, where the drift velocity may be as high as (3–5) × 10^7 cm/s and the lowest velocity of interfacial polaritons in the homogeneous material may reach $c/\sqrt{\varepsilon_0} \approx 5 \times 10^9$ cm/s. Therefore, the instability described in Section 1 may apparently arise only in structures where electron currents pass between semiconductor layers.

To examine the effect of dissipation on the plasma polariton properties, we proceed as follows. Let the collision frequency in semiconductor 1 be $\nu_1 \ll \omega_{L1}$ and semiconductor 2 be lossless. Let also $\nu_0 = 0$. Equation (9) will be solved numerically. The solution is illustrated in Fig. 4, where $k_x = k_x' + ik_x''$. Figure 4a shows the dependence of the frequency on the real part $k_x' d$ of the wavenumber, and Fig. 4b displays the dependence $\omega(k_x'' d)$ at $\nu_1 = 3 \times 10^{11}$ s^{-1} with $\bar{k}d = 0$. Comparing Fig. 4 with Fig. 1, we see that the dispersion curves with the positive (curve *1*) and negative (curve *2*) group velocities run in the same manner at $k_x' d \approx 0, \ldots, 20$. The damping in this range is described by curves *1* and *2* in Fig. 4b. For curve *1* in Fig. 4a, the damping is positive and small in the frequency range $\omega = 1.25 \times 10^{12}$–$1.75 \times 10^{12}$ s^{-1} and equals $k_x''/k_x' \approx 0.04$. Beyond this range, the damping grows considerably, reaching $k_x''/k_x' \approx 0.38$ by the end of curve *1* ($\omega \approx 1.86 \times 10^{12}$ s^{-1}, $k_x' d = 19.98$). For curve *2* in Fig. 4a, the damping curve is curve *2* in Fig. 4b, which is near the vertical axis, and $k_x'' d \approx 0$. Subsequently, for $\omega \approx 2 \times 10^{12}$ s^{-1}, k_x'' becomes negative and grows in magnitude. The negative value of k_x'' means that the wave amplitude increases along the positive 0*x* axis and decreases in the opposite direction. Such behavior of these polaritons is explained by the fact that for $k_x' d > 5$ (Fig. 4a), the group velocity is negative; that is, the natural wave decays in the direction of energy propagation [22, 23]. An importance feature of the curves is the presence of a bend at large values of $k_x' d$. In this range, $|k_x'' d|$ is seen to grow significantly. Thus, damping limits the value of $k_x' d$ and introduces a minimum of the phase velocity.

Let us estimate $(k_x)_{max}$ assuming that the collision frequency in semiconductor 1 $\nu_1 \ll \omega_{L1}$. Let $\omega \approx \omega_{ps}$; in other words, we consider the range near the asymptote in Fig. 1a. Then, we can put

$$k_x \gg \frac{\omega_{ps}}{c}\sqrt{\varepsilon_{1,2}}.$$

With this inequality taken into account,

$$k_{z1} = k_{z2} \approx ik_x, \tag{16}$$

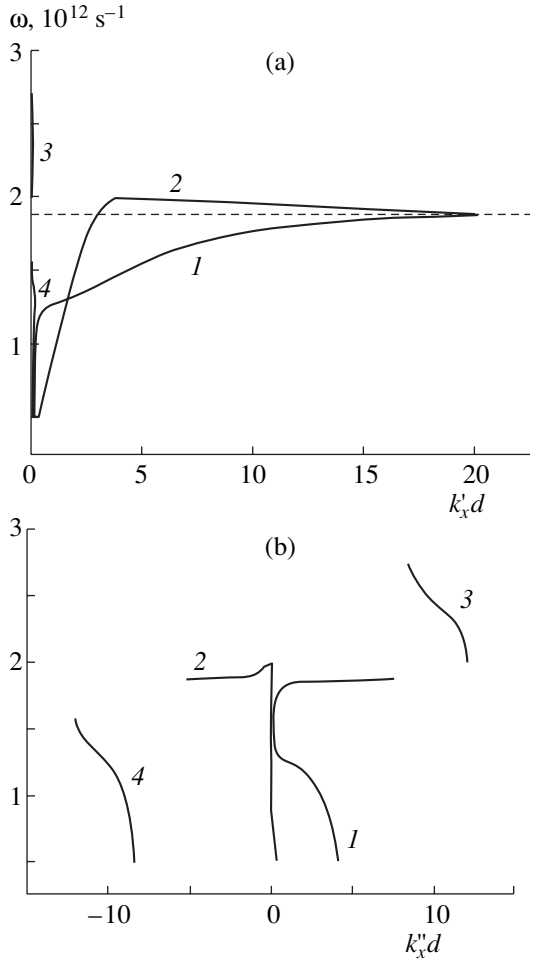

Fig. 4. Dispersion relation for plasma polaritons in the presence of spatial damping.

and Eq. (4) takes the form

$$\cos\bar{k}d = \cosh k_x d_1 \cosh k_x d_2 + \frac{1}{2}\left(\frac{\varepsilon_1}{\varepsilon_2} + \frac{\varepsilon_2}{\varepsilon_1}\right)\sinh k_x d_1 \sinh k_x d_2. \tag{17}$$

For large values of $k_x \cosh k_x d \approx \sinh k_x d \approx \exp(k_x d)/2$ and with $\omega_{L2} > \omega_{L1}$, we have

$$k_x' = \frac{1}{d}\ln\left\{\frac{8\omega_{L2}^4}{\omega_{ps}\omega_{L1}^2\nu_1}\frac{\varepsilon_{01}^2}{(\varepsilon_{01}+\varepsilon_{02})^2}\right\},$$
$$k_x'' = \frac{1}{d}\arctan\frac{\omega_{L2}^2}{\omega_{ps}\nu_1}. \tag{18}$$

Here, $|\cos\bar{k}d| \approx 1$. From (18), it follows that at $\nu_1 \longrightarrow 0$, $k_x' d \longrightarrow \infty$ and $k_x'' d \longrightarrow \pi/2$. The bend in the curve can be explained as follows. With $\nu_1 \neq 0$, $k_x' d$ takes a finite value and the phase shift over the period is somewhat

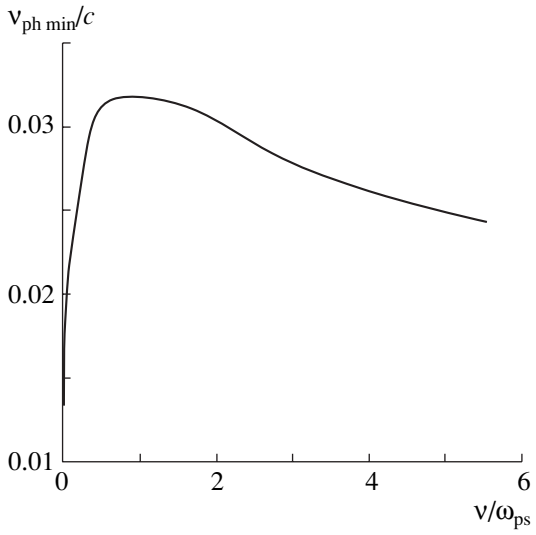

Fig. 5. Minimal polariton phase velocity vs. ν/ω_{ps}.

less than π when the wave travels in the negative z direction. Thus, the reflected wave "quenches" the incident one. This causes a forbidden band, i.e., a bend in the dispersion curve, to form.

The minimal phase velocity vs. ratio ν_1/ω_{ps} is depicted in Fig. 5. As this ratio grows, the phase velocity approaches the velocity of light. However, even at $\nu_1 > \omega_{ps}$, it amounts to only several percent of the velocity of light. As the numerical calculations show, the shape of the curve at high dissipation values depends on the structure geometry. Physically, this is explained by the fact that a portion of the energy is transferred in layers 2, where the damping was set equal zero.

Figure 4a shows two more waves with their dispersion curves located at $k_x' d \approx 0$ (curve *3*) and $|k_x'' d| \approx 10$ (curve *4*). This solution appears when only dissipation processes are included [24]. As follows from (8), the power flux along the 0x axis $P_x = 0$; along the 0z axis, its direction reverses in adjacent layers. The latter circumstance stems from the fact that $\varepsilon_1 > 0$ and $\varepsilon_2 < 0$ in the range of interest. Therefore, polaritons of this type do not propagate in the structure and decay near the point of origination.

Now consider the instability of natural waves in the presence of drift and dissipation. If $\omega_{L2} \gg \omega_{L1}$, the dispersion relation takes the form

$$(\omega - k_x v_0)[\varepsilon_{01}\omega^2 + (\omega_{L2}^2 - \varepsilon_{02}\omega^2)F_{1,2}] = -\frac{i\omega_{L1}^2\omega^2}{\nu_1}. \quad (19)$$

Substituting $\omega = k_x v_0 + \delta\omega$ for drift waves yields

$$\delta\omega = -\frac{i\omega_{L1}^2}{\nu_1\{\varepsilon_{01} + [\omega_{L2}^2/(k_x v_0)^2 - \varepsilon_{02}]F_{1,2}\}}. \quad (20)$$

In formulas (19) and (20), the value of $F_{1,2}$ found from Eq. (4) has the form

$$F_{1,2} = \frac{k_{z1}}{k_{ze}}(A \pm \sqrt{A^2 - 1}),$$
$$A = \frac{\cos k_{z1}d_1 \cos k_{z2}d_2 - \cos\bar{k}d}{\sin k_{z1}d_1 \sin k_{z2}d_2}. \quad (21)$$

Since $v_0 \ll c/\sqrt{\varepsilon_{01,02}}$,

$$A = \frac{\cos\bar{k}d - \cosh k_x d_1 \cosh k_x d_2}{\sinh k_x d_1 \sinh k_x d_2} \approx -1$$

and, hence, $F_{1,2} \approx -1$. Then,

$$\frac{\delta\omega}{\omega} \approx i\frac{\omega_{ps1}^2 k_x v_0}{[\omega_{ps2}^2 - (k_x v_0)^2]\nu_1}. \quad (22)$$

Thus, we have found that drift waves are unstable for frequencies below ω_{ps2}. The increment is maximal at frequencies near ω_{ps2}. This effect is accounted for by Fig. 3b. Near ω_{ps2}, a polariton band exists for which the associated equation is obtained by equating the expression in the brackets on the left of (19) to zero. The increment grows as the frequency approaches the resonance between a drift wave and polariton. At this point, the increment is maximal and is proportional to the square root of the right of (19). Note that the condition $k_x v_0 = \omega_{ps2}$ cannot be fulfilled, since $\delta\omega/\omega$ must be less than unity. The conclusion that space-charge waves are unstable at any frequency if the collision frequency is nonzero has been drawn in [7].

For collective plasma polaritons, we find from (19)

$$\frac{\delta\omega}{\omega} = -i\frac{\omega_{L1}^2\omega_F}{2\nu_1(\omega_F - k_x v_0)(\varepsilon_{01} + \varepsilon_{02}|F|)}. \quad (23)$$

Here, $\omega_F = \sqrt{\omega_{L2}^2|F|/(\varepsilon_{01} + \varepsilon_{02}|F|)}$ is the solution to the polariton equation. $|F|$ takes into account the periodicity of the structure. $|F| \longrightarrow 1$ if $k_x' d \longrightarrow \infty$; in this case, $\omega_F \longrightarrow \omega_{ps2}$. Polaritons are unstable if $k_x v_0 > \omega_F$.

CONCLUSION

Our results can be of interest in designing solid-state millimeter- and sub-millimeter-wave devices, where long-term interaction between drift or natural waves of the periodic structure (superlattice) is a crucial issue as in TWTs. The materials of choice for the layers are InSb, PbTe, or GaAs, and the layer thickness must be about several micrometers.

REFERENCES

1. Ya. K. Trokhimenko and V. N. Dmitruk, Izv. Vyssh. Uchebn. Zaved. Radioélektron. **14**, 1395 (1971).
2. J. Mullins, IEEE Spectr. **39** (7), 22 (2002).
3. A. I. Akhiezer and Ya. B. Faĭnberg, Dokl. Akad. Nauk SSSR **69**, 555 (1949).
4. D. Bohm and E. P. Gross, Phys. Rev. **75**, 1864 (1949).
5. V. P. Lopukhin and A. A. Vedenov, Usp. Fiz. Nauk **53** (1), 69 (1954).
6. E. A. Kornilov, S. A. Nekrashevich, Ya. B. Faĭnberg, *et al.*, Pis'ma Zh. Éksp. Teor. Fiz. **11**, 284 (1970) [JETP Lett. **11** (6), 185 (1970)].
7. A. F. Rusanov and V. M. Yakovenko, Radiotekh. Élektron. (Kharkov) **5** (3), 91 (2000).
8. D. Pines and J. Schrieffer, Phys. Rev. **124**, 1387 (1961).
9. Yu. A. Romanov and V. F. Dryakhlushin, Zh. Éksp. Teor. Fiz. **58**, 348 (1970) [Sov. Phys. JETP **31**, 187 (1970)].
10. E. P. Bogdanov, L. K. Orlov, and Yu. A. Romanov, Izv. Vyssh. Uchebn. Zaved. Radiofiz. **14**, 805 (1971).
11. E. P. Bogdanov, Yu. A. Romanov, and V. M. Troshin, Zh. Tekh. Fiz. **45**, 32 (1975) [Sov. Phys. Tech. Phys. **20**, 19 (1975)].
12. O. Buneman, Phys. Rev. **115**, 503 (1959).
13. V. P. Silin and A. A. Rukhadze, *Electromagnetic Properties of Plasma and Plasma-like Media* (Atomizdat, Moscow, 1961).
14. A. I. Akhiezer, I. A. Akhiezer, R. V. Polovin, *et al.*, *Electrodynamics of Plasma* (Nauka, Moscow, 1974).
15. M. C. Steel and B. Vural, *Wave Interactions in Solid State Plasmas* (McGraw Hill, New York, 1969; Atomizdat, Moscow, 1973).
16. B. B. Kadomtsev, *Collecive Interactions in Plasma* (Nauka, Moscow, 1976).
17. A. B. Mikhaĭlovskiĭ and É. A. Pashitskiĭ, Zh. Éksp. Teor. Fiz. **48**, 1787 (1965) [Sov. Phys. JETP **21**, 1197 (1965)].
18. M. Born and E. Wolf, *Principles of Optics*, 4th ed. (Pergamon, Oxford, 1969; Nauka, Moscow, 1973).
19. F. G. Bass, A. A. Bulgakov, and A. P. Tetervov, *High-Frequency Properties of Semiconductor Superlattices* (Nauka, Moscow, 1989).
20. K. R. Alfano, J. Opt. Soc. Am. **60** (1), 66 (1970).
21. G. R. Kovner, K. W. Alexander, K. J. Beil, *et al.*, Phys. Rev. B **14**, 1458 (1976).
22. A. A. Bulgakov and Z. E. Eremenko, Opt. Spektrosk. **66**, 1094 (1989) [Opt. Spectrosc. **66**, 640 (1989)].
23. I. M. Frank, Zh. Éksp. Teor. Fiz. **36**, 823 (1959) [Sov. Phys. JETP **9**, 580 (1959)].
24. A. C. Baynham and A. D. Boardman, J. Phys. C **2**, 619 (1969).

Translated by V. Isaakyan

Technical Physics, Vol. 48, No. 3, 2003, pp. 370–373. Translated from Zhurnal Tekhnicheskoĭ Fiziki, Vol. 73, No. 3, 2003, pp. 96–99.

EXPERIMENTAL INSTRUMENTS AND TECHNIQUES

Processing of Tracks and Beta-Ray Spectrograms with the MAS-1 Universal Setup

O. K. Egorov[1], T. A. Islamov[2, 3], V. G. Kalinnikov[2], N. T. Kambarova[3], V. V. Kolesnikov[1], T. M. Muminov[3], V. I. Silaev[1], and A. A. Solnyshkin[2]

[1] *State Scientific Center of the Russian Federation, Institute of Theoretical and Experimental Physics, Bol'shaya Cheremushkinskaya ul. 25, Moscow, 117218 Russia*

[2] *Joint Institute for Nuclear Research, Dubna, Moscow oblast, 141980 Russia*

[3] *Tashkent State University, Universitetskaya ul. 95, Vuzgorodok, Tashkent, 700095 Uzbekistan*

Received March 28, 2002; in final form, September 16, 2002

Abstract—Results of processing photoemulsion plates exposed in several experiments that were performed on the MAS-1 automated complex with a microscope are reported. Specifically, the case of detecting a charmed meson in the WA-95 (CERN) experiment is considered. Also, the processing of internal conversion electron spectrograms that are recorded with a beta-ray spectrograph equipped with a precision image-sensing TV system providing an accuracy of 1 μm in three coordinates is described. © *2003 MAIK "Nauka/Interperiodica".*

INTRODUCTION

Earlier, the MAS-1 universal setup [1], designed in the Institute of Theoretical and Experimental Physics, was used to search for neutrino interaction in nuclear photoemulsion exposed to a neutrino beam in the CERN SPS accelerator [2].

The basic parameters of the MAS-1 are as follows: the size of the objective table for emulsion scanning and making measurements is 450 × 450 mm, the scale reading in three coordinates is 1 μm, and the upward stroke is 50 mm. The setup is provided with a vacuum clamp to fix a photoemulsion plate and a TV system for image observation and memorizing.

The setup was designed for processing events in the WA-95 (CERN) experiment organized by the CHORUS collaboration to search for neutrino oscillations [3]. In that experiment, the exposed photoemulsion chamber was glued to a 400 × 400-mm polystyrene substrate in a definite order and events were sought in the semi-automatic regime (tuning to a desired coordinate was made automatically, and event coordinates were fixed by the operator). As an illustration, we will demonstrate a charmed meson (Fig. 1) detected in that experiment. Here, the blackening of each photoemulsion grain was measured.

However, the technique developed also allows one to measure the blackening of a set of grains and eventually to record spectral lines. In this work, we apply the MAS-1 setup to scan nuclear photoemulsion plates on which the internal conversion electron (ICE) lines of various radioactive nuclides were recorded with a beta-ray spectrograph and show the advantages of our approach over the microphotometry technology [4]. The photoplates used measured 400 × 15 mm and had a *P*-type emulsion layer 50 μm thick (available from the FOMOS Research and Production Amalgamation).

The parameters of beta-ray spectrographs were carefully considered in [4]. The basic ones are the fol-

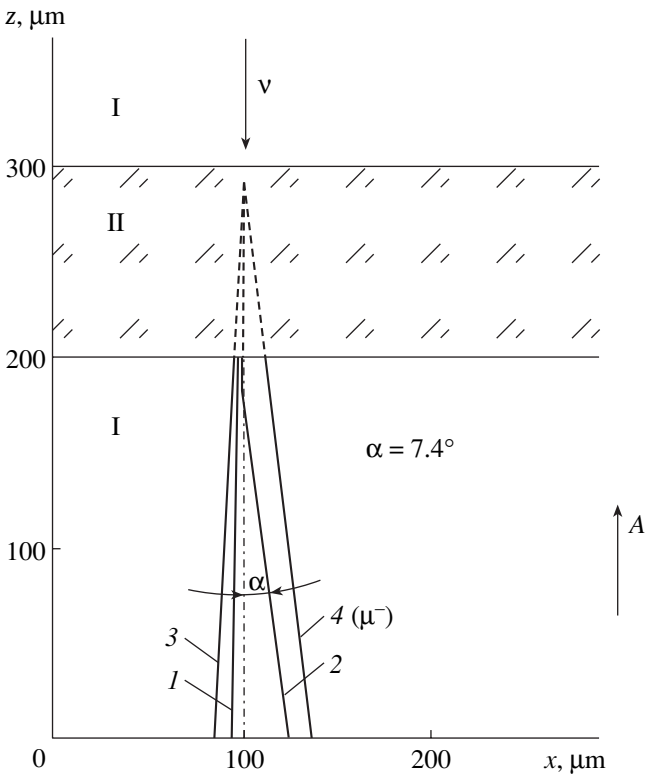

Fig. 1. Birth of a charmed meson in the MAS-1. Event 1272 = 1925, chamber 54, prediction track 212 (6)-hadron. (*1–4*) Track numbers. I, photoemulsion; II, polystyrene; *A*, direction of search for interaction vertex.

1063-7842/03/4803-0370$24.00 © 2003 MAIK "Nauka/Interperiodica"

Table 1. ^{169}Yb spectrum lines

Line	Position, μm	Width, μm	Intensity	Signal/background ratio
K	264100 ± 50	1500	1	11.40
*L*1	273300 ± 50	400	0.0175 ± 0.0002	2.20
*L*2	275000 ± 50	300	0.0019 ± 0.0002	0.76
*L*3	278200 ± 50	300	0.0026 ± 0.0002	0.93

lowing: the energy resolution is 0.03%, the energy range of electrons detected is 0–3000 keV, and the source activity is 5–30 mCi. As an electron recorder, plates with nuclear emulsion are used. The use of a photorecorder to detect electrons makes it possible to gain information about conversion electron energy spectra over a wide energy range and with a high resolution. However, to extract data of interest from photorecorders, one needs precision instruments equipped with sensing TV systems and tools for digitizing optical images. The TV camera must offer a high spatial resolution in order to provide good images of individual emulsion grains of size about 1 μm.

TV SYSTEM FOR IMAGE SENSING

The MAS-1 intended to perform measurements in nuclear photoemulsion was equipped with a special spectrophotometric CCD-based TV camera. Data processing with this camera is accomplished using dedicated algorithms that decompose an image into 512 × 512 cells, each memorizing the brightness in the interval 0–255 units.

The CCD-based TV camera operates in the optical range and has a maximal sensitivity at $\lambda = 0.5$ μm. A SONY CCB-M27B/CE camera with a CCD array is designed for the high-quality entry of black-and-white images into a PC. It generates a video signal and auxiliary signals and has the following parameters: the size of a CCD array is 1/2", the number of cells is 768 × 576, the sensitive area is 6.46 × 4.83 mm, the time of response of an electronic shutter is 1/10000–1/50 s, the time of signal accumulation is about 1 min, and the sensitivity is 0.251. The camera provides external synchronization for frame scan and automatic gain control. The camera is directly connected to its controller (placed in a computer), which digitizes the signals. The controller and camera operate with the same clock frequency, which provides high-quality imaging and precise matching between a digitized image and the physical raster of the CCD array.

The image-sensing TV system, which provides image entry, has the following parameters: the total number of pixels in the raster of the camera is 768 × 576, the time of image entry is 40 ms, the number of storage screens in the buffer is ~8, the number of tonal gradations is 256, and the clock frequency of frame decomposition is 14.1875 MHz. The system has input and output data coding tables, electronic control of tonal gradations, a 16-bit interface with the IBM PC bus, and a 4-bit data overlay.

The TV camera includes a CCD card, CCD control card, power supply card, and interface-and-controller card. The functions of the controller are changed by reprogramming. Some of the functions are user-programmable, and the others depend on programs wired in a programmable gate array. The wired-in programs specify the controller's operating parameters. They can be loaded into the controller at any time instant and as many times as desired. One loading of a wired-in program takes 80 ms.

TECHNIQUE FOR SCANNING BETA-RAY SPECTROGRAMS

Photoplates that recorded the ICE spectra from radioactive isotopes when exposed in the beta-ray spectrograph contained information on the energy, width, and intensity of the lines. After development and drying, they were rigidly fixed on the MAS-1 table. The thickness of the emulsion layer developed was ≈25 μm

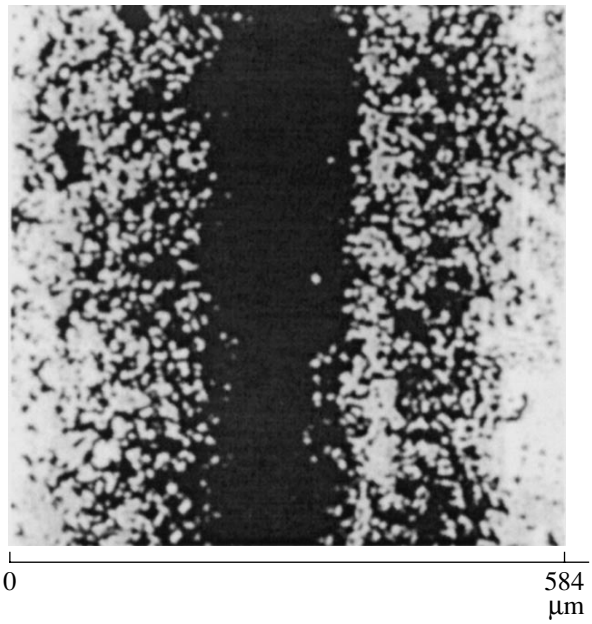

Fig. 2. Conversion electron lines in the photoemulsion in the MAS-1.

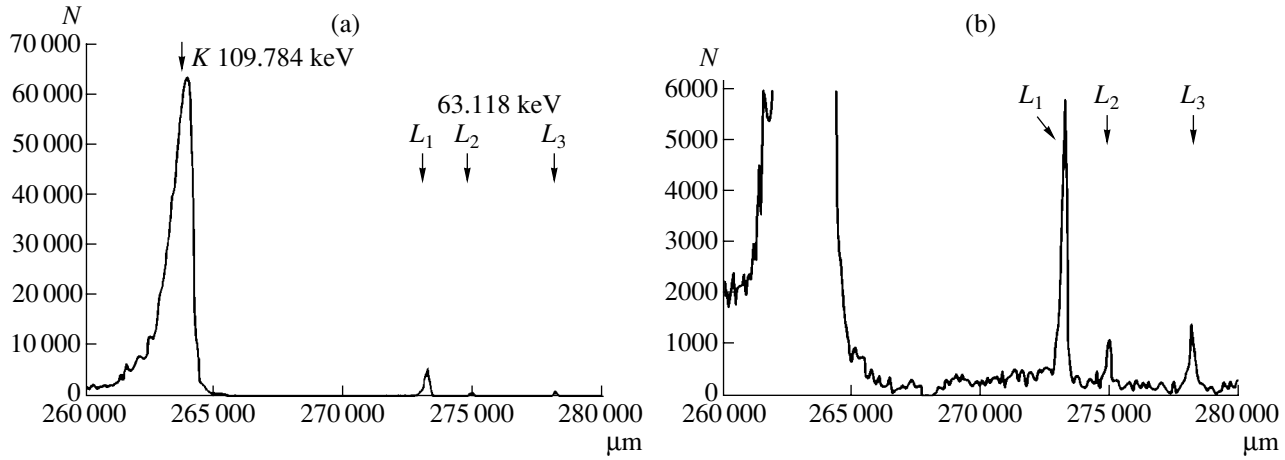

Fig. 3. Results of scanning (a) the ICE beta-ray spectrogram for the ^{169}Yb isotope (N is the number of black cells) and (b) the same spectrogram extended along the Y axis (the transition multipolarity is found from the ratio of the L line intensities).

at a glass substrate thickness of 2 mm. The photoemulsion exhibited black grains, whose density directly depends on the rate of nuclear transitions. Actually, the grain size displayed on the TV camera was ≈1 μm, occupying about ten cells of the CCD array. Such a resolution is sufficient for separating individual grains even if their sizes fluctuate considerably. The photoemulsion was illuminated by a parallel light beam formed by an optical system consisting of a 100-W incandescent lamp, condenser, and field objective. The image quality was electronically controlled with a special software suite. The tonal gradation was selected so that "dark" and "light" cells have brightnesses in the interval 0–127 and 128–255 units, respectively. An image recorded with the optical path of the TV camera under these conditions was fixed as a 512 × 512-cell frame and, after digitizing, filed. Figure 2 shows the photographic image of electrons for the Lu element that

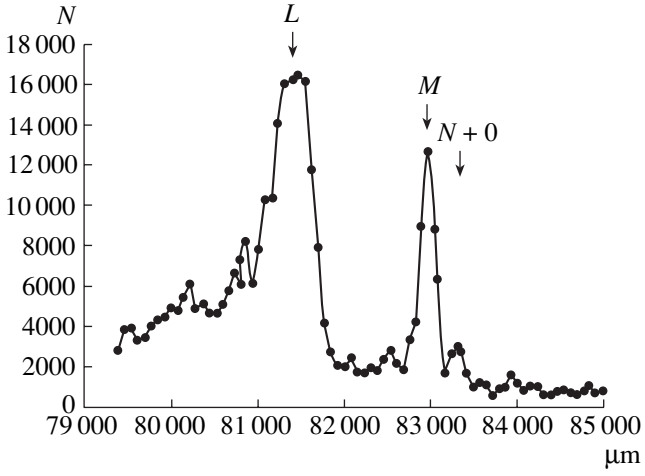

Fig. 4. Results of scanning the ICE beta-ray spectrogram for the ^{111}In isotope with an energy of 171.29 keV (N is the number of dark cells).

was displayed on the TV screen after appropriate tuning. Images recorded were processed by the special algorithm in several steps.

(1) The frame with an image is filtered to remove contaminants, defects, and emulsion damage.

(2) The brightness distribution on the frame is equalized; i.e., the distribution function is analytically extended over the entire possible range.

(3) The brightness of the frame is reduced to binary representation; that is, the brightness takes only the value 0 or 1.

(4) The number of dark cells (brightness 0) on the frame is calculated in the projection onto the axis normal to a spectral line being scanned (the number of these cells depends on the scan step).

The spectrum thus obtained (Fig. 2) exhibits closely spaced intense and faint lines. Usually, faint lines can be recorded by decreasing both the scan step and the optical magnification. This is because the lines diffuse greatly under a high magnification and closely spaced ones become indistinguishable because of insufficient statistics. The field of vision in Fig. 2 is 584 × 584 μm, and the spacing between the lines is 53 μm. Therefore, such spectrograms should be scanned with a step of no more than 25 μm because of the presence of faint lines. However, if the background noise is weak, the scan step can be selected in view of the signal-to-noise ratio.

During the scanning of photoplates on the MAS-1, the operator fixes the coordinates and determines the number of black spots in each field of vision with a computer operating in real time. Beta-ray spectrograms are scanned along the full length of the photoplate with the sensing system tuned once. In this case, the positions of ICE spectrum lines are determined with the same accuracy.

The results of scanning the beta-ray spectrograms of the ^{169}Yb isotope in the energy range above 50 keV with our technique are shown in Fig. 3. Table 1 lists data

Table 2. ^{111}In spectrum lines

Line	Position, μm	Width, μm	Intensity
L	81 395 ± 12	607	1
M	82 975 ± 5	216	0.340 ± 0.001
N + *O*	83 281 ± 8	273	0.048 ± 0.002

obtained by processing the lines in Fig. 3. Note that qualitatively our data are in good agreement with published data [5]; however, the lines are sharper and their location is much more accurate.

The intensities of the ICE spectrum lines for a $\approx^{163, 165}$Tm isotope mixture are presented in [6]. Due to the high sensitivity of the technique suggested, high-reliability measurements of the faint lines were performed.

New results were obtained by us when the beta-ray spectrogram of the ^{161}Hp isotope was scanned in the energy range up to 100 keV. The associated data are also presented in [6].

Figure 4 demonstrates the results of scanning the photoplate with the ICE spectrum for the ^{111}In isotope at energies of up to 500 keV. The intensities of three lines from this spectrum were calculated by approximating the lines by the Lorentz function under the assumption of linear background near these lines. The positions of the lines and their relative intensities are listed in Table 2. Earlier, these data were absent in the literature.

CONCLUSION

Thus, we pioneered the use of the MAS-1 universal setup for processing beta-ray spectrograms recorded on photoplates in beta-ray spectrographs in order to determine the relative intensities of spectral lines for a number of beta-ray isotopes. The MAS-1 is much more sensitive and provides much more accurate data than microphotometers [7].

ACKNOWLEDGMENTS

The authors are indebted to V.A. Ditlov, who suggested the use of the MAS-1 for processing beta-ray spectrogram, as well as K.Ya. Gromov and Yu.V. Khol'nov for their encouragement.

This work was supported by the Russian Foundation for Basic Research (grant no. 00-02-16695).

REFERENCES

1. Yu. D Aleshin, V. V. Kolesnikov, and V. I. Silaev, Prib. Tekh. Éksp., No. 2, 43 (1997).
2. Yu. D. Aleshin, O. K. Egorov, V. V. Kolesnikov, *et al.*, Prib. Tekh. Éksp., No. 5, 37 (1999).
3. Yu. D. Aleshin, V. V. Vinogradov, O. K. Egorov, *et al.*, Preprint No. 10-97, ITÉF (Institute of Theoretical and Experimental Physics, 1997).
4. A. A. Abdurazakov, T. A. Islamov, A. Kh. Kholmatov, *et al.*, *Atlas of Internal Conversion Electron Spectra in the Range A = 131–172* (Tashkent. Gos. Univ., Tashkent, 1991).
5. B. S. Dzhelepov and S. A. Shestopalova, *Decay Schemes for Radioactive Nuclei with A = 169–170* (Nauka, Leningrad, 1988).
6. Yu. D. Aleshin, T. A. Islamov, V. G. Kalinnikov, *et al.*, Prib. Tekh. Éksp., No. 3, 72 (2001).
7. T. A. Islamov, V. G. Kalinnikov, T. T. Kambarova, *et al.*, Pis'ma Zh. Tekh. Fiz. **27** (13), 76 (2001) [Tech. Phys. Lett. **27**, 563 (2001)].

Translated by V. Isaakyan

Technical Physics, Vol. 48, No. 3, 2003, pp. 374–375. Translated from Zhurnal Tekhnicheskoĭ Fiziki, Vol. 73, No. 3, 2003, pp. 100–101.

BRIEF COMMUNICATIONS

Estimation of the Pressure in a "Slow" Spark Discharge in a Cylindrical Water-Filled Chamber

G. A. Shneerson

St. Petersburg State Technical University, ul. Politekhnicheskaya 29, St. Petersburg, 195251 Russia

e-mail: integr@delfa.net

Received September 17, 2002

Abstract—On the assumption that a spark discharge in water is quasi-steady, its pressure and channel radius are calculated. It is shown that the key discharge parameter is the action integral $S = \int_0^t i^2\,dt$, where i is the current in the channel. The conductivity only slightly affects the computational results and thus can be assumed to be constant. The formulas obtained can be applied to a discharge along the axis of a cylindrical water-filled chamber if the deformation of its walls over the discharge time is negligibly small and the pulse duration is several times greater than the time of sound propagation in water from the axis of the chamber to its wall. At relatively low pressures ($P \le 10^8$ Pa), $P \sim R^{-4/3}$, where R is the chamber radius. *© 2003 MAIK "Nauka/Interperiodica".*

The pressure due to an electrical discharge in a water-filled cylindrical chamber with undeformable walls can be approximately calculated if it is assumed that the discharge is quasi-steady. This means that the discharge current rise time is much longer than the time of sound propagation from the axis of the chamber to its wall. It can also be assumed that the discharge channel is a cylinder of radius r_c that is coaxial with the chamber of constant radius R. It is known that the density of a medium inside the discharge channel is much lower than that of surrounding water; therefore, the plasma mass in the channel can be neglected. Under these assumptions, the water mass conservation law can be written as $\rho V' = \text{const}$, where ρ is the water density in the region $r_c < r < R$ and $V' = \pi(R^2 - r_c^2)$ is the water volume (per unit length). Hence,

$$\frac{d\rho}{\rho} = -\frac{dV'}{V'}. \tag{1}$$

The simplest equation of state for water (Tait's equation) has the form

$$P \approx P_0(\rho/\rho_0)^\alpha + A\lfloor(\rho/\rho_0)^\alpha - 1\rfloor,$$

where P is the pressure in the chamber, which is equal (in the quasi-steady regime) to the pressure in the discharge channel; ρ_0 is the initial water density; P_0 is the initial pressure; and $A = 3.05 \times 10^8$ Pa and $\alpha = 7.15$ [1]. If it is assumed that $P_0 \ll P$, the first term in the equation for pressure can be neglected.

Equation (1) can be transformed into

$$\rho = \rho_0 V_0'/V' = \rho_0 \frac{R^2}{R^2 - r_c^2}, \tag{2}$$

then,

$$P \approx A\left[\left(1 - \frac{r_c^2}{R^2}\right)^{-\alpha} - 1\right] = A[(1-x)^{-\alpha} - 1], \tag{3}$$

where $x = r_c^2/R^2$.

This equation can be solved jointly with the energy balance equation [2]

$$\frac{i^2(t)}{\pi\sigma r_c^2} = \frac{1}{\gamma - 1}\frac{d}{dt}(Pr_c^2) + P_c\frac{d}{dt}(r_c^2), \tag{4}$$

where $\gamma = 1.22$–1.30 is the adiabatic exponent of the plasma, σ is the plasma conductivity, and $i(t)$ is the discharge current.

In terms of the new variable

$$\tau = \frac{1}{A\pi^2 R^4}\int_0^t \frac{i^2}{\sigma}dt,$$

Eq. (4) takes the form

$$\frac{1}{x} = \frac{1}{\gamma - 1}\frac{d}{d\tau}(x\theta) + \theta\frac{d}{d\tau}x, \tag{5}$$

where $\theta = P/A = (1-x)^{-\alpha} - 1$. The solution to this equation is

$$\tau = \frac{x^2}{\gamma - 1}\theta + \frac{\gamma - 2}{\gamma - 1} \times\left[\frac{1 - (1-x)^{-\alpha+2}}{\alpha - 2} - \frac{1 - (1-x)^{-\alpha+1}}{\alpha - 1} - \frac{x^2}{2}\right]. \tag{6}$$

1063-7842/03/4803-0374$24.00

The applied energy per unit channel length is given by

$$w = \pi A R^2 \left\{ \frac{1}{\gamma - 1} x[(1-x)^{-\alpha} - 1] + \frac{1}{\alpha - 1}[(1-x)^{1-\alpha} - 1] - x \right\}. \quad (7)$$

The computational results shown in the figure are represented as the channel radius and pressure vs. the parameter τ (the graphs are plotted for the special case $\gamma = 1.25$ and $\alpha = 7.15$).

If the conductivity varies insignificantly over most of the discharge time, one can put $\sigma = \text{const} = (0.3\text{–}3.0) \times 10^4\ (\Omega\ \text{m})^{-1}$ [3]. In this case,

$$\tau = (S/\sigma)/(A\pi^2 R^4),$$

where $S = \int_0^t t^2\, dt$ is the so-called action integral, which is commonly encountered in the problems of electrical explosion of semiconductors and breakdown in gases.

Consider the case $r_c/R \ll 1$, when only the dominant term in binomial expansion (3) can be left:

$$(1 - r_c^2/R^2)^{-\alpha} \approx 1 + \alpha r_c^2/R^2.$$

Here, $P \approx A\alpha(r_c/R)^2$ and Eq. (4) takes the form

$$\frac{1}{2\pi^2 r_c^2} = \frac{\gamma + 1}{\gamma - 1} \frac{\alpha A}{R^2} r_c^3 \frac{dr_c}{d(S/\sigma)}. \quad (8)$$

Thus, we arrive at the relationships for the channel radius and pressure:

$$r_c = \left[\frac{3(\gamma - 1)R^2}{(\gamma + 1)\pi^2 \alpha A} \frac{S}{\sigma} \right]^{1/6}, \quad (9)$$

$$P = (\alpha A)^{2/3} \left[\frac{3(\gamma - 1)}{\pi^2 (\gamma + 1)} \frac{S}{\sigma} \right]^{1/3} R^{-4/3}. \quad (10)$$

It is noteworthy that, other conditions being equal, the pressure rises with diminishing radius as $P \sim R^{-4/3}$. The above expansion provides a reasonable estimate for many applications if $r_c/R \le 0.2$, which corresponds to $P \le 10^8$ Pa.

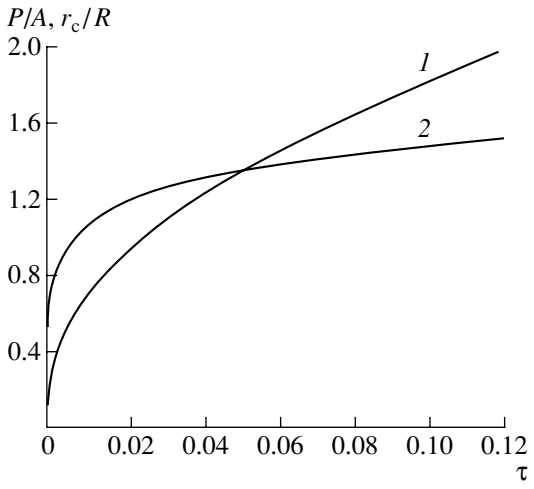

Time dependence of (*1*) the channel radius and (*2*) the pressure in the channel.

By way of example, let us estimate the pressure in the channel and the channel radius for a discharge in a cavity of radius $R = 2 \times 10^{-2}$ m at the instant the current reaches a maximum amplitude of 10 kA. The current rise time is $t_m = 2 \times 10^{-4}$ s, which is 15 times that of sound propagation from the axis of the chamber to its wall. Thus, the process is quasi-steady. In this case, $S \cong i_m^2 t_m/2 = 10^4\ \text{A}^2/\text{s}$. At $\sigma = 3 \times 10^4\ (\Omega\ \text{m})^{-1}$, the pressure estimated by formula (10) at the instant of current maximum is $P(t_m) \approx 1.5 \times 10^8$ Pa. The pressure is seen to depend on the conductivity only slightly, allowing the use of estimates for σ.

REFERENCES

1. R. H. Cole, *Underwater Explosions* (Van Nostrand, Princeton, 1948; Inostrannaya Literatura, Moscow, 1950).
2. K. A. Naugol'nykh and N. A. Roĭ, *Electrical Discharge in Water* (Nauka, Moscow, 1971).
3. I. Z. Okun', Zh. Tekh. Fiz. **41**, 302 (1971) [Sov. Phys. Tech. Phys. **16** (2), 227 (1971)].

Translated by B. Kalinin